Sub-Cycle Control of Strong-Field Processes on the Attosecond Timescale

Carlström, Stefanos

2016

Document Version:
Publisher's PDF, also known as Version of record

Sub-Cycle Control of Strong-Field Processes on the Attosecond Timescale

Sub-Cycle Control of Strong-Field Processes on the Attosecond Timescale

Stefanos Carlström

2017

LUND
UNIVERSITY

Akademisk avhandling som för avläggande av teknologie doktorsexamen vid tekniska fakulteten vid Lunds Universitet kommer att offentligen försvaras den 26 januari 2017, kl. 13:15 i Rydbergssalen, på Fysiska Institutionen, Professorsgatan 1, Lund.
Fakultetsopponent: Prof. Dr. Eric Cormier, Université de Bordeaux, France

Academic dissertation which, by due permission of the Faculty of Engineering at Lund University, will be publicly defended on Thursday 26th January, 2017, at 1:15pm in Rydberg's hall, at the Department of Physics, Professorsgatan 1, Lund, for the degree of Doctor of Philosophy in Engineering.
Faculty opponent: Prof. Dr. Eric Cormier, Université de Bordeaux, France

בס"ד

SUB-CYCLE CONTROL *of* STRONG-FIELD PROCESSES *on the* ATTOSECOND TIMESCALE

STEFANOS CARLSTRÖM

MMXVII

Sub-Cycle Control of Strong-Field Processes on the Attosecond Timescale

Keywords: High-order harmonic generation, quantum path interference, coherence

Division of Atomic Physics
Department of Physics
Faculty of Engineering, lth
Lund University
po box 118
se-221 00 Lund
Sweden

http://www.atomic.physics.lu.se

Printed in Sweden by Media-Tryck, Lund, 2016
Set in Garamond Premier Pro using Emacs 25.1.1, Org 9.0.1, and LuaLaTeX.
Musical score set using Lilypond.

issn: 0281-2762
Lund Reports on Atomic Physics, lrap: 531 (2016)

isbn: 978-91-7753-116-6 (print)
isbn: 978-91-7753-117-3 (pdf)

Аллилуіа

Благословенъ еси, Господи

Серге́й Васи́льевич Рахма́нинов

Оп. 37 — Всенощное бдение

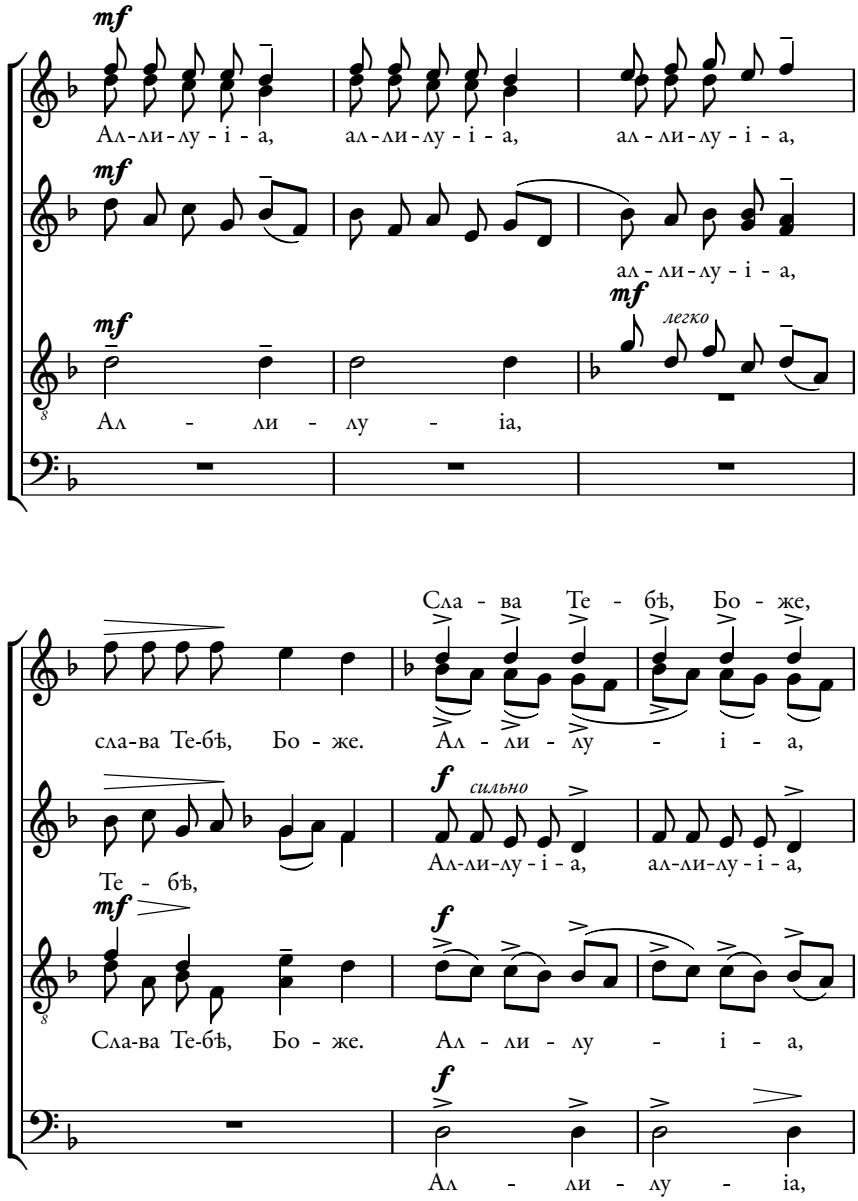

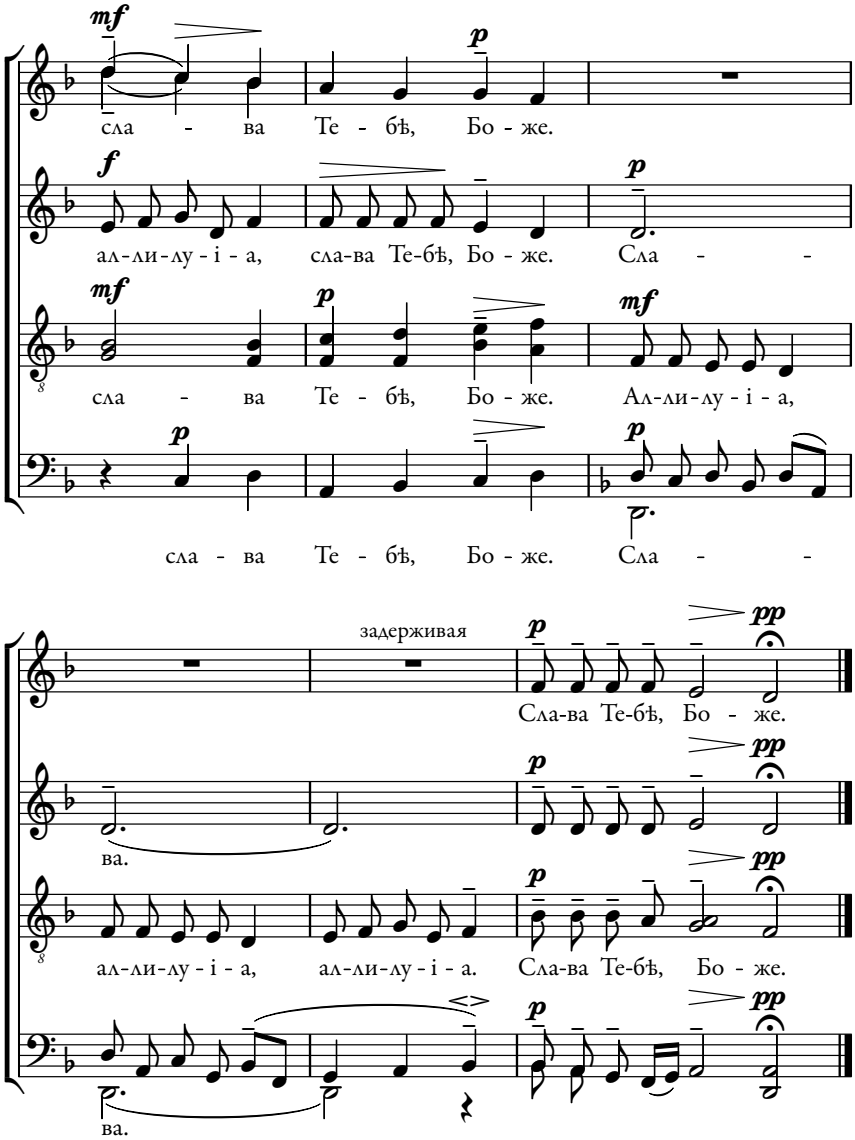
mf
p
сла - ва Те - бѣ, Бо - же.
f
p
ал-ли-лу - і - а, сла-ва Те-бѣ, Бо - же. Сла - -
mf
p
mf
сла - ва Те - бѣ, Бо - же. Ал-ли-лу - і - а,
p
p
сла - ва Те - бѣ, Бо - же. Сла - -
задерживая
p
pp
Сла-ва Те-бѣ, Бо - же.
ва.
ал-ли-лу - і - а, ал-ли-лу - і - а. Сла-ва Те-бѣ, Бо - же.
ва.

Abstract

This PhD thesis deals with the sub-cycle nature of ultrafast phenomena that occur in strong-field light–matter interactions. As it is of interest to control these phenomena, we must understand them in order to manipulate them. The tools at our disposal are intense laser pulses of short duration, and the systems we study are atoms. A host of exotic phenomena may occur in strong-field light–matter interaction, such as *high-order harmonic generation* and *above-threshold ionization*. These processes exhibit aspects of both quantum mechanics and classical mechanics, in a fascinating blend.

An important part of the work described in this thesis concerns the quantum paths of the electrons involved in these processes. The link between their journey and the time at which their journey begins is examined in a variety of ways. One property that quantum mechanical particles do not share with their classical counterparts is that the former may take a multitude of paths to reach their final destination. Furthermore, these paths may interfere such that the probability of detecting the particle is enhanced, suppressed, or sometimes even completely cancelled out.

Populärvetenskaplig sammanfattning

Denna avhandling behandlar olika sätt att förstå och kontrollera ultrasnabba fenomen. Med detta menas processer som äger rum under loppet av en cykel av synligt ljus (ungefär en *femtosekund*, en miljondels miljarddels sekund), eller under ännu kortare tidsintervall; detta är tidsskalor som vida understiger vår vardagliga fattningsförmåga. En elektron bunden till en atomkärna rör sig med en hastighet som är några hundradelar av ljusets, vilket innebär en omloppsbana med en periodtid som mäts i *attosekunder* – en attosekund är en miljarddels miljarddels sekund. Likaså sker processer som excitation och jonisation på dessa tidsskalor, vilka är alltför korta för konventionell elektronik att följa. Istället använder man sig av en stroboskopisk teknik, där en ultrakort ljuspuls används på samma sätt som en fotografisk blixt för att »frysa« förloppet.

I avhandlingen studeras dels den process som ligger till grund för de ultrakorta ljuspulserna, så kallad *hög övertonsgenerering*, som i sig är ett ypperligt exempel på en ultrasnabb process och dels användningen av dessa ultrakorta ljuspulser för att på djupet tränga in i den fysikaliska teori som beskriver mikrokosmos, kvantmekaniken.

Hög övertonsgenerering sker när ljuset från en stark laser fokuseras i till exempel en gas som joniseras. Den fria elektronen blir accelererad av ljuset och kan, om den stöter på den jon den lämnade, återinfångas och utstråla högenergetiskt ljus i form av korta ljuspulser. När det drivande laserljuset är så starkt som krävs för att hög övertonsgenerering skall vara möjlig, rör man sig samtidigt i det gränsland som existerar mellan den mer exotiska fysik som kvantmekaniken utgör och den klassiska fysiken som vi känner den från Newtons och Maxwells teorier. Till vilken grad låter sig den stundom absurda värld som mikrokosmos utgör förstås utifrån den intuition vi har från vår vardag? Detta har varit ett av målen med min avhandling.

Jag har också undersökt ett annat perspektiv; de fall där mikrokosmos avviker som mest från vår vardag. Speciellt har studerats det faktum att en mikroskopisk partikel inte tar *en* utan *flera* vägar för att nå sitt mål. Med så kallade interferometriska tekniker, som grundar sig på den mikroskopiska materiens vågnatur, är det möjligt att mäta den »hastighet« med vilken partikeln rör sig längs de olika vägarna. Detta experiment har flera beröringspunkter med Youngs berömda dubbelspalt, där ljuset bryts i två smala springor för att sedan interferera och ömsom förstärkas ömsom släckas ut på andra sidan.

En bild som kan hjälpa förståelsen för partiklarnas möjlighet att gå flera vägar samtidigt står att finna i musiken; det ljud som når åhöraren utgörs i ett givet ögonblick inte av endast en frekvens. I *polyfonisk musik* sammanvävs flera parallella stämmor till en välklingande harmoni. Detta är närmast att likna vid flera partiklar som går olika vägar och skiljer sig inte från vår intuitiva förståelse. Däremot avger varje enskilt instrument självt en mängd frekvenser samtidigt; dessa kallas övertoner och deras beskaffenhet avgör instrumentets unika klangfärg. På liknande sätt som vårt känsliga öra med lätthet kan skilja olika instrument åt, kan de känsliga mätningar avhandlingen baseras på, avgöra karaktären hos de olika vägar partiklarna tagit genom att studera deras »klangfärg«.

I avhandlingsarbetet har experiment utförts för att mäta ovan nämnda fenomen med en precision som överstiger vad som annars är vanligt inom forskningsfältet. Dock har tonvikten varit att med de teoretiska verktyg som finns till hands försöka förstå och förklara observationerna. Mycket av mitt arbete har skett med hjälp av superdatorer, eftersom beräkningarna kan vara väldigt krävande. För att superdatorernas kraft skall komma till nytta, är det viktigt att beräkningskoderna är effektiva och jag har lagt mycket tid på att lyckas med detta.

Contents

Thesis

Papers

List of Publications

I 'Noncollinear optical gating'
Christoph Michael Heyl, Samuel Nils Bengtsson, Stefanos Carlström, Johan Mauritsson, Cord Louis Arnold, and Anne L'Huillier
New Journal of Physics **16**(5) 052001 (2014)

II 'Phase metrology with multi-cycle two-colour pulses'
Carl Leon Michael Petersson, Stefanos Carlström, Kenneth Joseph Schafer, and Johan Mauritsson
Journal of Physics B: Atomic, Molecular and Optical Physics **49**(9) 095002 (2016)

III 'Sub-cycle ionization dynamics revealed by trajectory resolved, elliptically-driven high-order harmonic generation'
Esben Witting Larsen, Stefanos Carlström, Eleonora Lorek, Christoph Michael Heyl, David Paleček, Kenneth Joseph Schafer, Anne L'Huillier, Donatas Zigmantas, and Johan Mauritsson
Scientific Reports **6** 39006 (2016)

IV 'Spatially and spectrally resolved quantum path interference with chirped driving pulses'
Stefanos Carlström, Jana Preclíková, Eleonora Lorek, Esben Witting Larsen, Christoph Michael Heyl, David Paleček, Donatas Zigmantas, Kenneth Joseph Schafer, Mette B Gaarde, and Johan Mauritsson
Accepted for publication in: *New Journal of Physics*

V 'Dispersion control of attosecond pulse trains'
Chen Guo, Anne Harth, Stefanos Carlström, Yu-Chen Cheng, Sara Mikaelsson, Erik Mårsell, Arthur Losquin, Miguel Miranda, Kenneth Joseph Schafer, Anders Mikkelsen, Johan Mauritsson, Cord Louis Arnold, and Anne L'Huillier
Manuscript in preparation

VI 'Quantum coherence in photo-ionization with tailored XUV pulses'
Stefanos Carlström, Johan Mauritsson, Kenneth Joseph Schafer, Anne L'Huillier, and Mathieu Gisselbrecht
Manuscript in preparation

List of Abbreviations

ATI	above-treshold ionization. 24
CC	close-coupling approximation. 10
CEP	carrier–envelope phase. 27, 121
DME	dipole matrix elements. 73
FFT	fast Fourier transform. 133
FHT	fast Hankel transform. 134
FWHM	full-width at half maximum. 31
GDD	group delay dispersion. 121
GPU	graphics processing unit. 15
HF	Hartree–Fock. 9
HHG	high-order harmonic generation. 17
HH	high-order harmonic. 18
HO	harmonic order. 22
HWHM	half-width at half maximum. 50
MCHF	multi-configurational Hartree–Fock. 9
NOG	non-collinear optical gating. 62
QPD	quantum path distribution. 41
QPI	quantum path interference. 35
SAE	single-active-electron approximation. 10
SE	time-independent Schrödinger equation. 8
SFA	strong-field approximation. 21
SI	Système international d'unités. 5
TDSE	time-dependent Schrödinger equation. 7
VMIS	velocity map imaging spectroscopy. 26
XUV	extreme ultraviolet. 3

Thesis

Introduction

I

Nihil tam absurde dici potest, quod non dicatur ab aliquo philosophorum
There is nothing so absurd that it has not been said by some philosopher.

Marcus Tullius Cicero, 106–43 BC

The book you are holding in your hand, is my PhD thesis, an opus written to summarize the studies I have carried out during the past five years to reach enlightenment in the field of atomic physics. Enlightenment is still some way off, but I have learnt a thing or two that I would like to share with you.

Atomic physics is the area of physics that deals with atoms, once thought to be the smallest building blocks of matter. The word atom is derived from the Greek word ἄτομος (átomos), which means indivisible. The idea that all matter was composed of an entity that could not be divided was proposed by the Greek philosopher Democritos (Δημόκριτος, c. 460–c. 370 BC). Today, we know that atoms are, in fact, divisible. This does not mean that Democritos was wrong, but rather that the physicists and chemists of the nineteenth century applied the label to the wrong entity.

Atoms are, however, still very small – beyond what we can observe with our human senses. Since the advent of atomic physics, light has been used as to investigate atoms; first as a means of identification, through spectra that provide information allowing us to discern one atomic species from another, but recently also – and this is the topic of this thesis – as a means of influencing the atom. Light can interact with atoms in many ways, for instance, by exciting and ionizing them. The energies required for this range from 1 eV to 100 eV, which correspond to near-infrared light and *extreme ultraviolet* (XUV) light. In the present work, highly energetic light has been generated through a process called high-order harmonic generation. This process is capable of generating light with energies up to a few keV.

An intriguing aspect of the microcosmos is the wave nature of matter and its ability to reside in more than one state at a time. As a consequence of this, a particle can follow more than one path to its final destination. This is a recurring theme in my thesis; the identification and study of the pathways of rapidly moving electrons. In the same way that light enables us to study microscopic

matter, ultrashort pulses of light enable us to study ultrafast phenomena, such as ionization and quantum path interference.

Physics, being part of the positivistic system of science, requires continuous interplay between experimental study and theoretical interpretation to advance. A quantity may be measured in an experiment with arbitrary precision, but without a theoretical understanding of the underlying phenomena, one cannot claim to have gained any knowledge. One branch of theoretical physics that bridges the gap of experimental and theoretical physics, is numerical physics, wherein one can perform 'numerical experiments', turning on and off different aspects of the problem under consideration. This is an excellent way of disentangling those aspects that are relevant from those that only play a minor rôle.

Outside the realm of the natural sciences, my greatest pleasures lie in linguistics, history, music, and photography, and since I have always felt that everything we do should be permeated by *les beaux-arts*, I have often said, half-jokingly, half-seriously, that the main objective of science is to produce beautiful pictures. I hope that I have in some measure contributed to this endeavour.

1.1 Outline

This thesis is arranged in the following way. In §2, the theoretical framework and tools used in the thesis are described, while §3 describes strong-field light–matter interaction and the phenomena that occur under these circumstances. §§4–5 describe microscopic aspects of high-order harmonic generation, i.e. the rôle of the single atom in the process; the former chapter treats interference between the quantum paths in high-order harmonic generation, while the latter chapter discusses the effects of elliptical polarization of the driving field on the process. Macroscopic effects, i.e. the collective response of a multitude of atoms, are the subject of §6. Finally, §7 posits a new exciting way of studying similarities and differences between the wave nature of matter and light.

Some technical details are presented in the appendices. This means that this thesis can be read in two ways. The main text can be read foregoing the appendices altogether to obtain a brief overview of sub-cycle strong-field physics, while a more complete understanding of the field will be achieved by referring to the appendices as and when indicated in the main text. The work itself is, of course, embodied in the papers, which are to be found last in this thesis.

1.2 Notes

The *atomic unit system* of Hartree (1928) is used, unless otherwise stated. In this system, a number of important quantities, including the electron mass m_e, the elementary charge e, Planck's reduced constant $\hbar$, and Coulomb's constant $1/4\pi\varepsilon_0$, are all set to unity, such that, e.g. the Schrödinger equation

$$\mathrm{i}\hbar\frac{\partial}{\partial t}\Psi = \left(-\frac{\hbar^2}{2m_e}\nabla^2 + V\right)\Psi$$

instead reads

$$\mathrm{i}\frac{\partial}{\partial t}\Psi = \left(-\frac{\nabla^2}{2} + V\right)\Psi,$$

which simplifies the notation considerably, and makes the physics more visible. In atomic units, the relation between the strength of an electric field and its intensity is simply $I = \mathcal{E}^2$. [See appendix A for a list of derived units, and their values in *Système international d'unités* (SI).]

The primary polarization axis is usually taken to be $\mathbf{e}_z$, and $\mathbf{e}_x$ as the secondary axis, which means that the propagation axis is $\mathbf{e}_y$. This is still a right-handed coordinate system, since zxy is a cyclic permutation of xyz; the latter being the conventional order in electrodynamics. The reason for this difference in conventions is that linear polarization in the dipole approximation is described by one component of the dipole operator, where the z component is the one usually expressed using only one spherical harmonic, $Y_0^1(\vartheta, \phi)$.

A Brief Introduction to Quantum Dynamics

2

Physicists use the wave theory on
Mondays, Wednesdays and Fridays
and the particle theory on Tuesdays,
Thursdays and Saturdays

William Henry Bragg, 1862–1942

The theoretical language of attosecond science is that of time-dependent quantum mechanics, or quantum dynamics. The origin of quantum mechanics lies in the study of atomic spectra, a fervent activity in the late 19th century. Among the pioneers, the foremost was, without doubt, the spectroscopist Johannes 'Janne' Rydberg, in Lund. He is the discoverer of the famous *Rydberg formula* for the energy spectrum of hydrogen and alkali atoms:

$$\frac{\nu}{N_0} = \frac{1}{(m_1 + c_1)^2} - \frac{1}{(m_2 + c_2)^2} \tag{2.1}$$

or equivalently,

$$\frac{1}{\lambda_{\text{vac}}} = RZ^2 \left[\frac{1}{(n_1 + c_1)^2} - \frac{1}{(n_2 + c_2)^2} \right], \tag{2.2}$$

where λ_{vac} is the wavelength of the emitted/absorbed radiation in vacuum, $R = 10\,973\,731.568\,508(65)\,\text{m}^{-1}$ is the *Rydberg constant*, Z the nuclear charge, n_1 and n_2 represent the different energy levels of the atom, and c_1 and c_2 their respective quantum defects. The nucleus is assumed to be of infinite mass.

This model was purely empirical, i.e. it was based on measurements, and the first steps to explaining the cause of this behaviour were taken by Bohr (1913a,b,c). The Bohr model showed quantitative agreement with the line spectrum of hydrogen, but beyond this simple atom, it was difficult to reconcile the model to the experiments. It was not until Schrödinger (1926) formulated his famous *time-dependent Schrödinger equation* (TDSE),

$$\mathrm{i}\frac{\partial}{\partial t}\Psi(\mathbf{r};t) = H\Psi(\mathbf{r};t), \tag{2.3}$$

which laid the foundation of *wave mechanics*, later to be known as *quantum mechanics*, that it could be said there was an understanding of the physics behind atomic spectra. In this equation, Ψ is known as the *wavefunction*, which

describes the *state* of the physical system under consideration, and $\mathcal{H}$ is the *Hamiltonian* of the system, describing the particles and forces involved. The Hamiltonian is, in general, both space- and time-dependent. For a hydrogen atom in free space, the Hamiltonian can be written

$$\mathcal{H} = \mathcal{T} + \mathcal{U} = -\frac{\nabla^2}{2} - \frac{1}{r}, \tag{2.4}$$

where $\mathcal{T} = -\nabla^2/2$ is the operator of kinetic energy, and $\mathcal{U} = -\frac{1}{r}$ is the operator of potential energy, due to the atomic nucleus. For multi-electron atomic systems, the Hamiltonian not only includes the attraction of every electron towards the nucleus of charge Z, but also the mutual repulsion between all the electrons:

$$H_N = \sum_{i=1}^{N} \left(-\frac{\nabla_i^2}{2} - \frac{Z}{r_i} \right) + \sum_{ij} \frac{1}{r_{ij}}. \tag{2.5}$$

If the Hamiltonian can be separated into an atomic part and an interaction part, due to external forces, this is usually written

$$\mathcal{H} = H_0(\mathbf{r}) + H_{\mathrm{I}}(\mathbf{r}; t); \tag{2.6}$$

and the spatial argument is often suppressed.

2.1 Spectra

By making the *ansatz* that the solution of (2.3) can be written as a standing wave (this is possible if the Hamiltonian is purely space-dependent, for instance in the case $\mathcal{H} = H_0$),

$$\Psi(\mathbf{r}; t) = \exp(-\mathrm{i}E_n t)\phi_n(\mathbf{r}), \tag{2.7}$$

(2.3) reduces to the *time-independent Schrödinger equation* (SE):

$$\mathcal{H}\phi_n(\mathbf{r}) = E_n\phi_n(\mathbf{r}). \tag{2.8}$$

This is an *eigenvalue type* equation, the exact solution of which is only possible for hydrogen-like systems. However, being an eigenvalue problem means it belongs to a larger class of problems, namely those of linear algebra and *functional spaces*, developed by Hilbert, Neumann, and Nordheim (1928). As is common in linear algebra, the notion of bases plays an important role. Although the *one-electron* solutions of (2.7) are incorrect solutions for multi-electron atoms, they constitute a *complete set*, over which any wavefunction may be expanded:

$$\Phi = \sum_n c_n\phi_n, \tag{2.9}$$

where c_n are known as *expansion coefficients* (function arguments omitted for brevity). There are many ways of calculating these expansion coefficients, but the simplest one is *perturbation theory*, where the deviation of (2.8) from the one-electron problem (typically Coulombic repulsion between two electrons) is allowed to *perturb* the one-electron solutions, giving rise to a shift in the energies [see e.g. Landau and Lifshitz (1977), §38 for an overview].

2.1.1 The multi-configurational Hartree–Fock method

An exact, but purely numerical, method of solving (2.8) for a Hamiltonian of the form (2.5) was pioneered by Hartree (1928), and improved upon by Fock (1930), yielding the *Hartree–Fock* (HF) method. This was subsequently developed by Hartree's PhD student, Froese Fischer (1970), into the *multi-configurational Hartree–Fock* (MCHF) method, which is a systematic way of including the interaction between the electrons in an atomic system. Given a reference configuration, the full wavefunction is expanded over all permissible correlation configurations (i.e. those of the same symmetry); the zeroth-order approximation being the reference configuration itself. The expansion coefficients are found by iterative minimization and the state space is gradually expanded by adding more and more configurations to the calculation, until the desired quantities (usually the transition energy between two physical states of interest) have converged. For example, the $1s^2\ {}^1S_0$ ground state of helium might be expanded as

$$\begin{aligned} \Psi(1s^2) \approx\ & 0.99596347\ \Phi(1s^2) + 0.06233620\ \Phi(2p^2) \\ & - 0.00168155\ \Phi(1s2s) - 0.00350562\ \Phi(2p3p) \\ & - 0.00008620\ \Phi(1s3s) - 0.00739892\ \Phi(3s^2) \\ & - 0.06197355\ \Phi(2s^2) + 0.01040140\ \Phi(3p^2) \\ & + 0.00238955\ \Phi(2s3s) - 0.01210078\ \Phi(3d^2), \end{aligned} \tag{2.10}$$

where Ψ denotes the sought physical state, and Φ denotes the weighted contribution of a particular configuration to the state.

This method is implemented in the non-relativistic limit in the ATSP2K package (Froese Fischer, Brage, and Jönsson 1997; Froese Fischer et al. 2007). A relativistic implementation, GRASP2K, also exists (Jönsson et al. 2007, 2013).

2.1.2 The close-coupling approximation

The MCHF method works very well when dealing with *bound states* that have a finite extent, however, with increasing principle quantum number n, the ex-

tents of hydrogenic wavefunctions grow rapidly ($\langle r \rangle \sim n^2 a_0/Z$). The ATSP2K package is well-suited for $n \leq 15$. Furthermore, for an $N+1$-body system, the Hilbert space has the dimensionality $\mathbb{C}^{3N+3}$, which means that an $N+1$-body wavefunction including continuum orbitals (as is necessary for treating ionization) is unthinkable. If we restrict ourselves to the case of single ionization, the *close-coupling approximation* (CC) offers a means of expanding the wavefunction as

$$|(N+1), E, J\rangle = \mathrm{A} \sum_i^{n_t} |\gamma_i(N) \otimes k_i \ell_i\rangle + \sum_j |\gamma_j(N+1); E, J\rangle, \qquad (2.11)$$

where the first sum antisymmetrically couples N-body wavefunctions (called 'targets' in CC theory) to one electron of momentum k to form an $N+1$ system. The second sum includes $N+1$-body 'perturbers' that account for the correlation due to the bound states of the $N+1$ system. (For a thorough review, see Bartschat 1996.)

The computational package used in the present work, which implements the CC approximation, is called BSR (Zatsarinny 2006) and is used in conjunction with ATSP2K (Zatsarinny and Froese Fischer 2009) to provide the basis functions and dipole matrix elements for the calculations described in PVI.

2.1.3 *The single-active-electron approximation*

Most of the calculations presented in this thesis have been performed in the *single-active-electron approximation* (SAE), reducing the problem to essentially that of hydrogen. Deviations therefrom are treated using *pseudo-potentials* (Kulander and Rescigno 1991; Stevens et al. 1992), which are effective, short-range potentials that capture the interaction of the valence electron with the core electrons, to some extent. These are numeric potentials that depend on both radius and orbital quantum number ℓ and their short-rangedness ensures that they identically vanish after a certain radius, after which only the long-range Coulombic $-1/r$ potential remains. Since they do not allow any rearrangement of the core electrons, they can only provide a good spectrum for the valence electron, due to screening effects, but they cannot account for any multi-electron effects. However, in strong-field physics, the SAE approximation is usually a very good one, at least in the case of single ionization below the saturation intensity of the gas (Krause, Schafer, and Kulander 1992; Sanpera et al. 1995). For higher intensities, non-sequential double ionization may occur, for which SAE is no longer valid (Feist et al. 2008; Manschwetus et al. 2016).

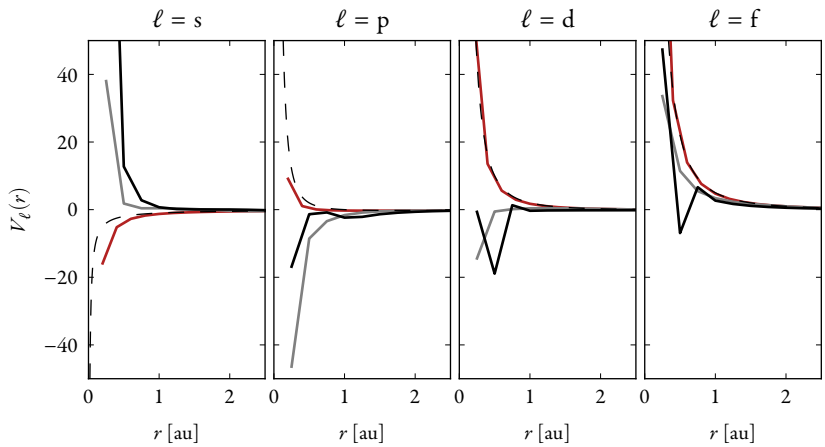

Figure 2.1: Potentials used for helium (red), neon (grey), and argon (black). The heavy lines show the pseudo-potential, $V_\ell(r)$, plus the centrifugal potential, $-1/r + \ell(\ell+1)/(2r^2)$, both of which depend on r and the orbital quantum number ℓ. The light dashed line is the hydrogenic long-range Coulomb potential plus the centrifugal potential, which corresponds to the force on the electron at long distances. For $\ell >$ d, the pseudo-potentials do not deviate appreciably from the hydrogenic case, and the potential is dominated by the centrifugal barrier. The fact that the s electron cannot penetrate the core in the case of neon and argon (due to the repulsive potential in the s channel), is an embodiment of the Pauli principle; the $\{2,3\}$s shell is already occupied in the ground state configuration of neon/argon.

2.2 Theory of time-dependent quantum mechanics

As stated above, any wavefunction may be expressed as a linear combination of basis functions. These need not be eigenfunctions of a specific operator, in fact they do not even need to be classical functions. We shall express this by considering a general basis set, spanned by the abstract vectors of a Hilbert space. The notation introduced by Dirac (1939), is commonly used in quantum mechanics. A vector is then written as $|\phi\rangle$, and its conjugate transpose* as $\langle\phi|$. Any vector in this Hilbert space may then be written as

* Formally its dual vector.

$$|\Psi\rangle = \sum_n c_n(t)|n\rangle. \tag{2.12}$$

Inserting this into (2.3), gives

$$\mathrm{i}\frac{\partial}{\partial t}\sum_n c_n(t)|n\rangle = \hat{H}\sum_n c_n(t)|n\rangle. \tag{2.13}$$

* This is not strictly necessary, but simplifies the discussion here. There are cases where non-orthogonal bases are useful.

Assuming orthogonality between the vectors,* that is, $\langle m|n\rangle = \delta_{mn}$, we can project (2.13) onto one of the basis vectors:

$$\mathrm{i}\frac{\partial}{\partial t}\sum_n c_n(t)\langle m|n\rangle = \langle m|H\sum_n c_n(t)|n\rangle \tag{2.14}$$

$$\iff \mathrm{i}\frac{\partial}{\partial t}c_m(t) = \sum_n c_n(t)\langle m|H|n\rangle. \tag{2.15}$$

By introducing the coefficient vector $\mathbf{c} = \begin{bmatrix} c_1 & c_2 & \dots & c_n \end{bmatrix}$, we can rewrite (2.15) as

$$\iff \mathrm{i}\frac{\partial}{\partial t}\mathbf{c}(t) = H\mathbf{c}(t), \tag{2.16}$$

where the *Hamiltonian matrix* has the elements $H_{mn} = \langle m|H|n\rangle$. The formal solution is given by

$$\mathbf{c}(t) = \mathrm{T}\exp\left[-\mathrm{i}\int_{-\infty}^{t}\mathrm{d}t' H(t')\right]\mathbf{c}(0), \tag{2.17}$$

where the time dependence of the Hamiltonian is written out explicitly. The time ordering operator T must be included since, in general, the Hamiltonian does not commute with itself at different times: $[H(t), H(t')]_- \neq 0$. This means that the infinitesimal sum the integral sign represents is not commutative either, but must be evaluated starting at the earliest time.

Time-dependent perturbation theory can be derived by expanding (2.17) in a Dyson series.

2.2.1 Magnus propagators

Another approach is to use a *propagator* which is an operator that given a state at a certain time, *propagates* it to any other time. It is written

$$\mathbf{c}(t_{n+1}) = \mathcal{U}(t_{n+1}, t_n)\mathbf{c}(t_n). \tag{2.18}$$

Magnus (1954) suggested that this propagator could be approximated by

$$\mathcal{U}(t_{n+1}, t_n) \approx \exp(\Omega^n), \tag{2.19}$$

where Ω^n is a matrix that can theoretically be chosen such that the approximation is, in fact, exact:

$$\Omega^n = -\mathrm{i}\int_{t_n}^{t_{n+1}}\mathrm{d}t' H(t'). \tag{2.20}$$

A common choice is the so-called *midpoint rule*, which is numerically correct to $\mathcal{O}(\tau^2)$, where the time step $\tau \equiv t_{n+1} - t_n$:

$$\Omega^n \approx -\mathrm{i}\tau H\left(t_n + \frac{\tau}{2}\right) \equiv -\mathrm{i}\tau H_{\hat{n}}. \tag{2.21}$$

A higher-order method using a two-stage Gaussian quadrature is [Blanes et al. 2009, (254)]

$$\Omega^n \approx -\frac{\mathrm{i}}{2}\tau(H_1 + H_2) - \frac{\sqrt{3}}{12}\tau^2 [H_2, H_1]_- , \tag{2.22}$$

where the Hamiltonian is evaluated at the quadrature nodes:

$$H_j \equiv H(t^n + c_j\tau), \quad c_{1,2} \equiv \frac{1}{2} \pm \frac{\sqrt{3}}{6}. \tag{2.23}$$

This method is temporally accurate to $\mathcal{O}(\tau^4)$, but entails computing the exponential of a commutator, the cost of which can be substantial. A better, commutator-free, scheme for operators of the form

$$A(t) = B + f(t)C, \tag{2.24}$$

is given by Alvermann, Fehske, and Littlewood (2012):

$$\mathcal{U}(t_{n+1}, t_n) \approx \exp[\tau_1(B + f_1 C)] \exp[\tau_2(B + f_2 C)] \exp[\tau_1(B + f_3 C)]. \tag{2.25}$$

The temporal accuracy of this method is also $\mathcal{O}(\tau^4)$, and the fact that three exponentials have to be computed for each time step, is mitigated by the possibility of using much larger time steps while maintaining the same accuracy. However, according to the Nyquist–Shannon sampling theorem (Nyquist 1928; Shannon 1949), it is still necessary to sample the time-dependent dipole moment at a sufficient number of time points for the calculation of dipole spectra. It can then be more advantageous in terms of execution time to choose a lower-order method for which the computational effort is lower. One possibility that has not yet been investigated is to calculate the time-dependent dipole moment for a sparse set of time points, using the higher-order method (2.25) and then *upsample* the signal before performing the Fourier transform to retrieve the dipole spectrum.

After finding an approximation for Ω^n, the next step is to approximate the matrix exponential in (2.19). The appropriate method of doing this is highly dependent on the matrix structure of Ω^n, which in turn depends on the choice of basis, $|n\rangle$. In this work, a number of methods have been used.

- Operator splitting [also known as *Strang Splitting*; Strang (1968) and Marchuk (1968)]. If the matrix has the form $C = A + B$ [as is the case in (2.6)], the exponential can be approximated by

$$\exp(C) = \exp(B/2)\exp(A)\exp(B/2) + \mathcal{O}([A, B]_-^2). \tag{2.26}$$

  The symmetric placement of the exponentials is important to preserve unitarity.
- Rational Padé (1892) approximants:

$$\exp(A) = \frac{1 + \frac{A}{2}}{1 - \frac{A}{2}} + \mathcal{O}(A^2), \tag{2.27}$$

  also known as the Crank–Nicolson scheme. In the field of ordinary differential equations, this corresponds to the trapezoidal rule. A rational polynomial of a matrix is to be understood as a two-stage method. To compute the action of the exponential of a matrix A on a vector $\mathbf{x}$, one first multiplies the vector by the numerator:

$$\mathbf{x}' = \left[1 + \frac{A}{2}\right]\mathbf{x}. \tag{2.28}$$

  The second step is to solve the system

$$\left[1 - \frac{A}{2}\right]\mathbf{y} = \mathbf{x}', \tag{2.29}$$

  thus

$$\exp(A)\mathbf{x} \approx \mathbf{y}. \tag{2.30}$$

  If the matrix A is tridiagonal, which is the case for three-point discretization of the kinetic operator, there are efficient methods for solving (2.29) using LU factorization.
- *Krylov methods* (Krylov 1931; Saad 1992, 2003), wherein the full matrix exponential is approximated by a subspace exponential; the subspace being by power iteration. This method of exponentiating a matrix can, in theory, be accurate to machine precision; however, if the integral in (2.20) is accurate to $\mathcal{O}(\tau^k)$, the full propagator in (2.19) can only be accurate to the same order. Nevertheless, this method is very useful for cases where it is not feasible to use other methods, due to the structure and/or the size of the Hamiltonian matrix.

2.2.2 *The single-active-electron approximation*

In the SAE, the TDSE reads

$$\mathrm{i}\frac{\partial}{\partial t}|\Psi\rangle = \left[-\frac{\nabla^2}{2} + V(\mathbf{r}) + H_I(\mathbf{r};t)\right]|\Psi\rangle. \tag{2.31}$$

Due to the non-locality of the pseudo-potentials near the origin, spectral methods are not suitable for propagation. Thus, it is not possible to work in the eigenbasis of the kinetic operator, and calculations are instead performed in the position basis. In this basis, the kinetic operator is non-local, so a three-point discretization obtained through a variational procedure is used, which accounts explicitly for the Coulomb singularity at the origin [for details, see Schafer et al. (2000) and Schafer (2009)].

Most of the calculations in the work described in this thesis were performed within the SAE (specifically PII, PIII, PIV, & PV). The algorithm is the same as that presented by Schafer (2009), but it has been translated to run on a *graphics processing unit* (GPU), a piece of hardware that is specialized for fast linear algebra. It has also been extended to the case of arbitrary polarization of the electric field in the z–x plane, as detailed in appendix C. In this algorithm, Ω^n is approximated using the midpoint rule (2.21) and the exponentiation is performed by a combination of Strang splitting (2.26), Padé approximants (for the atomic Hamiltonian), and rotations through a 2×2 method (Raedt 1987; Richardson 1991).

3 Strong-Field Light–Matter Interaction

Strong fields are those of strengths comparable to the binding Coulomb field of the atomic nucleus. In hydrogen, a single proton generates an electric field of $5.142 \times 10^{11}\,\mathrm{V\,m^{-1}}$, which corresponds to an electromagnetic field of intensity $3.509 \times 10^{16}\,\mathrm{W\,cm^{-2}}$ (these values are the atomic units of their respective quantities). Light fields approaching these strengths cannot be regarded as mere perturbations to the system. In fact, they are so strong that they can induce highly non-linear processes and even severely distort the binding potential of the atom. A quantity that is useful in characterizing these phenomena is the *Keldysh (1965) parameter*:

$$\gamma \equiv \frac{\omega\sqrt{2I_\mathrm{p}}}{\mathcal{E}}, \tag{3.1}$$

where ω is the angular frequency of the electromagnetic field, I_p the ionization potential of the atom that is being irradiated, and $\mathcal{E}$ the electromagnetic field strength. The Keldysh parameter delineates two regimes (see figure 3.1):

$\gamma \ll 1$ the *tunnelling regime*, where the binding potential is so distorted that it forms a barrier through which the electron may tunnel, and the angular frequency is sufficiently low that the electron has time to do so, and

$\gamma \gg 1$ the *multi-photon regime*, where either the field is too weak to distort the potential appreciably, or the angular frequency is too high for any quasi-stationary barrier to form [this picture is not complete, see Topcu and Robicheaux (2012)]. In this later case, stacking of photons to reach above the ionization potential provides a more adequate picture.

3.1 High-order harmonic generation

The process that enables and epitomizes attosecond science is that of *high-order harmonic generation* (HHG), discovered in the late 1980s by McPherson et al. (1987) and Ferray et al. (1988). By irradiating a gas with an intense laser, high-energy emission containing many multiples of the laser frequency was observed.

Subjecting a dielectric medium to intense radiation will induce polarization of the form:

$$\mathcal{P} = \sum_q \chi^{(q)} \mathcal{E}^q \tag{3.2}$$

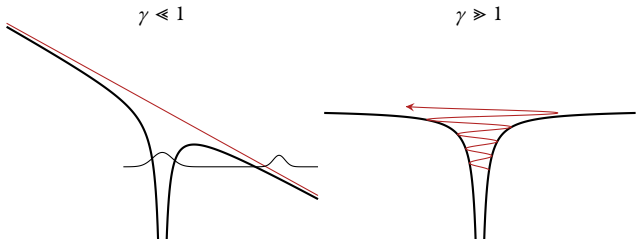

Figure 3.1: Illustration of the Keldysh parameter. Left: tunnel ionization, where the binding potential forms a barrier that is short enough for the electron to tunnel through it. Right: multi-photon ionization, where the electron 'jumps' up above the ionization threshold by absorbing the energy of multiple photons.

Since the electric field is dependent on time, the polarization will also vary with time and, according to Maxwell's equations of electrodynamics, a charge undergoing acceleration radiates. The dielectric medium will thus radiate with frequency components $q\omega$, $q \in \mathbb{N}$, where ω is the frequency of the electric field, often called the *fundamental frequency*. The *dielectric constants* $\chi^{(q)}$ depend on the material and usually vanish with increasing q. In the photon picture, this process corresponds to the absorption of q photons in succession followed by emission of one photon of energy $q\omega$. The probability of doing this is approximately p^q, where p is the probability of absorbing one photon. The harmonics generated in this fashion are called *perturbative harmonics*, since they can also be derived from perturbation theory. HHG is a radically different process. Firstly, the harmonic yield does not decrease exponentially with increasing order, at least for a large range of harmonic orders. Secondly, the electric field driving the HHG is so strong it cannot be considered a perturbation; instead it distorts the atomic potential to such a degree that tunnel ionization of the valence electron is possible. When an electron wave packet has been liberated this way, it will be accelerated in the electric field, and a small part of it may be driven back to the parent ion, where it recombines, or rather, interferes with the part of the wavefunction that was left behind. This interference generates a rapidly oscillating dipole, which is the source of the observed *high-order harmonic* (HH) radiation.

Since the external field is very strong, the wave packet moves according to the *Ehrenfest (1927) theorem* , which states that the trajectory of the position expectation value coincides with that of a classical particle. Because of this, it is common to describe HHG in a semi-classical model called the *simple man's model* or the *three-step model* (Schafer et al. 1993; Corkum 1993). This model describes the process in three separate steps: (i) the electron is ionized by the strong external field; (ii) it is then accelerated by the field and moves along its

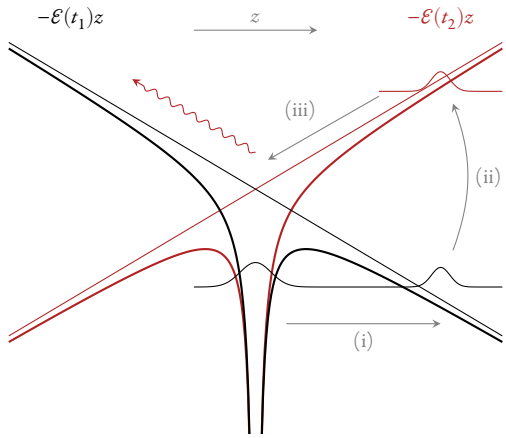

Figure 3.2: Three-step model of HHG. (i) The external field $\mathcal{E}(t)$ distorts the potential such that a barrier is formed, through which the electron can tunnel. (ii) The electron is subsequently accelerated in the external field. (iii) If the electron returns, it may recombine and give rise to emission of a photon.

classical trajectory in the combined field of the atom and the laser; and (iii) if the trajectory leads back to the parent ion, the electron may recombine leading to the emission of radiation with an energy $W_\mathrm{k} + I_\mathrm{p}$ (see figure 3.2). This is reminiscent of what was stated at the end of the previous paragraph. It is by virtue of the Ehrenfest theorem that our understanding from classical mechanics can be applied to the process of HHG, allowing the otherwise complicated wave motion to be divided into 'steps'. An alternate viewpoint was provided by Feynman (1965) in the path integral formulation of quantum mechanics, in which the electron takes all paths imaginable; the classical trajectory being the most likely.

Assuming that the ionic potential can be neglected after ionization, we can exactly solve the classical equations of motion of an electron in an electromagnetic field

$$\boldsymbol{\mathcal{E}}(t) = \Im\{\tilde{\boldsymbol{\mathcal{E}}}_0 \exp(\mathrm{i}\omega t)\}. \tag{3.3}$$

For a detailed derivation, see appendix B; here we quote the main result. The position of an electron appearing in the field at time t_i is given at all times by

$$\mathbf{r}(t) = \mathbf{r}_i + (t - t_i)\mathbf{p}_i + \frac{\mathcal{E}_0}{\omega^2}\Im\left(\mathfrak{p}\{\exp(\mathrm{i}\omega t) - [1 + \mathrm{i}\omega(t - t_i)]\exp(\mathrm{i}\omega t_i)\}\right), \tag{3.4}$$

where $\mathfrak{p}$ is the polarization vector.

Assuming $\mathbf{p}_i = 0$, we can express the instantaneous kinetic energy as

$$W_\mathrm{k}(t, t_i) = \frac{p^2}{2} = 2U_\mathrm{p}\left(\Re\left\{\mathfrak{p}[\exp(\mathrm{i}\omega t) - \exp(\mathrm{i}\omega t_i)]\right\}\right)^2, \tag{3.5}$$

where we have introduced the *ponderomotive energy*,

$$U_\mathrm{p} \equiv \frac{I_0}{4\omega^2}. \tag{3.6}$$

Recombination occurs at a time t_r, defined by

$$\mathbf{r}(t_r) = 0, \quad t_r > t_i. \tag{3.7}$$

This is a transcendental equation, which is not analytically solvable; however, a multitude of solutions exist and can be found numerically. Furthermore, of all pairs of (t_i, t_r), with the same final kinetic energy $W_\mathrm{k}(t_r, t_i)$, there are two pairs with an excursion time $\tau = t_r - t_i < T$, e.g. the electron returns within one oscillation of the fundamental field after ionization. The trajectory with the shorter excursion time ($\tau \lesssim 0.65T$) is termed the *short trajectory*, while the other trajectory is termed the *long trajectory*.

3.1.1 Linear HHG

Assuming linear polarization, $\boldsymbol{\mathcal{E}}(t) \parallel \mathbf{e}_z$, the motion is restricted to one dimension. Furthermore, it is usually assumed that the electron after ionization appears 'close' to the nucleus, with no initial velocity. Figure 3.3 shows characteristic trajectories for a range of different ionization times, t_i.

As seen in figure 3.3, the process described by the three-step model is repeated twice per cycle of the fundamental field, with alternating direction of ejection. This means that high-order harmonic radiation is emitted twice per cycle. A multi-cycle driving field will result in a train of XUV pulses. In the frequency domain this corresponds to only odd-order harmonics of the fundamental field (Alon, Averbukh, and Moiseyev 1998). From a physical point of view, this corresponds to the fact that in an isotropic medium, such as a noble gas, the even-order components of (3.3) must necessarily vanish, due to the inversion symmetry of the medium; upon inversion of the coordinates $\mathbf{r} \to -\mathbf{r}$, we have $\boldsymbol{\mathcal{E}} \to -\boldsymbol{\mathcal{E}}$ and $\boldsymbol{\mathcal{P}} \to -\boldsymbol{\mathcal{P}}$. Comparing with (3.2), this is only possible if $\chi^{(q)} = 0, \forall 2q \in \mathbb{Z}$. The emission of even-order harmonics is possible by breaking the symmetry of the process, either by using a non-symmetric medium (Franken et al. 1961; Ben-Tal, Moiseyev, and Beswick 1993; Kreibich et al. 2001) or a non-symmetric driving field (Perry and Crane 1993; Eichmann et al. 1995; Kim et al. 2005).

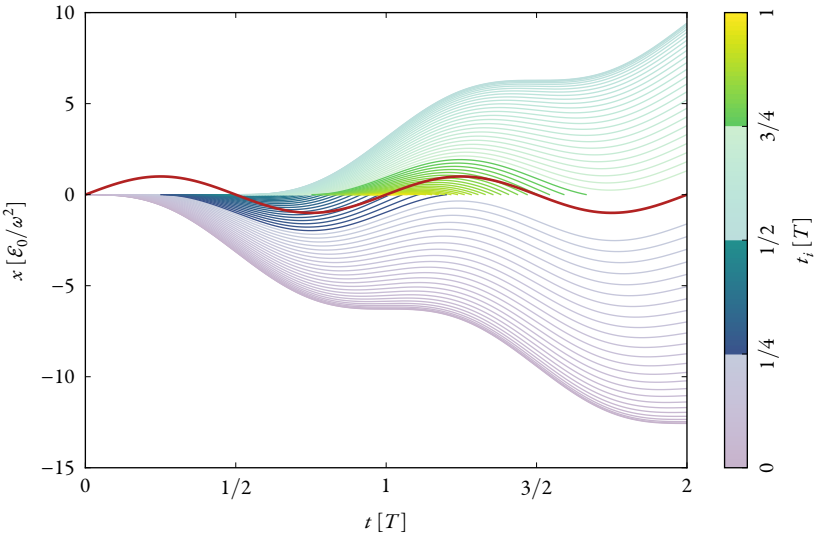

Figure 3.3: Characteristic classical trajectories of an electron driven by an oscillatory field. The colour scale corresponds to different ionization times t_i. Those trajectories that do not return to the parent ion are dimmed; they are important in above-threshold ionization. The driving field is shown in red, for reference.

3.1.2 *Strong-field approximation*

The most commonly used approximation in the description of HHG from gases is the *strong-field approximation* (SFA); (Lewenstein et al. 1994), which is, in essence, a quantum mechanical analogue of the three-step model. In its original formulation, it imposes a set of fairly strong approximations.

(1) Of all the bound states of the atom, only the ground state $|0\rangle$ contributes.
(2) The probability of remaining in the ground state is essentially unity.
(3) The free electrons propagate in the external field only, i.e. they are not influenced by the ionic potential.

The derivation can be found in appendix D. The time-dependent dipole is approximated as

$$\mathbf{r}(t) \approx \mathrm{i}\int_0^\infty \mathrm{d}\tau \left(\frac{\pi}{\varepsilon+\mathrm{i}\tau/2}\right)^{3/2} \underbrace{\mathbf{d}^*[\mathbf{p}_{\mathrm{st}}(t,\tau)-\mathcal{A}(t)]}_{\text{Step (iii)}} \underbrace{\exp[-\mathrm{i}S_{\mathrm{st}}(t,\tau)]}_{\text{Step (ii)}} \underbrace{\times\mathcal{E}(t-\tau)\cdot\mathbf{d}[\mathbf{p}_{\mathrm{st}}(t,\tau)-\mathcal{A}(t-\tau)]}_{\text{Step (i)}} + \text{c.c.} \tag{3.8}$$

The three-step model is very apparent in (3.8); at time $t-\tau$, the electron appears in the continuum with a momentum $\mathbf{p}_{\mathrm{st}}(t,\tau)-\mathcal{A}(t-\tau)$ [step (i); figure 3.2]. The acceleration in the external field [step (ii)] is contained in the propagator $\exp[-\mathrm{i}S_{\mathrm{st}}(t,\tau)]$, where $S_{\mathrm{st}}(t,\tau)$ is a stationary trajectory of the *quasi-classical action* S. Finally, at time t, the electron recombines [step (iii)] from a momentum state $\mathbf{p}_{\mathrm{st}}(t,\tau)-\mathcal{A}(t)$. The stationary momentum $\mathbf{p}_{\mathrm{st}}(t,\tau)$ is that which leads to a stationary trajectory on which an electron ionized at time $t-\tau$ returns to the parent ion at time t. The pre-factor $[\pi(\varepsilon+\mathrm{i}\tau/2)^{-1}]^{3/2}$ accounts for the quantum diffusion of the free electron during propagation.

From (3.8), it is obvious that different harmonics will have different phases, given by the quasi-classical action:

$$S(\mathbf{p},t_r,t_i)\equiv\int_{t_i}^{t_r}\mathrm{d}t\left\{\frac{[\mathbf{p}-\mathcal{A}(t)]^2}{2}+I_{\mathrm{p}}\right\}, \tag{3.9}$$

which depends on both which harmonic we are considering [the *harmonic order* (HO) is linked to the momentum $\mathbf{p}$], and which trajectory that generated the emission. Different trajectories of the same final momentum are linked to different pairs of ionization and recombination times, t_i, t_r. The fields they experience are thus different and thus also their accumulated phases. If we can tune the driving field, we can impart different phases on the different trajectories leading to the same harmonic order, as will be considered in the chapter on quantum path interference.

3.1.3 Semi-classical trajectories in HHG

Figure 3.4 shows the semi-classical trajectories of electrons ionized in the time window $[T/4, T/2]$. The least energetic short trajectory is that ionized the last and returning first: $(t_i,t_r)=(T/2,T/2)$, thus it has a vanishing excursion time and excursion length. Conversely, the least energetic long trajectory is ionized first and returning last: $(t_i,t_r)=(T/4,5T/4)$, which gives an excursion time of one laser cycle, and an excursion length of around one nanometre for optical wavelengths and moderate field strengths. Lastly, the most energetic trajectories of both classes of trajectories coincide, with an excursion time of about $0.65T$ and an excursion length of approximately half that of the longest trajectory.

3.2 ABOVE-THRESHOLD IONIZATION

It is apparent from figure 3.3 that many trajectories that do not return to the parent ion (dimmed colours). Instead, they lead to photoelectron emission at ener-

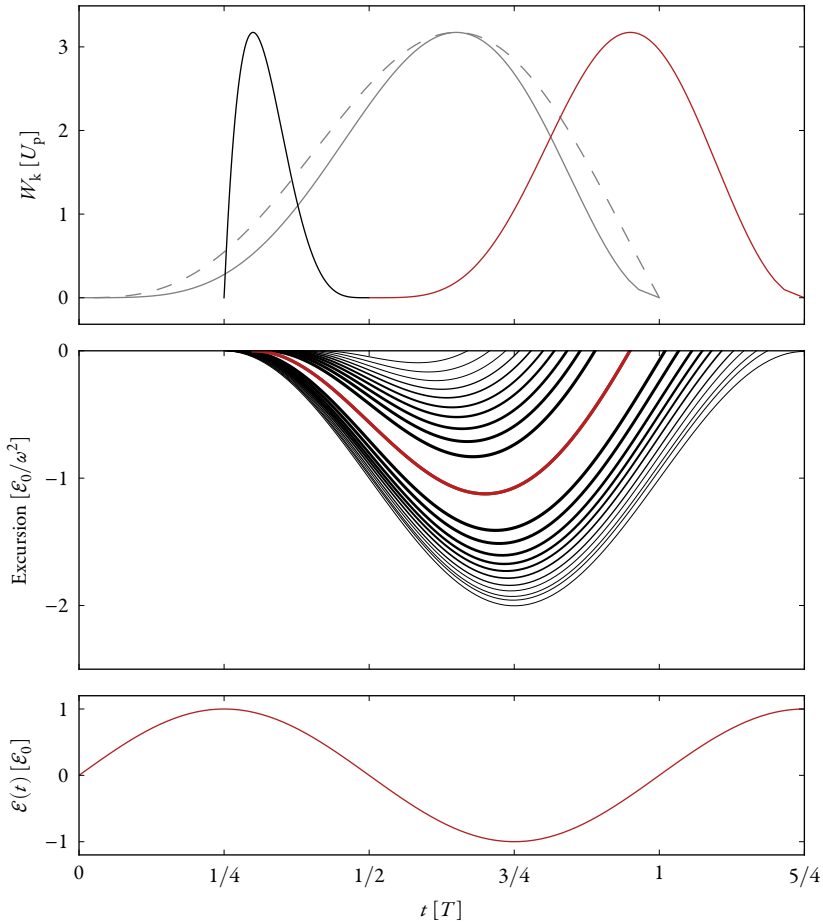

Figure 3.4: Classical picture of HHG. The upper panel shows the return kinetic energy as a function of ionization time t_i (black), return time t_r (red), and excursion time $\tau \equiv t_r - t_i$ (grey), found by solving (3.4) subject to $\mathbf{r}(t_r) = 0$. Also plotted, as a dashed line, is an approximation from the SFA, calculated by integrating the quasi-classical action (3.9) along the stationary trajectories in the field $\mathcal{E}(t) = \mathcal{E}_0 \cos(\omega t)$. The middle panel shows the trajectories generated in the time window $[T/4, T/2]$. The thickness of the lines indicates the return energy, and the most energetic trajectory is shown in red. The maximum excursion is $\sim 2\mathcal{E}_0/\omega^2$ which, for optical wavelengths and a driving intensity of 10^{14} W cm^{-2}, is of the order of a nanometre. The lower panel shows the fundamental driving field, for reference.

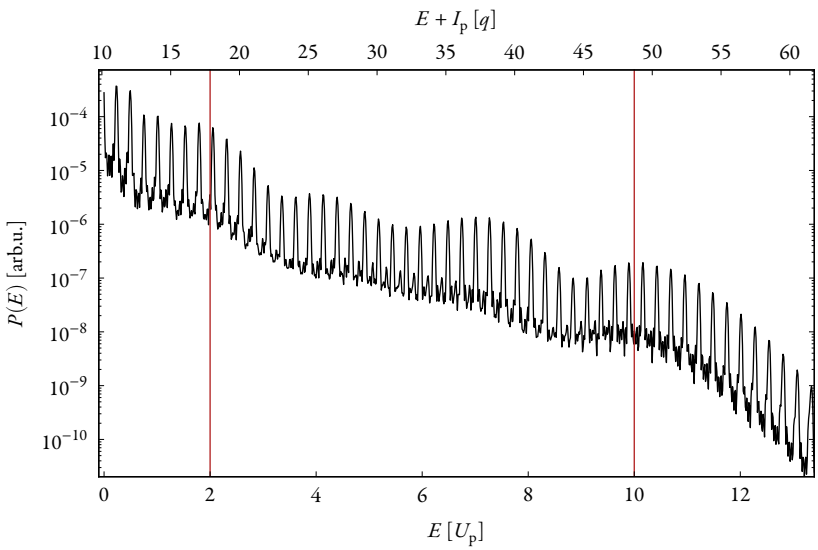

FIGURE 3.5: ATI spectrum from argon subjected to I=1 × 10^{14} W cm^{-2} of λ=800 nm, as calculated by the TDSE. The classical cut-offs, $2U_p$ for direct electrons and $10U_p$ for indirect electrons, are indicated by the vertical red lines.

gies high above the threshold, so-called *above-treshold ionization* (ATI); (Agostini et al. 1979). The maximal energy observed can be found by maximizing the second term of (3.5). The first term, $2U_p \cos(\omega t)$, corresponds to the energy given by the time-varying driving field, but when the electron leaves the interaction region, this term no longer contributes, and we are left with the kinetic energy imparted to the electron at the time of ionization, t_i. The maximum energy in *direct ionization* is thus $2U_p$, assuming spatial homogeneity of the driving field.

The trajectories that *do* lead back to the parent ion may, as dicussed above, recombine and generate HH emission. They may also scatter off the nucleus and emerge with a higher kinetic energy, in a kind of slingshot effect. The maximum attainable energy for this *indirect ionization*, $\sim 10U_p$, occurs in elastic backscattering (Paulus, Becker, and Walther 1995).

As in HHG, the repetition of the process every half cycle leads to a train of photoelectrons being emitted, which is represented in the energy domain as photoelectron peaks. However, every other half cycle, the electrons are ejected in opposite directions, which means the electrons emitted during two subsequent half cycles are distinguishable, even if they have the same final energy. This explains the existence of even orders in ATI as opposed to the case of HHG.

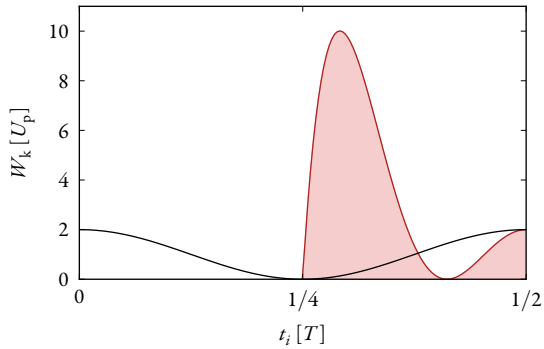

Figure 3.6: ATI time–energy link; as a function of time, the final kinetic energy of the directly ionized electrons is shown in black, i.e. (3.5). The red curve shows the *maximal* energy attainable by indirectly ionized electrons ionized at that time.

Figure 3.5 shows a theoretical ATI spectrum where these features can be observed.

Due to the classical nature of the trajectories, it is also possible to establish an ionization time–final energy link (ibid.); for the directly ionized electrons, this link is simply (3.5). There is a similar link for the indirectly ionized electrons, albeit not analytical, which can be found by maximizing the energy of the scattered electrons for each possible ionization time. This is shown in figure 3.6. It should be noted that for indirect electrons, *all* energies below this maximum energy can result from ionization at time t_i. Thus, only the maximum energy observed is an indication of the time of ionization, especially for $E = 10U_p$, which classically has only one associated time of ionization (as seen from figure 3.6).

The existence of this 'time–energy link' makes it possible to enhance or suppress selected parts of the photoelectron spectrum by increasing or reducing the ionization rate at the corresponding ionization time (this is the subject of PII, discussed in §3.3.2 below).

3.2.1 Angularly resolved Spectra

One important difference between HHG and ATI is that in the former case the emission is in the direction of propagation of the fundamental driving field, whereas in the latter case, the emission is confined to the polarization plane. The spectrum shown in figure 3.5 is the total cross-section obtained by angularly integrating over all channels. It is possible to obtain more information by

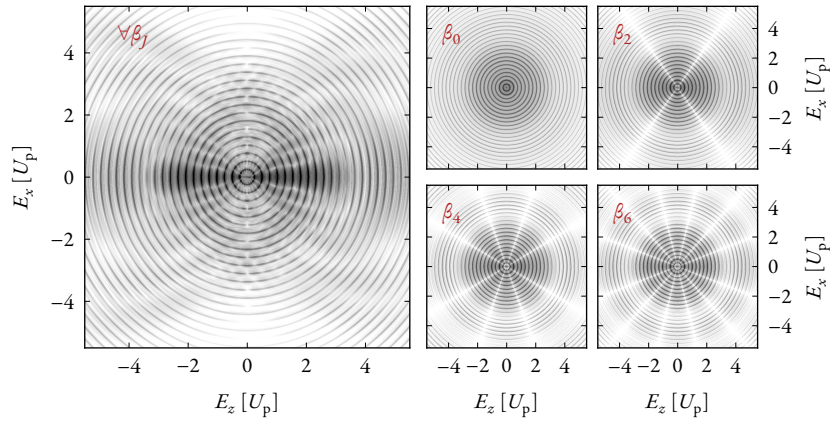

Figure 3.7: Angular distribution of photoelectrons from argon. The left panel shows the full distribution, the small panels on the right show the first few β channels, the first being the isotropic component proportional to the total cross-section. For processes of definite parity (such as one-photon ionization), only the even β channels are populated.

retaining the angularly resolved spectra and decomposing them in a series of *Legendre polynomials* in $\cos(\vartheta)$:

$$\mathcal{F}(E,\vartheta) \equiv \sum_{J=0}^{2L} \beta_J(E) P_J[\cos(\vartheta)], \tag{3.10}$$

where β_J are the expansion coefficients. The photoelectron spectrum of figure 3.5 has the angular distribution presented in figure 3.7. Experimentally, the angularly resolved spectra are obtained using *velocity map imaging spectroscopy* (VMIS); (Eppink and Parker 1997), yielding a 2D map that is a projection of the 3D continuum wavefunction onto a plane. In contrast to figure 3.7, the radial coordinate of the VMI spectra is proportional to the electron momentum rather than its kinetic energy. In the case of cylindrical symmetry, i.e. linear polarization of the fundamental driving field, the full 3D momentum distribution can be reconstructed using an inverse Abel transform (Dasch 1992; Vrakking 2001).

The decomposition (3.10) is amenable to integration over a hemisphere such as the 'forward' or 'backward' direction, due to the orthogonality of the Legendre polynomials on the unit circle. We can therefore define the energy-resolved asymmetry thus:

$$\aleph(E) \equiv \frac{\mathcal{F}_<(E) - \mathcal{F}_>(E)}{\mathcal{F}_<(E) + \mathcal{F}_>(E)}, \tag{3.11}$$

where <, > denote integration over the forward and backward directions, respectively. This quantity is useful in the analysis of the time–energy link.

3.3 Time–energy link in strong-field dynamics

The strong-field process described in the previous sections can be influenced by utilizing the time–energy link; the probability of tunnel ionization at time t_i is strongly dependent on the instantaneous field strength (Landau and Lifshitz 1977; see appendix E for an overview). One way of modulating the instantaneous field strength for short pulses is to vary the *carrier–envelope phase* (CEP), which breaks the time symmetry with respect to the centre of the pulse. For long pulses, the symmetry can be broken by adding a field of commensurate frequency to the fundamental driving field. By varying the relative phase of the two fields, control similar to that possible with the CEP for short pulses can be achieved. In the specific case of the addition of the second harmonic to the fundamental field, it is possible to generate a train which, in the spectral domain, contains both odd- and even-order harmonics. The admixture is decided by the relative strengths and phases of the two constituent fields (Mauritsson et al. 2006, 2009). It is therefore of importance to be able to measure and control the relative phase, a technique for which is presented below. A more detailed account is given in PII.

3.3.1 Carrier–envelope effects in HHG

For short driving pulses, the CEP has a dramatic effect on the electron trajectories in HHG (see figure 3.8), since its variation breaks the time symmetry. The emitted XUV radiation will propagate in the same direction as the driving field. Thus, it is not possible to spatially discriminate between radiation from electrons whose excursions are in the 'forward' or 'backward' directions, as was possible in the angularly resolved ATI measurements described above. It is, however, possible to tune the spectrum through the time–energy link (as can be seen in figure 3.9), and also change the time structure of the emitted XUV radiation. When all the trajectories are included in the calculation, interference results, and the spectrum is complicated, making interpretation difficult. When only the short trajectory is included, the HHG spectrum is considerably simplified, but some interference still occurs as the CEP is scanned. Rudawski et al. (2015) identified three spectral regions: a low-energy region that is not affected by variation in the CEP, a high-energy region, where the harmonics gradually transition from odd to even orders, and an intermediate-energy re-

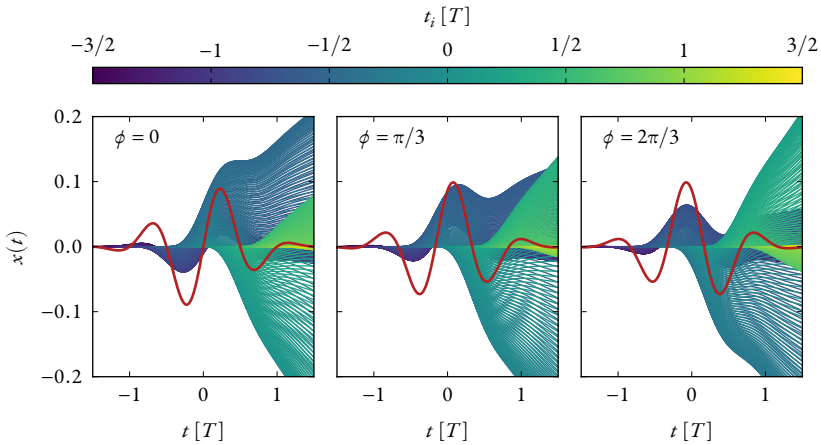

Figure 3.8: The effect of varying the CEP on the classical electron trajectories.

gion, with more complicated structures. The spectral profile 'fingerprints' the time structures generated; the transition in the high-energy region from odd to even harmonic orders signifies a gradual change from a phase difference of π between subsequent XUV pulses to a phase difference of 2π; the interference in the intermediate-energy region hints at the generation of multiple XUV pulses.

PV describes the effects going beyond changing the CEP, which is a first-order dispersion effect (see appendix F for an overview of ultra-fast optics). The frequency components of the fundamental pulse are dispersed by gradually inserting a piece of glass into the beam. The higher-order dispersion effects will lead to chirping of the fundamental pulse, thereby increasing its duration and decreasing its peak intensity. Figure 3.10 shows the experimental results as well as a theoretical scan, calculated using the TDSE. There are obvious similarities and differences between the experimental and the theoretical results. The most important differences are the lack of shoulders in the theory (for absolute glass insertions greater than half a mm), the blue shift of the harmonic orders in the experiment for small dispersions, and the clear compression of the harmonic orders in the theoretical results but not in the experimental results. The first of these differences is can probably be explained by the structure of the pulse in the experiment (depicted in figure 3.11), which when dispersed through glass will exhibit pre- and post-pulses strong enough to support HHG. The blue shift occurs when the generation medium is partly ionized, as the presence of plasma affects the refractive index causing the driving field to be blue-shifted, leading to blue-shifting of the harmonic orders as well. The TDSE calculation, being

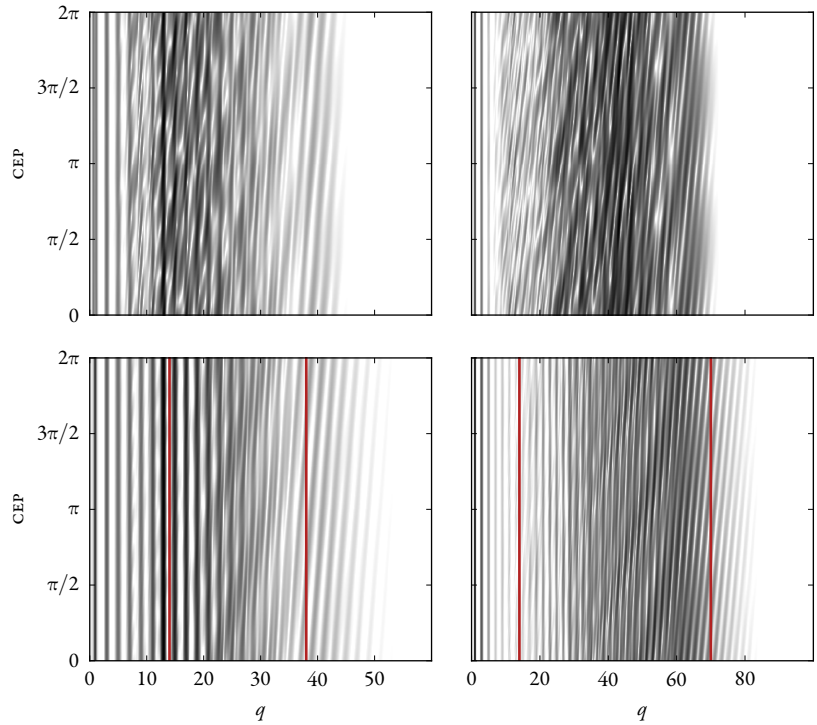

Figure 3.9: Theoretical CEP scan of HHG in argon (left column) and neon (right column), as calculated using the TDSE for a pulse duration of 6.2 fs, a driving wavelength of 850 nm and an intensity of 1.9×10^{14} W cm^{-2} for argon and 3.3×10^{14} W cm^{-2} for neon. The upper row includes all trajectories, while in the lower row, only the short trajectory is included (the manner in which this is done will be described in detail in §4). The vertical red lines approximately delineate the spectral regions identified by Rudawski et al. (2015). The greyscale is logarithmic.

a single-atom-type calculation, is totally devoid of such effects. The lack of a clear compression of the harmonic orders in the experiment is more difficult to explain, but we shall see that some things can be learnt all the same.

The qualitative similarities are convincing; most notably the fringes reminiscent of those in the CEP scan in figure 3.9. Their slope varies over the spectrum and as a function of the amount of glass insertion. From the TDSE calculations, it can be seen that the fringes are horizontal, i.e. the slope changes sign, where the harmonic orders are compressed. The same effect is observed in the experiment, although the compressions of the harmonics themselves are not visible. The sign change was in PV interpreted to occur at that amount of glass insertion for which the external chirp compensates the internal chirp of the HHG

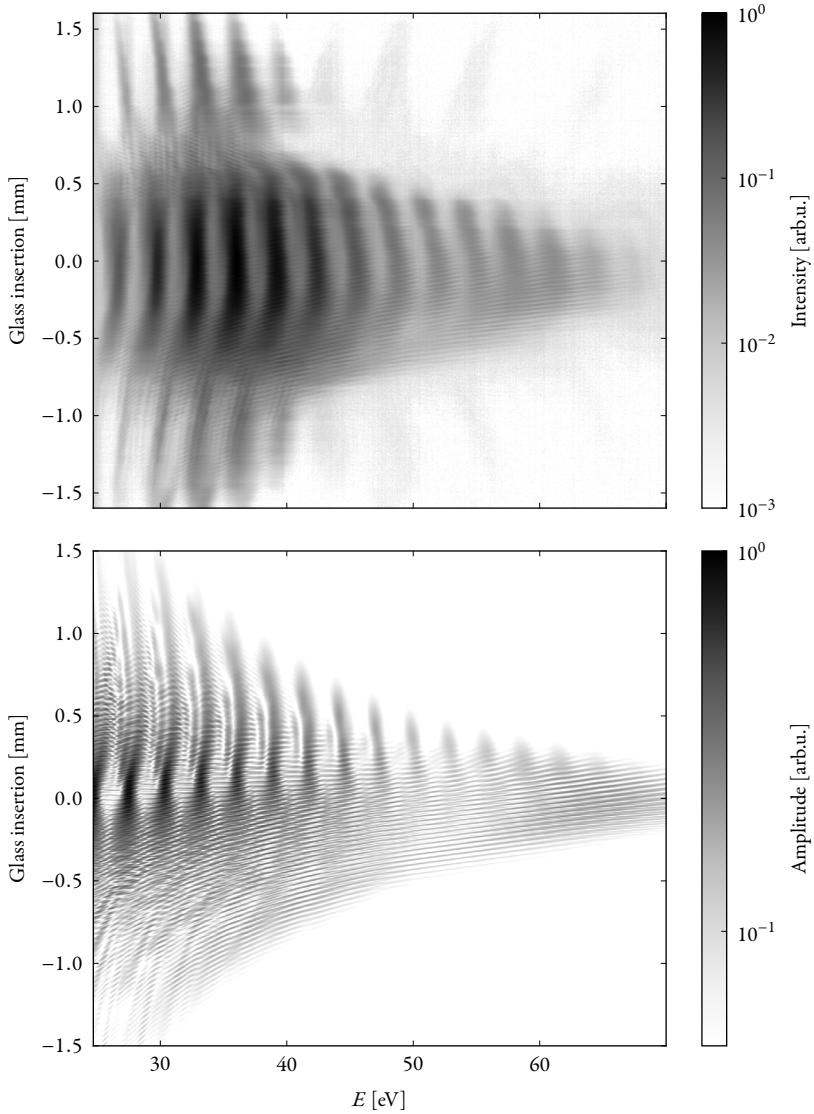

Figure 3.10: Dispersion scan performed by gradually inserting a BK7 glass wedge into the fundamental driving laser beam. The grating compressor is pre-compensated to third order in the dispersion for BK7 glass, which means at 'zero' glass insertion, the fundamental beam is Fourier-transform limited. Upper panel: experimental results, using the driving field depicted in figure 3.11. Lower panel: theoretical scan, as calculated using the TDSE, for a Gaussian pulse. A large blue shift due to ionization not present in the TDSE is visible in the experimental scan, which explains why the harmonic orders do not line up for minimum dispersion. The Cooper (1962) minimum at 50 eV (Wörner et al. 2009; Farrell et al. 2011) is visible in both the experimental and the theoretical results.

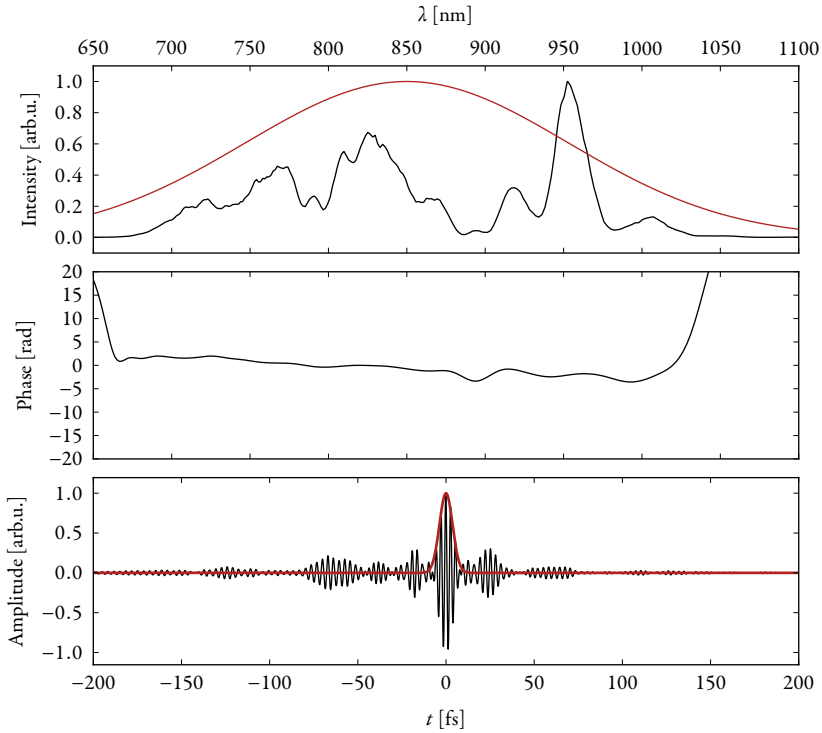

Figure 3.11: Experimental pulse in the spectral domain (upper and middle panels) and in the time domain (lower panel). The spectral distribution was retrieved using the d-scan algorithm presented by Miranda et al. (2012). The envelope of the driving pulse employed in the calculations, centred at 850 nm and of 6.2 fs duration [*full-width at half maximum* (FWHM) of intensity profile] is indicated in red.

process, characterized by the *dipole phase parameters* (which will be discussed at length in §4). Another notable feature is the diminished HH yield around 50 eV, due to the *Cooper (1962) minimum* present in the photoionization of argon.

3.3.2 *Multi-colour ATI*

In the field of electronics, the frequency and phase relationship between two signals $x(t)$ and $y(t)$ can be determined by *Lissajous (1857) curves*, in which one signal is plotted vs. the other. For commensurate frequencies, a closed curve is obtained, which can be used to infer the relative frequencies, amplitudes, and phase of the two signals.

As noted above, the ATI process can be controlled by introducing a second

field of another colour. If we specifically choose the added colour to be the second harmonic of the driving field, instead of (3.3), we have the following form (assuming linear polarization):

$$\mathcal{E}(t) = \mathcal{E}_1(t) + \mathcal{E}_2(t) = \mathcal{E}_0[\sin(\omega t) + \eta \sin(2\omega t + \phi)], \tag{3.12}$$

where η is the relative strength of the second harmonic and ϕ the relative phase. If the relative strength is small enough (usually a few percent), it does not significantly affect the free propagation, but it does affect the ionization rate, which is highly non-linearly dependent on the field strength (Perelomov, Popov, and Terent'ev 1966, 1967; Perelomov and Popov 1967; Ammosov, Delone, and Kraĭnov 1986; see also appendix E).

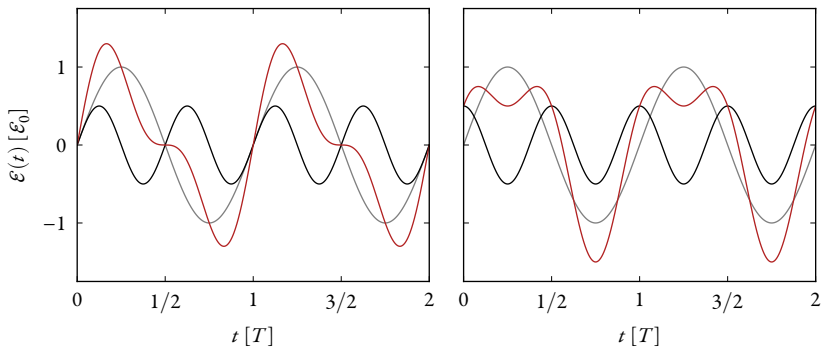

Figure 3.12: Symmetry breaking by the introduction of the second harmonic (black) of the driving field (grey). (NB that the second harmonic amplitude has been exaggerated for illustration.) Depending on the relative phase of the constituent fields, the resultant field (red) will enhance or suppress the tunnel-ionization at different time, compared to the monochromatic case. Left: $\phi = 0$, right: $\phi = \pi/2$.

The addition of the second harmonic makes the driving field asymmetric, as can be seen in figure 3.12. By sweeping the relative phase, we can thus enhance or suppress the ionization rate at specific times, and, as we saw above, there is a clear link between the ionization time and the final energy. Because of the special kind of asymmetry introduced by the second harmonic field, an energy that is enhanced in the forward direction will be suppressed in the backward direction (cf. figure 3.12). The energy-resolved asymmetry $\aleph(E)$ defined in (3.11) is thus a quantity that is directly influenced by the relative phase of the fundamental field and its second harmonic. Since the spectrum can be measured with high fidelity, the spectral asymmetry can be used to obtain information on the relative phase between $\mathcal{E}_1(t)$ and $\mathcal{E}_2(t)$.

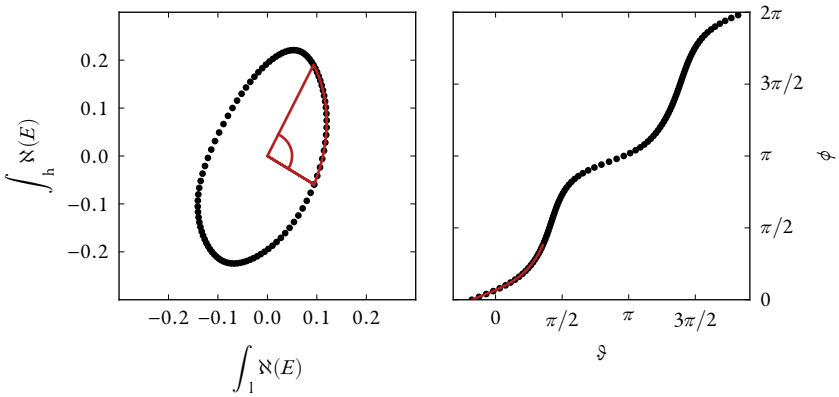

Figure 3.13: Stereo-ATI Lissajous-like curve. Left panel: The high-energy asymmetry $\int_h \aleph(E)$ plotted versus the low-energy asymmetry $\int_l \aleph(E)$. Right panel: The relation between the Lissajous angle ϑ and the phase ϕ between $\mathcal{E}_1(t)$ and $\mathcal{E}_2(t)$.

A very similar idea has already been implemented in a technique called stereo-ATI (Wittmann et al. 2009), where instead short pulses were used and the CEP was the control parameter (as noted above, the variation of the CEP breaks the time symmetry with respect to the pulse centre). PII describes an extension of this technique to the case of long pulses, using the ideas outlined above. Integrating the energy-resolved asymmetry $\aleph(E)$ over a low-energy range and a high-energy range, and plotting one versus the other, results in a Lissajous-like curve (see figure 3.13), which may be used to establish the phase relationship between the low- and high-energy parts of the spectrum. The relative phase of $\mathcal{E}_1(t)$ and $\mathcal{E}_2(t)$ field may then be determined through the time–energy link of the ATI process.

3.4 Résumé

In this chapter, the processes that occur in strong-field light–matter interaction (e.g. HHG & ATI) have been introduced. The concept of electron trajectories was introduced and their temporal, spectral, and spatial properties were discussed. Specifically, the use of the time–energy link was demonstrated as a means of establishing the relative phase of two commensurate fields, through an extension of the stereo-ATI technique to pulses of long duration. We will return to the electron trajectories in HHG repeatedly in the following chapters.

Quantum Path Interference

4

'Lao-Tse says: "You need to find the path". I have found it. You need to find it too...', 'Yes?...', 'I will cut off your head. Then, you will know the truth!'

Le Lotus bleu,
Georges Remi, 1907–1983

The observation of interference is clear evidence of the wave nature of the system being studied. In quantum mechanics, this manifests itself when the system reaches its final state by following more than one path, since in general each path is associated with its own phase accumulation. In PIV, this was studied in the case of HHG. As noted above, two main classes of trajectories (the short and the long) are responsible for the experimentally observed HH emission. Since the emission is proportional to the acceleration of the charge, it follows that observed interference in the emission arises from interference between the electron paths themselves, hence the term *quantum path interference* (QPI).

The emission from the short and the long trajectories, observed in the far field, will interfere if it overlaps, spatially and spectrally. In the experiment described in PIV, a grating spectrometer was used to separate the emission into its spectral components in the horizontal direction of the detector, while divergence of the emission was along the vertical direction (see figure 4.1).

Signs of interference can be already observed from this spectrum, as one or more rings are visible around each harmonic. The rings are modulated, sometimes completely disappearing. They originate from the interference of long-trajectory emission from different emitters and will be discussed in chapter §6, on macroscopic effects. What is not immediately visible in the spectrum, however, is the interference present between the short and the long trajectories. To reveal this interference, we must study how their relative phase can be influ-

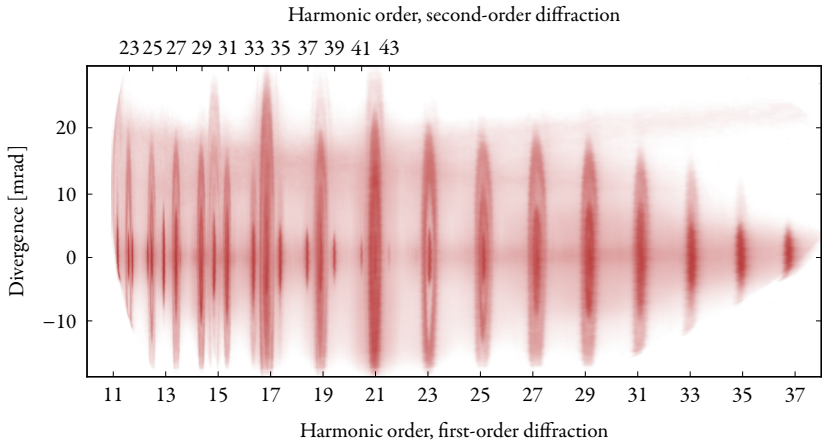

Figure 4.1: Experimental HH spectrum generated from argon using a driving wavelength of 1030 nm and an intensity of about 1×10^{14} W cm^{-2}. The grating used, a Hitachi 001-0639, was optimized for the plateau harmonics, which is why the second-order diffracted cut-off harmonics overlap with the first-order below-threshold harmonics. H011–13 & H037 are only partially visible due to the spatial extents of the micro-channel plate used.

enced; once we know how to do this, we can perform an interferometric measurement.

As discussed in §3.1.3, there is not only a time–energy link, but also a time–space link; hence the trajectories can be discriminated not only by their energy, but also by their excursion from the ion. Thus, another way of studying the paths is to separate them such that they do *not* interfere. Both approaches are described in the present chapter.

4.1 Quantum trajectories in HHG

The reason why the classical treatment of HHG is so successful, is that the position expectation value of the wave packet follows the classical trajectory, as noted above. However, it is still a wave, which means it accumulates phase during propagation. Different wave packets leading to the same final momentum will thus interfere. There are two main reasons why different wave packets can lead to the same final momentum. The first is that during one half cycle of the fundamental driving field, multiple trajectories are spawned that have the same final momentum upon return; the first two are, as mentioned above, the short trajectory and the long trajectory. The second reason is that the HHG pro-

cess repeats itself every half cycle, which means that all trajectories that are not stationary orbits in the external field will interfere destructively (Salières et al. 2001). These stationary orbits are exactly those that are in resonance with the harmonic orders of the fundamental driving field – the longer the driving pulse is, the more severe the resonance criterion is. In the limit of driving pulses of infinite duration, the harmonic emission can be written as a series of discrete harmonics

$$h(\omega) = \sum_{q\in\mathbb{N}} \frac{1-(-1)^q}{2} a_n \delta(q\omega_0), \tag{4.1}$$

where a_q is the amplitude of HOq with photon energy $q\omega_0$ (ω_0 being the fundamental frequency). A few-cycle driving pulse will lead to a more continuous spectral distribution of the harmonic emission.

One way to prove the link between the classical picture of HHG and the quantum trajectories, is to investigate the harmonic emission as calculated with the TDSE or the SFA from a trajectory perspective. If a single trajectory can be isolated, no interference will occur and there will be no modulation of the harmonic emission (this is true for the half-cycle response of a single emitter). We start by calculating the time-dependent dipole moment, using both the TDSE and the SFA (see figure 4.2). In the case of the SFA, since the integral in (3.8) runs over the excursion time, we can immediately calculate the emission at the peak intensity of the field (chosen to have a flat profile). To calculate the stationary behaviour of the TDSE, however, it is necessary to turn on the field slowly, and wait a sufficiently long time for the transient behaviour to decay. Furthermore, for reasons of numerical stability, the *acceleration* of the dipole moment is calculated.*

Due to the time–energy link in HHG, the quantum orbits can be revealed by performing a windowed Fourier transform – a *Gabor (1946) transform*:

$$G_x(t,f) \equiv \int_{-\infty}^{\infty} \mathrm{d}\tau \;\exp\left[-\frac{(\tau-t)^2}{2\sigma^2}\right] \exp(-\mathrm{j}\pi f\tau) x(\tau), \tag{4.2}$$

where σ is the width of the window – of the time-dependent dipole moment.† Figure 4.3 shows the quantum orbits in HHG calculated using the TDSE. In the upper panel, all the trajectories are included and, as a consequence, clear modulation of the quantum orbits is visible. Due to the time–space link, we can introduce a mask function at a suitable distance from the nucleus (see figure 4.3), such that all trajectories with excursion lengths longer than the longest short trajectory are absorbed [a more sophisticated method is to use a wavelet-based approach, as is done by Strelkov et al. (2011, 2012)]. The quantum orbits will

* This is because computing the expectation value of the dipole operator, $\langle r\rangle$, amplifies the contributions of large radial distance, where the resolution is poor.

† See last page for another satisfactory use of time–frequency analysis.

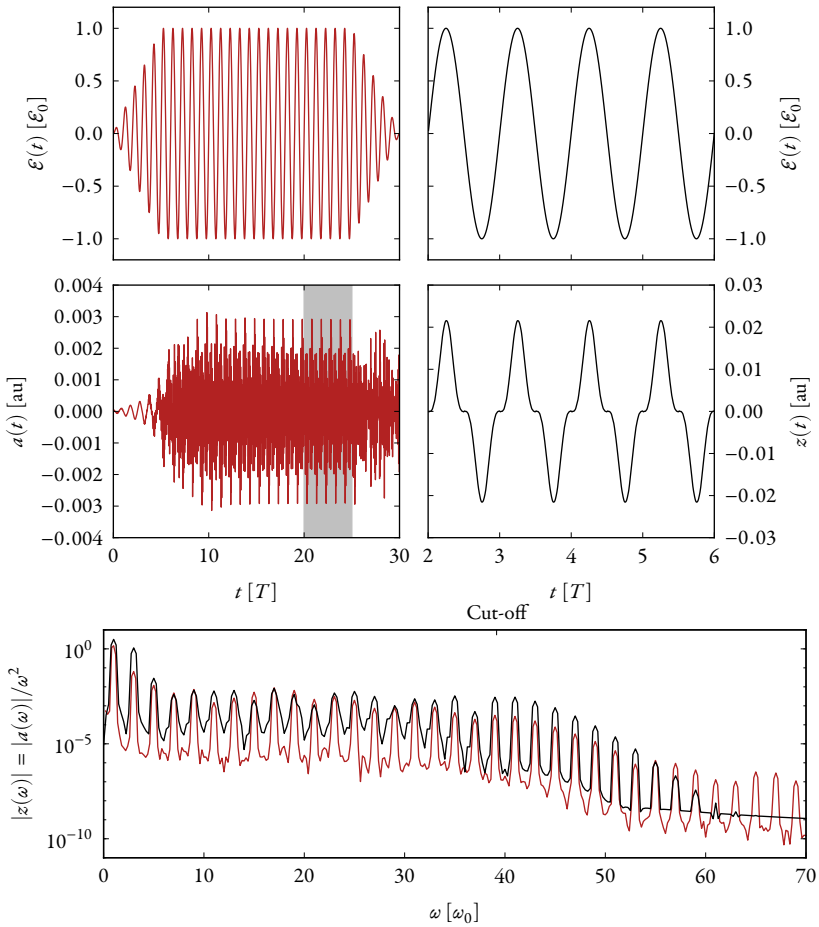

Figure 4.2: HHG calculated using the TDSE (red curves) and the SFA (black curves). The uppermost row shows the fundamental driving field of wavelength 1030 nm and intensity of approximately 1×10^{14} W cm^{-2} ($\implies U_p = 0.36$ au). For the TDSE calculation, a pseudopotential for argon (I_p=15.7596 eV≈0.5792 au, cut-off ~HO39) was used, while for the SFA calculation, the atom was a hydrogen model with a 1s ground state with the binding energy of argon. The middle row shows the time-dependent dipole response; the shaded part in the left column indicates the time window used to Fourier-transform the TDSE signal (which is also windowed) to find the spectrum shown in the lowermost panel. This panel shows a comparison between the HH spectra calculated using the TDSE and the SFA. The broad features of the two models are in agreement, however details are not.

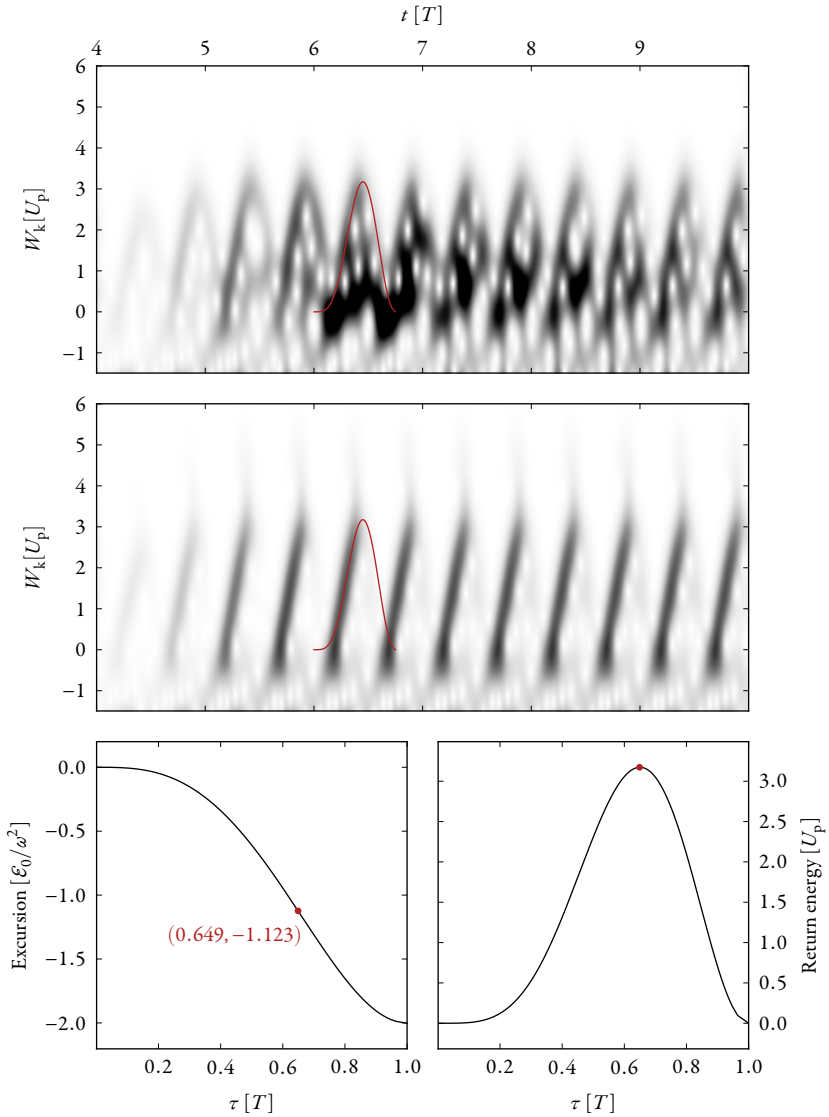

Figure 4.3: HHG quantum orbits, as calculated using the TDSE. Upper panel: all trajectories. Middle panel: short trajectory only, calculated by spatially masking the part of the wavefunction that extends outside a certain radius. The red curve shows the classical orbit, for comparison. Lower panels: excursion (left) and return energy (right) as functions of excursion time. The most energetic short trajectory makes an excursion of $\sim 1.1\mathcal{E}_0/\omega^2$ and has an excursion time of $\sim 0.65T$.

then lose all their modulation and emission will only occur within the time window of every cycle that is associated with the return times of the short trajectory. This is not too dissimilar from the way in which the short trajectory is selected in the experiment. There, the long trajectory can be spatially filtered out by placing a fixed aperture some distance away from the focus, thereby allowing only the less divergent emission of the short trajectory to pass (Bellini et al. 1998).

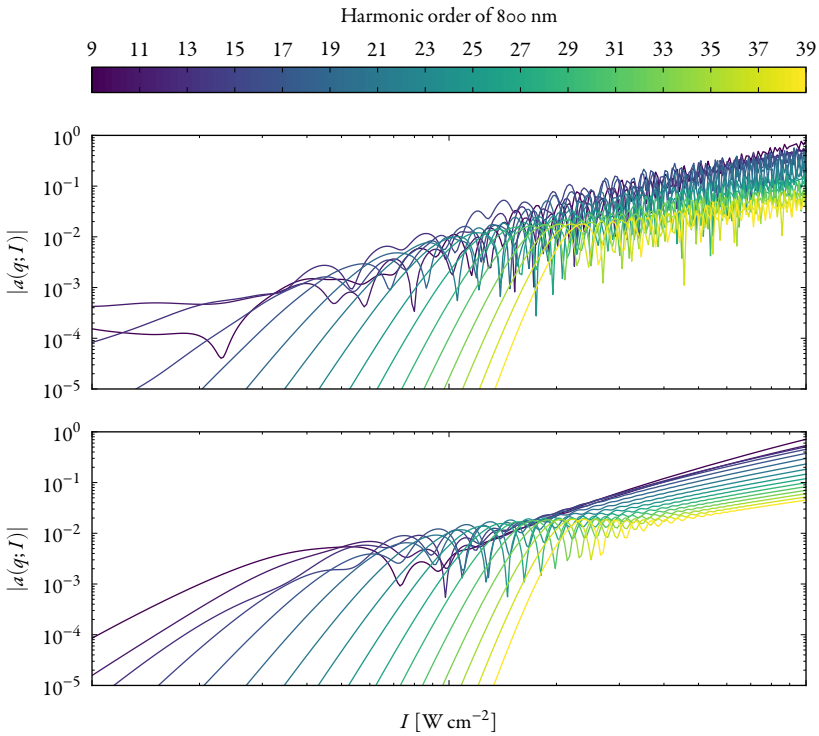

Figure 4.4: HHG yield as a function of intensity, as calculated using the SFA. The driving wavelength is 800 nm and the generation medium is argon. Upper panel: all trajectories included, which leads to strong amplitude modulation in the plateau regime. Lower panel: only the short trajectory is included, by limiting the maximum excursion time to $0.65T$. As can be seen in the plateau regime, the trajectory selection works well, since the modulation is suppressed. Some of the multi-trajectory character remains close to the transition point between the regimes.

4.2 Quantum path distributions

Another way of studying the quantum trajectories in HHG is to calculate the HH response as a function of the intensity of the fundamental field. A common model used to describe the harmonic emission is (Varjú et al. 2005b)

$$\mathcal{E}(\omega, I) = \sum_{qj} A_q(q\omega_0, I) \exp[\mathrm{i}\alpha_{qj} I], \tag{4.3}$$

which is very similar to a Fourier series decomposition along I (see appendix G for a motivation of this model). α_{qj} is a quantity conjugate to the intensity, called the *dipole phase parameter*. Figure 4.4 shows the HH yield and phase calculated with the SFA for a range of harmonic orders. In the upper panel, both the short and the long trajectories are included, which leads to strong modulation of the HH yield above a certain threshold intensity. In the lower panel, only the short trajectory is included. This is accomplished by setting the upper limit of the integral in (3.8) to $0.65T$, which is the approximate excursion time of the most energetic short trajectory. The modulation of the HH yield is almost completely suppressed; what modulation remains occurs in close proximity to the aforementioned intensity threshold. This threshold occurs at the boundary between the cut-off regime and the plateau regime, as illustrated in figure 4.5. In the plateau regime, which is the classically permissible regime (as discussed in §3.1), multiple trajectories exist and can interfere. This is the case above the cut-off intensity in the upper panel of figure 4.4. Below the cut-off intensity, in the classically forbidden cut-off regime, the two trajectories merge into one trajectory; this can be seen from the upper panel of figure 4.4, where below the cut-off intensity, the harmonic yield exhibits a smooth behaviour.

Returning to the model (4.3), it is clear that the individual trajectory contributions for one harmonic order q may be disentangled by Fourier transformation along I. Figure 4.6 shows exactly this. The Fourier transform resolves the harmonic emission into three major contributions: the short-trajectory contribution ($\alpha^* \approx 0$), the long-trajectory contribution ($\alpha^* \approx 2\pi$), and the cut-off trajectory contribution ($\alpha^* \approx \pi$). The reduced dipole parameter α^* is related to the dipole parameter through

$$\alpha^* \equiv 4\omega^3 \alpha I_0, \tag{4.4}$$

where ω is in atomic units, α in SI units, and $I_0 \approx 3.51 \times 10^{16}\,\mathrm{W\,cm^{-2}}$.

To further disentangle the trajectories of (4.3), we calculate the Gabor transform (4.2) $G_{\mathcal{E}_q}(I, \alpha)$ to reveal the *quantum path distribution* (QPD) of HOq. The calculated QPDs for all harmonic orders at the experimental peak

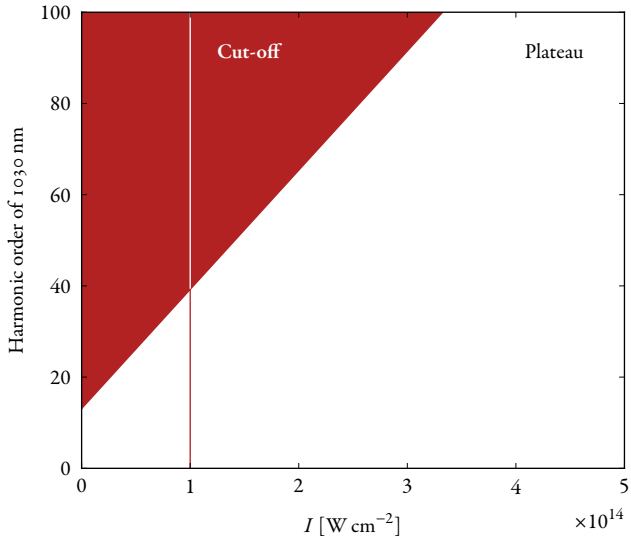

FIGURE 4.5: The classical cut-off law delineates two regions: in the upper left region, the harmonics are in the cut-off regime, whereas the lower right region corresponds to the plateau regime. The quantum paths generating the harmonics are very different in these two regimes. The vertical line indicates the approximate intensity in the experiments described in PIV.

intensity are shown in figure 4.7. In addition to the short and the long trajectories, multiple longer trajectories are visible. These have not yet been unambiguously identified experimentally, but are known from theory (Lewenstein et al. 1994).

4.3 QUANTUM PATH INTERFEROMETRY

From (4.3), an interferometric scheme presents itself in which the phase accumulation along the different trajectories is, in general, different. Two quantum paths to the same final state with different phase accumulation will interfere. It can be shown (see appendix G.4) that the interference term between the long and the short trajectory of HOq has the phase argument

$$(\alpha_{qs} - \alpha_{ql})I_0, \tag{4.5}$$

where I_0 is the peak intensity of the driving pulse. Thus, by adjusting the peak intensity, we can tune the 'arm length' of our interferometer. This was done to extract $\alpha_{qs} - \alpha_{ql}$ in PIV. Figure 4.8 shows the experimental results for HO17, ac-

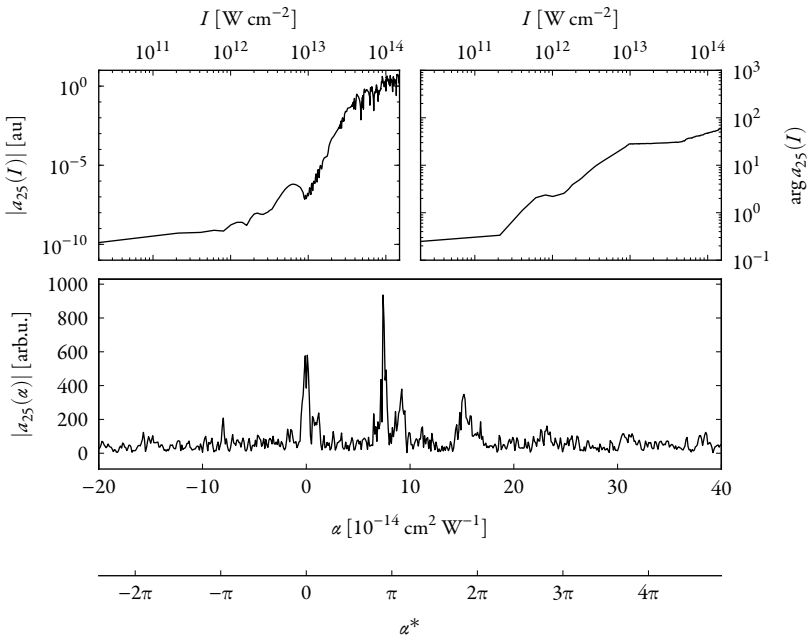

Figure 4.6: Upper row: Intensity dependence of the HH yield (left) and the phase (right) of HO25 of 1030 nm, calculated using the TDSE. Lower row: Identification of trajectories in HHG. Fourier transformation of the upper row along the intensity axis gives the harmonic emission expressed in the variable conjugate to intensity, the *dipole phase parameter* α. In its reduced form, α^* (4.4), the short trajectory corresponds to a value of $\alpha^* \approx 0$, the long trajectory corresponds to $\alpha^* \approx 2\pi$ and they meet in the cut-off at $\alpha^* \approx \pi$.

quired by taking a lineout along the central frequency of the harmonic from a spectrum of the kind shown in figure 4.1; the QPI patterns emerged as the peak intensity was varied. A model based on Gaussian beams (described in appendix G.4) was fitted to the experimental results, ensuring that the amount of fringes and their curvature were matched. This was done for HO11–37, and the corresponding values for α_{qs} and α_{ql} were extracted for all harmonic orders. The results can be seen in figure 4.9.

The variation in intensity was accomplished by chirping the fundamental pulse, which also imparts a spectral phase variation to the generated harmonics (see appendix G.3). However, at the central frequency of each harmonic order, the spectral phase variation vanishes, which is why the QPI patterns are symmetric with respect to the chirp (see figure 4.8). The spectral phase variation can be used as the basis for a spectral model of the interference (as described in ap-

pendix G.3). Fitting this model to lineouts taken along the spectral dimension at zero divergence of the experimental spectra (of which figure 4.1 is one example), provides a separate set of values of $\alpha_{s/l}$ for all harmonic orders. These values are also shown in figure 4.9 and, in general, they agree with the values extracted using the spatial model.

4.4 Résumé

In this chapter, the trajectory nature of HHG has been thoroughly investigated, both through theoretical reasoning and calculations and experimental measurements. The wave nature of microscopic matter is made apparent through the observed interference patterns, but the particle nature with its classical trajectories is emphasized through the ability to separate the trajectories in a very classical fashion (e.g. the mask function used to suppress the long trajectory emission) and observation of the disappearance of the interference.

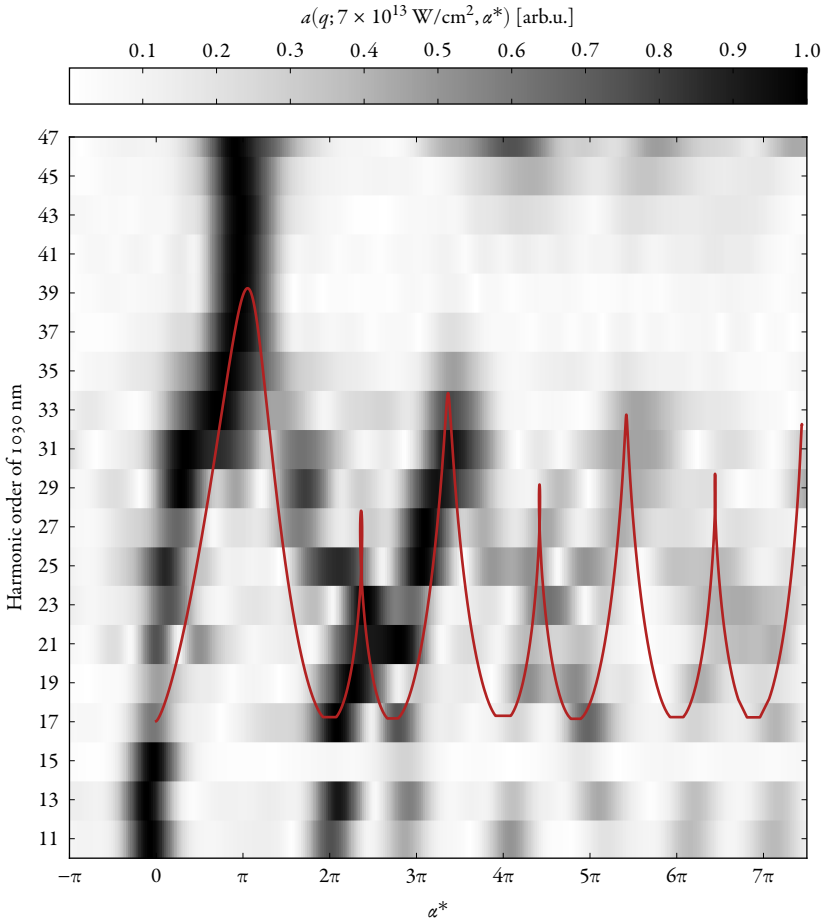

FIGURE 4.7: Quantum path distributions in HHG, calculated using the TDSE. The short ($\alpha^* \approx 0$) and the long ($\alpha^* \approx 2\pi$) trajectories are visible in the plateau regime ($q \lesssim 35$), beyond which they merge into a cut-off branch with $\alpha^* \approx \pi$. The red line is calculated from the SFA by integrating the quasi-classical action S_{st} (3.9) along the classical trajectories (3.4). Trajectories beyond the long trajectory are visible in the quantum path distributions and agree qualitatively with the SFA approximation. These have not yet been unambiguously identified experimentally.

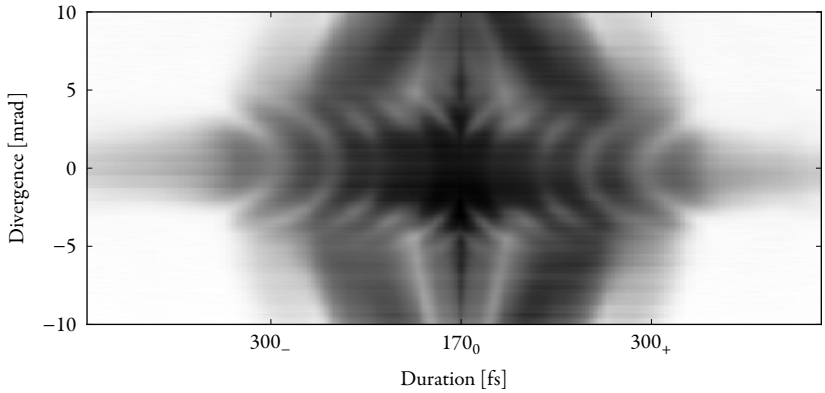

Figure 4.8: QPI from HO17 observed experimentally along the central frequency of the harmonic. For small divergences $\lesssim 5$ mrad, a clear interference pattern is visible; this is the region where the short and long trajectories spatially overlap. Pulse durations notated $300_{\pm}$ fs denote 300 fs pulse duration with positive/negative chirp. Accordingly, $170_{\circ}$ fs corresponds to a Fourier-transform-limited pulse duration of 170 fs. The greyscale is logarithmic in intensity.

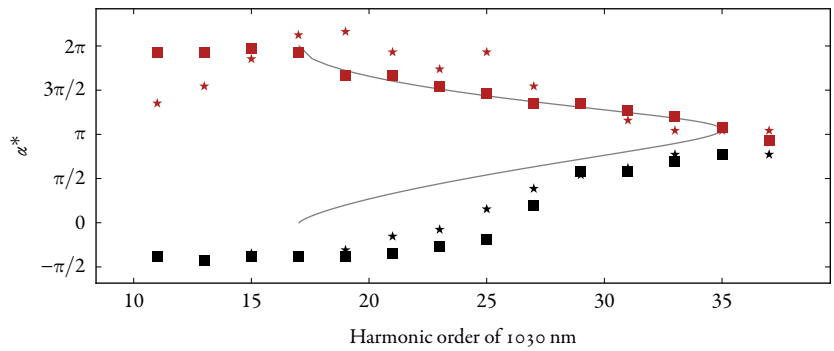

Figure 4.9: The squares and the stars show the values of α^* for the short (black) and long (red) trajectories, extracted using two complementary methods (for details, see PIV). The grey line is calculated from the quasi-classical action (3.9), assuming classical return and excursion times of the trajectories. This is the reason why the agreement is better for the long trajectory; the long trajectory being 'more classical' than the short trajectory.

5 Elliptical HHG

In the more general case of elliptical polarization of the field driving the HHG, the motion of the electrons is considerably more complicated than in the linear case. Naïvely, one would expect that the electron would not return at all, due to the added drift in the direction transverse to the major axis of the polarization ellipse, i.e. the harmonic yield would be proportional to $\delta(\xi)$, where ξ is the ellipticity of the driving field ($\xi = 0 \implies$ linear polarization, $\xi = \pm 1 \implies$ circular polarization). However, as has been observed previously by e.g. Burnett, Kan, and Corkum (1995) and again in PIII, the yield is proportional to

$$\exp\left[-\frac{\xi^2}{2\sigma_q^2}\right], \tag{5.1}$$

where σ_q is a measure of the sensitivity to ellipticity for harmonic order q. This can be understood as follows. In the tunnel-ionization step, the electron is not created with zero momentum, but with a normal distribution of momentum *centred* at zero (Ivanov, Spanner, and Smirnova 2005). This means that although the electron acquires a position drift in the transverse direction, there are some values of initial momentum that allow return (specifically those orthogonal to the instantaneous field vector at the moment of ionization). In the conjugate picture, this corresponds to *quantum diffusion*; an initial distribution of momentum leads to spreading of the wave packet after propagation, which means that even though the wave packet is displaced such that its centre of mass (corresponding to the position of the classical particle) is not at the origin, its probability density distribution still overlaps with the parent ion, thus

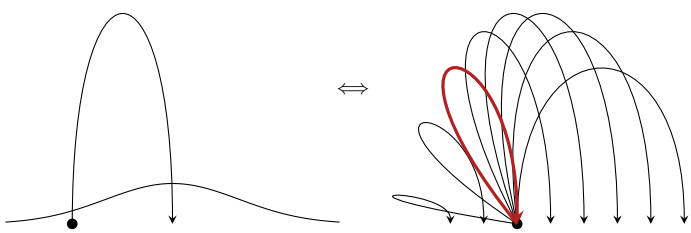

FIGURE 5.1: Quantum diffusion in elliptical HHG, as seen in two conjugate pictures. As the wave packet propagates, the uncertainty in position increases (left). This corresponds to an uncertainty in initial transverse momentum (right).

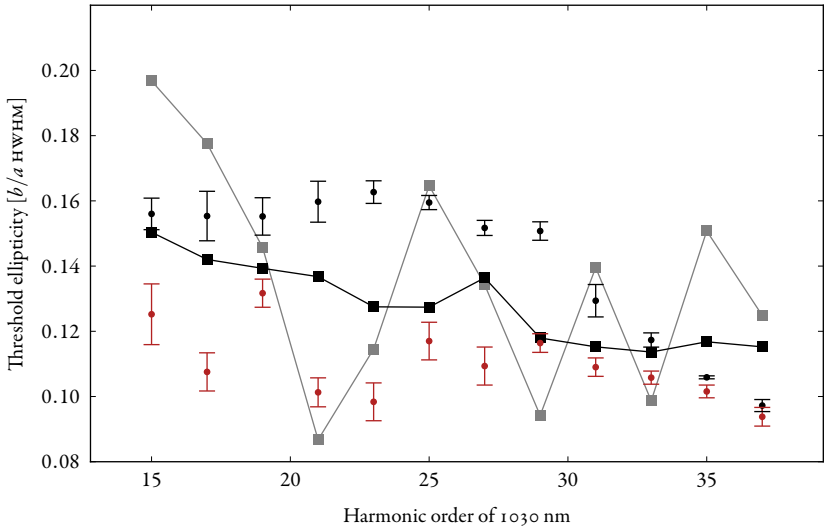

Figure 5.2: Observed threshold ellipticity as a function of harmonic order for the short (black) and the long (red) trajectories. The circles denote the experimental results, presented in PIII. Solving the TDSE including all trajectories gives the grey squares, which seemingly oscillates between the two trajectories as measured experimentally. This could be an indication that different trajectories dominate the response to ellipticity for different harmonics orders. Filtering out the long trajectory from the calculations gives the black squares. These show the same general trend as the experimental measurements, although about 20 % lower. This could be due to the fact that the TDSE calculation only reflects the single-atom response, whereas the experiment probes a range of intensities over the focal volume.

allowing recombination.

In PIII, the sensitivity of the harmonic orders to ellipticity, σ_q, was measured with high resolution (see figure 5.2). Additionally, through spatial separation of the two trajectories, it was possible to measure the trajectory-resolved sensitivity, σ_{qj}, where $j = 1, 2$ refers to the short and the long trajectories, respectively. With increasing harmonic order, σ_{q1} would decrease, which corresponds to higher sensitivity to ellipticity. This is intuitively correct, since increasing q would lead to an increase in the excursion time in the case of the short trajectory ($j = 1$). A longer excursion time increases the probability of the electron drifting away from the parent ion, decreasing the harmonic yield.

What was unexpected, however, was that for the long trajectory ($j = 2$), the sensitivity increased with increasing q, which is counterintuitive; increasing q for the long trajectory corresponds to shorter excursion times and presumably a decrease in phase accumulation. As we will see below, the reason is a combi-

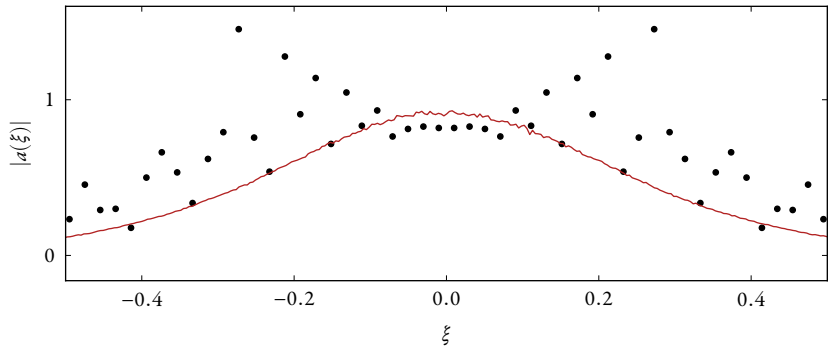

FIGURE 5.3: Ellipticity response of HO11, calculated using the TDSE, including all trajectories (hence the interference). The experimental ellipticity is shown in red, for reference. Both the theoretical and the experimental results have been normalized to the Gaussian that most closely fits the respective data.

nation of probabilities that must be considered at the sub-cycle level.

There are several reasons for the interest in elliptically driven HHG. For example, polarization gating for the generation of isolated pulses by the constructive addition of two counter-rotating circularly polarized pulses (Oron et al. 2005; Sola et al. 2006) relies on the fact that the HHG yield decreases drastically with the ellipticity, to achieve a few-cycle window of HHG. However, a more interesting use of ellipticity in HHG is its value as a probe of the limits of the three-step model, with respect to the ionization conditions, the propagation in the continuum, and the recombination probability. The three-step model has been very successful in describing HHG from linearly polarized light, but its success has also fostered a very classical way of thinking about the HHG process, to the extent that it is difficult to go beyond it in reasoning about the physics. Using an elliptically polarized driving field is very simple, yet it subtly alters all the aspects of the process; sometimes not so subtly, as we will see below. Understanding elliptically driven HHG is an important step towards crossing the mental barrier formed by the three-step model.

5.1 TDSE CALCULATIONS

The TDSE calculations shown in figure 5.2 were performed with a newly developed 3D code (described in appendix C), which is an extension of the algorithm described by Schafer (2009) to the case of arbitrary polarization in the $z - x$ plane. Calculating the time-dependent dipole moment acceleration, in

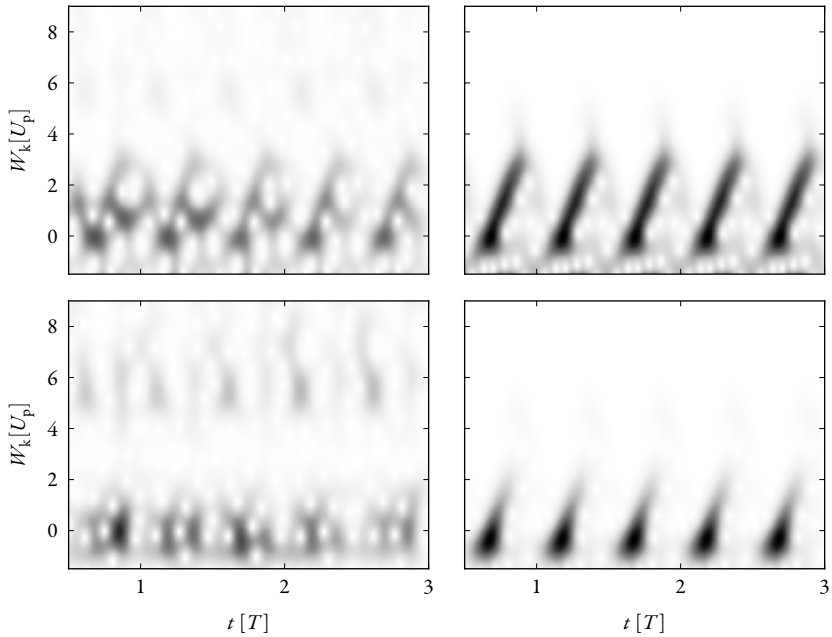

Figure 5.4: Quantum orbits along z (upper row) and x (lower row) for slightly elliptical polarization, $\xi = 0.1$. The left column includes all trajectories, while the right column shows the effect of introducing the mask function at a radius corresponding to the maximum excursion of the short trajectory.

the same way as described in §4.1, for a range of ellipticities, gives $a(q\omega_0, \xi)$ (see figure 5.3).

Since the dependence of the trajectories on ellipticity differs, their combined response is noisy. The same kind of filtering as outlined in §4.1 is therefore performed. The interference can be suppressed (see figure 5.4) by placing the mask function at the proper radius (see lower panels of figure 4.3), allowing the short-trajectory ellipticity response to be accessed (see figure 5.5). The bell-shaped curves are fitted with Gaussians to extract the *half-width at half maximum* (hwhm), which can be compared with the experimental data (the black circles & squares in figure 5.2). One reason why the theoretical values for the short trajectory are about 20 % lower, i.e. shows higher sensitivity to the ellipticity, could be the filtering, which places the mask function at the maximum excursion of the short trajectory at *linear* polarization. The maximum excursion decreases with increasing ellipticity, which means that some long-trajectory character is included, which can be seen in figure 5.4. It could also be that there is a difference in the intensity used in the calculations and that

of the experiment. It is notoriously difficult to establish the precise value of the intensity in an experiment such as this (only estimates are possible), and the experiment actually probes a range of intensities due to the spatial profile of the fundamental driving field, while the theoretical calculations are made for only one intensity.

Another drawback of this method is that it is difficult to assess ellipticity dependence of the long trajectory. One possibility would be to calculate the full response and subtract the short-trajectory response. However, this is problematic, since although the TDSE is a linear partial differential equation, the masking of the wavefunction is not a linear operation. Another option would be to 'repeat the experiment in the computer', by performing a far-field transform, as described in §6.2 below, and then spatially separate the short and the long trajectories. However, this would be prohibitively expensive due to the quadratic scaling of the 3D algorithm and merely reproducing the experimental results would not necessarily provide any added physical insight. Furthermore, this is not always possible because at higher intensities, the short trajectory can also have a substantial spatial divergence (Dubrouil et al. 2014). Some physical insight regarding the long trajectory behaviour, however, can be obtained through semi-classical calculations, as will be seen below.

An obvious deviation from the purely Gaussian ellipticity response of the HHG is clearly visible in figure 5.5 for HO13 (experiment and theory) and less so for HO11 (theory only), where a local minimum in harmonic yield occurs at linear polarization. This has been observed previously by Burnett, Kan, and Corkum (1995) and Weihe et al. (1995), and explained by Ivanov, Brabec, and Burnett (1996) as the interference of 'two returns' for the same trajectory. Only the long trajectories have this possibility, since they, if they miss the parent ion when passing $\mathbf{r} = 0$, will be driven back once more by the field. The short trajectories, however, will be driven away by the field, if they miss the parent ion (Yost et al. 2009; Hostetter et al. 2010). As we will see in the next section, there is another possible explanation; the harmonic yield is strongly dependent on the tunnelling rate, which is considerably decreased for the shortest trajectories since they are ionized at the zero-crossing of the driving field.

5.2 Semi-classical calculations

We will now describe the semi-classical calculations performed to model the ellipticity behaviour of the HHG, specifically that of the long trajectory emission. The long trajectories are 'more classical' in the sense that they experience higher field strengths (and are thus comparatively less influenced by the ionic poten-

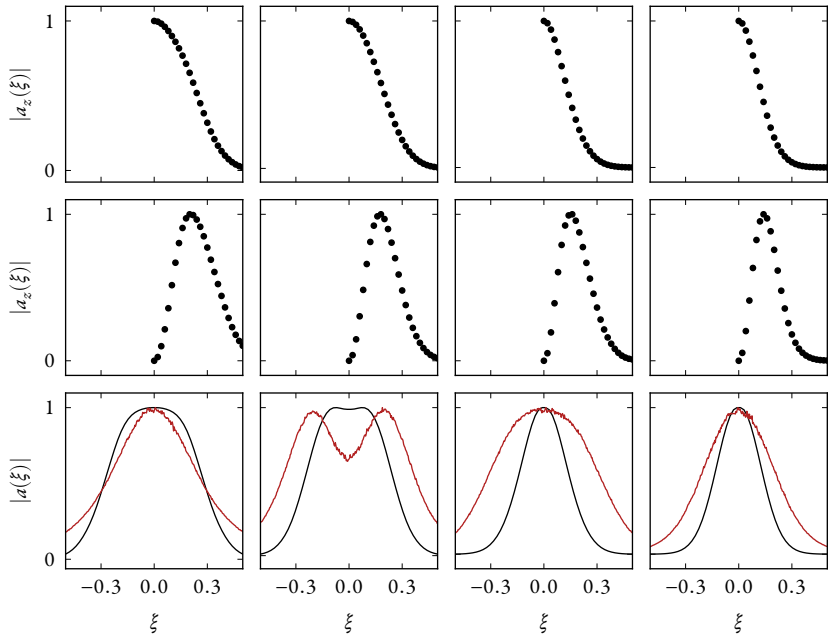

FIGURE 5.5: HO11–HO17 ellipticity response calculated using the TDSE (black), together with the experimental curves (red) for the short trajectory. The curves have been normalized to their respective maximum value. The upper row shows the z component of the time-dependent dipole acceleration, the middle row its x component, and the lower row its magnitude.

tial) and spend more time in the classically permissible region.

As discussed in conjunction with figure 5.1, the quantum diffusion of the wave packet during propagation in the electric field enables HHG even in the elliptical case. In the conjugate picture, the transverse drift acquired for elliptical polarization is compensated by an initial velocity transverse to the driving field at the time of ionization (Möller et al. 2012).

In the case of elliptically polarized light, (3.3) transforms into

$$\mathcal{E}(t) = \frac{\mathcal{E}_0}{\sqrt{1+\xi^2}} \begin{bmatrix} \sin(\omega t) \\ \xi \cos(\omega t) \end{bmatrix}, \tag{5.2}$$

where $\xi = b/a$ is the ratio between the minor and the major axes of the ellipse.

The position as a function of time can then be expressed as follows:

$$\mathbf{r}(t) = \mathbf{r}_i + (t - t_i)\mathbf{p}_i + \frac{E_0}{\omega^2\sqrt{1+\xi^2}} \begin{bmatrix} \sin(\omega t) - \sin(\omega t_i) - \omega(t - t_i)\cos(\omega t_i) \\ \xi[\cos(\omega t) - \cos(\omega t_i) + \omega(t - t_i)\sin(\omega t_i)] \end{bmatrix}. \tag{5.3}$$

The initial conditions are thus

$$\mathbf{r}_i = 0, \quad \mathbf{p}_i = \frac{p_\perp}{\sqrt{1+\xi^2}} \begin{bmatrix} \xi\cos(\omega t_i) \\ \sin(\omega t_i) \end{bmatrix}, \tag{5.4}$$

where $\mathbf{p}_i$ is the initial momentum, taken to be transverse to the electric field at the time of ionization, and $p_\perp$ its magnitude. According to Delone and Kraĭnov (1991), the uncertainty of the initial transverse momentum is given by

$$w(p_\perp) = A \exp\left[-\frac{2(2I_\mathrm{p} + p_\perp^2)^{3/2}}{3\mathcal{E}(t_i)}\right]. \tag{5.5}$$

For small transverse momenta, this probability can be expanded as

$$(2I_\mathrm{p} + p_\perp^2)^{3/2} = 2(2I_\mathrm{p}^3)^{1/2} + \frac{3}{2}(2I_\mathrm{p})^{1/2}p_\perp^2 + \mathcal{O}(p_\perp^4), \tag{5.6}$$

$$\implies w(p_\perp) = B \exp\left[-\frac{(2I_\mathrm{p})^{1/2}p_\perp^2}{\mathcal{E}(t_i)}\right], \tag{5.7}$$

which is the expression used by e.g. Strelkov (2006). In our case, however, we need the full expression (5.5), since the initial transverse momentum required for some of the longer trajectories can be quite large, as we will see below. Another important factor in HHG is the ionization rate, i.e. the probability of the first step in the three-step model. The tunnelling rate is calculated according to ADK theory (Ammosov, Delone, and Kraĭnov 1986), see appendix E for details.

Strelkov et al. (2012) give the following expression for the threshold ellipticity:

$$\xi_\mathrm{threshold} = \frac{\omega}{2\sqrt{\sqrt{2I_\mathrm{p}}\mathcal{E}(t_i)}}. \tag{5.8}$$

This follows the intuitive behaviour, i.e. trajectories of longer excursion time exhibit higher sensitivity to ellipticity, for both the short and the long trajectories classes.

To estimate the ellipticity dependence of the harmonic yield classically, we proceed as follows (for all ionization times $t_i \in [0.25T, 0.5T]$).

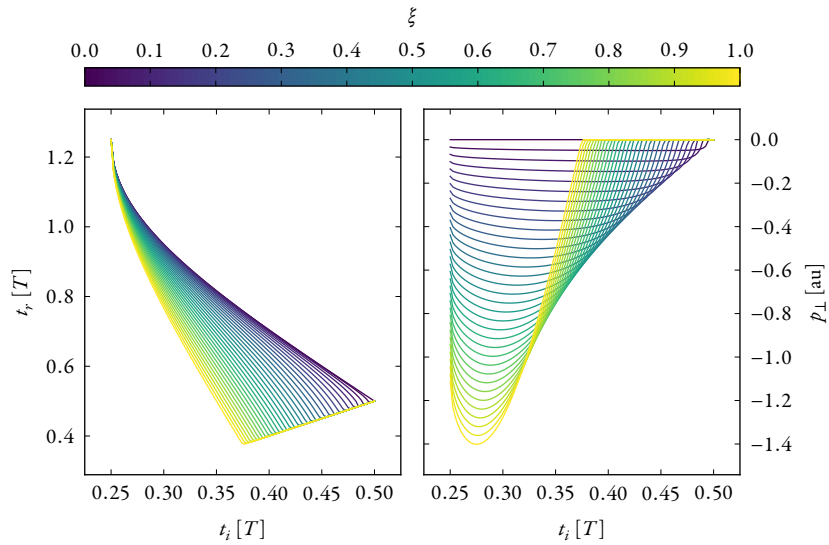

Figure 5.6: Return time (left) and required initial transverse momenta (right) as a function of ionization time for different ellipticities.

(1) (5.3) is solved numerically for t ($\xi = 0, p_\perp = 0$).
(2) For all $\xi \in (0, 1]$, (5.3) is solved numerically for t and $p_\perp$, using the values from the previous iteration as an initial estimate (see figure 5.6).
(3) The return energy is calculated (see figure 5.7).
(4) The following probabilities are calculated (see figure 5.8):

    (a) the ionization probability at time t_i from ADK theory, given the instantaneous field strength $\mathcal{E}(t_i)$,
    (b) the probability of having the required initial transverse momentum $p_\perp$ according to (5.5), and
    (c) the combined probability of generating a harmonic with energy $W_\mathrm{k} + I_\mathrm{p}$ as a product of the previous steps.

(5) Finally, the probability is extracted along the iso-energetic curves of figure 5.8 to give the yield curves presented in figure 5.9. These curves are fitted with Gaussians to obtain an estimate of the threshold ellipticity as a function of harmonic order; this is plotted as the solid lines in figure 5.10.

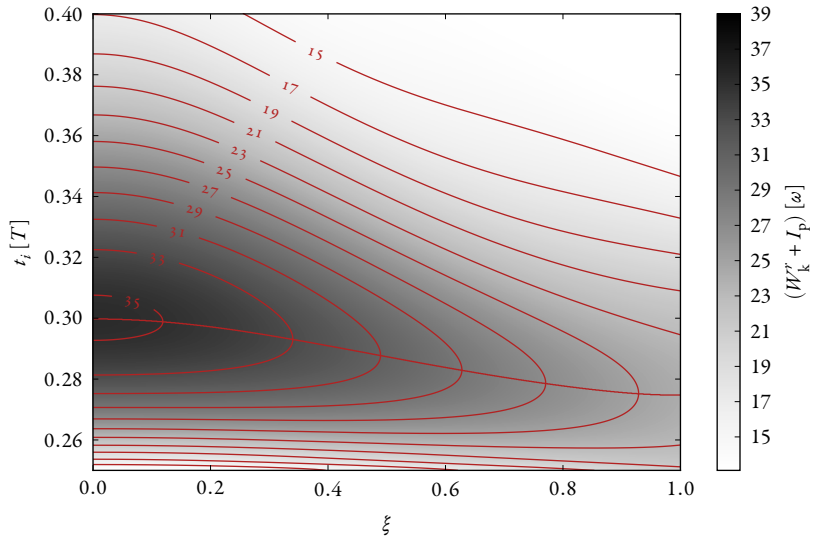

FIGURE 5.7: Return energy as a function of ionization time and ellipticity. This directly determines the energy of the emitted harmonics, and the contours are the iso-energetic lines, corresponding to the harmonics between the threshold I_p and the cutoff. The almost horizontal curve indicates how the classical cut-off moves to earlier ionization times with increasing ellipiticity.

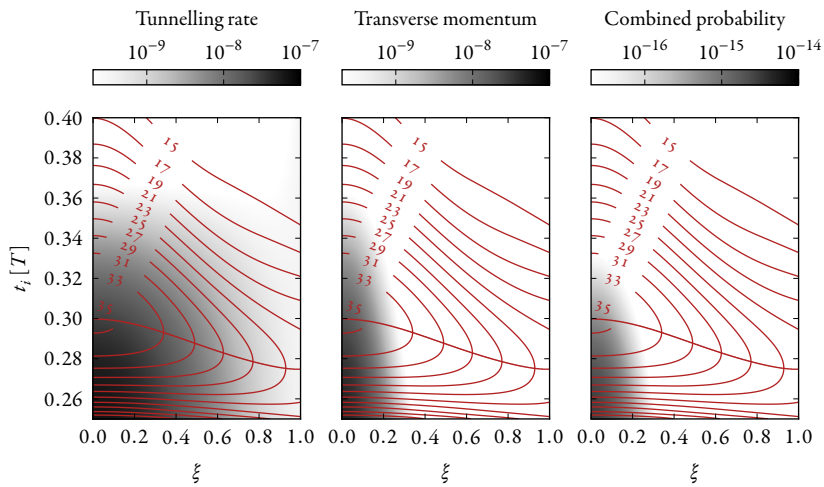

FIGURE 5.8: The constituent and combined probabilities determining the HH yield, for ionization times t_i and ellipticities ξ. Left: Tunnelling rate. Middle: Probability of having the required initial transverse momentum $p_\perp$ to enable the electron to return. Right: Combined probability of tunnel-ionization at time t_i and having the required initial transverse momentum $p_\perp$ to enable the electron to return.

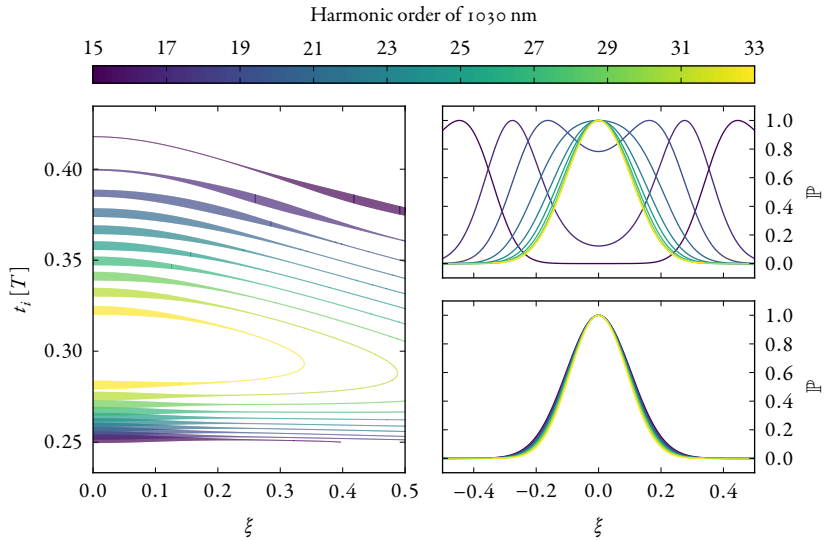

Figure 5.9: Left: The iso-energetic contours of figure 5.7, where the thickness of the line is scaled by the combined probability in figure 5.8. The right column shows the yield curves for different harmonic orders, i.e. the value along the iso-energetic contours in the left column, as a function of probability, for the short trajectory (upper panel) and the long trajectory (lower panel). All the curves are all normalized to their maximum values. For the shortest trajectories, the probability initially increases with ellipticity, since the field strength is very low. This bears some resemblance to the observed ellipticity response of near-threshold harmonics, cf. figure 5.5.

Figure 5.10 shows the results of the semi-classical model outlined above, together with the experimental results. Also shown is the effect of expanding (5.5) over small momenta to yield (5.7). Most notably, the short trajectory appears to be more sensitive than the long trajectory [this is, however, not the case for (5.8), which is also based on (5.7)]. Comparing with figure 5.6, it can be seen that the initial transverse momentum required for return to the parent ion can be quite substantial.

The reason why the short-trajectory behaviour is not captured by the semi-classical model is mainly that the low-energetic short trajectories are the least classical ones; they experience comparably low field strengths and spend little time in the continuum. It can be seen in figure 5.9 that they exhibit a minimum at linear polarization, due to the vanishing ionization probability. When increasing the ellipticity, the field vector at the time of ionization is no longer identically zero for the shortest short trajectory, and the ionization rate increases. For even larger ellipticities, this effect is countered by the decreasing probabil-

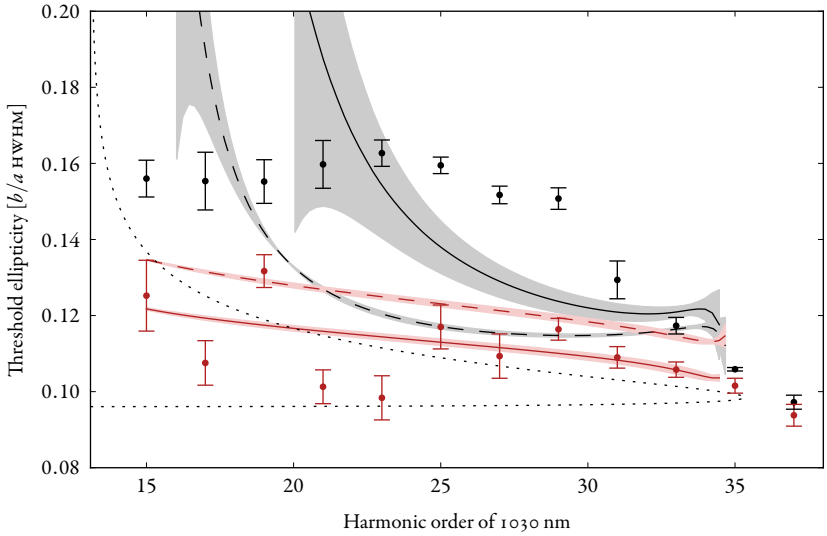

Figure 5.10: Comparison of the different classical models with the experimental data. The solid lines show the classical model as described above, taking into account the ionization rate according to ADK theory and the initial transverse momentum distribution as given by (5.5). The dashed lines show the effect of the Taylor expansion over small momenta, (5.7). The shaded regions indicate the uncertainty of the classical models, derived from the fit. Finally, the dotted line is (5.8) by Strelkov et al. (2012)

ity of having the initial transverse momentum required for return to the parent ion.

5.3 Résumé

The long-trajectory ellipticity response is governed by an intricate combination of the time–energy link for the harmonic orders and the probability of tunnel ionization at the right moment, with the appropriate initial transverse momentum. It is essential that the sub-cycle dynamics are properly accounted for, to describe the observed long trajectory behaviour.

To reconcile the experimental results with the theoretical calculations for the short trajectory, as presented in figure 5.2, it would be useful to perform an experiment in which the threshold ellipticity was measured for a range of driving field intensities. It may also be useful to perform the ellipticity measurements in such a way that that the intensity is maintained when the ellipticity is increased, as a means of decoupling the ellipticity response of the HHG from

the intensity dependence. This is an experiment that is planned for the future, together with a deeper study of the anomalous ellipticity behaviour of the harmonics close to threshold.

In this chapter, the extension of HHG to elliptically polarized driving fields has been studied. The very classical understanding from linear HHG does break down to some extent, and many quantum effects have to be taken into account to understand what is observed.

6 Macroscopic Effects in HHG

Macroscopic effects are those that arise due to interference between adjacent or subsequent emitters, and may be beneficial or detrimental in the application of HHG. On the one hand, they can be used to select emission from one trajectory only (as noted previously), thereby improving the spatial and spectral properties of the harmonic emission; while on other, it may be difficult to *phase match* the HHG process across the entire generation medium, leading to a decrease in overall harmonic flux, compared with the potential flux from all emitters being in phase.

In this chapter, we will study two macroscopic effects; the first one is a clever technique used to achieve angular separation of HH emission from subsequent events, precluding the interference that normally occurs between them (as discussed in §4.1). The second effect is the intensity dependence of the dipole phase parameters, which in §4 were assumed to be constant. An intensity dependence of α leads to a macroscopic phase variation over the near-field focal plane. In the far field, this manifests itself as an amplitude modulation. These two effects are similar in the sense that they both result from wavefront modulation in the focus.

6.1 Non-collinear optical gating

A new method for generating isolated pulses is proposed in PI. The idea is to cross two optical pulses at an angle (see figure 6.1). At the crossing-point of the two pulses, a wavefront will result. The wavefront rotates as the pulses propagate, thereby achieving angular streaking of the HHG. The HH emission will be mainly directed perpendicularly to this wavefront, which will in turn on the relative phase of the two pulses (see figure 6.2).

If the two pulses are propagating at angles $\pm\gamma$ with respect to to the z axis, they can be written

$$\mathcal{E}_{\pm}(t, \mathbf{r}) \equiv \mathcal{E}_{\pm}(t)\mathcal{E}(\mathbf{r}) \exp(\mathrm{j}\mathbf{k}_{\pm} \cdot \mathbf{r}), \tag{6.1}$$

where $\mathcal{E}_{\pm}(t)$ is the temporal profile, $\mathcal{E}(\mathbf{r})$ the spatial profile, and the wavevector

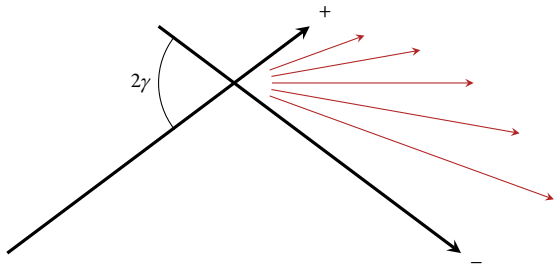

FIGURE 6.1: Non-collinear optical gating. Crossing two pulses, + and −, at an angle 2γ leads to the resultant HH emission having a wavevector that is a linear combination of the wavevectors of the two pulses. The time-dependent weights of the wavevectors are proportional to the field strengths of the two pulses at the crossing-point. By tuning the delay between the pulses, the rate at which the emission angle is streaked during one cycle of the fundamental field can be maximized, leading to maximal spatial separation in the far field of the emitted XUV.

$\mathbf{k}_\pm \equiv \pm[\sin(\gamma)\mathbf{e}_x + \cos(\gamma)\mathbf{e}_z]$. The total field is given by

$$\begin{aligned}\mathcal{E}_{\text{tot}}(t,\mathbf{r}) \equiv \mathcal{E}_+(t,\mathbf{r}) + \mathcal{E}_-(t,\mathbf{r}) &= \left[\xi \equiv \frac{\mathcal{E}_-(t)}{\mathcal{E}_+(t)}\right] \\ &= \mathcal{E}_+(t)\mathcal{E}(\mathbf{r})[\exp(\mathrm{j}\mathbf{k}_+\cdot\mathbf{r}) + \xi\exp(\mathrm{j}\mathbf{k}_-\cdot\mathbf{r})].\end{aligned} \tag{6.2}$$

The normal to the resulting wavefront at the crossing-point makes an angle β with the z axis:

$$\begin{aligned}\beta &\equiv \frac{\partial}{\partial x}\arg\{\mathcal{E}_{\text{tot}}(\mathbf{r})|_{z=0}\} = \frac{\partial}{\partial x}\arctan\left[\frac{\Im\{\mathcal{E}_{\text{tot}}(\mathbf{r})\}}{\Re\{\mathcal{E}_{\text{tot}}(\mathbf{r})\}}\bigg|_{z=0}\right] \\ &= \frac{\partial}{\partial x}\arctan\left[\frac{\sin(\mathbf{k}_+\cdot\mathbf{r}) + \xi\sin(\mathbf{k}_-\cdot\mathbf{r})}{\cos(\mathbf{k}_+\cdot\mathbf{r}) + \xi\cos(\mathbf{k}_-\cdot\mathbf{r})}\bigg|_{z=0}\right] \\ &= \frac{\partial}{\partial x}\arctan\left\{\frac{\sin[\sin(\gamma)x] + \xi\sin[-\sin(\gamma)x]}{\cos[\sin(\gamma)x] + \xi\cos[-\sin(\gamma)x]}\right\} \\ &= \lceil|\gamma| \lll 1\rfloor = \frac{\partial}{\partial x}\gamma x\frac{1-\xi}{1+\xi} = \gamma\frac{1-\xi}{1+\xi}.\end{aligned} \tag{6.3}$$

Assuming Gaussian temporal shape of the pulses, with duration τ and a relative delay of Δt, i.e.

$$\mathcal{E}_\pm(t) = \mathcal{E}_0\exp\left[-2\ln(2)\frac{(t\mp\Delta t/2)^2}{\tau^2}\right], \tag{6.4}$$

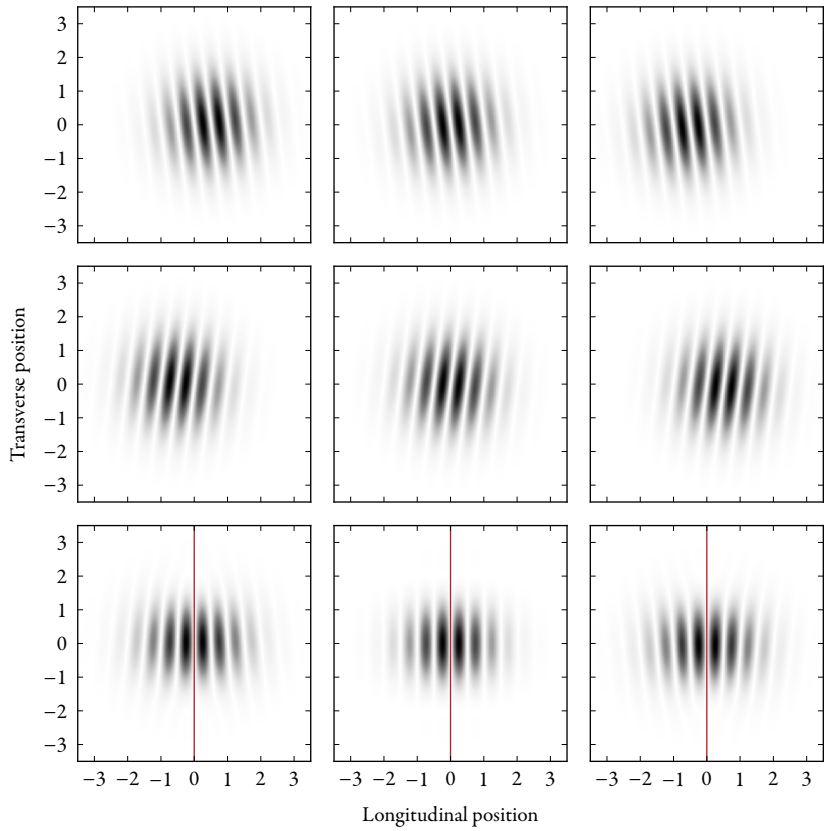

Figure 6.2: Rotating wavefronts generated at the crossing-point of two optical pulses, for different relative pulse delays. The two upper rows show two pulses propagating at an angle of $\pm 7°$ with respect to to the longitudinal axis, while the lower row shows the resultant field formed by superposing the two pulses shown above it. The middle column shows the effect of no relative pulse delay (the resulting wavefronts are perpendicular to the longitudinal axis), while the left and right columns show the patterns resulting from a relative pulse delay of $\mp\tau$, where τ is the pulse duration. Each subsequent wavefront is rotated slightly with respect to the previous one, leading to an angular streaking of, e.g. HH emission, if the combined field is used as driving the field in HHG. This picture is conjugate to the picture presented in figure 6.1.

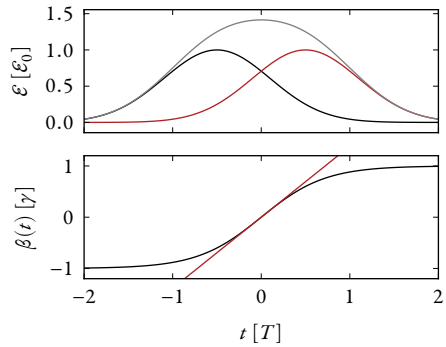

FIGURE 6.3: Wavefront angle as a function of time. The upper panel shows two Gaussian pulses (red and black), with a relative delay of $\Delta t = \tau$. The resultant field is shown in grey. The lower panel shows the wavefront angle (6.3) of the interference grating over time, together with the linear approximation (6.5). NB that the maximum angle can never be larger than $\pm\gamma$.

we can find the wavefront rotation speed where it is highest, by making a Taylor expansion around $t = 0$:

$$\begin{aligned}\frac{\partial}{\partial t}\beta \approx \frac{\partial}{\partial t}\gamma\frac{1-\xi}{1+\xi} = \left[\frac{\exp[a(t+b)^2] - \exp[a(t-b)^2]}{\exp[a(t+b)^2] + \exp[a(t-b)^2]} = 2abt + \mathcal{O}(t^3)\right] \\ \approx 2\ln(2)\gamma\frac{\Delta t}{\tau^2},\end{aligned} \tag{6.5}$$

where $a = -2\ln(2)$ and $b = -\frac{\Delta t}{2}$. This case is illustrated in figure 6.3.

By choosing the appropriate conditions (relative delay of the pulses, non-collinear angle, &c.), it is possible to angularly separate the radiation from subsequent emission events, hence the name, *non-collinear optical gating* (NOG). The angular separation in the near field leads to spatial separation in the far field. With no overlap in the far field, the emission from separate events cannot interfere and no harmonic structures appear, but rather continuous spectra, which can support isolated pulses. This has been experimentally demonstrated by Louisy et al. (2015). A further extension of the technique was realized by Hickstein et al. (2015), by circularly polarizing the driving pulses with opposite handedness with respect to one another. In this way, they were able to generate angularly separated circularly polarized high-order harmonics.

A very similar technique is the so-called *attosecond lighthouse* presented by Vincenti and Quéré (2012), in which the fundamental *itself* is angularly chirped, e.g. by passing the incoming light through a slightly tilted glass wedge.

This is easier to accomplish, but suffers from the drawback that the fundamental field co-propagates with the generated XUV emission. Using the NOG technique, the generating pulses continue to propagate with angles $\pm\gamma$ after crossing, whereas the XUV emission propagates at a very small angle to the optical axis, which means that the driving field and the XUV pulses are automatically separated in the far field. Depending on the degree of modulation of the driving pulses by the HHG process, they could conceivably be reused in a pump–probe scheme.

6.2 Off-axis interference

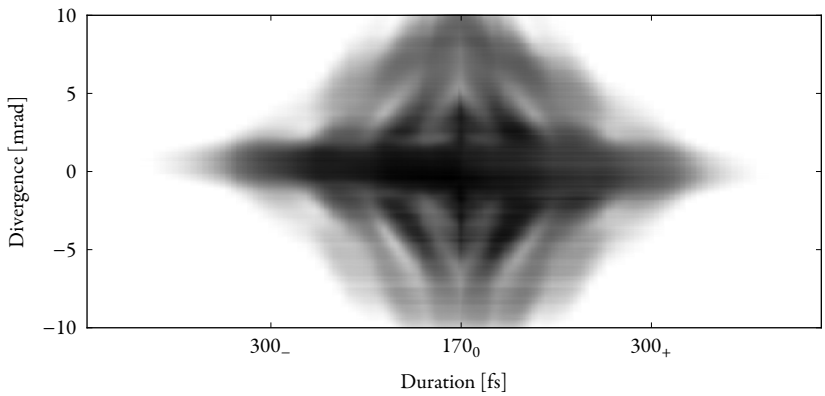

Figure 6.4: Experimentally measured interference patterns in HHG from argon: H027 of 1030 nm. The pattern arising from short–long trajectory interference is visible for small divergences, $\lesssim$5 mrad (cf. figure 4.8, where the on-axis interference is clearer). For larger divergences, an interference pattern of a different kind can be seen. The greyscale is logarithmic.

In §4, the interference between the short and the long trajectories in HHG was discussed. However, as noted there, this is not the only source of interference observed. Modulation is also visible off-axis, where no short-trajectory emission exists (see figure 6.4). In PIV, it was shown that this interference could be explained by the long-trajectory emission of adjacent atoms in the focal plane. Since the HH emission is written in the form (4.3), and in the focal plane the driving field will have a Gaussian spatial profile,

$$I(r) = I_0(\tau)\exp\left(-\frac{r^2}{2r_0^2}\right), \tag{6.6}$$

there will be a considerable wavefront modulation of the collective long-trajectory emission. As we saw in §6.1, wavefront modulation leads to a

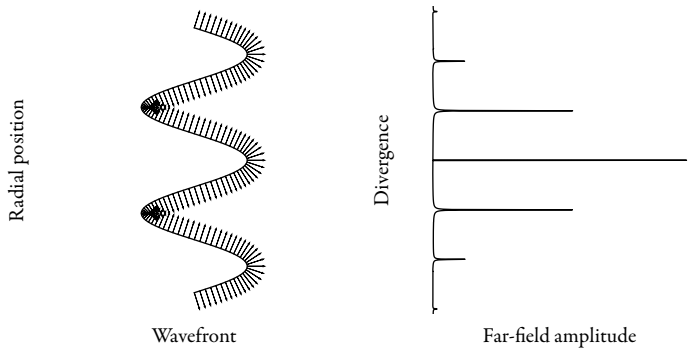

Figure 6.5: Wavevector bunching as a result of periodic wavefront modulation. Left: A sinusoidally varying wavefront, with the wavevector indicated as normals to the wavefront. Right: Far-field amplitude, with a main peak in the middle (corresponding to on-axis propagation) and side peaks due to wavefront modulation.

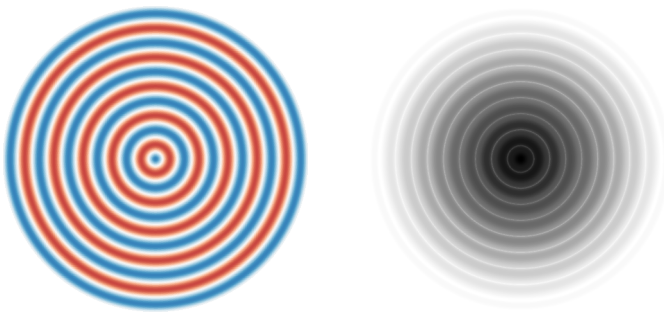

Figure 6.6: The 2D equivalent of figure 6.5. A cylindrically symmetric near-field pattern, with radially periodic *phase* (left) will give rise to a ring-like pattern in the far-field *amplitude* (right; logarithmic colour scale).

change in direction of the HH emission. If the wavefronts in the near field have a circular pattern, as will be the case when combining (4.3) and (6.6), this will result in repeated focusing and defocusing of the light in the far field ('bunching' of the wavevectors, see figures 6.5 & 6.6) or, equivalently, as ring-like structures.

This argument is *necessary* to explain the appearance of the rings observed in

the far-field amplitude. However, as was shown in PIV, the argument is not *sufficient* to explain the response of the rings with respect to intensity. We therefore turn to a model of the harmonic emission that is more complete than (4.3).

6.2.1 Adiabatic model of HH emission

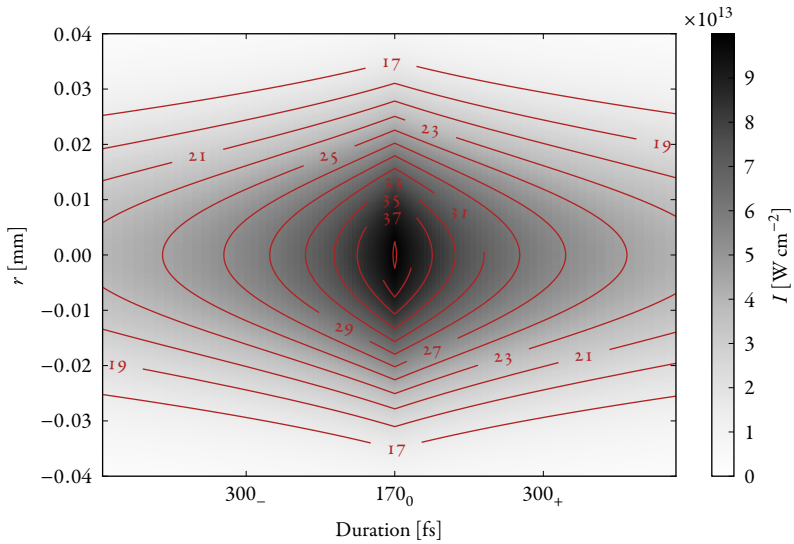

Figure 6.7: Fundamental intensity as a function of pulse duration and spatial profile. The contours indicate the classical cut-off intensitites for the different harmonics, i.e. outside each contour, the corresponding harmonic is in the cut-off regime.

We introduce an adiabatic model of the harmonic emission of order q:

$$\mathcal{E}_q(I) = \sum_j a_{qj}(I) \exp[\mathrm{i}\phi_{qj}(I)]. \tag{6.7}$$

This model is very similar to (4.3) used when studying the QPI between the short and the long trajectories. However, the intensity dependence of the phase is no longer purely linear (this approximation only holds in the plateau regime). The off-axis emission probes a larger range of intensities due to the larger excursion of the long trajectory; increasingly so with higher harmonic order (see figure 6.7 for an illustration of this). Therefore, (6.7) is more adequate in describing the off-axis emission. The adiabicity lies in that $a_{qj}(I)$ and $\phi_{qj}(I)$ are taken from the calculations described in §4.1; the near-field amplitude is thus modelled as a collection of emitters radiating the steady-state response of the HHG. Because

of this, there are, by definition, no transients and the harmonics are essentially 'monochromatic'. The model is only valid for the central harmonic energies, and can only be used for modelling the observed far-field spatial patterns. To model the spectral patterns, the transient behaviour of the HHG process must be included, i.e. for real pulses, a time-varying envelope must be used instead of the flat profile used in §4.1.

6.2.2 *Far-field propagation*

The manner in which the far-field amplitudes are calculated is detailed in appendix H, and essentially amounts to calculating the Fourier transform of the near-field complex amplitude.

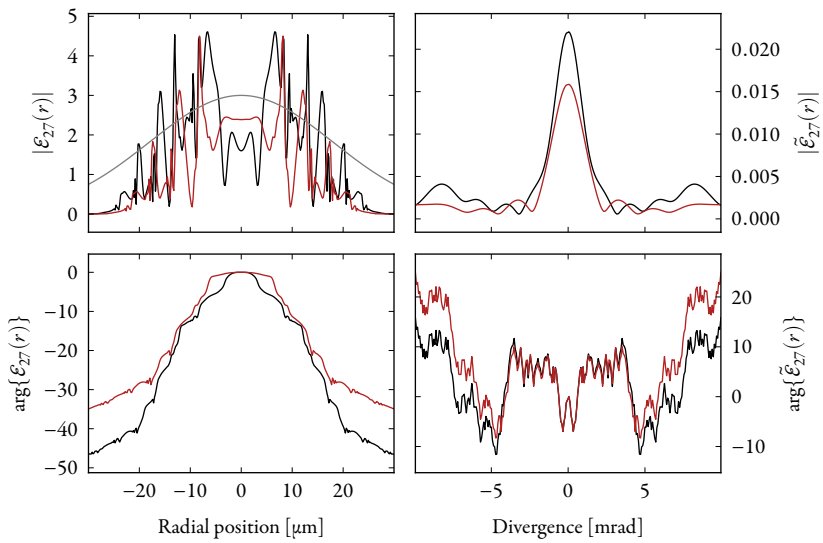

Figure 6.8: Propagation of HO27, calculated using the adiabatic model of the TDSE, to the far field, for $\tau = 170$ fs (black) and $\tau = 200$ fs (red). The left column shows the near-field amplitude (above) and phase (below). Although the fundamental driving field has a Gaussian spatial profile (shown for reference, in grey), the complex amplitude of the harmonic emission is noticeably modulated, cf. figures 4.4 & 4.6. Comparing with figure 6.7, the harmonic is in the cut-off regime for $|r| \gtrsim 20$ μm for $\tau = 170$ fs, while for $\tau = 200$ fs, the cut-off occurs for $|r| \gtrsim 10$ μm. This is most visible in the near-field phase, which changes slope around the transition into the cut-off regime. The right column shows the far-field amplitude (above) and phase (below). Also here, strong modulation can be seen; the small side lobes of the far-field amplitude constitute the observed rings.

To emulate the far-field interference patterns, we proceed as follows.

(1) The spatial profile is calculated according to (6.6) for each pulse duration τ (for each chirp) of the fundamental driving field,
(2) The near-field complex amplitude is calculated using the adiabatic model (6.7), with the intensity taken from the spatial profile calculated above,
(3) The far-field amplitude is then calculated using the far-field transform.

This is illustrated in figures 6.8 & 6.9.

6.3 Résumé

In this chapter, two effects of wavefront modulation on HHG have been discussed. The first effect was induced through the crossing of two pulses at an angle and with a delay with respect to one another. In this way, a wavefront rotation was achieved such that the HH radiation emitted from subsequent events could be angularly separated. Having no spatial overlap, the emitted pulses cannot interfere and their continuous spectral structure is preserved, which is a requirement for the generation of isolated attosecond pulses.

The second effect arose from the harmonic process itself, specifically the intensity dependence of the phase of the quantum paths, which leads to wavefront modulation over the spatial profile of the driving field. Although not an example of QPI per se, the different emitters are phase-locked through the known variation in spatial intensity of the fundamental. The resulting wavefront modulation in the near field leads to a far-field amplitude modulation, the precise nature of which can only be fully understood by considering the microscopic response beyond the simplest model, (4.3).

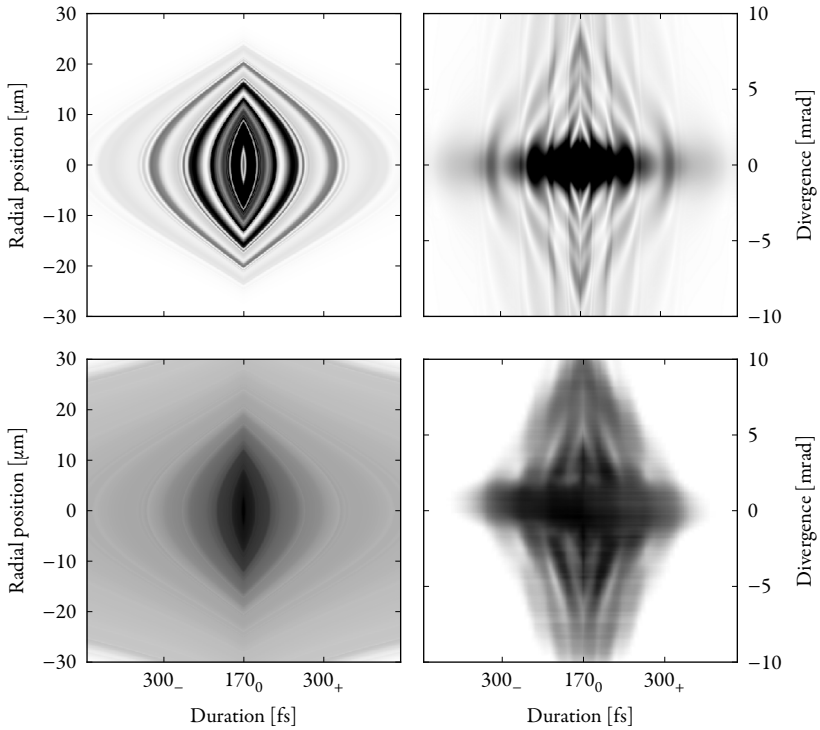

Figure 6.9: Near- and far-field profiles for ho27, calculated using the tdse. Similarly to figure 6.8, the left column shows the near-field amplitude (above) and phase (below) are shown, but here as a function not only of the radial position, but also the fundamental pulse duration, as induced by changing the chirp. The right column shows the far-field amplitude is shown, as calculated by propagating the adiabatic model through a Fourier transform (above) and the experimental result (below). The time axis is the same as in figure 4.8. The theoretical results (shown on a linear greyscale) and the experimental results (shown on a logarithmic greyscale) agree qualitatively, with respect to the overall shape of the interference structures, although the details are lacking in the experimental results. The theoretical results have a much higher dynamic range than do the experimental results. Both sets of results have been saturated to highlight the off-axis structures.

Coherence Control using xuv Pulses

7

– 'Balzampleu ! fit le Suisse, qui, malgré l'admirable collection de jurons que possède la langue allemande, avait pris l'habitude de jurer en français.

Alexandre Dumas, père, 1802–1870

Quantum path interference occurs, as we have seen earlier, when the quantum system takes more than one indistinguishable path from its initial state to the final state. Earlier, we have studied such quantum paths in HHG, which is driven by a strong field. The quantum paths are then very close to classical, in that the wave packet follows the trajectory of the classical electron. In this chapter, we will discuss another type of quantum path, for which there is no classical analogue. Upon photoionization of an atom, the final state of the system is an ion coupled to a photoelectron. Due to spin–orbit coupling, the ground state of the ion may be split into several substates; for the singly charged ions of the non-radioactive noble gases heavier the helium, the spin–orbit splitting results in two substates with a separation ranging from 0.1 eV in neon to 1.3 eV in xenon (see table 7.1). If the atom is

Table 7.1: Some properties of the non-radioactive noble gases heavier than He. ΔE_{s-o} is the spin–orbit splitting of the ionic ground state $np^5\ ^2P^o$. The uncertainty in time derived from the the Heisenberg uncertainty principle is $\Delta t \geq (2\Delta E_{s-o})^{-1}$. A coherent superposition of two states with an energy difference of ΔE_{s-o} will have a quantum beat period of $T = 2\pi\Delta E_{s-o}^{-1}$.

Element	Z	n	ΔE_{s-o} [eV]	Δt [fs]	T [fs]
Ne	10	2	0.09676024	3.4	42.8
Ar	18	3	0.17749368	1.9	23.3
Kr	36	4	0.665808	0.5	6.2
Xe	54	5	1.306423	0.3	3.2

photoionized with an ultrashort pulse, we have no way of discerning whether the residual ion is left in the upper or the lower substate, due to the large bandwidth of the ionizing pulse. The longer the duration of interaction, the more spectrally narrow the pulse becomes, and at some point, the contributions of the different ionic states become apparent in the photoelectron spectrum as

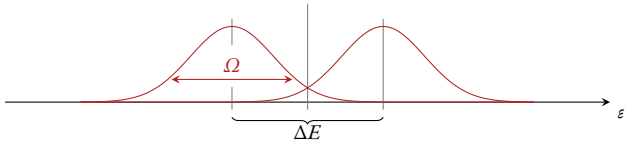

FIGURE 7.1: Overlap between two quantum paths separated by ΔE. The spectral bandwidth, Ω, of the ionizing pulse is inversely proportional to the duration of the pulse.

two peaks, separated by the spin–orbit splitting. When these peaks are fully resolved, there will no longer be multiple paths to the same final energy of the ejected photoelectron, and the paths may no longer interfere.

Coherence is a measure of the ability to produce stationary interference patterns. The *coherence time* is the average time this interference can be observed. In the case of quantum paths in the photoionization process discussed above, coherence is a measure of their indistinguishability. The Heisenberg uncertainty principle sets a lower limit on the pulse duration required for the quantum paths to be resolved:

$$\Delta t \geq \frac{1}{2\Delta E_{s-o}}. \tag{7.1}$$

For the noble gases considered, Δt ranges from 7 fs to 0.5 fs. The period time for light of optical wavelengths is around 1 fs, which means that for xenon, for example, the coherence would be lost on a sub-cycle timescale. However, as can be seen in figure 7.1, even though the peaks are resolved, they do still overlap to some extent. This implies that some degree of indistinguishability remains, which is measured as a partial coherence. If we assume that the ejected photoelectron has a Gaussian energy distribution, due to the spectral distribution of the ionizing pulse (see figure 7.1; cf. appendix F for useful relations in ultrafast optics), the photoelectron spectrum will have two peaks separated by the spin–orbit splitting ΔE_{s-o}. The overlap between the two peaks will then have the amplitude

$$W(\omega) = \exp\left[-\frac{\left(\varepsilon - \frac{\Delta E_{s-o}}{2}\right)^2}{2\Omega^2}\right] + \exp\left[-\frac{\left(\varepsilon + \frac{\Delta E_{s-o}}{2}\right)^2}{2\Omega^2}\right], \tag{7.2}$$

where ε is the photoelectron energy and Ω the ionizing pulse bandwidth. At the point of smallest overlap, i.e. precisely in the middle between the two photoelectron peaks, the overlap amplitude is

$$W(0) = 2\exp\left(-\frac{1}{4}\frac{\Delta E_{s-o}^2}{2\Omega^2}\right) = 2\exp\left[-\frac{(\Delta E_{s-o}\tau)^2}{32\ln(2)}\right], \tag{7.3}$$

Table 7.2: Ionization channels accessible via one-photon ionization from the ground state of any noble gas, heavier than He. The channel configurations are given in *jK* coupling, also known as pair coupling, since the levels of noble gases are likely to appear in pairs.

№	Ion config	Ion term	j	ℓ	K	J	Configuration
1	np^5	$^2P^o$	$3/2$	d	$1/2$	1	$np^5(^2P^o_{3/2})kd\ ^2[1/2]_1$
2	np^5	$^2P^o$	$3/2$	s	$3/2$	1	$np^5(^2P^o_{3/2})ks\ ^2[3/2]_1$
3	np^5	$^2P^o$	$3/2$	d	$3/2$	1	$np^5(^2P^o_{3/2})kd\ ^2[3/2]_1$
4	np^5	$^2P^o$	$1/2$	s	$1/2$	1	$np^5(^2P^o_{1/2})ks\ ^2[1/2]_1$
5	np^5	$^2P^o$	$1/2$	d	$3/2$	1	$np^5(^2P^o_{1/2})kd\ ^2[3/2]_1$
6	$nsnp^6$	^2S	$1/2$	p	$1/2$	1	$nsnp^6(^2S_{1/2})kp\ ^2[1/2]_1$
7	$nsnp^6$	^2S	$1/2$	p	$3/2$	1	$nsnp^6(^2S_{1/2})kp\ ^2[3/2]_1$

where τ is the intensity FWHM pulse duration of the ionizing pulse. The joint probability in the middle between the peaks is then

$$|W(0)|^2 \propto \exp\left[-\frac{(\Delta E_{s-o}\tau)^2}{16\ln(2)}\right]. \tag{7.4}$$

In this chapter we study the conditions under which coherence can be established using the XUV pulses we have been studying in previous chapters. We will begin by describing the model system for which the calculations were performed. After briefly surveying the mathematical tools used for analysis of coherence in quantum mechanical systems, we will study neon and xenon, the two nobles gases with the smallest and largest spin–orbit splitting of those listed in table 7.1, respectively. Once the reason for the loss of coherence is understood, we shall see that there is a way of circumventing this by employing a tailored ionizing pulse, and we will find the degree of coherence that can be obtained for a given set of pulse parameters.

7.1 Model system

Figure 7.2 shows a sketch of the model system employed in the calculations. For each harmonic, the electron will have two components in its kinetic energy distribution, corresponding the difference between the harmonic energy and the two spin–orbit substates of the ionic ground state. If the separation between the harmonics is the same as the spin–orbit splitting, there will be two pathways to the same final energy of the electron, and interference may be possible. In fact, there is more than one way to reach the continuum via one-photon ioniza-

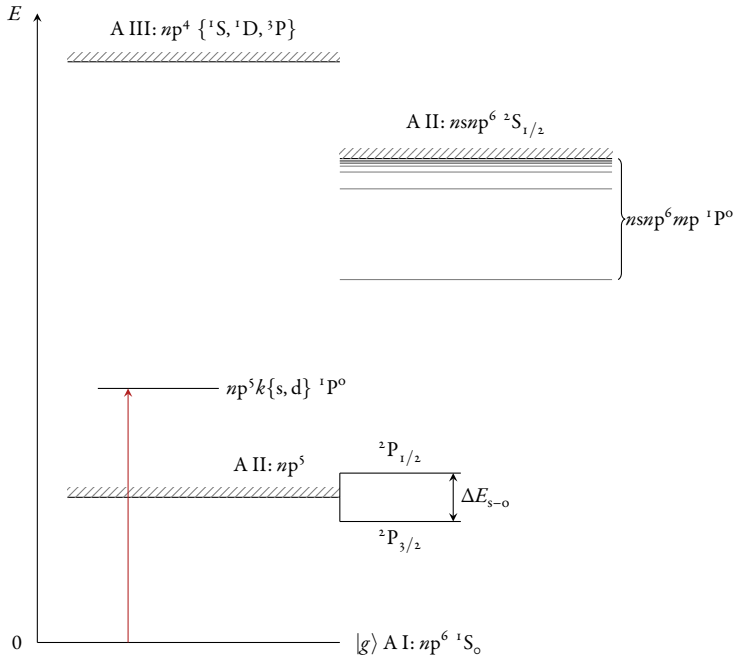

FIGURE 7.2: Ionization of a noble gas heavier than He. The lowest-lying ionic ground state has a spin–orbit splitting with terms $^2P_{3/2,1/2}$. The second ionic threshold, $nsnp^6$, supports a Rydberg series which will decay through autoionization, giving rise to *Fano (1935, 1961) resonances*. Below this series, the continuum is flat.

tion, as is evident from table 7.2. However, only channels 3 & 5 provide a set of quantum numbers that are identical apart from the spin–orbit substate of the ion. Requiring the quantum numbers to be identical is equivalent to requiring the final states to be the same.

7.2 CALCULATIONS

7.2.1 Tools

The calculations were performed as detailed in §2.2, using a combination of a fourth-order commutator-free propagator (Alvermann, Fehske, and Littlewood 2012) and a Krylov exponentiator (Krylov 1931; Lanczos 1950; Saad 1992, 2003). If the $nsnp^6$ threshold is neglected, the problem reduces to that of a single active electron. However, the electron spin is not included in the wavefunction expansion in the SAE approximation used in this work, and therefore, no spin–orbit splitting is present. Instead, the calculations were performed in a

base consisting of bound states found using MCHF coupled to continuum states in the CC approximation (§§2.1.1–2.1.2). Since we are interested in noble gases, the *jK* coupling scheme (Cowan 1981) was used. The interaction is expressed in the length gauge. Furthermore, since the photoionization is in the weak-field regime, only one-photon transitions from the ground state are allowed ($J \leq 1$) and mixing of singlet and triplet terms is neglected.

The coherence of a quantum system can be analysed using the *density matrix* formalism (Landau and Lifshitz 1977, §14). The *density matrix* operator is defined as

$$\rho = |\Psi\rangle\langle\Psi|. \tag{7.5}$$

For a two-level system, the wavefunction can be written as a superposition $|\Psi\rangle = a|1\rangle + b|2\rangle$. The density matrix then has the form

$$\rho = \begin{bmatrix} a \\ b \end{bmatrix} \begin{bmatrix} a^* & b^* \end{bmatrix} = \begin{bmatrix} |a|^2 & ab^* \\ a^*b & |b|^2 \end{bmatrix}, \tag{7.6}$$

where the diagonal matrix elements provide a measure of the population in each level, and the off-diagonal matrix elements are known as the coherences.

For a more complicated system, in which there are many degrees of freedom, some of them might not be observed in the experiment; we may write the state as $|a;\varsigma\rangle$, where ς is the unobserved quantity. To take this into account in the calculation, a *reduced density matrix* is formed by taking the *trace* of the density matrix over the unobserved degrees of freedom:

$$\rho_a \equiv \int \mathrm{d}\varsigma\ \langle\varsigma|a_1;\varsigma_1\rangle\langle a_2;\varsigma_2|\varsigma\rangle. \tag{7.7}$$

This is used here to access the coherence between the ionic substates $^2\mathrm{P}^\mathrm{o}_{3/2,\,1/2}$ by tracing over the unobserved photoelectron energies and angular momenta (for details, see PVI).

7.2.2 Neon

Figure 7.3 shows the photoionization cross-section of neon and the constituent *dipole matrix elements* (DME) as a function of photoelectron energy, up to the $2s^1 2p^6$ threshold (below which a Rydberg series appears). Irradiating neon with the 15th harmonic of 800 nm ionizes the atom, but the photoelectron has an energy below the lowest Rydberg state of the second threshold, and thus the continuum is flat. Figure 7.4 shows the real-time ionization of neon, for different pulse durations. As is expected, when the duration of the pulse is large,

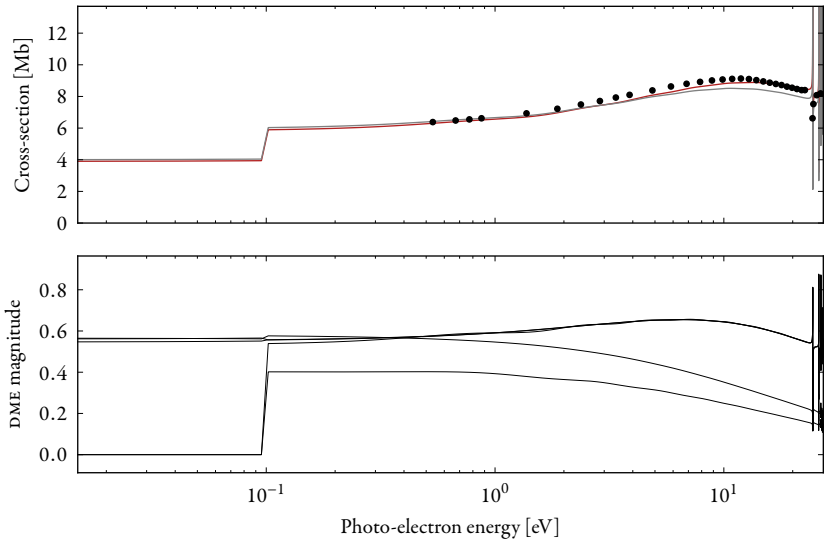

FIGURE 7.3: Upper panel: photoionization cross-section of neon as a function of photoelectron energy, calculated using ATSK2K & BSR. The red line shows the length gauge result, while the grey line shows the velocity gauge result. The experimental results of Samson and Stolte (2002) are shown as dots for comparison. Lower panel: Ionization-channel-resolved dipole matrix elements for channels 1–5 (cf. table 7.2). The energy axis has been logarithmically scaled to focus on the spin–orbit splitting of ∼0.1 eV, where only channels 1–3 contribute to the total cross-section.

the multiple paths to the same final state cease to exist and the coherence is lost.

Figure 7.5 shows the coherence of the ionic substates as a function of pulse duration. As expected, the coherence decreases monotonically. However, it remains for a substantial range of pulse durations exceeding the time uncertainty predicted by the Heisenberg uncertainty relation (3.4 fs according to table 7.1). In fact, as can be seen in figure 7.4, the coherence is only completely lost when the pulse duration exceeds the quantum beat period 42.8 fs. This is in line with the experimental results of Goulielmakis et al. (2010), who observed loss of coherence in Kr^+ when the pulse duration exceeded the quantum beat period 6.2 fs. The reason for this can be understood as follows. A system in an equal superposition of two states, will have a state evolution of the form

$$\begin{aligned} |\Psi(t)\rangle &= \frac{1}{\sqrt{2}}[\exp(-\mathrm{i}E_1 t)|1\rangle + \exp(-\mathrm{i}E_2 t)|2\rangle] \\ &= \frac{\exp(-\mathrm{i}E_1 t)}{\sqrt{2}}[|1\rangle + \exp(-\mathrm{i}\Delta E t)|2\rangle], \end{aligned} \tag{7.8}$$

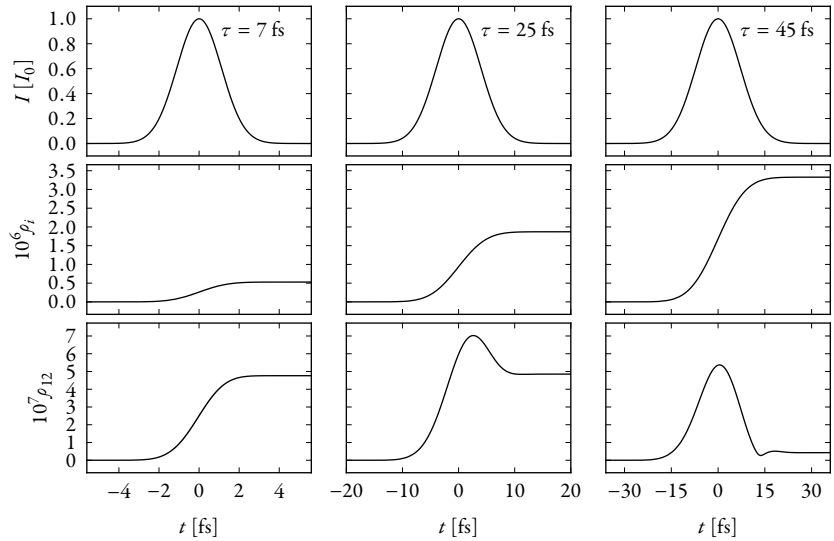

Figure 7.4: Real-time coherence build-up between the spin–orbit substates in singly ionized neon, for three different pulse durations (intensity FWHM). Upper row: the normalized intensity envelopes of the ionizing field, HO15 of 800 nm. $I_0 = 1 \times 10^8$ W cm^{-2}. Middle row: the population in the ionic substates, channels 3 & 5. The difference in population between the substates is negligible. Lower row: the coherence between the substates. Interestingly, for pulse durations longer then the quantum beat period (τ=45 fs), coherence is transiently built up, but disappears when the driving field induces dephasing.

where $\Delta E = E_2 - E_1$. This system can be regarded as a kind of 'clock' whose period is exactly the quantum beat period. The interaction of this superposition with an electric field will 'speed up' or 'slow down' the clock. If after one revolution the clock has been advanced or delayed such that it has dephased, the superposition will start to decohere. This explains why the loss of coherence is observed after one quantum beat period.

7.2.3 Xenon

As xenon has a considerably larger spin–orbit splitting, one would expect it to decohere much faster than neon (cf. table 7.1). When xenon is ionized the same way as was described above for the case of neon, i.e. by a single-frequency pulse, this is indeed the case. However, by employing an ionizing pulse consisting of two frequencies (see figure 7.6), created, for example, by HHG, it is possible to ensure the existence of a two indistinguishable pathways to the same final

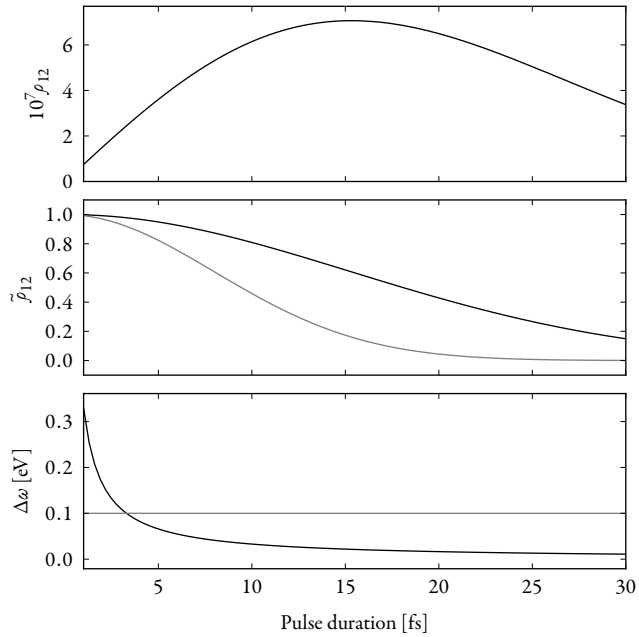

Figure 7.5: The upper panel shows the coherence, ρ_{12}, between the ionic substates of neon after the pulse has passed, as a function of pulse duration. Initially, the magnitude of the coherence increases with increasing pulse duration, but this is due to the increase in population possible through the longer interaction time. The middle panel shows the degree of coherence (black), which normalizes the coherence to the population of both states under consideration. The grey curves shows the prediction of (7.4). The lower panel shows the spectral bandwidth (black) of the ionizing pulse as a function of pulse duration. The grey horizontal line indicates the spin–orbit splitting of neon, which crosses the bandwidth curve at 3.4 fs.

photoelectron energy, provided that the harmonic separation is the same as the spin–orbit splitting of the ionic ground state. This is the key point of PVI. Figure 7.7 shows the coherence as a function of time for two cases. The first case is ionization using a pulse with a single frequency, as in the case of neon above. The quantum system decoheres quite rapidly, in accordance with the discussion above; i.e. when the quantum beat period is exceeded, the coherence has essentially disappeared. The second case is that depicted in figure 7.6, for a number of different *detuning ratios*, defined as

$$d \equiv \frac{\Delta\omega}{\Delta E_{\text{s-o}}}, \tag{7.9}$$

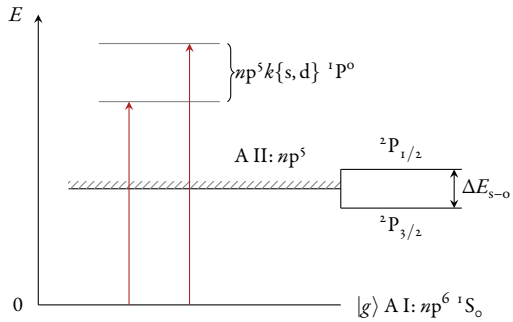

Figure 7.6: Resonant ionization of a noble gas heavier than He, using two phase-locked harmonics, leads to four pathways for the photoelectron. If the harmonic separation equals the spin–orbit splitting of the ionic ground state, two of these pathways lead to the same final photoelectron energy.

where $\Delta\omega$ is the harmonic separation. If $d = 1$, the degree of coherence does not depend on the duration of the ionizing pulse, and the coherence is retained indefinitely, or rather, as long as the phase relation between the frequency components of the ionizing pulse is remains stable. Employing the clock analogue once more, the case $d = 1$ can be regarded as the driving pulse stimulating the ionic substate superposition at the same 'time' for every revolution of the 'clock'. We have thus found a method for efficiently creating a superposition between the ionic substates. We can increase the population in each substate over a long interaction time, without inducing dephasing and losing the coherence between the substates.

7.3 Résumé

In this chapter, the coherence of ionic substates was discussed, together with ways of influencing it by tailoring the ionizing XUV pulse. In particular, if the XUV pulse consists of two frequencies differing by the ionic substate separation, the coherence between the substates can be retained for times much longer than would normally be expected from the Heisenberg uncertainty principle.

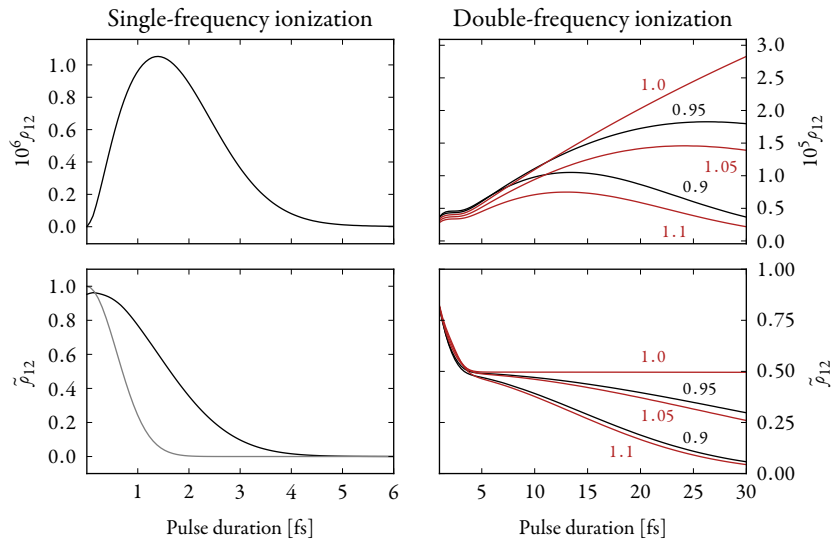

Figure 7.7: Left column: Coherence (upper panel) and degree of coherence (lower panel) of the ionic substates of xenon when ionized with a single-frequency pulse, as a function of pulse duration. For pulse durations exceeding the quantum beat period, 3.2 fs, the coherence is lost. Again, the grey line corresponds to (7.4). Right column: Coherence (upper panel) and degree of coherence (lower panel) for ionization in the case depicted in figure 7.6, for five different values of the detuning ratio d. In the resonant case ($d = 1$), the degree of coherence does not depend on the pulse duration.

8 Conclusions & Outlook

The recurring theme in this thesis is the quantum paths of electrons in ultrafast processes; understanding them, measuring them, and controlling them. Their admixture of quantum and classical character makes their study highly interesting.

The work presented herein can undoubtedly can be improved upon. The scheme for generating isolated attosecond pulses presented in PI has already been implemented, but not that proposed in PII. It is clear from the earlier work on stereo-ATI for short pulses, and the link between CEP and the relative phase of two-colour fields, that the idea is sound. However, the experimental challenges are still unknown. The realization of the long-pulse stereo-ATI technique is one of the reasons for the purchase of a new laser system similar to that used in the studies described in PIII & PIV. These two studies could benefit from being repeated in a systematic fashion. What is missing from the former is mainly an intensity scan of the ellipticity response, to decouple the interdependence of intensity and ellipticity in HHG; while the latter, although showing beautiful interference patterns, lacks the statistics necessary to validate a true metrological technique, as well as a way of linking the long trajectories interferometrically to establish their relative phase.

Personally, I am intrigued by the possibility of probing the wave nature of matter to the extent that has been possible in the present work. The quantum path formalism of Feynman (1965) has also come to light beautifully through the work on QPI. Being able to match the experimental results so closely, as shown in PIV, was most gratifying.

In the future, I would like to participate in the research on the effects of correlation on the ultrafast processes, an activity that has only just begun. Correlation effects have been treated for decades in the field of atomic structure. There, the effects of the, in some sense time-dependent contributions (such as emission and reabsorption of polarization photons, &c.) are included in a completely time-independent manner, since they amount to the calculation of matrix elements, *once*. Therefore, the calculations are tractable. In quantum dynamics however, these matrix elements have to be constantly recalculated as the basis is ever-changing due to the interaction. Marrying these two disciplines presents a formidable challenge, both in terms of identifying the calculations necessary, as well as actually performing them. Nonetheless, this is the way forward, since the effects of correlation are becoming increasingly visible in experiments.

9 Acknowledgements

I'm traveling light
It's au revoir

Leonard Cohen, 1934–2016

I would like to thank those that have made this thesis work possible. Foremost, my main supervisor Johan Mauritsson is to be thanked for giving me the opportunity to engage in the very exciting activity at the frontier of basic research, and for his generosity. My co-supervisor Kenneth J Schafer has never tired to answer my endless questions, and has always shown interest in my ideas, discussing at length related and unrelated topics. My second co-supervisor, as well as first contact with quantum mechanics, Lars Engström has provided me the link to 'real atomic physics'. This has been very helpful in going beyond the single-active-electron approximation, and understanding all the coupling schemes one might choose from when designing an atom.

Although not formally being my supervisors, Anne L'Huillier, Mette Gaarde, and Mathieu Gisselbrecht have taken care of me, as if I were, always kindly supporting me, and providing me with insight into advanced physics.

My research work has been performed in close collaboration with a few persons I would like to thank especially: Esben Witting Larsen, who smiles and is always willing to help; the very kind Jana Preclíková from Bohemian paradise; Christoph Heyl, who has been a fantastic room mate and a fantastic German-sparring partner; Eleonora Lorek with *'Fingerspitzengefühl* for the emotions of others, and recognition of their importance; Anne Harth, who believes in our projects and always asks interesting questions; Chen Guo, who always helps me understand theory by giving me ultrafast answers; and my former master student Leon Petersson, with whom I have had many interesting discussion over common and wholly different viewpoints.

The atmosphere in the Lund Atto group has really been fantastic; for this I would like to thank past and present members: Cord Arnold, Samuel Bengtsson, Fernando Brizuela, David Busto, Filippo Campi, Yu-Chen Cheng, Hélène Coudert-Alteirac, Marcus Dahlström, Diego Guenot, my current, fantastic room mate Neven Ibraković, Marcus Isinger, Per Johnsson, Byunghoon Kim, Katrin Klünder, Marija Kotur, David Kroon, Jan Lahl,

Arthur Losquin, Maïté Louisy, Sylvain Maclot, Bastian Manschwetus, Sara Mikaelsson, Miguel Nicolau da Costa Ribeiro de Miranda, Saikat Nandi, Lana Neoričić, Jasper Peschel, Linnea Rading, Piotr Rudawski & Agnieszka Rudawska, Jörg Schwenke, Emma Rose Simpson, Hampus Wikmark, and Shiyang Zhong. These five years would not have been as enjoyable as they have been, without you! The same can be said about the other people on the same floor: Åsa Bengtsson, Carl Ekström, Jenny Karlsson, Adam Kinos, Stefan Kröll, Amélie Jarnac, Qian Li, Hans Lundberg, Anna Persson, Lars Rippe, Mahmood Sabooni, Diana Serrano, Chien-Ming Tu, Andreas Walther, Xiaocui Wang, and Yan Ying. Thank you for your camaraderie!

I would like to thank Camilla Bengtsson, Bertil Hermansson, Åke Laszlo Johansson, Anne Petersson Jungbeck, Emin Kacamaku, Harriet Lindahl, Anders Persson, and Jakob Testad for always keeping the wheels spinning, and division head Claes-Göran Wahlström for overseeing the well-being of the division.

From the *Lund–Malmö Center of Atomic Systems* (LUMCAS) group, I would especially like to thank Tomas Brage and Jon Grumer; from the extended LUMCAS family, I would like to thank Charlotte Froese Fischer, Alan Hibbert, Kevin Dunseath & Mariko Dunseath-Terao, and Oleg Zatsarinny (without whose help, PVI would not have been possible). During my stay at Nordita in Stockholm 2015, I met many nice persons; of these, I would like to thank Eva Lindroth who hosted the summer school, Sølve Selstø, and Tor Kjellsson.

Lastly, I would like to thank my friends and relations, especially my dear Mother, και δόξα τω Θεώ.

Appendices

Atomic Units

A

Atomic units are used to simplify calculations in atomic physics via a coordinate transform in which important quantities are set to unity. In the Hartree atomic units system, the following identities hold:

$$m_e = e = \hbar = 4\pi\varepsilon_0 = 1$$

All other quantities are derived from these, giving the following values in SI units for one unit in atomic units [table taken from Häßler (2009)]:

Quantity		Value
Angular momentum	$\hbar$	$1.054\,571\,726 \times 10^{-34}\,\mathrm{J\,s}$
Mass	m_e	$9.109\,383 \times 10^{-31}\,\mathrm{kg}$
Charge	e	$1.602\,176\,53 \times 10^{-19}\,\mathrm{C}$
Length	$a_0 = \frac{4\pi\varepsilon_0\hbar^2}{m_e e^2}$	$5.291\,772\,085\,9 \times 10^{-11}\,\mathrm{m}$
Velocity	$v_B = \frac{e^2}{4\pi\varepsilon_0\hbar}$	$2.187\,691\,263\,3 \times 10^{6}\,\mathrm{m\,s^{-1}}$
Momentum	$m_e v_B$	$1.992\,851\,66 \times 10^{-24}\,\mathrm{kg\,m\,s^{-1}}$
Time	$\tau_0 = \frac{a_0}{v_B}$	$2.418\,884\,30 \times 10^{-17}\,\mathrm{s}$
Frequency	τ_0^{-1}	$4.134\,137\,38 \times 10^{16}\,\mathrm{Hz}$
Energy	$E_h = \frac{m_e e^4}{(4\pi\varepsilon_0)^2\hbar^2}$	$4.359\,744\,17 \times 10^{-18}\,\mathrm{J}$
Electric field	$\mathcal{E}_0 = \frac{e}{4\pi\varepsilon_0 a_0^2}$	$5.142\,206\,51 \times 10^{11}\,\mathrm{V\,m^{-1}}$
Intensity	$\frac{\varepsilon_0 c_0}{2}\mathcal{E}_0^2$	$3.509\,445\,2 \times 10^{16}\,\mathrm{W\,cm^{-2}}$

B

Equations of Motion in Strong Fields

If we neglect the potential due to the atom, we obtain a very simple set of equations of motion for the electron, after ionization:

$$\dot{q} = Aq + f(t), \tag{B.1}$$

with

$$q = \begin{bmatrix} \mathbf{r} \\ \mathbf{p} \end{bmatrix}, \quad A = \begin{bmatrix} 0 & 1 \\ 0 & 0 \end{bmatrix}, \quad f(t) = \begin{bmatrix} 0 \\ -\boldsymbol{\mathcal{E}}(t) \end{bmatrix},$$

that is, $\mathbf{r}$ is the position of the electron and $\mathbf{p}$ its momentum. $\boldsymbol{\mathcal{E}}(t)$ is the (arbitrarily polarized) electric field. The solution of this system of equations is given by

$$q(t) = q_h(t) + q_f(t), \tag{B.2}$$

where the homogeneous solution is given by

$$q_h(t) = \exp[A(t - t_i)]q_i = \begin{bmatrix} 1 & t - t_i \\ 0 & 1 \end{bmatrix} q_i. \tag{B.3}$$

The inhomogeneous solution, due to the electric field, is given by

$$\begin{aligned} q_f(t) &= \exp[A(t - t_i)] \int_{t_i}^{t} \mathrm{d}t' \exp[-A(t' - t_i)] f(t') \\ &= \begin{bmatrix} 1 & t - t_i \\ 0 & 1 \end{bmatrix} \int_{t_i}^{t} \mathrm{d}t' \begin{bmatrix} 1 & -(t' - t_i) \\ 0 & 1 \end{bmatrix} \begin{bmatrix} 0 \\ -\boldsymbol{\mathcal{E}}(t') \end{bmatrix} \\ &= \begin{bmatrix} 1 & t - t_i \\ 0 & 1 \end{bmatrix} \int_{t_i}^{t} \mathrm{d}t' \begin{bmatrix} (t' - t_i)\boldsymbol{\mathcal{E}}(t') \\ -\boldsymbol{\mathcal{E}}(t') \end{bmatrix}. \end{aligned} \tag{B.4}$$

If we assume that the field is the imaginary part of a complex field,

$$\boldsymbol{\mathcal{E}}(t) = \Im\{\tilde{\boldsymbol{\mathcal{E}}}_0 \exp(\mathrm{i}\omega t)\}, \quad \tilde{\boldsymbol{\mathcal{E}}}_0 \equiv \mathcal{E}_0 \mathfrak{p}, \quad \mathfrak{p} \in \mathbb{C}^2, \tag{B.5}$$

polarized in the z–x plane and propagating along y, we obtain the solution

$$\begin{aligned}
\tilde{q}_f(t) &= \tilde{\mathcal{E}}_0 \begin{bmatrix} 1 & t-t_i \\ 0 & 1 \end{bmatrix} \int_{t_i}^{t} \mathrm{d}t' \begin{bmatrix} (t'-t_i)\exp(\mathrm{i}\omega t') \\ -\exp(\mathrm{i}\omega t') \end{bmatrix} \\
&= \frac{\tilde{\mathcal{E}}_0}{\omega^2} \begin{bmatrix} 1 & t-t_i \\ 0 & 1 \end{bmatrix} \begin{bmatrix} [\exp(\mathrm{i}\omega t') - \mathrm{i}\omega(t'-t_i)\exp(\mathrm{i}\omega t')]_{t_i}^{t} \\ \mathrm{i}\omega[\exp(\mathrm{i}\omega t) - \exp(\mathrm{i}\omega t_i)] \end{bmatrix} \\
&= \frac{\tilde{\mathcal{E}}_0}{\omega^2} \begin{bmatrix} 1 & t-t_i \\ 0 & 1 \end{bmatrix} \begin{bmatrix} \exp(\mathrm{i}\omega t) - \exp(\mathrm{i}\omega t_i) - \mathrm{i}\omega(t-t_i)\exp(\mathrm{i}\omega t) \\ \mathrm{i}\omega[\exp(\mathrm{i}\omega t) - \exp(\mathrm{i}\omega t_i)] \end{bmatrix} \\
&= \frac{\tilde{\mathcal{E}}_0}{\omega^2} \begin{bmatrix} \exp(\mathrm{i}\omega t) - [1 + \mathrm{i}\omega(t-t_i)]\exp(\mathrm{i}\omega t_i) \\ \mathrm{i}\omega[\exp(\mathrm{i}\omega t) - \exp(\mathrm{i}\omega t_i)] \end{bmatrix}
\end{aligned} \tag{B.4*}$$

$$\Longrightarrow$$

$$q(t) = \begin{bmatrix} 1 & t-t_i \\ 0 & 1 \end{bmatrix} q_i + \Im \left\{ \frac{\tilde{\mathcal{E}}_0}{\omega^2} \begin{bmatrix} \exp(\mathrm{i}\omega t) - [1 + \mathrm{i}\omega(t-t_i)]\exp(\mathrm{i}\omega t_i) \\ \mathrm{i}\omega[\exp(\mathrm{i}\omega t) - \exp(\mathrm{i}\omega t_i)] \end{bmatrix} \right\}. \tag{B.2*}$$

The first term represents a linear drift due to initial momentum, while the second term shows the oscillatory behaviour of the trajectory due to the driving field. (B.2*) characterizes the classical motion of an electron in a field, arbitrarily polarized in the z–x plane. It can be specialized to the elliptical case, by setting

$$\mathfrak{p} = \frac{1}{\sqrt{1+\xi^2}} \begin{bmatrix} 1 \\ \mathrm{i}\xi \end{bmatrix}, \tag{B.6}$$

where ξ is the ratio between the minor and major axes of the polarization ellipse, assumed to be aligned along z; $\xi = 0$ corresponds to linear polarization and $\xi = \pm 1$ to right-/left-handed circular polarization.

At any time (assuming $\mathbf{p}_i = 0$), the kinetic energy of the electron is given by

$$\begin{aligned}
W_\mathrm{k} = \frac{p^2}{2} &= \frac{1}{2\omega^2} \left(\Re \left\{ \tilde{\mathcal{E}}_0 [\exp(\mathrm{i}\omega t) - \exp(\mathrm{i}\omega t_i)] \right\} \right)^2 \\
&= 2U_\mathrm{p} \left(\Re \left\{ \mathfrak{p} [\exp(\mathrm{i}\omega t) - \exp(\mathrm{i}\omega t_i)] \right\} \right)^2,
\end{aligned} \tag{B.7}$$

where

$$U_\mathrm{p} \equiv \frac{1}{T} \int_T \mathrm{d}t \frac{p^2(t)}{2} = \frac{\mathcal{E}_0^2}{4\omega^2} \equiv \frac{I_0}{4\omega^2} \tag{B.8}$$

is the cycle-averaged wiggle energy, called the *ponderomotive energy*.

C Full 3D Code

An extension of the algorithm described by Schafer (2009) to the case of arbitrary polarization in the z–x plane is presented, for the length gauge only, where the interaction Hamiltonian is of the form $H_I(t) = \mathcal{E}(t) \cdot \boldsymbol{r}$. Non-linearly polarized light $\implies$ m-mixing, i.e. m is no longer conserved, as is the case for linear polarization. If we write the discretized wavefunction as

$$|\Psi(\mathbf{r},t)\rangle \to |\Psi\rangle_i^j = \sum_{\ell m} \varphi_\ell^m(r_j,t_i)|\ell m\rangle \equiv \sum_{\ell m} |\varphi_\ell^m\rangle_i^j, \tag{C.1}$$

where i is the time step index and j the radial index, the number of partial waves is given by

$$\begin{aligned} &\ell \in [0,L], \quad m_\ell \in \{-\ell..\ell\} \\ &\implies N_{m_\ell} = 2\ell + 1 \\ &\implies N_p = \sum_{\ell=0}^{L} 2\ell + 1 = (L+1)\frac{2L+2}{2} = (L+1)^2. \end{aligned} \tag{C.2}$$

The total memory requirements would thus be $N_r(L+1)^2 \times 128$ bytes.* If $N_r = 1024$, then 6 GB of working memory would theoretically allow for 393 216 partial waves, which is approximately 626 full ℓ channels, i.e. not truncated in m_ℓ. Such a number of ℓ channels is rarely needed for HHG calculations, the required number usually being 30–40. If the polarization is close to linear along z, it may be possible to truncate the wavefunction in m_ℓ. As can be seen from (C.2), the memory requirements of the full 3D wavefunction (as well as the computational costs) grows quadratically with maximum L. In the case of linear polarization and conserved m, the growth is linear with L.

* Assuming double precision complex data type.

The storage layout for the wavefunction is

$$|\Psi\rangle_i = \begin{bmatrix} |\mathrm{s}\rangle_i & |\mathrm{p}\rangle_i & |\mathrm{d}\rangle_i & \dots & |L\rangle_i \end{bmatrix}^\top, \tag{C.3}$$

with

$$|\ell\rangle_i = \begin{bmatrix} |\varphi_\ell^{-\ell}\rangle_i & \dots & |\varphi_\ell^0\rangle_i & \dots & |\varphi_\ell^\ell\rangle_i \end{bmatrix}^\top, \tag{C.4}$$

i.e. each rotational symmetry has its own segment. This layout will give a logical structure for the Hamiltonian, as we will see below.

C.1 LENGTH GAUGE HAMILTONIAN

The Hamiltonian is decomposed into three pieces,

$$H(t) = H_0 + H^z(t) + H^x(t), \tag{C.5}$$

separating the z and x components of the interaction Hamiltonian

$$H_I(t) = \boldsymbol{\mathcal{E}}(t) \cdot \boldsymbol{r} = H^z(t) + H^x(t) \equiv \mathcal{E}_z(t)z + \mathcal{E}_x(t)x. \tag{C.6}$$

As shown in §2.2, the solution of the TDSE involves calculating matrix elements of the type

$$\langle m|H|n\rangle. \tag{C.7}$$

Since the angular basis we have chosen in the position basis is represented by the spherical harmonics

$$\langle \mathbf{r}|\ell m\rangle \equiv Y_m^\ell(\vartheta,\varphi), \tag{C.8}$$

the interaction Hamiltonian matrix elements can be expressed in terms of spherical tensorial couplings, readily calculated using *Wigner 3j symbols* (Regge 1958; Landau and Lifshitz 1977, §106; Lindgren 1986, §2.3).

C.1.1 *3j symbols*

The 3*j* symbols are defined as

$$\begin{aligned}\begin{pmatrix} j_1 & j_2 & j_3 \\ m_1 & m_2 & m_3 \end{pmatrix} &= \Delta(j_1,j_2,j_3)(-)^{j_1-j_2-m_3}\sqrt{(j_1+m_1)!\,(j_1-m_1)!} \\ &\times \sqrt{(j_2+m_2)!\,(j_2-m_2)!\,(j_3+m_3)!\,(j_3-m_3)!} \\ &\times \sum_k \frac{(-)^k}{(j_1+j_2-j_3-k)!\,(j_1-m_1-k)!\,(j_2+m_2-k)!} \\ &\times \frac{1}{(j_3-j_2+m_1+k)!\,(j_3-j_1-m_2+k)!}\frac{1}{k!},\end{aligned} \tag{C.9}$$

where

$$\Delta(j_1,j_2,j_3) = \sqrt{\frac{(j_1+j_2-j_3)!\,(j_1-j_2+j_3)!\,(-j_1+j_2+j_3)!}{(j_1+j_2+j_3+1)!}}. \tag{C.10}$$

Actually calculating (C.9) is a daunting task, but Racah (1942) derived symmetry properties that simplify the problem. For instance, the following 'selection rules' hold:

$$\begin{cases} \text{I} & \sum_i m_i = 0 \\ \text{II.I} & \sum_i j_i \in \mathbb{Z}, \quad \text{II.II}\ \frac{1}{2}\sum_i j_i \in \mathbb{Z}, m_i = 0, \forall i \\ \text{III} & |m_i| \le j_i \\ \text{IV} & |j_1 - j_2| \le j_3 \le j_1 + j_2 \end{cases} \tag{C.11}$$

There are also some special cases that will be useful below:

$$\begin{pmatrix} j_1 & j_2 & j_1+j_2 \\ m_1 & m_2 & -m_1-m_2 \end{pmatrix} = (-)^{j_1-j_2+m_1+m_2}\sqrt{\frac{(2j_1)!\,(2j_2)!}{(2j_1+2j_2+1)!}}\times \sqrt{\frac{(2j_1)!\,(2j_2)!}{(j_1+m_1)!\,(j_1-m_1)!\,(j_2+m_2)!\,(j_2-m_2)!}} \tag{C.12}$$

$$\begin{pmatrix} j_1 & j_2 & j_3 \\ 0 & 0 & 0 \end{pmatrix} = (-)^p\sqrt{\frac{(j_1+j_2-j_3)!\,(j_1-j_2+j_3)!\,(-j_1+j_2+j_3)!}{(2p+1)!}} \times \frac{p!}{(p-j_1)!\,(p-j_2)!\,(p-j_3)!}, \qquad 2p = j_1+j_2+j_3 \tag{C.13}$$

C.1.2 *Spherical tensors and 3j symbols*

From Lindgren (1986, (2.100)), we have

$$C^k_q \equiv \sqrt{\frac{4\pi}{2k+1}}Y^k_q(\mathbf{e}_r), \tag{C.14}$$

where C^k_q is a spherical tensor of rank k. Likewise, from ibid., (2.124), we have

$$\begin{aligned} \langle \ell m|C^k_q|\ell' m'\rangle &= \sqrt{\frac{4\pi}{2k+1}}\int \mathrm{d}\Omega\ Y^{\ell *}_m Y^k_q Y^{\ell'}_{m'} \\ &= (-)^{\ell-m}\begin{pmatrix} \ell & k & \ell' \\ -m & q & m' \end{pmatrix}\langle \ell\|\mathbf{C}^k\|\ell'\rangle, \end{aligned} \tag{C.15}$$

where the reduced matrix element is given by [Lindgren 1986, (2.127)]

$$\langle \ell \| \mathbf{C}^k \| \ell' \rangle = (-)^{\ell} \sqrt{(2\ell+1)(2\ell'+1)} \begin{pmatrix} \ell & k & \ell' \\ 0 & 0 & 0 \end{pmatrix}. \tag{C.16}$$

We immediately see that if

$$m' = m - q, \tag{C.17}$$

the resultant $3j$ symbols in (C.15) & (C.16) correspond to the special cases (C.12) & (C.13).

C.1.3 *Dipole operators*

We now have everything we need to calculate the angular part of the dipole matrix elements.

$$Y_0^1(\vartheta,\varphi) = \sqrt{\frac{3}{4\pi}} \cos\vartheta \quad Y_{\pm 1}^1(\vartheta,\varphi) = \mp\sqrt{\frac{3}{8\pi}} \sin\vartheta \exp(\pm i\varphi) \tag{C.18}$$

$$u = \sum_{ij} |i\rangle\langle i|u|j\rangle\langle j| = \sum_{ij} |i\rangle u_{ij} \langle j|, \quad |i\rangle \equiv |\ell_i m_i\rangle \tag{C.19}$$

$$\frac{z}{r} = \cos\vartheta = \sqrt{\frac{4\pi}{3}} Y_0^1(\vartheta,\varphi) = C_0^1 \tag{C.20}$$

$$\begin{aligned}
\frac{z_{ij}}{r} &= \langle i | C_0^1 | j \rangle \\
&= (-)^{2\ell_i - m_i} \sqrt{(2\ell_i+1)(2\ell_j+1)} \begin{pmatrix} \ell_i & 1 & \ell_j \\ -m_i & 0 & m_j \end{pmatrix} \begin{pmatrix} \ell_i & 1 & \ell_j \\ 0 & 0 & 0 \end{pmatrix} \\
&= (-)^{m_i} \sqrt{(2\ell_i+1)(2\ell_j+1)} \underbrace{\begin{pmatrix} \ell_i & 1 & \ell_j \\ -m_i & 0 & m_j \end{pmatrix}}_{\text{I} \implies \Delta m = 0} \underbrace{\begin{pmatrix} \ell_i & 1 & \ell_j \\ 0 & 0 & 0 \end{pmatrix}}_{\text{II.II, IV} \implies \Delta \ell = \pm 1} \\
&= (-)^{m} \sqrt{(2\ell+1)(2\ell\pm 2+1)} \begin{pmatrix} \ell & 1 & \ell \pm 1 \\ -m & 0 & m \end{pmatrix} \begin{pmatrix} \ell & 1 & \ell \pm 1 \\ 0 & 0 & 0 \end{pmatrix}
\end{aligned} \tag{C.21}$$

It is sufficient to calculate $\begin{pmatrix} \ell & 1 & \ell+1 \\ -m & 0 & m \end{pmatrix}$, since by symmetry,

$$\begin{pmatrix} \ell & 1 & \ell-1 \\ -m & 0 & m \end{pmatrix} = \begin{pmatrix} \ell-1 & 1 & \ell \\ m & 0 & -m \end{pmatrix} = \begin{pmatrix} \ell' & 1 & \ell'+1 \\ -m & 0 & m \end{pmatrix}.$$

$$\begin{aligned} \begin{pmatrix} \ell & 1 & \ell+1 \\ -m & 0 & m \end{pmatrix} &= (-)^{\ell-1+m}\sqrt{\frac{(2\ell)!\,2(\ell+1-m)!\,(\ell+1+m)!}{(2\ell+3)!\,(\ell-m)!\,(\ell+m)!}} \\ &= (-)^{\ell-1+m}\sqrt{\frac{2(\ell+1+m)(\ell+1-m)}{(2\ell+3)(2\ell+2)(2\ell+1)}} \end{aligned} \tag{C.22}$$

$$\begin{aligned} \Longrightarrow \boxed{c_m^\ell} \equiv \frac{z^+_{\ell m}}{r} =& (-)^m\sqrt{(2\ell+1)(2\ell+3)} \\ &\times (-)^{\ell-1+m}\sqrt{\frac{2(\ell+1+m)(\ell+1-m)}{(2\ell+3)(2\ell+2)(2\ell+1)}} \\ &\times (-)^{\ell-1}\sqrt{\frac{2(\ell+1)(\ell+1)}{(2\ell+3)(2\ell+2)(2\ell+1)}} \\ =& \boxed{\sqrt{\frac{(\ell+m+1)(\ell-m+1)}{(2\ell+3)(2\ell+1)}}} \end{aligned} \tag{C.23}$$

$$\frac{x}{r} = \sin\vartheta\cos\varphi = \sqrt{\frac{2\pi}{3}}[Y^1_{-1}(\vartheta,\varphi) - Y^1_1(\vartheta,\varphi)] = \frac{1}{\sqrt{2}}[C^1_{-1} - C^1_1] \tag{C.24}$$

$$\begin{aligned} \frac{x_{ij}}{r} =& \frac{1}{\sqrt{2}}\langle i|C^1_{-1} - C^1_1|j\rangle \\ =& \frac{(-)^{2\ell_i-m_i}}{\sqrt{2}}\sqrt{(2\ell_i+1)(2\ell_j+1)}\begin{pmatrix} \ell_i & 1 & \ell_j \\ 0 & 0 & 0 \end{pmatrix} \\ &\times\left[\begin{pmatrix} \ell_i & 1 & \ell_j \\ -m_i & -1 & m_j \end{pmatrix} - \begin{pmatrix} \ell_i & 1 & \ell_j \\ -m_i & 1 & m_j \end{pmatrix}\right] \\ =& \frac{(-)^m}{\sqrt{2}}\sqrt{(2\ell+1)(2\ell\pm2+1)}\begin{pmatrix} \ell & 1 & \ell\pm1 \\ 0 & 0 & 0 \end{pmatrix} \\ &\times\left[\begin{pmatrix} \ell & 1 & \ell\pm1 \\ -m & -1 & m+1 \end{pmatrix} - \begin{pmatrix} \ell & 1 & \ell\pm1 \\ -m & 1 & m-1 \end{pmatrix}\right] \end{aligned} \tag{C.25}$$

Again, by symmetry, we have $\begin{pmatrix} \ell & 1 & \ell-1 \\ -m & 1 & m-1 \end{pmatrix} = -\begin{pmatrix} \ell-1 & 1 & \ell \\ m-1 & 1 & -m \end{pmatrix}$

$$= -\begin{pmatrix} \ell' & 1 & \ell'+1 \\ m' & 1 & -m'-1 \end{pmatrix} = \begin{pmatrix} \ell' & 1 & \ell'+1 \\ -m' & -1 & m'+1 \end{pmatrix}.$$

$$\begin{pmatrix} \ell & 1 & \ell+1 \\ -m & -1 & m+1 \end{pmatrix} = (-)^{\ell-2+m}\sqrt{\frac{(2\ell)!\,2(\ell-m)!\,(\ell+2+m)!}{(2\ell+3)!\,(\ell-m)!\,(\ell+m)!\,2}}$$

$$= (-)^{\ell-2+m}\sqrt{\frac{(\ell+2+m)(\ell+1+m)}{(2\ell+3)(2\ell+2)(2\ell+1)}} \tag{C.26}$$

$$\implies \boxed{b_m^\ell} \equiv 2\frac{x_{\ell m}^{++}}{r} = 2\frac{(-)^m}{\sqrt{2}}\sqrt{(2\ell+1)(2\ell+3)}(-)^{\ell-2+m}(-)^{\ell-1}$$

$$\times\sqrt{\frac{(\ell+2+m)(\ell+1+m)}{(2\ell+3)(2\ell+2)(2\ell+1)}}\sqrt{\frac{2(\ell+1)(\ell+1)}{(2\ell+3)(2\ell+2)(2\ell+1)}}$$

$$= \boxed{\sqrt{\frac{(\ell+m+2)(\ell+m+1)}{(2\ell+3)(2\ell+1)}}} \tag{C.27}$$

See figure C.1 for a visualization of (C.23) & (C.27).

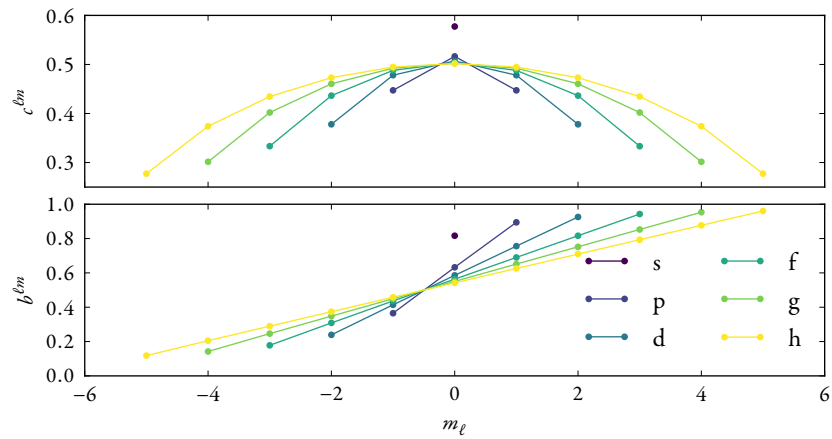

FIGURE C.1: Dipole coupling matrix elements. Upper panel: matrix elements of z, which only couples partial waves with $\Delta m_\ell = 0$, hence the symmetry about $m_\ell = 0$. Lower panel: matrix elements of x, which couples partial waves with $\Delta m_\ell = \pm 1$.

C.1.4 Matrix

We are now ready to construct the matrix representation of the Hamiltonian in the basis of the spherical harmonics. The radial grid point distance is defined by

$$\rho \equiv r_{j+1} - r_j \tag{C.28}$$

and the time step by

$$\tau \equiv t_{i+1} - t_i. \tag{C.29}$$

- The atomic Hamiltonian is given by

$$H_0 = \mathcal{T} + \mathcal{U} = -\frac{\nabla^2}{2} + V(\mathbf{r}). \tag{C.30}$$

The kinetic operator $\mathcal{T}$ is radially non-local. The potential operator $\mathcal{U}$ is approximated using the pseudo-potentials, described in §2.1.3. These consist of two parts, an angularly non-local, short-range potential, and an angularly, local long-range potential, due to the residual Coulomb interaction. The action of the atomic Hamiltonian can thus be approximated by

$$[H_0|\Psi\rangle]_i^{\ell m j} \approx \left\{ -\frac{\left[\Delta_\rho^2\right]^j}{\rho^2} + V_\ell(r_j) \right\} |\varphi_\ell^m\rangle_i^j, \tag{C.31}$$

which is tridiagonal in r and diagonal in ℓ, m. Δ_ρ^2 denotes a three-point discretization of the kinetic operator, which explicitly takes into account the boundary condition at the origin (Schafer et al. 2000):

$$\left[\Delta_\rho^2|\varphi_\ell^m\rangle_i\right]^j = \left[\alpha_j|\varphi_\ell^m\rangle_i^{j+1} - 2\beta_j|\varphi_\ell^m\rangle_i^j - \alpha_{j-1}|\varphi_\ell^m\rangle_i^{j-1}\right], \tag{C.32}$$

with

$$\alpha_j = \frac{j^2}{j^2 - 1/4} \to 1, \qquad 2\beta_j = 2\frac{j^2 - j + 1/2}{j^2 - j + 1/4} \to 2, \quad j \to \infty. \tag{C.33}$$

- The action of the z component of the interaction Hamiltonian is given (exactly) by

$$[H^z|\Psi\rangle]_i^{\ell m j} = \tilde{c}_i^{\ell m j}|\varphi_{\ell+1}^m\rangle_i^j + \tilde{c}_i^{\ell-1\, m j}|\varphi_{\ell-1}^m\rangle_i^j, \tag{C.34}$$

where

$$\tilde{c}_i^{\ell m j} = \mathcal{E}_z\left(t_i + \frac{\tau}{2}\right) c_m^\ell r_j. \tag{C.35}$$

H^z is diagonal in r, tridiagonal in ℓ, and diagonal in m.

- The action of the x component of the interaction Hamiltonian is given (exactly) by

$$\begin{aligned}[H^x|\Psi\rangle]_i^{\ell mj} =& \tilde{b}_i^{\ell mj}|\varphi_{\ell+1}^{m+1}\rangle_i^j - \tilde{b}_i^{\ell\,-mj}|\varphi_{\ell+1}^{m-1}\rangle_i^j \\ &+ \tilde{b}_i^{\ell-1\,m-1\,j}|\varphi_{\ell-1}^{m-1}\rangle_i^j - \tilde{b}_i^{\ell-1\,-m-1\,j}|\varphi_{\ell-1}^{m+1}\rangle_i^j,\end{aligned} \tag{C.36}$$

  where

$$\tilde{b}_i^{\ell mj} = \frac{1}{2}\mathcal{E}_x\left(t_i + \frac{\tau}{2}\right) b_m^\ell r_j. \tag{C.37}$$

  H^x is diagonal in r and tridiagonal in ℓ, m.

The Hamiltonian matrix at time t_i thus has the following form:

$$[H]_i = \left[\begin{array}{c|ccc|ccc|c}
h_0^{\mathrm{s}} & -\hat{\mathrm{s}}_0^x & \hat{\mathrm{s}}_0^z & \hat{\mathrm{s}}_0^x & & & & \\
\hline
-\hat{\mathrm{s}}_0^x & h_0^{\mathrm{p}} & & & -\hat{\mathrm{p}}_1^x & \hat{\mathrm{p}}_{-1}^z & \hat{\mathrm{p}}_{-1}^x & \\
\hat{\mathrm{s}}_0^z & & h_0^{\mathrm{p}} & & & -\hat{\mathrm{p}}_0^x & \hat{\mathrm{p}}_0^z & \hat{\mathrm{p}}_0^x \\
\hat{\mathrm{s}}_0^x & & & h_0^{\mathrm{p}} & & & -\hat{\mathrm{p}}_{-1}^x & \hat{\mathrm{p}}_1^z & \hat{\mathrm{p}}_1^x \\
\hline
 & -\hat{\mathrm{p}}_1^x & & & h_0^{\mathrm{d}} & & & & \\
 & \hat{\mathrm{p}}_{-1}^z & -\hat{\mathrm{p}}_0^x & & & h_0^{\mathrm{d}} & & & \\
 & \hat{\mathrm{p}}_{-1}^x & \hat{\mathrm{p}}_0^z & -\hat{\mathrm{p}}_{-1}^x & & & h_0^{\mathrm{d}} & & \cdots \\
 & & \hat{\mathrm{p}}_0^x & \hat{\mathrm{p}}_1^z & & & & h_0^{\mathrm{d}} & \\
 & & & \hat{\mathrm{p}}_1^x & & & & & h_0^{\mathrm{d}} \\
\hline
 & & & & & \vdots & & & \ddots
\end{array}\right], \tag{C.38}$$

where

$$\ell_m^z = \mathcal{E}_z\left(t_i + \frac{\tau}{2}\right) c_m^\ell r, \tag{C.39}$$

and

$$\ell_m^x = \frac{1}{2}\mathcal{E}_x\left(t_i + \frac{\tau}{2}\right) b_m^\ell r. \tag{C.40}$$

C.2 INTEGRATION

The integration (also called *time-stepping*) of the TDSE is performed using a short-time propagator

$$|\Psi\rangle_{i+1} \equiv \mathcal{U}(t_i + \tau, t_i)|\Psi\rangle_i, \tag{C.41}$$

where the propagator is approximated using symmetric Strang splitting [this makes the propagator unitary to $\mathcal{O}(\tau^3)$]

$$\begin{aligned}\mathcal{U}(t_i + \tau, t_i) &\approx \exp\left(-\mathrm{i}H_i\tau\right) \\ &\approx \exp\left(-\mathrm{i}H_i^x\frac{\tau}{2}\right)\exp\left(-\mathrm{i}H_i^z\frac{\tau}{2}\right)\exp\left(-\mathrm{i}H_0\tau\right) \\ &\quad\times\exp\left(-\mathrm{i}H_i^z\frac{\tau}{2}\right)\exp\left(-\mathrm{i}H_i^x\frac{\tau}{2}\right).\end{aligned} \tag{C.42}$$

The main proportion of the computational time will be spent on (C.41), and the rest of the time on calculating the time-dependent dipole moment, described below. It is therefore essential that the implementation of (C.42) is efficient. To this end, the integrator was implemented on a GPU, which is highly tuned for parallel linear algebra. The GPU is manufactured by Nvidia, and the provided programming library provided, CUDA (Nickolls et al. 2008), contains an implementation of BLAS (Lawson et al. 1979; Dongarra et al. 1988, 1990), a few routines from LAPACK (Anderson et al. 1999), as well as the facility for user-defined computational kernels that operate in parallel.

C.2.1 H_0

Since H_0 is diagonal in ℓ and m, we can apply its suboperators separately for each partial wave:

$$\exp\left(-\mathrm{i}H_0\tau\right) = \prod_{\ell m}\otimes\exp\left(-\mathrm{i}h_0^\ell\tau\right). \tag{C.43}$$

We approximate the exponential using its Padé form:

$$\exp\left(-\mathrm{i}h_0^\ell\tau\right) \approx \frac{1-\mathrm{i}h_0^\ell\frac{\tau}{2}}{1+\mathrm{i}h_0^\ell\frac{\tau}{2}}. \tag{C.44}$$

Since h_0^ℓ is independent of m, we can apply (C.44) to all partial waves of the same symmetry in parallel. We thus treat the part of the wavefunction of symmetry ℓ as an $N_r \times (2\ell+1)$ matrix (each column corresponds to a partial wave, and each

row to a specific radius), and apply the numerator of (C.44) as a matrix–matrix product (where the first matrix is tridiagonal). The denominator of (C.44) is applied by performing a tridiagonal matrix–matrix solution, for which an optimized routine based on LU factorization exists in LAPACK, ?gtsv.

C.2.2 H_i^z

Since H_i^z is diagonal in r and m, we can apply the exponential as

$$\exp\left(-\mathrm{i}H_i^z\tau\right) = \prod_m \otimes \exp\left(-\mathrm{i}h_i^{z,m}\tau\right), \tag{C.45}$$

where

$$h_i^{z,m} = \begin{bmatrix} & \widehat{|m|}_m^z & & & \\ \widehat{|m|}_m^z & & \widehat{|m|+1}_m^z & & \\ & \widehat{|m|+1}_m^z & & \widehat{|m|+2}_m^z & \\ & & \widehat{|m|+2}_m^z & & \ddots \\ & & & \ddots & \end{bmatrix}, \tag{C.46}$$

e.g. for $m = 0$,

$$h_i^{z,0} = \begin{bmatrix} & \hat{\mathrm{s}}_0^z & & & \\ \hat{\mathrm{s}}_0^z & & \hat{\mathrm{p}}_0^z & & \\ & \hat{\mathrm{p}}_0^z & & \hat{\mathrm{d}}_0^z & \\ & & \hat{\mathrm{d}}_0^z & & \ddots \\ & & & \ddots & \end{bmatrix}, \tag{C.47}$$

while for $m = \pm 1$,

$$h_i^{z,\pm 1} = \begin{bmatrix} & \hat{\mathrm{p}}_{\pm 1}^z & & & \\ \hat{\mathrm{p}}_{\pm 1}^z & & \hat{\mathrm{d}}_{\pm 1}^z & & \\ & \hat{\mathrm{d}}_{\pm 1}^z & & \hat{\mathrm{f}}_{\pm 1}^z & \\ & & \hat{\mathrm{f}}_{\pm 1}^z & & \ddots \\ & & & \ddots & \end{bmatrix}. \tag{C.48}$$

$h^{z,m}$ is exponentiated by means of Richardson's 2×2 splitting method, which entails dividing the matrix into an even and an odd part:

$$h_i^{z,m} = h_i^{z,m,\mathrm{e}} + h_i^{z,m,\mathrm{o}} = \begin{bmatrix} & \widehat{|m|}_m^z & & & \\ \widehat{|m|}_m^z & & 0 & & \\ & 0 & & \widehat{|m|+2}_m^z & \\ & & \widehat{|m|+2}_m^z & & \ddots \\ & & & \ddots & \end{bmatrix} + \begin{bmatrix} & 0 & & & \\ 0 & & \widehat{|m|+1}_m^z & & \\ & \widehat{|m|+1}_m^z & & 0 & \\ & & 0 & & \ddots \\ & & & \ddots & \end{bmatrix}, \tag{C.49}$$

where each 2×2 subblock is exponentiated exactly as

$$\exp\left\{-\mathrm{i}\begin{bmatrix} 0 & a \\ a & 0 \end{bmatrix}\right\} = \begin{bmatrix} \cos a & -\mathrm{i}\sin a \\ -\mathrm{i}\sin a & \cos a \end{bmatrix}, \tag{C.50}$$

which is basically a rotation. A great deal of time is spent on calculating $\sin a$ & $\cos a$ (Richardson 1991). We thus have the approximation

$$\exp\left(-\mathrm{i}h_i^{z,m}\frac{\tau}{2}\right) \approx \exp\left(-\mathrm{i}h_i^{z,m,\mathrm{e}}\frac{\tau}{2}\right)\exp\left(-\mathrm{i}h_i^{z,m,\mathrm{o}}\frac{\tau}{2}\right). \tag{C.51}$$

C.2.3 H_i^x

If we divide H_i^x into two parts, one with all the plus signs, and one with all the minus signs, we can write it as $H_i^x = H_i^{x+} + H_i^{x-}$. The wavefunction then breaks up into sets of invariant subspaces $\{|\psi\rangle_i^{k\pm}\}$. For H_i^{x-}, the first few subspaces are:

$$|\psi\rangle_i^{0-} = \begin{bmatrix} |\varphi_{\mathrm{s}}^{0}\rangle_i \\ |\varphi_{\mathrm{p}}^{-1}\rangle_i \\ |\varphi_{\mathrm{d}}^{-2}\rangle_i \\ \vdots \end{bmatrix} \quad |\psi\rangle_i^{1-} = \begin{bmatrix} |\varphi_{\mathrm{p}}^{0}\rangle_i \\ |\varphi_{\mathrm{d}}^{-1}\rangle_i \\ |\varphi_{\mathrm{f}}^{-2}\rangle_i \\ \vdots \end{bmatrix} \quad |\psi\rangle_i^{2-} = \begin{bmatrix} |\varphi_{\mathrm{p}}^{1}\rangle_i \\ |\varphi_{\mathrm{d}}^{0}\rangle_i \\ |\varphi_{\mathrm{f}}^{-1}\rangle_i \\ \vdots \end{bmatrix}, \tag{C.52}$$

while for H_i^{x+}, the first few subspaces are:

$$|\psi\rangle_i^{0+} = \begin{bmatrix} |\varphi_{\mathrm{s}}^{0}\rangle_i \\ |\varphi_{\mathrm{p}}^{1}\rangle_i \\ |\varphi_{\mathrm{d}}^{2}\rangle_i \\ \vdots \end{bmatrix} \quad |\psi\rangle_i^{1+} = \begin{bmatrix} |\varphi_{\mathrm{p}}^{0}\rangle_i \\ |\varphi_{\mathrm{d}}^{1}\rangle_i \\ |\varphi_{\mathrm{f}}^{2}\rangle_i \\ \vdots \end{bmatrix} \quad |\psi\rangle_i^{2+} = \begin{bmatrix} |\varphi_{\mathrm{p}}^{1}\rangle_i \\ |\varphi_{\mathrm{d}}^{0}\rangle_i \\ |\varphi_{\mathrm{f}}^{-1}\rangle_i \\ \vdots \end{bmatrix}. \tag{C.53}$$

H_i^{x-} then also breaks up into these subspaces, and the sub-Hamiltonians there are tridiagonal:

$$h_i^{x-,\ell} = \begin{bmatrix} & -\ell_0^x & & & \\ -\ell_0^x & & -(\ell+1)_1^x & & \\ & -(\ell+1)_1^x & & -(\ell+2)_2^x & \\ & & -(\ell+2)_2^x & & \ddots \\ & & & \ddots & \end{bmatrix} \tag{C.54}$$

and similarly for the H_i^{x+} part. All these sub-Hamiltonians can then be exponentiated using Richardson's 2×2 method, as for H_i^z.

C.3 Time-dependent dipole moment calculation

The radiated field is proportional to the acceleration of the time-dependent dipole moment. Since the dipole operator increases linearly with the radius, numerical errors at the outer boundary of the discretized wavefunction (where the precision is already very low) will be amplified. This makes convergence of the time-dependent dipole moment very difficult and the subsequent calculation of the acceleration will not be accurate. Instead we calculate the expectation value of the acceleration directly, using the identities

$$\begin{aligned} \frac{\mathrm{d}}{\mathrm{d}t}\langle \boldsymbol{r}\rangle &= \mathrm{i}\langle [H(t), \boldsymbol{r}]_-\rangle, \\ \frac{\mathrm{d}^2}{\mathrm{d}t^2}\langle \boldsymbol{r}\rangle &= -\langle [H(t), [H(t), \boldsymbol{r}]_-]_-\rangle. \end{aligned} \tag{C.55}$$

$$\begin{aligned} -\boldsymbol{a} \equiv -\frac{\mathrm{d}^2}{\mathrm{d}t^2}\langle \boldsymbol{r}\rangle &= \langle [H(t), [H(t), \boldsymbol{r}]_-]_-\rangle \\ &= \langle [H(t), [H_0, \boldsymbol{r}]_-]_-\rangle = \langle H(t)\,[H_0, \boldsymbol{r}]_-\rangle - \langle [H_0, \boldsymbol{r}]_-\, H(t)\rangle \\ &\left[\langle [H_0, \boldsymbol{r}]_-\, H(t)\rangle = \langle H^\dagger(t)\,[H_0, \boldsymbol{r}]_-^\dagger\rangle^* = -\langle H(t)\,[H_0, \boldsymbol{r}]_-\rangle^*\right] \\ &= 2\Re\{\langle \Psi | H(t)\,[H_0, \boldsymbol{r}]_-\,|\Psi\rangle\} = 2\Re\{\langle 2|1\rangle\}, \end{aligned} \tag{C.56}$$

where

$$|1\rangle \equiv [H_0, \boldsymbol{r}]_-\,|\Psi\rangle \qquad |2\rangle \equiv H(t)|\Psi\rangle. \tag{C.57}$$

Since the Hamiltonian has the form

$$H(t) = H_0 + H_\mathrm{I}(t) = \mathcal{T} + \mathcal{V} + \boldsymbol{\mathcal{E}}(t)\cdot\boldsymbol{r}, \tag{C.58}$$

we must calculate the commutator of all the constituent parts with the dipole operator $\boldsymbol{r}$. We can calculate the z and the x components separately.

C.3.1 *Acceleration form of the dipole*

We separate the atomic Hamiltonian into a radial kinetic part, an angular kinetic part, and a potential part:

$$H_0 = \mathcal{T}_r + \mathcal{L} + \mathcal{V} \tag{C.59}$$

Since

$$z = r\sum_{\ell m} c_m^{\ell-1}|\ell m\rangle\langle \ell - 1; m| + c_m^{\ell}|\ell m\rangle\langle \ell + 1; m| \tag{C.60}$$

is simple in comparison with

$$x = \frac{r}{2}\sum_{\ell m} b_{m-1}^{\ell-1}|\ell m\rangle\langle \ell-1; m-1| - b_{-m-1}^{\ell-1}|\ell m\rangle\langle \ell-1; m+1| + b_{m}^{\ell}|\ell m\rangle\langle \ell+1; m+1| - b_{-m}^{\ell}|\ell m\rangle\langle \ell+1; m-1|, \tag{C.61}$$

we only demonstrate the derivation for the latter. We start with the angular kinetic operator, $[\mathcal{L}, x]_-$:

$$\mathcal{L} = \frac{1}{2r^2}\sum_{\ell m} \ell(\ell+1)|\ell m\rangle\langle \ell m| \tag{C.62}$$

$$x\mathcal{L} = \frac{1}{4r}\sum_{\ell m}|\ell m\rangle\{(\ell-1)\ell[b_{m-1}^{\ell-1}\langle \ell-1; m-1| - b_{-m-1}^{\ell-1}\langle \ell-1; m+1|] + (\ell+1)(\ell+2)[b_{m}^{\ell}\langle \ell+1; m+1| - b_{-m}^{\ell}\langle \ell+1; m-1|]\} \tag{C.63}$$

$$\mathcal{L}x = \frac{1}{4r}\sum_{\ell m}|\ell m\rangle\{\ell(\ell+1)[b_{m-1}^{\ell-1}\langle \ell-1; m-1| - b_{-m-1}^{\ell-1}\langle \ell-1; m+1| + b_{m}^{\ell}\langle \ell+1; m+1| - b_{-m}^{\ell}\langle \ell+1; m-1|]\} \tag{C.64}$$

$$\implies [\mathcal{L}, x]_- = \frac{1}{2r}\sum_{\ell m}|\ell m\rangle\{\ell[b_{m-1}^{\ell-1}\langle \ell-1; m-1| - b_{-m-1}^{\ell-1}\langle \ell-1; m+1|] - (\ell+1)[b_{m}^{\ell}\langle \ell+1; m+1| - b_{-m}^{\ell}\langle \ell+1; m-1|]\}. \tag{C.65}$$

We then continue with the potential operator, $[\mathcal{U}, x]_-$:

$$\mathcal{U} = \sum_{\ell m} V_\ell(r)|\ell m\rangle\langle \ell m| \tag{C.66}$$

$$\mathcal{U}x = \frac{r}{2}\sum_{\ell m}|\ell m\rangle V_\ell(r)[b_{m-1}^{\ell-1}\langle \ell-1; m-1| - b_{-m-1}^{\ell-1}\langle \ell-1; m+1| + b_{m}^{\ell}\langle \ell+1; m+1| - b_{-m}^{\ell}\langle \ell+1; m-1|] \tag{C.67}$$

$$x\mathcal{U} = \frac{r}{2}\sum_{\ell m}|\ell m\rangle\{V_{\ell-1}(r)[b_{m-1}^{\ell-1}\langle \ell-1; m-1| - b_{-m-1}^{\ell-1}\langle \ell-1; m+1|] + V_{\ell+1}(r)[b_{m}^{\ell}\langle \ell+1; m+1| - b_{-m}^{\ell}\langle \ell+1; m-1|]\} \tag{C.68}$$

$$\Delta V_\ell(r) \equiv V_\ell(r) - V_{\ell+1}(r) \tag{C.69}$$

$\Longrightarrow$

$$[\mathcal{V}, x]_- = -\frac{r}{2}\sum_{\ell m} |\ell m\rangle\{\Delta V_{\ell-1}[b^{\ell-1}_{m-1}\langle \ell-1; m-1| - b^{\ell-1}_{-m-1}\langle \ell-1; m+1|] - \Delta V_\ell[b^\ell_m\langle \ell+1; m+1| - b^\ell_{-m}\langle \ell+1; m-1|]\}. \tag{C.70}$$

Finally, we calculate the commutator for the radial kinetic operator, $[\mathcal{T}_r, x]_-$. Since it is neither radially nor angularly local, we adopt this compact notation:

$$\binom{j}{\ell m} \equiv \varphi^m_\ell(r_j, t_i)|\ell m\rangle. \tag{C.71}$$

$$[\mathcal{T}_r|\psi\rangle]^j_\ell = -\frac{1}{2\rho^2}[\alpha_{j-1}\binom{j-1}{\ell m} - \beta_j\binom{j}{\ell m} + \alpha_j\binom{j+1}{\ell m}] \tag{C.72}$$

$$\begin{aligned}
[\mathcal{T}_r x|\psi\rangle]^j_\ell = \\
-\frac{1}{4\rho^2}\{b^{\ell-1}_{m-1} &[\alpha_{j-1}r_{j-1}\binom{j-1}{\ell-1\ m-1} - \beta_j r_j\binom{j}{\ell-1\ m-1} + \alpha_j r_{j+1}\binom{j+1}{\ell-1\ m-1}] \\
-b^{\ell-1}_{-m-1} &[\alpha_{j-1}r_{j-1}\binom{j-1}{\ell-1\ m+1} - \beta_j r_j\binom{j}{\ell-1\ m+1} + \alpha_j r_{j+1}\binom{j+1}{\ell-1\ m+1}] \\
+b^{\ell}_{m} &[\alpha_{j-1}r_{j-1}\binom{j-1}{\ell+1\ m+1} - \beta_j r_j\binom{j}{\ell+1\ m+1} + \alpha_j r_{j+1}\binom{j+1}{\ell+1\ m+1}] \\
-b^{\ell}_{-m} &[\alpha_{j-1}r_{j-1}\binom{j-1}{\ell+1\ m-1} - \beta_j r_j\binom{j}{\ell+1\ m-1} + \alpha_j r_{j+1}\binom{j+1}{\ell+1\ m-1}]\}
\end{aligned} \tag{C.73}$$

$$\begin{aligned}
[x\mathcal{T}_r|\psi\rangle]^j_\ell = \\
-\frac{r_j}{4\rho^2}\{b^{\ell-1}_{m-1} &[\alpha_{j-1}\binom{j-1}{\ell-1\ m-1} - \beta_j\binom{j}{\ell-1\ m-1} + \alpha_j\binom{j+1}{\ell-1\ m-1}] \\
-b^{\ell-1}_{-m-1} &[\alpha_{j-1}\binom{j-1}{\ell-1\ m+1} - \beta_j\binom{j}{\ell-1\ m+1} + \alpha_j\binom{j+1}{\ell-1\ m+1}] \\
+b^{\ell}_{m} &[\alpha_{j-1}\binom{j-1}{\ell+1\ m+1} - \beta_j\binom{j}{\ell+1\ m+1} + \alpha_j\binom{j+1}{\ell+1\ m+1}] \\
-b^{\ell}_{-m} &[\alpha_{j-1}\binom{j-1}{\ell+1\ m-1} - \beta_j\binom{j}{\ell+1\ m-1} + \alpha_j\binom{j+1}{\ell+1\ m-1}]\}
\end{aligned} \tag{C.74}$$

$$
\begin{aligned}
\implies [[\mathcal{T}_r, x]_- |\psi\rangle]^j_\ell = \\
-\frac{1}{4\rho}\{ & b^{\ell-1}_{m-1} && [-\alpha_{j-1}(^{j-1}_{\ell-1\ m-1}) + \alpha_j(^{j+1}_{\ell-1\ m-1})] \\
& -b^{\ell-1}_{-m-1} && [-\alpha_{j-1}(^{j-1}_{\ell-1\ m+1}) + \alpha_j(^{j+1}_{\ell-1\ m+1})] \\
& +b^{\ell}_{m} && [-\alpha_{j-1}(^{j-1}_{\ell+1\ m+1}) + \alpha_j(^{j+1}_{\ell+1\ m+1})] \\
& -b^{\ell}_{-m} && [-\alpha_{j-1}(^{j-1}_{\ell+1\ m-1}) + \alpha_j(^{j+1}_{\ell+1\ m-1})]\}
\end{aligned}
\tag{C.75}
$$

The final expression for $[H_0, x]_-$ becomes

$$
\begin{aligned}
\implies [[H_0, x]_- |\psi\rangle]^j_\ell = \frac{1}{2}\{ & b^{\ell-1}_{m-1} && \left(\frac{\ell}{r_j} - r_j\Delta V_{\ell-1}\right)(^{j}_{\ell-1\ m+1}) \\
& - b^{\ell-1}_{-m-1} && \left(\frac{\ell}{r_j} - r_j\Delta V_{\ell-1}\right)(^{j}_{\ell-1\ m-1}) \\
& - b^{\ell}_{m} && \left(\frac{\ell+1}{r_j} - r_j\Delta V_{\ell}\right)(^{j}_{\ell+1\ m+1}) \\
& + b^{\ell}_{-m} && \left(\frac{\ell+1}{r_j} - r_j\Delta V_{\ell}\right)(^{j}_{\ell+1\ m-1})\} \\
-\frac{1}{4\rho}\{ & b^{\ell-1}_{m-1} && [-\alpha_{j-1}(^{j-1}_{\ell-1\ m-1}) + \alpha_j(^{j+1}_{\ell-1\ m-1})] \\
& -b^{\ell-1}_{-m-1} && [-\alpha_{j-1}(^{j-1}_{\ell-1\ m+1}) + \alpha_j(^{j+1}_{\ell-1\ m+1})] \\
& +b^{\ell}_{m} && [-\alpha_{j-1}(^{j-1}_{\ell+1\ m+1}) + \alpha_j(^{j+1}_{\ell+1\ m+1})] \\
& -b^{\ell}_{-m} && [-\alpha_{j-1}(^{j-1}_{\ell+1\ m-1}) + \alpha_j(^{j+1}_{\ell+1\ m-1})]\}
\end{aligned}
\tag{C.76}
$$

Introducing the potential factor

$$
\pi^j_\ell \equiv \frac{\ell+1}{r_j} - r_j\Delta V_\ell, \tag{C.77}
$$

we have

$$\begin{aligned}[|1\rangle_x]^j_\ell = \frac{1}{4\rho}\{ & b^{\ell-1}_{m-1} && [\alpha_{j-1}\binom{j-1}{\ell-1\ m-1} + \pi^j_{\ell-1}\binom{j}{\ell-1\ m-1}2\rho - \alpha_j\binom{j+1}{\ell-1\ m-1}] \\ & - b^{\ell-1}_{-m-1} && [\alpha_{j-1}\binom{j-1}{\ell-1\ m+1} + \pi^j_{\ell-1}\binom{j}{\ell-1\ m+1}2\rho - \alpha_j\binom{j+1}{\ell-1\ m+1}] \\ & + b^{\ell}_{m} && [\alpha_{j-1}\binom{j-1}{\ell+1\ m+1} - \pi^j_{\ell}\binom{j}{\ell+1\ m+1}2\rho - \alpha_j\binom{j+1}{\ell+1\ m+1}] \\ & - b^{\ell}_{-m} && [\alpha_{j-1}\binom{j-1}{\ell+1\ m-1} - \pi^j_{\ell}\binom{j}{\ell+1\ m-1}2\rho - \alpha_j\binom{j+1}{\ell+1\ m-1}]\},\end{aligned} \tag{C.78}$$

which is what we need to calculate the x component of (C.56).

C.3.2 *Hydrogen*

In the case of hydrogen, the commutator for the acceleration form of the dipole can be calculated analytically, since the potential operator is local everywhere:

$$\begin{aligned}[H, \boldsymbol{r}]_- &= [T, \boldsymbol{r}]_- + 0 + 0 \\ &= \frac{1}{2}\left[p^2, \boldsymbol{r}\right]_- = \frac{1}{2}\left[p_x^2 + p_y^2 + p_z^2, \boldsymbol{r}\right]_- \\ \implies \langle [H, u]_- \rangle &= \frac{1}{2}\langle [p_u^2, u]_- \rangle = \frac{1}{2}\langle p_u [p_u, u]_- + [p_u, u]_- p_u \rangle \\ &= \langle -\mathrm{i} p_u \rangle = \langle -\frac{\partial}{\partial u} \rangle \\ \implies \langle \left[H, \frac{\partial}{\partial u}\right]_- \rangle &= 0 + \langle \left[\mathcal{U}, \frac{\partial}{\partial u}\right]_- \rangle + \langle \left[\boldsymbol{\mathcal{E}} \cdot \boldsymbol{r}, \frac{\partial}{\partial u}\right]_- \rangle \\ &= \underbrace{\langle \mathcal{U} \frac{\partial}{\partial u} \rangle}_{\substack{= 0 \text{ since } \mathcal{U} \text{ is spherically} \\ \text{symmetric (thus even) and} \\ \frac{\partial}{\partial u} \text{ changes the parity of } |Y\rangle, \\ \text{yielding an odd integrand.}}} - \langle \frac{\partial}{\partial u} \mathcal{U} \rangle + \langle \mathcal{E}_u \underbrace{\left[u, \frac{\partial}{\partial u}\right]_-}_{[u, \mathrm{i}p_u]_- = -1} \rangle \\ &= -\langle \frac{\partial \mathcal{U}}{\partial u} \rangle - \langle \mathcal{E}_u \rangle = -\langle \frac{\partial r}{\partial u} \frac{\partial \mathcal{U}}{\partial r} \rangle - \mathcal{E}_u \\ &= \left[r = \sqrt{x^2 + y^2 + z^2} \right] \\ &= -\langle \frac{u}{\sqrt{x^2 + y^2 + z^2}} \frac{\partial \mathcal{U}}{\partial r} \rangle - \mathcal{E}_u = -\langle \frac{u}{r} \frac{\partial \mathcal{U}}{\partial r} \rangle - \mathcal{E}_u \\ &= \left[\mathcal{U}(r) = \frac{Z}{r} \right] = \langle f(\vartheta, \varphi) \frac{Z}{r^2} \rangle - \mathcal{E}_u.\end{aligned} \tag{C.79}$$

The Strong-Field Approximation

D

In this appendix, a detailed derivation of the main result of Lewenstein et al. (1994) is provided, together with a brief overview of the saddle-point method which is used to make calculations within the SFA tractable. Finally, the deviations of the SFA from reality are surveyed. An alternative derivation using the Volkov picture can be found in (Ivanov and Smirnova 2014).

D.1 Preliminaries

The SAE-TDSE in the length gauge reads:

$$\mathrm{i}\frac{\partial}{\partial t}|\Psi(\mathbf{x},t)\rangle = \left[-\frac{1}{2}\nabla^2 + V(\mathbf{x}) - \boldsymbol{\mathcal{E}}(t)\cdot\mathbf{x}\right]|\Psi(\mathbf{x},t)\rangle, \tag{D.1}$$

where the electric field is related to the magnetic vector potential as

$$\boldsymbol{\mathcal{E}}(t) = -\frac{\partial}{\partial t}\boldsymbol{\mathcal{A}}(t). \tag{D.2}$$

The SFA in its original formulation was developed for a particular set of parameters: the ground state $|0\rangle$ is assumed to be spherically symmetric (as is the case in the noble gases), it has an ionization potential $I_\mathrm{p} \gg \omega$, usually $I_\mathrm{p} \sim 5 - 20\omega$, where ω is the frequency of the driving field. The ponderomotive potential $U_\mathrm{p} < U_\mathrm{sat}$ (the saturation level of the medium), such that the ground state probability remains approximately unity. The ground state is further assumed to be the only contributing bound state, and the free electrons are not influenced by the atomic potential $V(\mathbf{x})$.

D.2 Solving the Equations of Motion

We make the *ansatz* that the wavefunction can be written

$$|\Psi(t)\rangle = \exp(\mathrm{i}I_\mathrm{p}t)\left[a(t)|0\rangle + \int \mathrm{d}^3\mathbf{v}\, b(\mathbf{v},t)|\mathbf{v}\rangle,\right] \tag{D.3}$$

where $|\mathbf{v}\rangle$ constitutes an orthogonal basis, corresponding to the *kinetic momentum*. NB $\frac{\partial}{\partial t}\mathbf{v} = 0$. This basis obeys the following orthogonalities:

- $\langle\mathbf{v}|\mathbf{v}'\rangle = \delta(\mathbf{v}-\mathbf{v}')$

- $\langle \mathbf{v}|\mathbf{x}|\mathbf{v}'\rangle = \langle \mathbf{v}|\mathrm{i}\nabla_{\mathbf{v}}|\mathbf{v}'\rangle = \mathrm{i}\nabla_{\mathbf{v}}\delta(\mathbf{v}-\mathbf{v}')$

Inserting (D.3) into (D.1), and assuming $a(t) \sim 1$ gives:

$$\exp(\mathrm{i}I_{\mathrm{p}}t)\left[-I_{\mathrm{p}}|0\rangle - I_{\mathrm{p}}\int \mathrm{d}^3\mathbf{v}' b(\mathbf{v}',t)|\mathbf{v}'\rangle + \mathrm{i}\int \mathrm{d}^3\mathbf{v}'\dot{b}(\mathbf{v}',t)|\mathbf{v}'\rangle\right] =$$
$$\exp(\mathrm{i}I_{\mathrm{p}}t)\left[-\frac{1}{2}\nabla^2 + V(\mathbf{x}) - \boldsymbol{\mathcal{E}}(t)\cdot\mathbf{x}\right]\left[a(t)|0\rangle + \int \mathrm{d}^3\mathbf{v}' b(\mathbf{v}',t)|\mathbf{v}'\rangle\right],$$

since $\frac{\partial}{\partial t}b(\mathbf{v},t) = \frac{\mathrm{d}}{\mathrm{d}t}b(\mathbf{v},t)$. Project from left with $\langle\mathbf{v}|$:

$$\begin{aligned}
\iff -I_{\mathrm{p}}b(\mathbf{v},t) + \mathrm{i}\dot{b}(\mathbf{v},t) =& \langle\mathbf{v}|\left[-\frac{1}{2}\nabla^2 + V(\mathbf{x}) - \boldsymbol{\mathcal{E}}(t)\cdot\mathbf{x}\right] \\
&\times\left[a(t)|0\rangle + \int \mathrm{d}^3\mathbf{v}' b(\mathbf{v}',t)|\mathbf{v}'\rangle\right] \\
=& \langle\mathbf{v}| - \frac{\nabla^2}{2}|0\rangle + \int \mathrm{d}^3\mathbf{v}' b(\mathbf{v},t)\langle\mathbf{v}| - \frac{\nabla^2}{2}|\mathbf{v}'\rangle + \\
& \langle\mathbf{v}|V(\mathbf{x})|0\rangle + \int \mathrm{d}^3\mathbf{v}' b(\mathbf{v},t)\langle\mathbf{v}|V(\mathbf{x})|\mathbf{v}'\rangle + \\
& \langle\mathbf{v}| - \boldsymbol{\mathcal{E}}(t)\cdot\mathbf{x}|0\rangle + \\
& \int \mathrm{d}^3\mathbf{v}' b(\mathbf{v},t)\langle\mathbf{v}| - \boldsymbol{\mathcal{E}}(t)\cdot\mathbf{x}|\mathbf{v}'\rangle \\
=& b(\mathbf{v},t)\frac{v^2}{2} - \boldsymbol{\mathcal{E}}(t)\cdot\mathbf{d}(\mathbf{v}) - \mathrm{i}\boldsymbol{\mathcal{E}}(t)\cdot\nabla_{\mathbf{v}}b(\mathbf{v},t),
\end{aligned}$$

where we have defined $\mathbf{d}(\mathbf{v}) = \langle\mathbf{v}|\mathbf{x}|0\rangle$.

$$\implies \dot{b}(\mathbf{v},t) = -\left[\mathrm{i}\left(\frac{v^2}{2} + I_{\mathrm{p}}\right) + \boldsymbol{\mathcal{E}}(t)\cdot\nabla_{\mathbf{v}}\right]b(\mathbf{v},t) + \mathrm{i}\boldsymbol{\mathcal{E}}(t)\cdot\mathbf{d}(\mathbf{v}) \qquad \text{(D.4)}$$

Variable change to *canonical momentum*; $\mathbf{p} = \mathbf{v} + \boldsymbol{\mathcal{A}}(t) \implies \mathbf{v} = \mathbf{p} - \boldsymbol{\mathcal{A}}(t)$:

$$\frac{\partial}{\partial v_i} = \frac{\partial p_i}{\partial v_i}\frac{\partial}{\partial p_i} = \frac{\partial}{\partial p_i}$$

$$\bar{b}(\mathbf{p},t) \equiv b[\mathbf{v} - \boldsymbol{\mathcal{A}}(t), t]$$

$$\implies \dot{\bar{b}}(\mathbf{p},t) = \left(\frac{\partial\mathbf{p}}{\partial t}\cdot\nabla_{\mathbf{p}} + \frac{\partial t}{\partial t}\frac{\partial}{\partial t}\right)\bar{b}(\mathbf{p},t) = \left[-\boldsymbol{\mathcal{E}}(t)\cdot\nabla_{\mathbf{p}} + \frac{\partial}{\partial t}\right]\bar{b}(\mathbf{p},t)$$

$$\implies \frac{\partial}{\partial t}\bar{b}(\mathbf{p},t) = -\mathrm{i}\left(\frac{[\mathbf{p} - \boldsymbol{\mathcal{A}}(t)]^2}{2} + I_{\mathrm{p}}\right)\bar{b}(\mathbf{p},t) + \mathrm{i}\boldsymbol{\mathcal{E}}(t)\cdot\mathbf{d}[\mathbf{p} - \boldsymbol{\mathcal{A}}(t)] \qquad \text{(D.4*)}$$

An inhomogeneous, linear, first-order ordinary differential equation $y' + g(x)y = h(x)$ has the solution

$$y = \mathrm{e}^{-G(x)}\left[\int^x h(x)\mathrm{e}^{G(x)}\,\mathrm{d}x\right] + C\mathrm{e}^{-G(x)},\ G(x) \equiv \int^x g(x)\,\mathrm{d}x.$$

The integrating factor of (D.4*) is then

$$\begin{aligned}
\mathrm{e}^{G(t)} &= \exp\left\{\mathrm{i}\int^t \mathrm{d}t'\left(\frac{[\mathbf{p}-\boldsymbol{\mathcal{A}}(t')]^2}{2} + I_\mathrm{p}\right)\right\} \\
&= \exp\left\{\mathrm{i}\int^t \mathrm{d}t'\frac{[\mathbf{p}-\boldsymbol{\mathcal{A}}(t')]^2}{2} + I_\mathrm{p}\right\} \\
&\left[\int^x \mathrm{d}x'' - \int^{x'} \mathrm{d}x'' = \int_{x'}^x \mathrm{d}x''\right] \\
\Longrightarrow\ \bar{b}(p,t) &= \exp\left\{-\mathrm{i}\int^t \mathrm{d}t''\frac{[\mathbf{p}-\boldsymbol{\mathcal{A}}(t'')]^2}{2} + I_\mathrm{p}\right\} \\
&\quad\times \mathrm{i}\int_{-\infty}^t \mathrm{d}t'\boldsymbol{\mathcal{E}}(t')\cdot\mathbf{d}[\mathbf{p}-\boldsymbol{\mathcal{A}}(t')] \\
&\quad\times \exp\left\{\mathrm{i}\int^{t'} \mathrm{d}t''\frac{[\mathbf{p}-\boldsymbol{\mathcal{A}}(t'')]^2}{2} + I_\mathrm{p}\right\} \qquad \text{(D.5)} \\
&= \mathrm{i}\int_{-\infty}^t \mathrm{d}t'\boldsymbol{\mathcal{E}}(t')\cdot\mathbf{d}[\mathbf{p}-\boldsymbol{\mathcal{A}}(t')] \\
&\quad\times \exp\left\{-\mathrm{i}\int_{t'}^t \mathrm{d}t''\frac{[\mathbf{p}-\boldsymbol{\mathcal{A}}(t'')]^2}{2} + I_\mathrm{p}\right\},
\end{aligned}$$

or equivalently, returning to kinetic momentum:

$$\begin{aligned}
b(\mathbf{v},t) &= \mathrm{i}\int_{-\infty}^t \mathrm{d}t'\boldsymbol{\mathcal{E}}(t')\cdot\mathbf{d}[\mathbf{v}+\boldsymbol{\mathcal{A}}(t)-\boldsymbol{\mathcal{A}}(t')] \\
&\quad\times \exp\left\{-\mathrm{i}\int_{t'}^t \mathrm{d}t''\frac{[\mathbf{v}+\boldsymbol{\mathcal{A}}(t)-\boldsymbol{\mathcal{A}}(t'')]^2}{2} + I_\mathrm{p}\right\}.
\end{aligned} \qquad \text{(D.5*)}$$

D.3 DIPOLE MOMENT

The interpretation of (D.5*) is very clear: at time t', the electron is ionized into the continuum state with momentum $\mathbf{v}$, after which it propagates in the external

electric field until time t. The amplitude at time t is the integral of all ionization events from the beginning of the electric field up until t.

We then calculate the time-dependent dipole moment:

$$\begin{aligned}
\mathbf{x}(t) &\equiv \langle \Psi(t)|\mathbf{x}|\Psi(t)\rangle \\
&= \left[a^*(t)\langle 0| + \int \mathrm{d}^3\mathbf{p}'\bar{b}^*(\mathbf{p}',t)\langle \mathbf{p}'|\right]\mathbf{x}\left[a(t)|0\rangle + \int \mathrm{d}^3\mathbf{p}\bar{b}(\mathbf{p},t)|\mathbf{p}\rangle\right] \\
&= \lceil a(t) \sim 1 \rfloor \\
&= \int \mathrm{d}^3\mathbf{p}\ \mathbf{d}_x^*(\mathbf{p})\bar{b}(\mathbf{p},t) + \text{c.c.} + \underbrace{\iint \mathrm{d}^3\mathbf{p}'\,\mathrm{d}^3\mathbf{p}\langle \mathbf{p}'|\mathbf{x}|\mathbf{p}\rangle\bar{b}^*(\mathbf{p}',t)b(\mathbf{p},t)}_{\text{This is neglected in the original article}} \\
&\approx \mathrm{i}\int_{-\infty}^{t}\mathrm{d}t' \int \mathrm{d}^3\mathbf{p}\ \mathbf{d}^*[\mathbf{p}-\mathcal{A}(t)]\exp[-\mathrm{i}S(\mathbf{p},t,t')] \\
&\qquad\qquad \times \mathcal{E}(t')\cdot\mathbf{d}[\mathbf{p}-\mathcal{A}(t')] + \text{c.c.},
\end{aligned} \tag{D.6}$$

where we have defined the quasi-classical action as

$$S(\mathbf{p},t,t') \equiv \int_{t'}^{t}\mathrm{d}t''\left\{\frac{[\mathbf{p}-\mathcal{A}(t'')]^2}{2} + I_\mathrm{p}\right\}, \tag{D.7}$$

and c.c. denotes the complex conjugate. It is worth noting that the expression for the time-dependent dipole moment (D.6) is a five-dimensional integral, whereas solving the original TDSE is a three-dimensional problem. This increase in complexity is alleviated using the saddle-point method introduced below. A further disadvantage is that integrating (D.6) is quadratic in the time variables, i.e. the chosen time window and the number of time steps per cycle. Integrating the TDSE is purely linear in all time variables.

The stationary points of the quasi-classical action are given by

$$0 = \nabla_\mathbf{p} S(\mathbf{p},t,t') = \nabla_\mathbf{v}\int_{t'}^{t}\mathrm{d}t''\frac{\mathbf{v}^2}{2} + I_\mathrm{p} = \int_{t'}^{t}\mathrm{d}t''\mathbf{v} = \mathbf{x}(t)-\mathbf{x}(t'). \tag{D.8}$$

We thus find that the electrons must recombine at the same position they were ionized from.

D.4 THE SADDLE-POINT METHOD

D.4.1 Method of steepest descent

The saddle-point method is an extension of Laplace's method (Laplace 1774; Debye 1909) for the approximation of integrals of complex-valued functions. We can use it to approximate an integral of the type

$$I = \int_{-\infty}^{\infty} \mathrm{d}x\, f(x) \exp[\lambda S(x)], \tag{D.9}$$

where we only consider those values of x where $S(x)$ is maximized. Let these points be $\{x_i\}$. We then have

$$S(x) \approx S(x_i) - \frac{1}{2} \left|-S''(x_i)\right| (x - x_i)^2 \tag{D.10}$$

in the vicinity of x_i. The integral then becomes

$$\begin{aligned} I &\approx \sum_i [f(x_i) + \mathcal{O}(\lambda^{-1})] \int_{-\infty}^{\infty} \mathrm{d}x \exp\left[S(x_i) - \frac{1}{2}\left|-S''(x_i)\right| (x - x_i)^2\right] \\ &= \sum_i [f(x_i) + \mathcal{O}(\lambda^{-1})] \exp[\lambda S(x_i)] \int_{-\infty}^{\infty} \mathrm{d}x \exp\left[-\frac{\lambda}{2}\left|-S''(x_i)\right| (x - x_i)^2\right] \\ &= \sum_i [f(x_i) + \mathcal{O}(\lambda^{-1})] \exp[\lambda S(x_i)] \sqrt{\frac{2\pi}{\lambda \left|-S''(x_i)\right|}} \\ &\approx \sum_i f(x_i) \exp[\lambda S(x_i)] \sqrt{\frac{2\pi}{\lambda \left|-S''(x_i)\right|}}. \end{aligned} \tag{D.11}$$

Similarly, in n dimensions, we obtain

$$I \approx \sum_i f(\mathbf{x}_i) \exp[\lambda S(\mathbf{x}_i)] \sqrt{\frac{(2\pi)^n}{\lambda \left|-S''(\mathbf{x}_i)\right|}}, \tag{D.12}$$

where $\left|-S''(\mathbf{x}_i)\right|$ now denotes the determinant of the Hessian* of $-S(\mathbf{x}_i)$.

* Matrix containing all possible second derivatives of a function of many variables.

The intuitive argument that only $x \in \{x_i\}$ contribute for which $S(x)$ is maximized only holds for $\lambda \in \mathbb{R}_{>0}$. For the case when $\mathrm{i}\lambda \in \mathbb{R}$, e.g. purely imaginary λ, the saddle points are rather those where $S(x)$ is *minimized*, since oscillations of high frequency will quickly average to zero.

D.4.2 Application to HHG

Applying this method to evaluate the integral over $\mathbf{p}$ in (D.6), we find

$$
\begin{aligned}
x(t) \approx\ & \mathrm{i}\int_{-\infty}^{t} \mathrm{d}t' \int \mathrm{d}^3\mathbf{p}\ \mathbf{d}^*[\mathbf{p}-\boldsymbol{\mathcal{A}}(t)]\exp[-\mathrm{i}S(\mathbf{p},t,t')] \\
&\times \boldsymbol{\mathcal{E}}(t')\cdot\mathbf{d}[\mathbf{p}-\boldsymbol{\mathcal{A}}(t')] + \text{c.c.}, \\
\approx\ & \mathrm{i}\int_{0}^{\infty} \mathrm{d}\tau\ \mathbf{d}^*[\mathbf{p}_{\mathrm{st}}(t,\tau)-\boldsymbol{\mathcal{A}}(t)]\exp\{-\mathrm{i}\underbrace{S[\mathbf{p}_{\mathrm{st}}(t,\tau),t,t-\tau]}_{\equiv S_{\mathrm{st}}(t,\tau)}\} \\
&\times \boldsymbol{\mathcal{E}}(t-\tau)\mathbf{d}[\mathbf{p}_{\mathrm{st}}(t,\tau)-\boldsymbol{\mathcal{A}}(t-\tau)]\sqrt{\frac{(2\pi)^3}{-\mathrm{i}\,|-S''(\mathbf{p},t,t-\tau)|}} + \text{c.c.} \\
=\ & \left[\begin{aligned}
&|-S''(\mathbf{p},t,t-\tau)| = \left|-\frac{\partial^2}{\partial p_i \partial p_j}S(\mathbf{p},t,t-\tau)\right|, \quad i,j=x,y,z \\
&= \left|-\frac{\partial^2}{\partial p_i \partial p_j}\int_{t-\tau}^{t}\mathrm{d}t''\left\{\frac{[\mathbf{p}-\boldsymbol{\mathcal{A}}(t'')]^2}{2}+I_{\mathrm{p}}\right\}\right| \\
&= -\left|\int_{t-\tau}^{t}\mathrm{d}t''\frac{\partial^2}{\partial p_i \partial p_j}\frac{p^2-[\mathbf{p},\boldsymbol{\mathcal{A}}(t)]_+ + \boldsymbol{\mathcal{A}}^2(t)}{2}\right| \\
&= \left[\frac{\partial^2}{\partial p_i \partial p_j}p^2 = 2\delta_{ij}\right] = -\left(\int_{t-\tau}^{t}\mathrm{d}t''\right)^3 = -\tau^3
\end{aligned}\right] \\
=\ & \mathrm{i}\int_{0}^{\infty}\mathrm{d}\tau\ \sqrt{\frac{(2\pi)^3}{\mathrm{i}\tau^3}}\mathbf{d}^*[\mathbf{p}_{\mathrm{st}}(t,\tau)-\boldsymbol{\mathcal{A}}(t)]\exp[-\mathrm{i}S_{\mathrm{st}}(t,\tau)] \\
&\times \boldsymbol{\mathcal{E}}(t-\tau)\mathbf{d}[\mathbf{p}_{\mathrm{st}}(t,\tau)-\boldsymbol{\mathcal{A}}(t-\tau)] + \text{c.c.} \\
=\ & \mathrm{i}\int_{0}^{\infty}\mathrm{d}\tau\left(\frac{\pi}{\varepsilon+\mathrm{i}\tau/2}\right)^{3/2}\mathbf{d}^*[\mathbf{p}_{\mathrm{st}}(t,\tau)-\boldsymbol{\mathcal{A}}(t)]\exp[-\mathrm{i}S_{\mathrm{st}}(t,\tau)] \\
&\times \boldsymbol{\mathcal{E}}(t-\tau)\mathbf{d}[\mathbf{p}_{\mathrm{st}}(t,\tau)-\boldsymbol{\mathcal{A}}(t-\tau)] + \text{c.c.}
\end{aligned}
\tag{D.13}
$$

where we have defined the excursion time $\tau \equiv t - t'$, chosen the stationary trajectories $\mathbf{p}_{\mathrm{st}}(t,\tau)$

$$
\mathbf{p}_{\mathrm{st}}(t,\tau) = \frac{\mathbf{x}(t)-\mathbf{x}(t-\tau)}{\tau} = \frac{1}{\tau}\int_{t-\tau}^{t}\mathrm{d}t'\boldsymbol{\mathcal{A}}(t') \tag{D.14}
$$

and used those to evaluate the action, $S_{\mathrm{st}}(t,\tau)$:

$$
S_{\mathrm{st}}(t,\tau) \equiv \int_{t-\tau}^{t}\mathrm{d}t''\frac{[\mathbf{p}_{\mathrm{st}}-\boldsymbol{\mathcal{A}}(t'')]^2}{2} + I_{\mathrm{p}}, \tag{D.15}
$$

and introduced an infinitesimal regulator ε (such that the integrand is defined everywhere);

$$\zeta(\tau) = \left(\frac{\pi}{\varepsilon + \mathrm{i}\tau/2}\right)^{3/2} \tag{D.16}$$

accounts for the quantum diffusion of the electron during propagation.

If we assume $\mathcal{E}(t) = \mathcal{E}_0 \cos(t)$, i.e. linear polarization along $\mathbf{e}_z$ and $\omega = 1$ $\implies U_\mathrm{p} = \mathcal{E}^2/4$, the action can be calculated explicitly:

$$\begin{aligned}
S_\mathrm{st}(t,\tau) &= \int_{t-\tau}^{t} \mathrm{d}t'' \, \frac{[p_\mathrm{st} - \mathcal{A}(t'')]^2}{2} + I_\mathrm{p} \\
&= \int_{t-\tau}^{t} \mathrm{d}t'' \, \frac{\left\{\left[\frac{1}{\tau}\int_{t-\tau}^{t} \mathrm{d}t' \, \mathcal{A}(t')\right] - \mathcal{A}(t'')\right\}^2}{2} + I_\mathrm{p} \\
&= \int_{t-\tau}^{t} \mathrm{d}t'' \, \frac{1}{2}\left[\frac{1}{\tau}\int_{t-\tau}^{t} \mathrm{d}t' \, \mathcal{A}(t')\right]^2 + \frac{1}{2}\int_{t-\tau}^{t} \mathrm{d}t'' \, \mathcal{A}^2(t'') \\
&\quad - \int_{t-\tau}^{t} \mathrm{d}t'' \, \left[\frac{1}{\tau}\int_{t-\tau}^{t} \mathrm{d}t' \, \mathcal{A}(t')\right] \mathcal{A}(t'') + I_\mathrm{p} \\
&= I_\mathrm{p}\tau - \frac{1}{2\tau}\left[\int_{t-\tau}^{t} \mathrm{d}t' \, \mathcal{A}(t')\right]^2 + \frac{1}{2}\int_{t-\tau}^{t} \mathrm{d}t'' \, \mathcal{A}^2(t'') \\
&= \left[\begin{array}{l} \mathcal{E} = -\dfrac{\partial \mathcal{A}}{\partial t} \implies \mathcal{A}(t) = -\mathcal{E}_0 \sin(t) \\ \qquad\qquad \implies \displaystyle\int^{t} \mathrm{d}t' \, \mathcal{A}(t') = \mathcal{E}_0 \cos(t) \\ \qquad\qquad \implies \displaystyle\int^{t} \mathrm{d}t'' \, \mathcal{A}^2(t'') = 2U_\mathrm{p}\left[t - \frac{\sin(2t)}{2}\right] \end{array}\right] \\
&= (I_\mathrm{p} + U_\mathrm{p})\tau - U_\mathrm{p}\left\{\frac{2[\cos(t) - \cos(t-\tau)]^2}{\tau} + \sin(\tau)\cos(2t-\tau)\right\} \\
&= \left[\begin{array}{l} \dfrac{1+\cos(2t)}{2} - 2\cos(t)\cos(t-\tau) + \dfrac{1+\cos(2t-2\tau)}{2} \\ = 1 + \cos(\tau)\cos(2t-\tau) - 2\cos(t)\cos(t-\tau) \\ = 1 + [1 - 2\sin^2(\tau/2)]\cos(2t-\tau) - \cos(\tau) - \cos(2t-\tau) \end{array}\right] \\
&= (I_\mathrm{p} + U_\mathrm{p})\tau - 2U_\mathrm{p}[1 - \cos(\tau)]/\tau - U_\mathrm{p} C(\tau)\cos(2t-\tau),
\end{aligned} \tag{D.17}$$

where

$$C(\tau) \equiv \sin(\tau) - 4\sin^2(\tau/2)/\tau. \tag{D.18}$$

D.5 DIPOLE MATRIX ELEMENTS

The dipole transition matrix elements are usually approximated as transitions from a hydrogenic 1s state to a plane wave continuum:

$$\begin{aligned}
\frac{2\sqrt{2}\pi^2}{\alpha^{3/4}}\langle \mathbf{k}|\hat{z}|100\rangle &= \int \mathrm{d}\mathbf{r}\exp(-\mathrm{i}\mathbf{k}\cdot\mathbf{r})\hat{z}\exp(-\sqrt{\alpha}r) \\
&= \int \mathrm{d}\Omega \int \mathrm{d}r\, r^3\cos\vartheta\exp[-(\mathrm{i}k\cos\vartheta+\sqrt{\alpha})r] \\
&= \int \mathrm{d}\Omega \frac{3!\cos\vartheta}{(-)^4(\mathrm{i}k\cos\vartheta+\sqrt{\alpha})^4} \\
&= 6\int \mathrm{d}\varphi \int_{-1}^{1} \mathrm{d}(\cos\vartheta)\frac{\cos\vartheta}{(\mathrm{i}k\cos\vartheta+\sqrt{\alpha})^4} \\
&= 12\pi\left[\frac{\mathrm{i}k(-3)\cos\vartheta-\sqrt{\alpha}}{-6k^2(\mathrm{i}k\cos\vartheta+\sqrt{\alpha})^3}\right]_{-1}^{1} \\
&= 2\pi\left[\frac{3\mathrm{i}k+\sqrt{\alpha}}{k^2(\mathrm{i}k+\sqrt{\alpha})^3}-\frac{3\mathrm{i}k(-1)+\sqrt{\alpha}}{k^2(-\mathrm{i}k+\sqrt{\alpha})^3}\right] \\
&= 2\pi\frac{(3\mathrm{i}k+\sqrt{\alpha})(-\mathrm{i}k+\sqrt{\alpha})^3+(3\mathrm{i}k-\sqrt{\alpha})(\mathrm{i}k+\sqrt{\alpha})^3}{k^2(k^2+\alpha)^3} \\
&= -\mathrm{i}32\pi\sqrt{\alpha}\frac{k^2\mathbf{k}}{k^2(k^2+\alpha)^3} = -\mathrm{i}2^5\pi\alpha^{2/4}\frac{\mathbf{k}}{(k^2+\alpha)^3} \\
\implies \langle \mathbf{k}|\hat{d_z}|100\rangle &= -\mathrm{i}\frac{2^{7/2}\alpha^{5/4}}{\pi}\frac{\mathbf{k}}{(k^2+\alpha)^3},
\end{aligned} \tag{D.19}$$

where $\alpha = 2I_\mathrm{p}$.

The *oscillator strength* is a measure of the line strength of a transition and is defined as

$$f_{12} \equiv \frac{2m_\mathrm{e}\omega\,|D_{12}|^2}{3\hbar}, \tag{D.20}$$

where D_{12} is the dipole matrix element between levels $|1\rangle$ and $|2\rangle$ and ω the energy separation.

D.6 CODE

A simple implementation of the SFA was developed as a JULIA (Bezanson et al. 2014) package. It is freely available from https://github.com/jagot/SFA.jl. The code

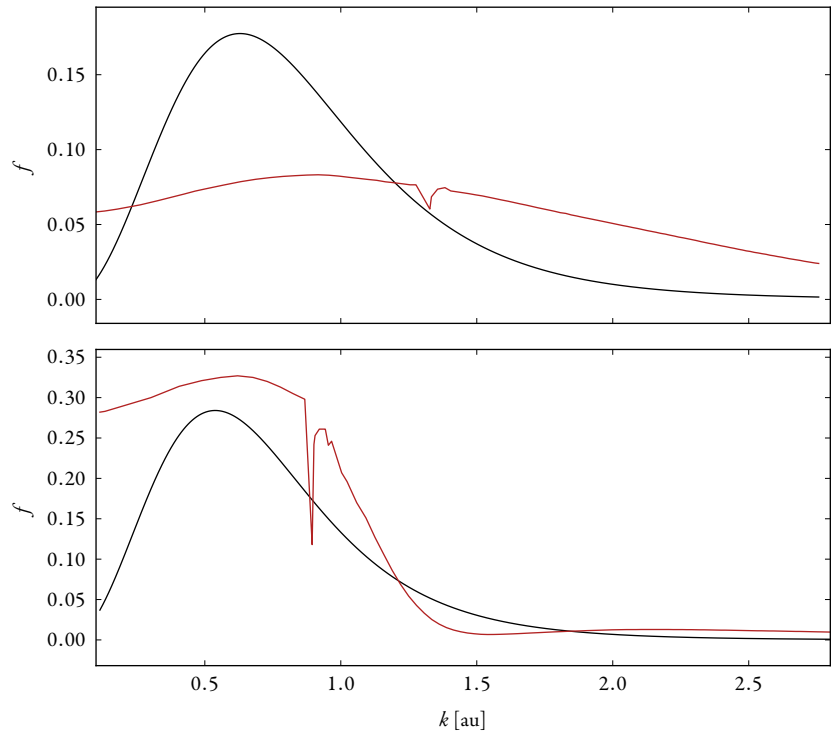

Figure D.1: Oscillator strengths of neon (upper panel) and argon (lower panel), experimental data (red lines) taken from Samson and Stolte 2002, compared with theoretical oscillator strengths (black line) given by (D.19) & (D.20).

listing below shows the routine that performs the integral over the excursion times in (D.13).

```
function calc_i(i, offset, jmin, δt, Av, Ev, Ip, d)
  τ = reverse(1:i+offset)*δt   # excursion times
  nτ = length(τ)

  At = Av[i+offset]

  pτ = 0
  dx = 0im

  for j = nτ:-1:jmin
    ζ = (π/(1e-10 + im*(τ[j]-δt)/2))^(3/2)    # (D.16)

    AtP = Av[j]
    EtP = Ev[j]
    pτ += AtP    # ∑_j A(t_i − τ_j)
    p = pτ*δt/τ[j]    # (δt/τ) ∑_j A(t_i − τ_j) ~ (D.14)
    dion = d(p - AtP)
    drec = d(p - At)

    # (D.15) using trapezoidal integration
    S = trapzv(0.5(p - Av[j:i+offset-1]).^2 + Ip, δt)

    dx += ζ*conj(drec)*exp(-im*S)*EtP*dion # integrand of (D.13) at τ_j
  end
  -imag(dx)    # x(t_i)
end
```

Using the code is very simple; this example yields the output shown in figure D.2.

```
using SFA

# Atom
Ip,d = hydrogen_like(15.7596/27.211)    # hydrogen-like argon

# Driving field
λ = 1030e-9 # m
I = 1e14 # W/cm^2
ndt = 200 # Steps per cycle
ω,T,A,E = field(λ,I)

# Integration limits: calculate x(t) for t ∈ [2T, 5T], allowing a maximal
```

```
# excursion time of 0.65T.
tlims = (2,5,-0.65)

x,t = propagate(A,E,Ip,d,tlims,T,ndt)
```

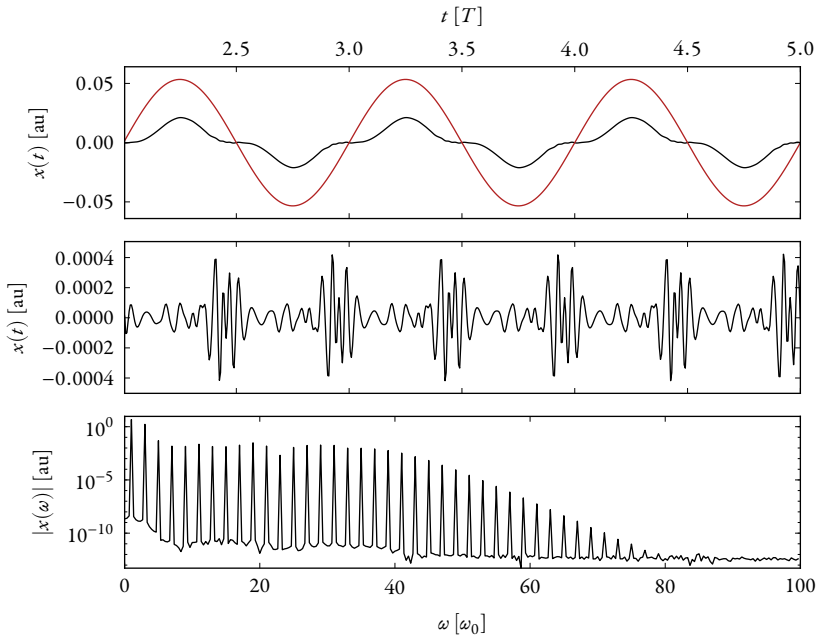

FIGURE D.2: Results obtained from the simple SFA code: The upper panel shows $x(t)$ (in black) in the time interval $[2T, 5T]$. The fundamental field is shown in red, for reference. The middle panel shows $x(t)$ after applying a highpass filter with a cut-off frequency of 12ω, revealing the XUV bursts that occur every half cycle. The lower panel shows the dipole spectrum obtained via a Fourier transform.

Tunnelling Ionization in Elliptical HHG

E

A short overview of the tunnelling theory employed in the classical model of elliptical HHG is provided here. Static, weak-field* ionization of hydrogen can be calculated using the simple formula given by Landau and Lifshitz (1977, §77):

* Weak in comparison to the binding potential of the atom

$$w_{\text{stat}}(\mathcal{E}) = \frac{4}{\mathcal{E}} \exp\left(-\frac{2}{3\mathcal{E}}\right). \tag{E.1}$$

Perelomov, Popov, and Terent'ev (1966) derived a generalization of (E.1) for alternating, low-frequency fields, and Ammosov, Delone, and Kraĭnov (1986) generalized the theory further to non-hydrogenic atoms and ions. ADK theory states that tunnelling ionization by an alternating, elliptical field can be written

$$w(\mathcal{E}, \xi) = w_{\text{stat}}(\mathcal{E}) w_{\text{ellipt}}(\mathcal{E}, \xi), \tag{E.2}$$

where

$$\begin{aligned} w_{\text{stat}}(\mathcal{E}) \equiv & \left(\frac{3\mathcal{E}n^{*3}}{\pi Z^3}\right)^{1/2} \frac{Z^2}{2n^{*2}} \left(\frac{2}{n^*}\right)^{2n^*} \frac{1}{2\pi n^*} \frac{(2\ell+1)(\ell+|m|)!}{2^{|m|}(|m|)!\,(\ell-|m|)!} \\ & \times \left(\frac{2Z^3}{\mathcal{E}n^{*3}}\right)^{2n^*-|m|-1} \exp\left(-\frac{2}{3}\frac{Z^3}{n^{*3}\mathcal{E}}\right), \end{aligned} \tag{E.3}$$

and

$$w_{\text{ellipt}}(\mathcal{E}, \xi) \equiv \left[\frac{\xi(1+\xi)}{2}\right]^{-1/2} a\left(\frac{1-\xi}{3\xi}\frac{Z^3}{n^{*3}\mathcal{E}}\right), \tag{E.4}$$

$$a(x) = \exp(-x) I_0(x) \to \frac{1}{\sqrt{2\pi x}}, \quad x \to \infty. \tag{E.5}$$

$I_0(x)$ is a modified Bessel function of the first kind, n^* is an effective principle quantum number and Z is the residual charge. For ionization from the ground state of argon, we have $n^* = 0.93$ and $Z = 1$ (ibid.). In the case of linear polarization, (E.4) reduces through (E.5) to

$$w_{\text{linear}}(\mathcal{E}) \equiv \left[\frac{3\mathcal{E}}{\pi}\left(\frac{n^*}{Z}\right)^3\right]^{1/2}, \tag{E.6}$$

since $\xi \to 0 \implies x \to \infty$. In all instances, $\mathcal{E}$ should be substituted by the instantaneous field strength at the time of ionization, $\mathcal{E}(t_i)$.

ADK theory is a valid approximation in our case, since we are within the tunnelling regime (Fu, Zhao, and Zhou 2012; Zhao, Liu, and Zhou 2014); for a peak intensity of 1×10^{14} W/cm^2, and a wavelength of 1030 nm, the Keldysh parameter is $\gamma = [I_p/2U_p]^{1/2} \approx 0.9$. For lower intensities, one would have to turn to PPT theory (Perelomov, Popov, and Terent'ev 1966, 1967; Perelomov and Popov 1967).

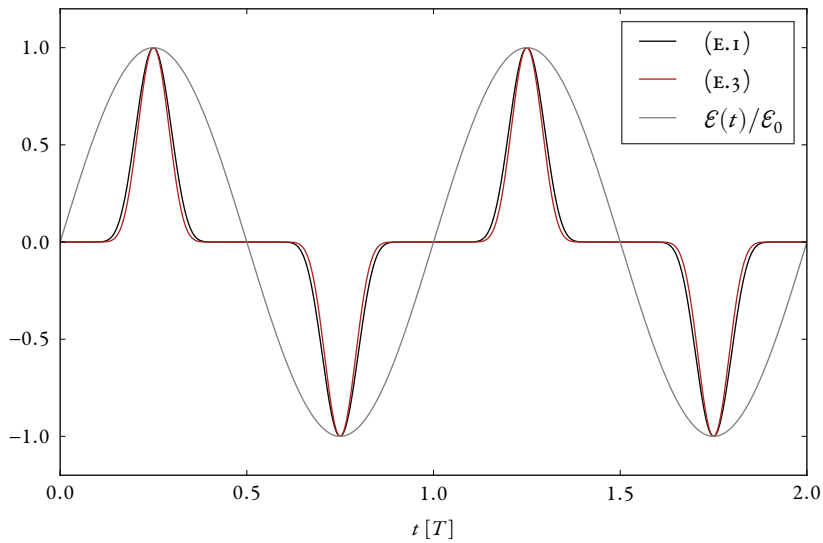

FIGURE E.1: Normalized tunnelling rate as a function of time, according to Landau and Lifshitz (1977) (black) and Ammosov, Delone, and Kraĭnov (1986) (for $\ell_0 = 0$ and $m_0 = 0$; red) for an electric field of intensity 10^{14} W cm^{-2}.

Ultrafast Optics

F

Ultrafast optics concerns light pulses whose duration is of the order of a few cycles of the carrier wavelength. In this regime, the relative phase of the carrier and the envelope, the CEP becomes very important, since it affects the temporal symmetry of the pulse. Since pulses of very short duration necessarily have a large bandwidth, the propagation of such pulses will also be affected by dispersion, measured by the *group delay dispersion* (GDD), which is the second derivative of the phase with respect to the angular frequency.

F.1 Dispersion through ideal media

The relation between the time domain and the spectral domain for a Gaussian function is given by

$$\exp(-\alpha t^2) \leftrightarrow \frac{1}{\sqrt{2\alpha}} \exp\left(-\frac{\omega^2}{4\alpha}\right). \tag{F.1}$$

A Gaussian pulse in frequency domain can be written

$$\begin{aligned} \mathcal{E}(\omega) &= N \exp\left[-\frac{(\omega-\omega_0)^2}{2\Omega^2} + \mathrm{j}\eta(\omega-\omega_0)^2 + \mathrm{j}\phi_0\right] \\ &= N \exp\left[-(\omega-\omega_0)^2\left(\frac{1}{2\Omega^2} + \mathrm{j}\eta\right) + \mathrm{j}\phi_0\right], \end{aligned} \tag{F.2}$$

where ω_0 is the central frequency, Ω is the standard deviation (std.dev.) of the frequency, η is proportional to GDD, and ϕ_0 is the CEP. This corresponds to a Gaussian function with a complex variance

$$\alpha = \frac{1}{4}\left(\frac{1}{2\Omega^2} + \mathrm{j}\eta\right)^{-1}. \tag{F.3}$$

The std.dev. is related to the intensity envelope FWHM τ_0 through

$$\sigma = \frac{\tau_0}{2\sqrt{2\ln 2}} \implies \sqrt{\exp\left(-\frac{t^2}{2\sigma^2}\right)} = \exp\left(-\frac{t^2}{2\sigma^2}\frac{1}{2}\right) \equiv \exp\left(-\frac{t^2}{2(\sigma')^2}\right), \tag{F.4}$$

which gives an amplitude std.dev.

$$\sigma' = \sqrt{2}\sigma = \frac{\tau_0}{2\sqrt{\ln 2}}. \tag{F.5}$$

The frequency domain std.dev. Ω as a function of FWHM τ_0 is

$$2\Omega^2 = 4\alpha \implies \Omega = \sqrt{2\alpha} = \sqrt{2\frac{1}{2(\sigma')^2}} = \frac{1}{\sigma'} = \frac{2\sqrt{\ln 2}}{\tau_0}, \tag{F.6}$$

$$\implies \gamma^{-1} \equiv 2\Omega^2 = \frac{8\ln 2}{\tau_0^2}. \tag{F.7}$$

In the time domain, the pulse is the given by

$$\begin{aligned}
\mathcal{E}(t) &= \underbrace{N\sqrt{2\alpha}}_{A(\eta)} \exp(\mathrm{j}\omega_0 t + \mathrm{j}\phi_0) \exp(-\alpha t^2) \\
&= \left[\begin{array}{r} \text{Peak field strength } \mathcal{E}_0, \eta = 0 \implies \\ A(\eta)/\mathcal{E}_0 = \left(\frac{1}{2\Omega^2}\right)^{1/2} \left(\frac{1}{2\Omega^2} + \mathrm{j}\eta\right)^{-1/2} = \sqrt{\frac{\gamma}{\gamma + \mathrm{j}\eta}} \\ = \sqrt{\frac{\gamma(\gamma - \mathrm{j}\eta)}{\gamma^2 + \eta^2}} = \sqrt{\frac{\gamma}{\sqrt{\gamma^2 + \eta^2}}} \exp[\mathrm{j}\phi(\eta)], \\ \phi(\eta) \equiv \operatorname{atan2}(-\eta, \gamma)/2 \end{array}\right] \\
&= A(\eta) \exp(\mathrm{j}\omega_0 t + \mathrm{j}\phi_0) \exp\left[-\frac{1}{4(\gamma + \mathrm{j}\eta)} t^2\right] = \left[\frac{1}{\gamma + \mathrm{j}\eta} = \frac{\gamma - \mathrm{j}\eta}{\gamma^2 + \eta^2}\right] \\
&= A(\eta) \exp(\mathrm{j}\omega_0 t) \exp\left[-\frac{1}{4}\frac{\gamma - \mathrm{j}\eta}{\gamma^2 + \eta^2} t^2\right] \\
&= A(\eta) \exp(\mathrm{j}\omega_0 t + \mathrm{j}\phi_0) \exp\left[-\frac{1}{4}\frac{\gamma}{\gamma^2 + \eta^2} t^2 + \mathrm{j}\frac{1}{4}\frac{\eta}{\gamma^2 + \eta^2} t^2\right] \\
&\equiv A(\eta) \exp(\mathrm{j}\omega_0 t + \mathrm{j}\phi_0) \exp\left[-a(\eta) t^2 + \mathrm{j}\frac{b(\eta)}{2} t^2\right]
\end{aligned} \tag{F.8}$$

The additional phase $\phi(\eta)$ amounts to a GDD-dependent CEP. To decouple CEP effects from GDD effects, $\phi(\eta)$ is neglected, and CEP is introduced solely through ϕ_0. $\operatorname{atan2}(y, x)$ denotes the principal value of the argument of $x + y\mathrm{j}$, to disambiguate which quadrant of the complex plane the phasor is found in.

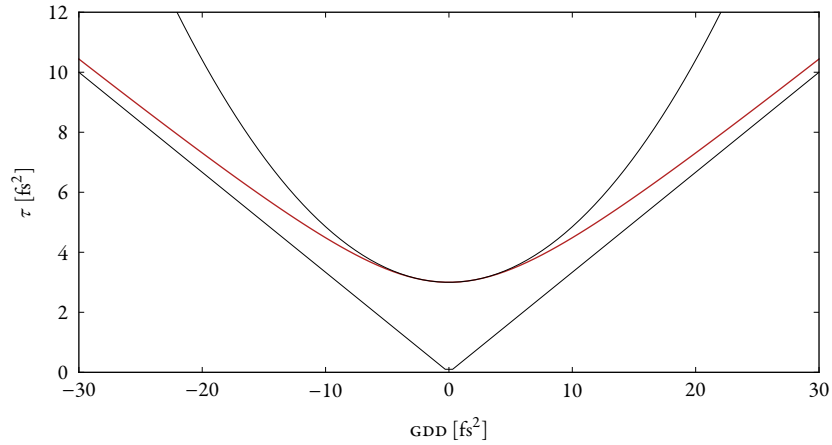

Figure F.1: FWHM as a function of GDD (red), together with the two asymptotic approximations given in (F.9).

Non-zero GDD introduces a stretching of the FWHM (depicted in figure F.1):

$$\tilde{\sigma} = \frac{1}{\sqrt{2a(\eta)}} \implies \tau = 2\sqrt{\ln 2}\tilde{\sigma} = \sqrt{\frac{2\ln 2}{a(\eta)}} = \sqrt{\frac{8\ln 2(\gamma^2+\eta^2)}{\gamma}}$$
$$= \sqrt{1+\frac{\eta^2}{\tau_0^4}}\tau_0 \approx \begin{cases} \left(1+\dfrac{\eta^2}{2\tau_0^4}\right)\tau_0, & \eta \ll \tau_0^2, \\ \dfrac{|\eta|}{\tau_0}, & \eta \gg \tau_0^2. \end{cases} \tag{F.9}$$

The effect of introducing GDD is shown in figure F.2.

The instantaneous frequency of the field (F.8) is given by

$$\omega(t) \equiv \frac{\partial}{\partial t}\arg\mathcal{E}(t) = \omega_0 + b(\eta)t = \omega_0 + \frac{1}{2}\frac{\eta}{\gamma^2+\eta^2}t \approx \omega_0 + \frac{t}{2\eta}, \quad \eta \gg \tau_0^2, \tag{F.10}$$

where $b(\eta)$ is the *chirp parameter*. This parameter can alternatively be written as a function of the pulse duration and the Fourier-transform limited pulse duration as

$$b(\tau) = \pm\frac{4\ln 2}{\tau^2}\sqrt{\frac{\tau^2}{\tau_0^2}-1}, \tag{F.11}$$

which is plotted in figure F.3. As is obvious from (F.10), the chirp parameter is a measure of the change in the carrier frequency per unit time. There exists a

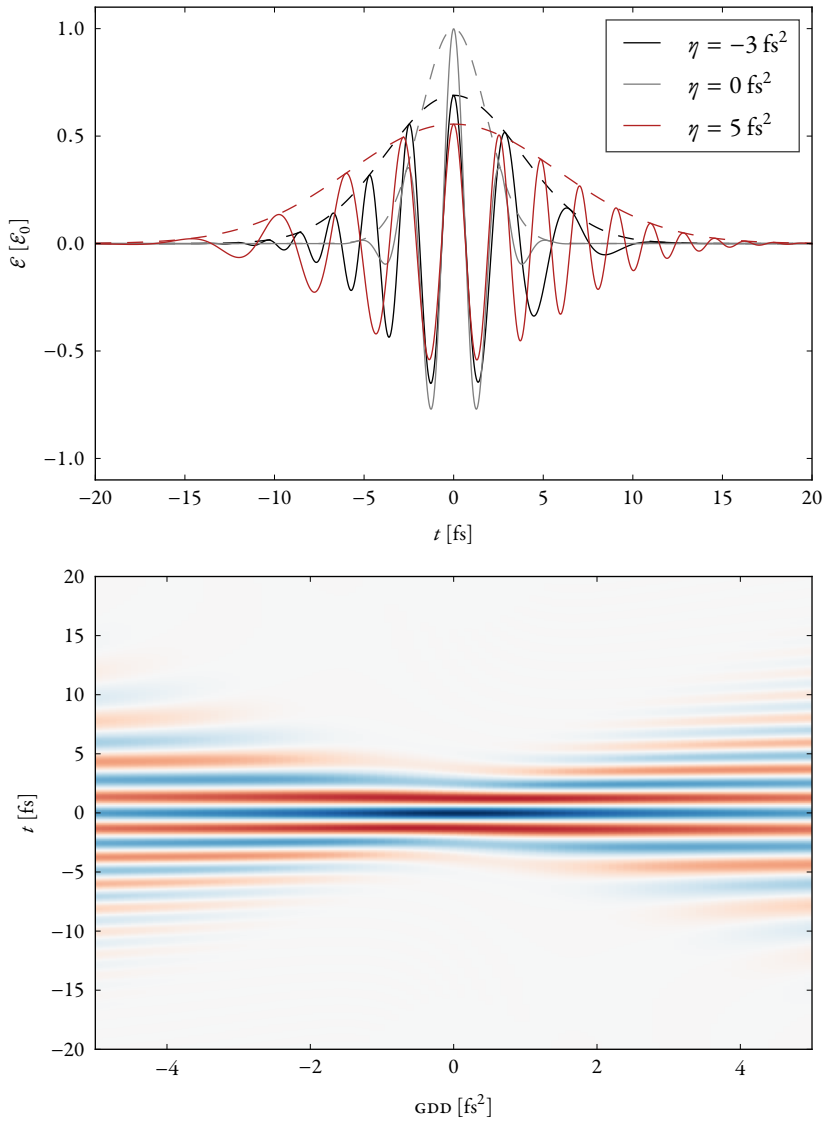

FIGURE F.2: Example of the effect of introducing GDD on an ultrashort pulse with $\lambda = 800$ nm, and Fourier-tranform limited duration 3 fs (intensity FWHM). $\phi(\eta)$ in the amplitude neglected $\implies$ carrier wavelength centred at $t = 0$.

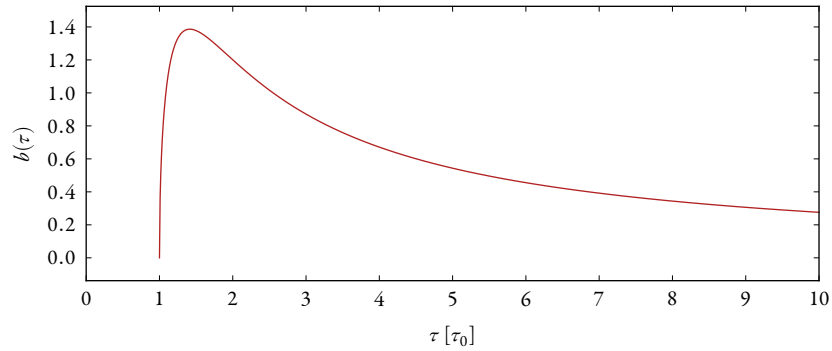

FIGURE F.3: The chirp parameter (F.11) as a function of pulse duration τ.

pulse duration for which the chirp parameter is maximized, which is reasonable, since the bandwidth is finite; for pulses of infinite duration, the change in the instantaneous frequency must necessarily vanish.

F.2 DISPERSION THROUGH NON-IDEAL MEDIA

In non-ideal media, the dispersion cannot be described by CEP and GDD only, i.e. the Taylor expansion of the phase with respect to the energy has components beyond second order. For such media, the refractive index is most practically represented by the empirical Sellmeier equation

$$n^2(\lambda) = 1 + \sum_{i=1}^{3} \frac{B_i \lambda^2}{\lambda^2 - C_i}, \tag{F.12}$$

where λ is given in μm and B_i, C_i are experimentally determined coefficients. For the commonly used borosilicate crown glass (BK7), these coefficients are:

i	B_i	C_i [μm^2]
1	1.039 612 12	$6.000\,698\,67 \times 10^{-3}$
2	0.231 792 344	$2.001\,791\,44 \times 10^{-2}$
3	1.010 469 45	$1.035\,606\,53 \times 10^{2}$

A pulse passing through a medium of length d and a refractive index $n(\lambda)$, will be dispersed as

$$\exp(-\mathrm{j}kd), \tag{F.13}$$

where

$$k = k_0 n(\lambda) = \frac{2\pi n(\lambda)}{\lambda}. \tag{F.14}$$

It is useful to subtract the linear component of the wavevector:

$$\tilde{k} \equiv k - \omega \left.\frac{\partial k}{\partial \omega}\right|_{\omega_0}, \tag{F.15}$$

and substitute this for k in (F.13), to keep the pulse centred in the frame of reference. The effect of (F.13) using a medium described by (F.12) is most readily calculated using a numerical Fourier transform.

Phases in QPI

G

The models used in PIV for the spatial and spectral lineouts are derived in this appendix, together with the reasons for their relevance. They are both based on the same model for the microscopic response: a simple, trajectory-resolved decomposition of the XUV electric field generated in the HHG. The spatial model is propagated to the far field to yield the far-field spatial variation along the central frequency of each harmonic, using Gaussian beams, which are basic solutions to Helmholtz' equation in the paraxial approximation. The spectral model modelling the spectral variation along zero divergence, is simply the spectral variation in the near field.

G.1 Introduction

We use the model given by Varjú et al. (2005a):

$$\mathcal{E}(t) = \sum_{qj} A_{qj}(t) \exp[\mathrm{i}\Psi_{qj}(t)], \tag{G.1}$$

where the phase is

$$\Psi_{qj}(t) = q\Phi_0(t) + \Phi_{qj}(t) + \Phi_{qj}^{\text{disp.prop.}} \tag{G.2}$$

The instantaneous frequency of harmonic order q and trajectory j is given by

$$\omega_{qj}(t) = \frac{\partial}{\partial t}\Psi_{qj}(t) \tag{G.3}$$

The phase (G.2) depends on three contributions.

(1) Contribution from the fundamental field:

$$q\Phi_0(t) = q\omega t + q\phi_0 + \frac{qb(\tau)}{2}t^2, \tag{G.4}$$

$$\implies q\frac{\partial}{\partial t}\Phi_0(t) = q\omega + qb(\tau)t$$

where ϕ_0 is the CEP and $b(\tau)$ is the chirp rate (F.11) of the fundamental [τ is the pulse duration – when the pulse is Fourier-limited, $b(\tau_0) = 0$].

(2) The phase $\Phi_{qj}(t)$ is due to the generation process and depends on the intensity (Taylor-expanded around the peak intensity, I_0):

$$\Phi_{qj}(t) = \Phi_{qj}[I(t)] \approx \Phi_{qj}(I_0) + \frac{\partial \Phi_{qj}}{\partial I} I(t). \tag{G.5}$$

(3) We neglect $\Phi_{qj}^{\text{disp.prop.}}$, which is the phase acquired through propagation in the medium.

The total phase is thus

$$\Psi_{qj}(t) \approx q\omega t + q\phi_0 + \frac{qb(\tau)}{2} t^2 + \Phi_{qj}(I_0) + \alpha_{qj} I(t), \tag{G.6}$$

where

$$\alpha_{qj} = +\frac{\partial \Phi_{qj}}{\partial I}. \tag{G.7}$$

We identify α_{qj} with the positive derivative, since we customarily want $q\omega t$ and $\alpha_{qj} I(t)$ to have the same sign.

G.1.1 Motivation

The motivation for the Taylor expansion in (G.5) comes from the SFA; in (D.13), the phase depends on the quasi-classical action (D.17):

$$\begin{aligned} S_{\text{st}}(t,\tau) &= (I_{\text{p}} + U_{\text{p}})\tau - 2U_{\text{p}}[1 - \cos(\tau)]/\tau - U_{\text{p}} C(\tau)\cos(2t - \tau) \\ &= I_{\text{p}}\tau + I\{\tau - 2[1 - \cos(\tau)]/\tau - C(\tau)\cos(2t - \tau)\}/4, \end{aligned} \tag{D.17*}$$

since $U_{\text{p}} = I/4$ when $\omega = 1$. Classically, for each harmonic and trajectory, there exists a pair of return and excursion times, (t, τ), such that (D.17*) only varies with intensity. Since for two different trajectories leading to the same harmonic order, the pair (t, τ) is, in general, different, the prefactor of I in (D.17*) differs between trajectories, see figure G.1.

G.2 GAUSSIAN INTENSITY

With a Gaussian field intensity

$$I(t) = I_0(\tau) \exp\left(-\frac{4\ln 2}{\tau^2} t^2\right) \implies \frac{\partial}{\partial t} I = -\frac{8\ln 2}{\tau^2} I(t), \tag{G.8}$$

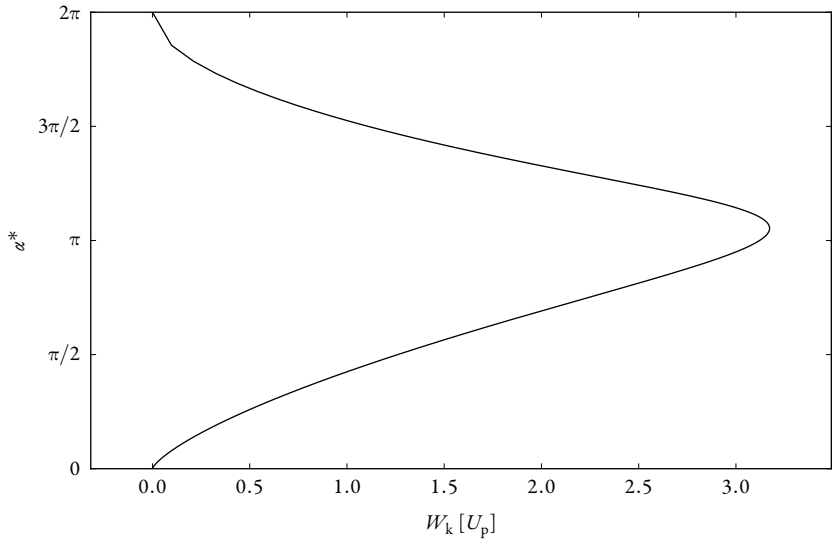

FIGURE G.1: α^* from the SFA, calculated by inserting the classical return and excursion times into (D.17*).

the instantaneous frequency becomes

$$\omega_{qj}(t) = q\omega + qb(\tau)t - \frac{\partial \Phi_{qj}}{\partial I}\frac{8\ln 2}{\tau^2}I(t) \approx q\omega + \left[qb(\tau) - \gamma\frac{\partial \Phi_{qj}}{\partial I}\right]t, \quad \text{(G.9)}$$

where

$$\gamma \equiv -I_0(\tau)\frac{8\ln 2}{\tau^2}. \quad \text{(G.10)}$$

G.3 SPECTRAL MODEL

The spectral model is then given by

$$\begin{aligned}\mathcal{E}(t) &= \sum_{qj} A_{qj}(t)\exp[\mathrm{i}\Psi_{qj}(t)] \\ &\approx \sum_{qj} C_{qj} I^{\frac{n}{2}}(t)\exp\left[\mathrm{i}q\omega t + \mathrm{i}q\phi_0 + \mathrm{i}\frac{qb(\tau)}{2}t^2 + \mathrm{i}\Phi_{qj}(I_0) + \mathrm{i}\alpha_{qj}I(t)\right].\end{aligned} \quad \text{(G.11)}$$

We do not have access to the absolute phase, so the reduced model becomes

$$\mathcal{E}(t) \approx \sum_{qj} C_{qj} I^{\frac{n}{2}}(t)\exp\left[\mathrm{i}q\omega t + \mathrm{i}\frac{qb(\tau)}{2}t^2 + \mathrm{i}\alpha_{qj}I(t)\right]. \quad \text{(G.12)}$$

By Fourier transforming (G.12) separately for each chirp of the fundamental driving field, we obtain the spectral QPI patterns.

G.4 SPATIAL MODEL

The spatial model is acquired by propagating (G.1) to the far field. This is done in the paraxial approximation, using Gaussian beams:

$$\tilde{\mathcal{E}}(t,r,z) = \mathit{\Pi}(z)\mathcal{E}(t,r), \tag{G.13}$$

where the near field is given by (G.11), additionally taking the radial variation of $I(t,r)$ into account:

$$\mathcal{E}(t,r) \approx \sum_{qj} C_{qj} I^{\frac{n}{2}}(t,r) \mathrm{e}^{\mathrm{i}q\omega t + \mathrm{i}q\phi_0 + \mathrm{i}qb(\tau)t^2/2 + \mathrm{i}\Phi_{qj}(I_0) + \mathrm{i}\alpha_{qj} I(t,r)}, \tag{G.14}$$

with

$$I(t,r) = I_0(\tau) \exp\left(-\frac{4\ln 2}{\tau^2}t^2\right) \exp\left(-\frac{r^2}{r_0^2}\right). \tag{G.15}$$

The spatial lineouts are taken along the central frequency of each harmonic and they are symmetric with respect to the chirp parameter. We therefore conjecture that they only depend on the peak intensity as a function of the chirp, and not the time structure of the driving field:

$$\begin{aligned}\mathcal{E}(r) \approx \sum_{qj} C_{qj} &\left[I_0(\tau) \exp\left(-\frac{r^2}{r_0^2}\right)\right]^{\frac{n}{2}} \\ &\times \exp\left[\mathrm{i}q\phi_0 + \mathrm{i}\Phi_{qj}(I_0) + \mathrm{i}\alpha_{qj} I_0(\tau) \exp\left(-\frac{r^2}{r_0^2}\right)\right],\end{aligned} \tag{G.16}$$

In the parabolic approximation, a Gaussian beam can be propagated exactly to the far field. A linearly polarized Gaussian beam has the form

$$\boldsymbol{\mathcal{E}}_{\mathrm{GB}}(r,z) = \mathcal{E}_0 \mathbf{e}_x \frac{w_0}{w(z)} \exp\left[-\frac{r^2}{w^2(z)}\right] \exp\left\{-\mathrm{i}\left[kz + k\frac{r^2}{2R(z)} - \zeta(z)\right] + \mathrm{i}\eta\right\}, \tag{G.17}$$

where $\mathcal{E}_0$ is the peak field strength, $\mathbf{e}_x$ the polarization direction, w_0 the beam waist (diameter), $w(z) = w_0\sqrt{1 + z^2/z_R^2}$ the beam width, z_R the Rayleigh range, $k = 2\pi/\lambda$ the wavevector, $R(z) = z(1 + z_R^2/z^2)$ the wavefront curvature and $\zeta(z) = \arctan(z/z_R)$ the Gouy phase. η is an additional phase shift.

Expressing one term in the sum (G.16), corresponding to a single trajectory (q,j), in the parabolic approximation, we obtain the following expression [(q,j) indices omitted for brevity; all quantities must be evaluated at their respective wavelength, e.g. $k = k_q$, &c.]:

$$\mathcal{E}_{qj}(r) \approx C_{qj}\left[I_0(\tau)\exp\left(-\frac{r^2}{r_0^2}\right)\right]^{\frac{n}{2}}\exp\left[\mathrm{i}\alpha_{qj}I_0(\tau)\left(1-\frac{2r^2}{r_0^2}\right)\right]. \quad \text{(G.18)}$$

Comparing with (G.17), we can express (G.18) as a Gaussian beam with its beam waist *shifted* to $-z_f$

$$\begin{aligned}\mathcal{E}_{qj}(r) &\approx \mathcal{E}_{\mathrm{GB}}(r,z_f)\\ &= \mathcal{E}_0\frac{w_0}{w(z_f)}\exp\left\{-\frac{r^2}{w^2(z_f)}-\mathrm{i}\left[kz_f+k\frac{r^2}{2R(z_f)}-\zeta(z_f)\right]+\mathrm{i}\eta\right\},\end{aligned} \quad \text{(G.19)}$$

with the amplitude-related factors as

$$\mathcal{E}_0 = C_{qj}\frac{w(z_f)}{w_0}I_0^{\frac{n}{2}}(\tau), \quad w(z_f) = \frac{r_0}{\sqrt{n}},$$

and the phase-dependent parts as

$$R_f \equiv R(z_f) = \frac{kr_0^2}{4\alpha_{qj}I_0(\tau)}, \quad \eta = q\phi_0 + \Phi_{qj}(I_0) + \alpha_{qj}I_0(\tau) + kz_f - \zeta(z_f).$$

Solving for (z_R, z_f), we obtain the following expressions:

$$z_R = \frac{\pi\lambda R_f^2 r_0^2/n}{\lambda^2 R_f^2 + \pi r_0^4/n^2}, \qquad z_f = \frac{\pi^2 R_f\, r_0^4/n^2}{\lambda^2 R_f^2 + \pi r_0^4/n^2}. \quad \text{(G.20)}$$

Finally, the far-field amplitude can be written

$$\begin{aligned}\tilde{\mathcal{E}}_{qj}(r,z) &= \Pi(z)\mathcal{E}_{qj}(r)\\ &= \mathcal{E}_0\frac{w_0}{w(\tilde{z})}\exp\left[-\frac{r^2}{w^2(\tilde{z})}\right]\exp\left\{-\mathrm{i}\left[k\tilde{z}+k\frac{r^2}{2R(\tilde{z})}-\zeta(\tilde{z})\right]+\mathrm{i}\eta\right\},\end{aligned} \quad \text{(G.21)}$$

with $\tilde{z} \equiv z + z_f$. If only two trajectories ($j = s, l$) are involved, the far-field intensity for one specific harmonic order q can be written

$$I_q \propto \left|\tilde{\mathcal{E}}_q(r,z)\right|^2 = \left|\tilde{\mathcal{E}}_{qs}(r,z)\right|^2 + \left|\tilde{\mathcal{E}}_{ql}(r,z)\right|^2 + 2\left|\tilde{\mathcal{E}}_{qs}(r,z)\right|\left|\tilde{\mathcal{E}}_{ql}(r,z)\right|\cos[\chi_q(r,z)], \quad \text{(G.22)}$$

where

$$\begin{aligned}\chi_q(r,z) = &-\frac{kr^2}{2}\left[\frac{1}{R_{qs}(\tilde{z}_{qs})} - \frac{1}{R_{ql}(\tilde{z}_{ql})}\right] \\ &+ [\zeta(\tilde{z}_{qs}) - \zeta(\tilde{z}_{ql})] - [\zeta(z_{fqs}) - \zeta(z_{fql})] \\ &+ [\Phi_{qs}(I_0) - \Phi_{ql}(I_0)] + (\alpha_{qs} - \alpha_{ql})I_0(\tau).\end{aligned} \tag{G.23}$$

This is our interferometer. Everything except

$$[\Phi_{qs}(I_0) - \Phi_{ql}(I_0)] + (\alpha_{qs} - \alpha_{ql})I_0(\tau)$$

can be deduced from experimental parameters. Fitting (G.22) to the experimental lineouts provides access to these unknowns.

H Far-Field Propagation

Far field propagation is used to transfer a near-field electromagnetic wave to the far field. In the paraxial approximation of Helmholtz' equation, the far-field transform is proportional to the Fourier transform. For the case of cylindrical symmetry, the calculations can be simplified.

H.1 Far-Field Propagation in Cartesian Coordinates

In the *Fraunhofer regime* the far-field amplitude is given by (Goodman 1996)

$$U(x,y) = \frac{\exp(\mathrm{j}kz)\exp[\mathrm{j}\frac{k}{2z}(x^2+y^2)]}{\mathrm{j}\lambda z} \iint_{-\infty}^{\infty} \mathrm{d}\xi\,\mathrm{d}\eta \exp\left[-\mathrm{j}\frac{2\pi}{\lambda z}(x\xi+y\eta)\right] U(\xi,\eta) \tag{H.1}$$

> *Aside from multiplicative phase factors preceding the integral, this expression is simply the Fourier transform of the aperture distribution, evalutated at the frequencies*
>
> $$f_X = x/\lambda z \qquad f_Y = y/\lambda z$$
>
> *Goodman (ibid., p. 74)*

$$\begin{aligned} \Longrightarrow\ U(x,y) &= \frac{\exp(\mathrm{j}kz)\exp[\mathrm{j}\frac{k}{2z}(x^2+y^2)]}{\mathrm{j}\lambda z}\mathcal{F}\{U(\xi,\eta)\}(x/\lambda z, y/\lambda z) \\ &= \left[k \equiv \frac{2\pi}{\lambda}\right] \\ &= -\mathrm{j}\frac{k}{2\pi z}\exp(\mathrm{j}kz)\exp\left[\mathrm{j}\frac{k}{2z}(x^2+y^2)\right] \\ &\quad \times \mathcal{F}\{U(\xi,\eta)\}(kx/2\pi z, ky/2\pi z), \end{aligned} \tag{H.2}$$

where the Fourier transform $\mathcal{F}\{U(\xi,\eta)\}$ can be efficiently calculated via the *fast Fourier transform* (FFT); (Gauss 1866; Cooley and Tukey 1965; Frigo 1999), which for $N \times N$ problems has a computational complexity of $\mathcal{O}[N^2\log(N^2)]$.

H.2 HANKEL TRANSFORM

It can be shown that in cylindrical coordinates, the Fourier transform becomes

$$\mathcal{F}\{g(r,\vartheta)\} = \sum_{k=-\infty}^{\infty} c_k(-\mathrm{j})^k \exp(\mathrm{j}k\phi) H_k\{g_R(r)\}, \tag{H.3}$$

where

$$c_k = \frac{1}{2\pi}\int_0^{2\pi} \mathrm{d}\vartheta \;\exp(-\mathrm{j}k\vartheta) g_\Theta(\vartheta) \tag{H.4}$$

is the angular transform (simply a Fourier transform on the interval $[0, 2\pi)$) and the radial transform is given by

$$H_k\{g_R(r)\} \equiv 2\pi \int_0^{\infty} \mathrm{d}r\; r J_k(2\pi r\rho) g_R(r), \tag{H.5}$$

which is the definition of a *Hankel transform* of order k. J_k is a Bessel function of the first kind and order k.

The Hankel transform can be efficiently calculated via the *fast Hankel transform* (FHT). An implementation that evaluates the transform at the roots of the Bessel function is given by Guizar-Sicairos and Gutiérrez-Vega (2004) and a code can be found at https://github.com/jagot/Hankel.jl. The method has a computational complexity of $\mathcal{O}[N_k \log(N_k) N_r^2]$.

H.3 FAR-FIELD PROPAGATION OF CYLINDRICALLY SYMMETRIC FUNCTIONS

For the cylindrically symmetric case $[g(r,\vartheta) = g_R(r) \implies c_k = \delta_k]$, the far-field integral transforms to

$$\begin{aligned} U(r) &= 2\pi \frac{\exp(\mathrm{j}kz)\exp\left(\mathrm{j}\frac{k}{2z}r^2\right)}{\mathrm{j}\lambda z} \int_0^{\infty} \mathrm{d}\rho\, \rho J_0\left(\frac{2\pi r\rho}{\lambda z}\right) g_R(\rho) = \left[k \equiv \frac{2\pi}{\lambda}\right] \\ &= -\mathrm{j}\frac{k}{2\pi z}\exp(\mathrm{j}kz)\exp\left(\mathrm{j}\frac{k}{2z}r^2\right) 2\pi \int_0^{\infty} \mathrm{d}\rho\, \rho J_0\left(\frac{kr\rho}{z}\right) g_R(\rho) \\ &= -\mathrm{j}\frac{k}{2\pi z}\exp(\mathrm{j}kz)\exp\left(\mathrm{j}\frac{k}{2z}r^2\right) H_0\{g_R(\rho)\}(kr/2\pi z). \end{aligned} \tag{H.6}$$

In this case, the computational complexity of the FHT reduces to $\mathcal{O}(N_r^2)$, which is considerably better than using the FFT.

Bibliography

Agostini, Pierre, F. Fabre, G. Mainfray, Guillaume Petite, and N. K. Rahman (1979). 'Free-Free Transitions Following Six-Photon Ionization of Xenon Atoms'. *Physical Review Letters* **42**.17, pp. 1127–1130. DOI: 10.1103/physrevlett.42.1127.

Alon, Ofir E., Vitali Averbukh, and Nimrod Moiseyev (1998). 'Selection Rules for the High Harmonic Generation Spectra'. *Physical Review Letters* **80**.17, pp. 3743–3746. DOI: 10.1103/physrevlett.80.3743.

Alvermann, A, H Fehske, and P B Littlewood (2012). 'Numerical time propagation of quantum systems in radiation fields'. *New Journal of Physics* **14**.10, p. 105008. DOI: 10.1088/1367-2630/14/10/105008.

Ammosov, Maxim V, Nikolai B Delone, and Vladimir P Kraĭnov (1986). 'Tunnel ionization of complex atoms and of atomic ions in alternating electromagnetic field'. *Soviet Physics—Journal of Experimental and Theoretical Physics* **64**, pp. 1191–1194.

Anderson, E., Z. Bai, C. Bischof, S. Blackford, J. Demmel, J. Dongarra, J. Du Croz, A. Greenbaum, S. Hammarling, A. McKenney, and D. Sorensen (1999). *LAPACK Users' Guide*. Third. Philadelphia, PA: Society for Industrial and Applied Mathematics. ISBN: 0-89871-447-8.

Bartschat, Klaus (1996). *Computational atomic physics : electron and positron collisions with atoms and ions*. Berlin New York: Springer. ISBN: 978-3-642-64655-3.

Bellini, Marco, Claire Lyngå, A. Tozzi, Mette B Gaarde, Theodor Wolfgang Hänsch, Anne L'Huillier, and Claes-Göran Wahlström (1998). 'Temporal Coherence of Ultrashort High-Order Harmonic Pulses'. *Physical Review Letters* **81**.2, pp. 297–300. DOI: 10.1103/physrevlett.81.297.

Ben-Tal, Nir, Nimrod Moiseyev, and A Beswick (1993). 'The effect of Hamiltonian symmetry on generation of odd and even harmonics'. *Journal of Physics B: Atomic, Molecular and Optical Physics* **26**.18, p. 3017. DOI: 10.1088/0953-4075/26/18/012.

Bezanson, Jeff, Alan Edelman, Stefan Karpinski, and Viral B. Shah (2014). 'Julia: A Fresh Approach to Numerical Computing'. eprint: 1411.1607.

Blanes, S., F. Casas, J.A. Oteo, and J. Ros (2009). 'The Magnus expansion and some of its applications'. *Physics Reports* **470**.5-6, pp. 151–238. DOI: 10.1016/j.physrep.2008.11.001.

Bohr, Niels (1913a). 'I. On the constitution of atoms and molecules'. *Philosophical Magazine Series 6* **26**.151, pp. 1–25. DOI: 10.1080/14786441308634955.

— (1913b). 'II. On the constitution of atoms and molecules'. *Philosophical Magazine Series 6* **26**.153, pp. 476–502. DOI: 10.1080/14786441308634993.

— (1913c). 'III. On the constitution of atoms and molecules'. *Philosophical Magazine Series 6* **26**.155, pp. 857–875. DOI: 10.1080/14786441308635031.

Burnett, Neal H, C Kan, and Paul Bruce Corkum (1995). 'Ellipticity and polarization effects in harmonic generation in ionizing neon'. *Physical Review A* **51**.5, R3418. DOI: 10.1103/physreva.51.r3418.

Carlström, Stefanos, Johan Mauritsson, Kenneth Joseph Schafer, Anne L'Huillier, and Mathieu Gisselbrecht (2017). *Quantum coherence in photo-ionization with tailored XUV pulses*.

Carlström, Stefanos, Jana Preclíková, Eleonora Lorek, Esben Witting Larsen, Christoph Michael Heyl, David Paleček, Donatas Zigmantas, Kenneth Joseph Schafer, Mette B Gaarde, and Johan Mauritsson (2016). 'Spatially and spectrally resolved quantum path interference with chirped driving pulses'. *New Journal of Physics* **18**.12, p. 123032. DOI: 10.1088/1367-2630/aa511f.

Cooley, James W. and John W. Tukey (1965). 'An algorithm for the machine calculation of complex Fourier series'. *Mathematics of Computation* **19**, pp. 297–301. DOI: 10.1090/s0025-5718-1965-0178586-1.

Cooper, John W. (1962). 'Photoionization from Outer Atomic Subshells. A Model Study'. *Physical Review* **128**.2, pp. 681–693. DOI: 10.1103/physrev.128.681.

Corkum, Paul Bruce (1993). 'Plasma perspective on strong field multiphoton ionization'. *Physical Review Letters* **71**.13, pp. 1994–1997. DOI: 10.1103/physrevlett.71.1994.

Cowan, Robert (1981). *The theory of atomic structure and spectra*. Berkeley: University of California Press. ISBN: 0520038215.

Dasch, Cameron J. (1992). 'One-dimensional tomography: a comparison of Abel, onion-peeling, and filtered backprojection methods'. *Applied Optics* **31**.8, p. 1146. DOI: 10.1364/ao.31.001146.

Debye, Peter Joseph William (1909). 'Näherungsformeln für die Zylinderfunktionen für große Werte des Arguments und unbeschränkt veränderliche Werte des Index'. *Mathematische Annalen* **67**.4, pp. 535–558. DOI: 10.1007/bf01450097.

Delone, Nikolai B and Vladimir P Kraĭnov (1991). 'Energy and angular electron spectra for the tunnel ionization of atoms by strong low-frequency radiation'. *Journal of the Optical Society of America B* **8**.6, p. 1207. DOI: 10.1364/josab.8.001207.

Dirac, Paul Adrien Maurice (1939). 'A new notation for quantum mechanics'. *Mathematical Proceedings of the Cambridge Philosophical Society* **35**.03, p. 416. DOI: 10.1017/s0305004100021162.

Dongarra, Jack J., Jeremy Du Croz, Sven Hammarling, and I. S. Duff (1990). 'A set of level 3 basic linear algebra subprograms'. *ACM Transactions on Mathematical Software* **16**.1, pp. 1–17. DOI: 10.1145/77626.79170.

Dongarra, Jack J., Jeremy Du Croz, Sven Hammarling, and Richard J. Hanson (1988). 'An extended set of FORTRAN basic linear algebra subprograms'. *ACM Transactions on Mathematical Software* **14**.1, pp. 1–17. DOI: 10.1145/42288.42291.

Dubrouil, A., O. Hort, F. Catoire, D. Descamps, S. Petit, E. Mével, Vasily V Strelkov, and E. Constant (2014). 'Spatio–spectral structures in high-order harmonic beams generated with Terawatt 10-fs pulses'. *Nature Communications* **5**. DOI: 10.1038/ncomms5637.

Ehrenfest, Paul (1927). 'Bemerkung über die angenäherte Gültigkeit der klassischen Mechanik innerhalb der Quantenmechanik'. *Zeitschrift für Physik* **45**.7, pp. 455–457. DOI: 10.1007/bf01329203.

Eichmann, H, A Egbert, S Nolte, C Momma, B Wellegehausen, W Becker, S Long, and JK McIver (1995). 'Polarization-dependent high-order two-color mixing'. *Physical Review A* **51**.5, R3414. DOI: 10.1103/physreva.51.r3414.

Eppink, André T. J. B. and David H. Parker (1997). 'Velocity map imaging of ions and electrons using electrostatic lenses: Application in photoelectron and photofragment ion imaging of molecular oxygen'. *Review of Scientific Instruments* **68**.9, p. 3477. DOI: 10.1063/1.1148310.

Fano, Ugo (1935). 'Sullo spettro di assorbimento dei gas nobili presso il limite dello spettro d'arco'. *Il Nuovo Cimento* **12**.3, pp. 154–161. DOI: 10.1007/bf02958288.

— (1961). 'Effects of Configuration Interaction on Intensities and Phase Shifts'. *Physical Review* **124** (6), pp. 1866–1878. DOI: 10.1103/physrev.124.1866.

Farrell, J. P., L. S. Spector, B. K. McFarland, P. H. Bucksbaum, M. Gühr, M. B. Gaarde, and K. J. Schafer (2011). 'Influence of phase matching on the Cooper minimum in Ar high-order harmonic spectra'. *Physical Review A* **83**.2. DOI: 10.1103/physreva.83.023420.

Feist, J, S Nagele, R Pazourek, E Persson, BI Schneider, LA Collins, and J Burgdörfer (2008). 'Nonsequential two-photon double ionization of helium'. *Physical Review A* 77.4, p. 043420. URL: http://pra.aps.org/abstract/PRA/v77/i4/e043420.

Ferray, M, Anne L'Huillier, X F Li, L A Lompré, G Mainfray, and C Manus (1988). 'Multiple-harmonic conversion of 1064 nm radiation in rare gases'. *Journal of Physics B: Atomic, Molecular and Optical Physics* **21**.3, pp. L31–L35. DOI: 10.1088/0953-4075/21/3/001.

Feynman, Richard (1965). *Quantum mechanics and path integrals*. New York: McGraw-Hill. ISBN: 0-07-020650-3.

Fock, Vladimir (1930). 'Näherungsmethode zur Lösung des quantenmechanischen Mehrkörperproblems'. *Zeitschrift für Physik* **61**.1-2, pp. 126–148. DOI: 10.1007/bf01340294.

Franken, Peter A, Alan E Hill, CW Peters, and G Weinreich (1961). 'Generation of optical harmonics'. *Physical Review Letters* 7.4, p. 118. DOI: 10.1103/physrevlett.7.118.

Frigo, Matteo (1999). 'A fast Fourier transform compiler'. English. *ACM SIGPLAN Notices* **34**.5, 169–180. DOI: 10.1145/301631.301661.

Froese Fischer, Charlotte (1970). 'A multi-configuration Hartree–Fock program'. *Computer Physics Communications* **1**.3, pp. 151–166. DOI: 10.1016/0010-4655(70)90002-0.

Froese Fischer, Charlotte, Tomas Brage, and Per Jönsson (1997). *Computational atomic structure : an MCHF approach*. Bristol, UK Philadelphia, Penn: Institute of Physics Publ. ISBN: 0-7503-0466-9.

Froese Fischer, Charlotte, Georgio Tachiev, Gediminas Gaigalas, and Michel R. Godefroid (2007). 'An MCHF atomic-structure package for large-scale calculations'. *Computer Physics Communications* **176**.8, pp. 559–579. DOI: 10.1016/j.cpc.2007.01.006.

Fu, Yan-Zhuo, Song-Feng Zhao, and Xiao-Xin Zhou (2012). 'Multiphoton and tunneling ionization of atoms in an intense laser field'. *Chinese Physics B* **21**.11, p. 113101. DOI: 10.1088/1674-1056/21/11/113101.

Gabor, Dennis (1946). 'Theory of communication. Part 1: The analysis of information'. *Journal of the Institution of Electrical Engineers-Part III: Radio and Communication Engineering* **93**.26, pp. 429–441. DOI: 10.1049/ji-3-2.1946.0074.

Gauss, Carl Friedrich (1866). 'Nachlass: Theoria interpolationis methodo nova tractata'. In: *Werke*. Vol. 3. Königliche Gesellschaft der Wissenschaften, Göttingen, pp. 265–330. URL: https://archive.org/stream/werkecarlf03gausrich#page/n277/mode/2up.

Goodman, Joseph (1996). *Introduction to Fourier optics*. New York: McGraw-Hill. ISBN: 0071142576.

Goulielmakis, Eleftherios, Zhi-Heng Loh, Adrian Wirth, Robin Santra, Nina Rohringer, Vladislav S. Yakovlev, Sergey Zherebtsov, Thomas Pfeifer, Abdallah M. Azzeer, Matthias F. Kling, Stephen R. Leone, and Ferenc Krausz (2010). 'Real-time observation of valence electron motion'. *Nature* **466**.7307, pp. 739–743. DOI: 10.1038/nature09212.

Guizar-Sicairos, Manuel and Julio César Gutiérrez-Vega (2004). 'Computation of quasi-discrete Hankel transforms of integer order for propagating optical wave fields'. *Journal of the Optical Society of America A* **21**.1, p. 53. DOI: 10.1364/josaa.21.000053.

Guo, Chen, Anne Harth, Stefanos Carlström, Yu-Chen Cheng, Sara Mikaelsson, Erik Mårsell, Arthur Losquin, Miguel Miranda, Kenneth Joseph Schafer, Anders Mikkelsen, Johan Mauritsson, Cord Louis Arnold, and Anne L'Huillier (2017). *Dispersion control of attosecond pulse trains*.

Hartree, Douglas Rayner (1928). 'The Wave Mechanics of an Atom with a Non-Coulomb Central Field. Part I. Theory and Methods'. *Mathematical Proceedings of the Cambridge Philosophical Society* **24**.01, p. 89. DOI: 10.1017/s0305004100011919.

Häßler, Stefan (2009). 'Generation of Attosecond Pulses in Atoms and Molecules'. PhD thesis. Université Paris-Sud XI and Commissariat à l'Energie Atomique, Saclay. URL: http://tel.archives-ouvertes.fr/tel-00440190/fr.

Heyl, Christoph Michael, Samuel Nils Bengtsson, Stefanos Carlström, Johan Mauritsson, Cord Louis Arnold, and Anne L'Huillier (2014). 'Noncollinear optical gating'. *New Journal of Physics* **16**.5, p. 052001. DOI: 10.1088/1367-2630/16/5/052001.

Hickstein, Daniel D., Franklin J. Dollar, Patrik Grychtol, Jennifer L. Ellis, Ronny Knut, Carlos Hernández-Garcıa, Dmitriy Zusin, Christian Gentry, Justin M. Shaw, Tingting Fan, Kevin M. Dorney, Andreas Becker, Agnieszka Jaroń-Becker, Henry C. Kapteyn, Margaret M. Murnane, and Charles G. Durfee (2015). 'Non-collinear generation of angularly isolated circularly polarized high harmonics'. *Nature Photonics* **9**.11, pp. 743–750. DOI: 10.1038/nphoton.2015.181.

Hilbert, David, John von Neumann, and Lothar Nordheim (1928). 'Über die Grundlagen der Quantenmechanik'. *Mathematische Annalen* **98**.1, pp. 1–30. DOI: 10.1007/bf01451579.

Hostetter, James A, Jennifer L Tate, Kenneth Joseph Schafer, and Mette B Gaarde (2010). 'Semiclassical approaches to below-threshold harmonics'. *Physical Review A* **82**.2, p. 023401. DOI: 10.1103/physreva.82.023401.

Ivanov, Misha Yu., Thomas Brabec, and Neal H Burnett (1996). 'Coulomb corrections and polarization effects in high-intensity high-harmonic emission'. *Physical Review A* **54**.1, p. 742. DOI: 10.1103/physreva.54.742.

Ivanov, Misha Yu. and Olga Smirnova (2014). 'Ionization in strong low-frequency fields: from quantum *S*-matrix to classical pictures'. In: ed. by Thomas Schultz and Marc Vrakking. Wiley-VCH. Chap. 6, pp. 179–200.

Ivanov, Misha Yu., Michael Spanner, and Olga Smirnova (2005). 'Anatomy of strong field ionization'. *Journal of Modern Optics* **52**.2-3, pp. 165–184. DOI: 10.1080/09500340420002753 60.

Jönsson, Per, Gediminas Gaigalas, Jacek Bieroń, Charlotte Froese Fischer, and Ian P. Grant (2013). 'New version: Grasp2K relativistic atomic structure package'. *Computer Physics Communications* **184**.9, pp. 2197–2203. DOI: 10.1016/j.cpc.2013.02.016.

Jönsson, Per, X. He, Charlotte Froese Fischer, and Ian P. Grant (2007). 'The Grasp2K relativistic atomic structure package'. *Computer Physics Communications* **177**.7, pp. 597–622. DOI: 10.1016/j.cpc.2007.06.002.

Keldysh, Leonid Veniaminovich (1965). 'Ionization in the Field of a Strong Electromagnetic Wave'. *Journal of Experimental and Theoretical Physics* **20**.5. Received: May 23, 1964, p. 1307.

Kim, I Jong, Chul Min Kim, Hyung Taek Kim, Gae Hwang Lee, Yong Soo Lee, Ju Yun Park, David Jaeyun Cho, and Chang Hee Nam (2005). 'Highly Efficient High-Harmonic Generation in an Orthogonally Polarized Two-Color Laser Field'. *Physical Review Letters* **94**.24. DOI: 10.1103/physrevlett.94.243901.

Krause, Jeffrey L., Kenneth Joseph Schafer, and Kenneth C Kulander (1992). 'High-order harmonic generation from atoms and ions in the high intensity regime'. *Physical Review Letters* **68**.24, pp. 3535–3538. DOI: 10.1103/physrevlett.68.3535.

Kreibich, Thomas, Manfred Lein, Volker Engel, and E. K. U. Gross (2001). 'Even-Harmonic Generation due to Beyond-Born-Oppenheimer Dynamics'. *Physical Review Letters* **87**.10. DOI: 10.1103/physrevlett.87.103901.

Krylov, Aleksey Nikolaevich (1931). 'О численном решении уравнения, которым в технических вопросах определяются частоты малых колебаний материальных систем'. *Известия Академии наук СССР. VII серия. Отделение математических и естественных наук* 4, pp. 491–539. URL: http://mi.mathnet.ru/izv5215.

Kulander, Kenneth C and T.N. Rescigno (1991). 'Effective potentials for time-dependent calculations of multiphoton processes in atoms'. *Computer Physics Communications* **63**.1-3, pp. 523–528. DOI: 10.1016/0010-4655(91)90273-n.

Lanczos, Cornelius (1950). 'An Iteration Method for the Solution of the Eigenvalue Problem of Linear Differential and Integral Operators'. *Journal of Research of the National Bureau of Standards* **45**.4, pp. 255–282.

Landau, Lev Davidovich and Evgeny Mikhailovich Lifshitz (1977). *Quantum mechanics : non-relativistic theory*. 3rd. Vol. 3. Course of Theoretical Physics. Oxford New York: Pergamon Press. ISBN: 978-0-08-020940-1.

Laplace, Pierre-Simon de (1774). 'Mémoires de Mathématique et de Physique, Tome Sixième'. In: Académie Royale des Sciences. Chap. Mémoire sur la probabilité des causes par les évènemans, pp. 621–656.

Larsen, Esben Witting, Stefanos Carlström, Eleonora Lorek, Christoph Michael Heyl, David Paleček, Kenneth Joseph Schafer, Anne L'Huillier, Donatas Zigmantas, and Johan Mauritsson (2016). 'Sub-cycle ionization dynamics revealed by trajectory resolved, elliptically-driven high-order harmonic generation'. *Scientific Reports* **6**, p. 39006. DOI: 10.1038/srep39006.

Lawson, C. L., R. J. Hanson, D. R. Kincaid, and F. T. Krogh (1979). 'Basic Linear Algebra Subprograms for Fortran Usage'. *ACM Transactions on Mathematical Software* **5**.3, pp. 308–323. DOI: 10.1145/355841.355847.

Lewenstein, Maciej, Philippe Balcou, Misha Yu. Ivanov, Anne L'Huillier, and Paul Bruce Corkum (1994). 'Theory of high-harmonic generation by low-frequency laser fields'. *Physical Review A* **49**.3, p. 2117. DOI: 10.1103/physreva.49.2117.

Lindgren, Ingvar (1986). *Atomic many-body theory*. Berlin New York: Springer-Verlag. ISBN: 978-3-540-16649-8.

Lissajous, Jules Antoine (1857). 'Mémoire sur l'Etude optique des mouvements vibratoires'. In: *Annales de chimie et de physique*. Vol. 51. 3rd series, pp. 147–232.

Louisy, Maïté, Cord Louis Arnold, Miguel Miranda, Esben Witting Larsen, Samuel Nils Bengtsson, David Kroon, Marija Kotur, Diego Guénot, Linnea Rading, Piotr Rudawski, Fernando Brizuela, Filippo Campi, Byunghoon Kim, Amélie Jarnac, Aurélien Houard, Johan Mauritsson, Per Johnsson, Anne L'Huillier, and Christoph Michael Heyl (2015). 'Gating attosecond pulses in a noncollinear geometry'. *Optica* **2**.6, p. 563. DOI: 10.1364/optica.2.000563.

Magnus, Wilhelm (1954). 'On the exponential solution of differential equations for a linear operator'. *Communications on Pure and Applied Mathematics* 7.4, pp. 649–673. DOI: 10.1002/cpa.3160070404.

Manschwetus, Bastian, Linnea Rading, Filippo Campi, Sylvain Maclot, Hélène Coudert-Alteirac, Jan Lahl, Hampus Wikmark, Piotr Rudawski, Christoph Michael Heyl, Balasz Farkas, Tarek Mohamed, Anne L'Huillier, and Per Johnsson (2016). 'Two-photon double ionization of neon using an intense attosecond pulse train'. *Physical Review A* **93**.6. DOI: 10.1103/physreva.93.061402.

Marchuk, Gurij Ivanovich (1968). 'Some application of splitting-up methods to the solution of mathematical physics problems'. eng. *Aplikace matematiky* **13**.2, pp. 103–132. URL: http://eudml.org/doc/14518.

Mauritsson, Johan, Jan Marcus Dahlström, Erik Mansten, and Thomas Fordell (2009). 'Sub-cycle control of attosecond pulse generation using two-colour laser fields'. *Journal of Physics B: Atomic, Molecular and Optical Physics* **42**.13, p. 134003. DOI: 10.1088/0953-4075/42/13/134003.

Mauritsson, Johan, Per Johnsson, Erik Gustafsson, Anne L'Huillier, Kenneth Joseph Schafer, and Mette B Gaarde (2006). 'Attosecond pulse trains generated using two color laser fields'. *Physical Review Letters* **97**.1, p. 013001. DOI: 10.1103/physrevlett.97.013001.

McPherson, A., G. Gibson, H. Jara, U. Johann, T. S. Luk, I. A. McIntyre, K. Boyer, and C. K. Rhodes (1987). 'Studies of multiphoton production of vacuum-ultraviolet radiation in the rare gases'. *Journal of the Optical Society of America B* **4**.4, p. 595. DOI: 10.1364/josab.4.000595.

Miranda, Miguel, Cord Louis Arnold, Thomas Fordell, Francisco Silva, Benjamín Alonso, Rosa Weigand, Anne L'Huillier, and Helder Crespo (2012). 'Characterization of broadband few-cycle laser pulses with the d-scan technique'. *Optics Express* **20**.17, pp. 18732–18743. DOI: 10.1364/oe.20.018732.

Möller, Max, Yan Cheng, Sabih D. Khan, Baozhen Zhao, Kun Zhao, Michael Chini, Gerhard G. Paulus, and Zenghu Chang (2012). 'Dependence of high-order-harmonic-generation yield on driving-laser ellipticity'. *Physical Review A* **86**.1, p. 011401. DOI: 10.1103/physreva.86.011401.

Nickolls, John, Ian Buck, Michael Garland, and Kevin Skadron (2008). 'Scalable parallel programming with CUDA'. *Queue* **6**.2, p. 40. DOI: 10.1145/1365490.1365500.

Nyquist, H (1928). 'Certain Topics in Telegraph Transmission Theory'. *Transactions of the American Institute of Electrical Engineers* **47**.2, pp. 617–644. DOI: 10.1109/5.989875.

Oron, Dan, Yaron Silberberg, Nirit Dudovich, and David M. Villeneuve (2005). 'Efficient polarization gating of high-order harmonic generation by polarization-shaped ultrashort pulses'. *Physical Review A* **72**.6. DOI: 10.1103/physreva.72.063816.

Padé, Henri (1892). 'Sur la représentation approchée d'une fonction par des fractions rationnelles'. fre. *Annales scientifiques de l'École Normale Supérieure* **9**, pp. 3–93. URL: http://eudml.org/doc/81047.

Paulus, Gerhard G., W. Becker, and H. Walther (1995). 'Classical rescattering effects in two-color above-threshold ionization'. *Physical Review A* **52**.5, pp. 4043–4053. DOI: 10.1103/physreva.52.4043.

Perelomov, AM and VS Popov (1967). 'Ionization of atoms in an alternating electric field: III'. *Soviet Physics—Journal of Experimental and Theoretical Physics* **25**.2.

Perelomov, AM, VS Popov, and MV Terent'ev (1966). 'Ionization of atoms in an alternating electric field'. *Soviet Physics—Journal of Experimental and Theoretical Physics* **23**.5, pp. 924–934.

— (1967). 'Ionization of atoms in an alternating electric field: II'. *Soviet Physics—Journal of Experimental and Theoretical Physics* **24**.1, pp. 207–217.

Perry, Michael D and John K Crane (1993). 'High-order harmonic emission from mixed fields'. *Physical Review A* **48**.6, R4051. DOI: 10.1103/physreva.48.r4051.

Petersson, Carl Leon Michael, Stefanos Carlström, Kenneth Joseph Schafer, and Johan Mauritsson (2016). 'Phase metrology with multi-cycle two-colour pulses'. *Journal of Physics B: Atomic, Molecular and Optical Physics* **49**.9, p. 095002. DOI: 10.1088/0953-4075/49/9/095002.

Racah, Giulio (1942). 'Theory of Complex Spectra. II'. *Physical Review* **62**.9-10, pp. 438–462. DOI: 10.1103/physrev.62.438.

Raedt, Hans De (1987). 'Product formula algorithms for solving the time dependent Schrödinger equation'. *Computer Physics Reports* **7**.1, pp. 1–72. DOI: 10.1016/0167-7977(87)90002-5.

Regge, T. (1958). 'Symmetry properties of Clebsch-Gordon's coefficients'. *Il Nuovo Cimento* **10**.3, pp. 544–545. DOI: 10.1007/bf02859841.

Richardson, John L. (1991). 'Visualizing quantum scattering on the CM-2 supercomputer'. *Computer Physics Communications* **63**.1-3, pp. 84–94. DOI: 10.1016/0010-4655(91)90240-l.

Rudawski, Piotr, Anne Harth, Chen Guo, Eleonora Lorek, Miguel Miranda, Christoph Michael Heyl, Esben Witting Larsen, Jan Ahrens, Oliver Prochnow, Thomas Binhammer, Uwe Morgner, Johan Mauritsson, Anne L'Huillier, and Cord Louis Arnold (2015). 'Carrier-envelope phase dependent high-order harmonic generation with a high-repetition rate OPCPA-system'. *European Physics Journal D* **69**.3. DOI: 10.1140/epjd/e2015-50568-y.

Saad, Yousef (1992). 'Analysis of some Krylov subspace approximations'. *SIAM Journal on Numerical Analysis*.

— (2003). *Iterative Methods for Sparse Linear Systems*. Society for Industrial & Applied Mathematics (SIAM). DOI: 10.1137/1.9780898718003.

Salières, Pascal, Bertrand Carré, Laurent Le Déroff, Felix Grasbon, Gerhard G. Paulus, Herbert Walther, Richard Kopold, Wilhelm Becker, Dejan B. Milošević, Anna Sanpera, and Maciej Lewenstein (2001). 'Feynman's Path-Integral Approach for Intense-Laser-Atom Interactions'. *Science* **292**.5518, pp. 902–905. DOI: 10.1126/science.108836.

Samson, J.A.R. and W.C. Stolte (2002). 'Precision measurements of the total photoionization cross-sections of He, Ne, Ar, Kr, and Xe'. *Journal of Electron Spectroscopy and Related Phenomena* **123**.2-3, pp. 265–276. DOI: 10.1016/s0368-2048(02)00026-9.

Sanpera, A., Per Jönsson, J. B. Watson, and K. Burnett (1995). 'Harmonic generation beyond the saturation intensity in helium'. *Physical Review A* **51**.4, pp. 3148–3153. DOI: 10.1103/physreva.51.3148.

Schafer, Kenneth Joseph (2009). 'Numerical Methods in Strong Field Physics'. In: ed. by Thomas Brabec. Vol. Strong Field Laser Physics. Springer, pp. 111–145. ISBN: 978-0-387-40077-8. DOI: 10.1007/978-0-387-34755-4_6.

Schafer, Kenneth Joseph, Mette B Gaarde, Kenneth C Kulander, B. Sheehy, and Lou F. DiMauro (2000). 'Calculations of strong field multiphoton processes in alkali metal atoms'. *AIP Conference Proceedings* **525**.1. Ed. by Kenneth Kulander, Louis DiMauro, and Richard R. Freeman, pp. 45–58. DOI: 10.1063/1.1291925.

Schafer, Kenneth Joseph, Baorui Yang, Lou F. DiMauro, and Kenneth C Kulander (1993). 'Above threshold ionization beyond the high harmonic cutoff'. *Physical Review Letters* 70.11, pp. 1599–1602. DOI: 10.1103/physrevlett.70.1599.

Schrödinger, Erwin (1926). 'An Undulatory Theory of the Mechanics of Atoms and Molecules'. *Physical Review* **28**.6, pp. 1049–1070. DOI: 10.1103/physrev.28.1049.

Shannon, Claude Elwood (1949). 'Communication in the presence of noise'. *Proceedings of the IRE* **37**.1, pp. 10–21. DOI: 10.1109/jrproc.1949.232969.

Sola, IJ, E Mével, L Elouga, E Constant, Vasily V Strelkov, L Poletto, P Villoresi, E Benedetti, J-P Caumes, S Stagira, et al. (2006). 'Controlling attosecond electron dynamics by phase-stabilized polarization gating'. *Nature Physics* **2**.5, pp. 319–322.

Stevens, Walter J., Morris Krauss, Harold Basch, and Paul G. Jasien (1992). 'Relativistic compact effective potentials and efficient, shared-exponent basis sets for the third-, fourth-, and fifth-row atoms'. *Canadian Journal of Chemistry* 70.2, pp. 612–630. DOI: 10.1139/v92-085.

Strang, Gilbert (1968). 'On the Construction and Comparison of Difference Schemes'. *SIAM Journal on Numerical Analysis* **5**.3, pp. 506–517. DOI: 10.1137/0705041.

Strelkov, Vasily V (2006). 'Theory of high-order harmonic generation and attosecond pulse emission by a low-frequency elliptically polarized laser field'. *Physical Review A* **74**.1, p. 013405. DOI: 10.1103/physreva.74.013405.

Strelkov, Vasily V, A. A. Gonoskov, I. A. Gonoskov, and M. Yu. Ryabikin (2011). 'Origin for Ellipticity of High-Order Harmonics Generated in Atomic Gases and the Sublaser-Cycle Evolution of Harmonic Polarization'. *Physical Review Letters* **107**.4. DOI: 10.1103/physrevlett.107.043902.

Strelkov, Vasily V, M. A. Khokhlova, A. A. Gonoskov, I. A. Gonoskov, and M. Yu. Ryabikin (2012). 'High-order harmonic generation by atoms in an elliptically polarized laser field: Harmonic polarization properties and laser threshold ellipticity'. *Physical Review A* **86**.1. Quantum path selection, wavelet. DOI: 10.1103/physreva.86.013404.

Topcu, Turker and Francis Robicheaux (2012). 'Dichotomy between tunneling and multiphoton ionization in atomic photoionization: Keldysh parameter γ versus scaled frequency Ω'. *Physical Review A* **86**.5. DOI: 10.1103/physreva.86.053407.

Varjú, Katalin, Yann Mairesse, Pierre Agostini, P. Breger, B. Carré, L. J. Frasinski, E. Gustafsson, Per Johnsson, Johan Mauritsson, H. Merdji, and et al. (2005a). 'Reconstruction of Attosecond Pulse Trains Using an Adiabatic Phase Expansion'. *Physical Review Letters* **95**.24. DOI: 10.1103/physrevlett.95.243901.

Varjú, Katalin, Yann Mairesse, B Carré, Mette B Gaarde, Per Johnsson, S Kazamias, R López-Martens, Johan Mauritsson, Kenneth Joseph Schafer, Philippe Balcou, et al. (2005b). 'Frequency chirp of harmonic and attosecond pulses'. *Journal of Modern Optics* **52**.2-3, pp. 379–394. DOI: 10.1080/09500340412331301542.

Vincenti, Henri and Fabien Quéré (2012). 'Attosecond Lighthouses: How To Use Spatiotemporally Coupled Light Fields To Generate Isolated Attosecond Pulses'. *Physical Review Letters* **108**.11. DOI: 10.1103/physrevlett.108.113904.

Vrakking, Marc J. J. (2001). 'An iterative procedure for the inversion of two-dimensional ion/photoelectron imaging experiments'. *Review of Scientific Instruments* **72**.11, p. 4084. DOI: 10.1063/1.1406923.

Weihe, F. A., S. K. Dutta, G. Korn, D. Du, P. H. Bucksbaum, and P. L. Shkolnikov (1995). 'Polarization of high-intensity high-harmonic generation'. *Physical Review A* **51**.5, R3433–R3436. DOI: 10.1103/physreva.51.r3433.

Wittmann, T, B Horvath, W Helml, MG Schätzel, X Gu, AL Cavalieri, Gerhard G. Paulus, and Reinhard Kienberger (2009). 'Single-shot carrier–envelope phase measurement of few-cycle laser pulses'. *Nature Physics* **5**.5, pp. 357–362. DOI: 10.1038/nphys1250.

Wörner, Hans Jakob, Hiromichi Niikura, Julien B. Bertrand, P. B. Corkum, and D. M. Villeneuve (2009). 'Observation of Electronic Structure Minima in High-Harmonic Generation'. *Physical Review Letters* **102**.10. DOI: 10.1103/physrevlett.102.103901.

Yost, Dylan C., Thomas R. Schibli, Jun Ye, Jennifer L. Tate, James Hostetter, Mette B Gaarde, and Kenneth Joseph Schafer (2009). 'Vacuum-ultraviolet frequency combs from below-threshold harmonics'. *Nature Physics* **5**.11, pp. 815–820. DOI: 10.1038/nphys1398.

Zatsarinny, Oleg (2006). 'BSR: B-spline atomic R-matrix codes'. *Computer Physics Communications* **174**.4, pp. 273–356. DOI: 10.1016/j.cpc.2005.10.006.

Zatsarinny, Oleg and Charlotte Froese Fischer (2009). 'Atomic structure calculations using MCHF and BSR'. *Computer Physics Communications* **180**.11, pp. 2041–2065. DOI: 10.1016/j.cpc.2009.06.007.

Zhao, Song-Feng, Lu Liu, and Xiao-Xin Zhou (2014). 'Multiphoton and tunneling ionization probability of atoms and molecules in an intense laser field'. *Optics Communications* **313**, pp. 74–79. DOI: 10.1016/j.optcom.2013.09.074.

Index

Ein Buch ohne Index ist kein Buch.

Theodor Mommsen, 1817–1903

Papers

Comments on Publications

I 'Noncollinear optical gating'
Christoph Michael Heyl, Samuel Nils Bengtsson, Stefanos Carlström, Johan Mauritsson, Cord Louis Arnold, and Anne L'Huillier
New Journal of Physics **16**(5) 052001 (2014)
A novel way of angularly separating the emission of subsequent high-order harmonic pulses to achieve single-attosecond pulses instead of attosecond pulse trains. The generation is driven by two non-collinearly overlapping driving pulses that together form a rotating interference in the generation medium. I partook in the initial discussions of the concept, the mathematical modelling, and writing of the manuscript.

II 'Phase metrology with multi-cycle two-colour pulses'
Carl Leon Michael Petersson, Stefanos Carlström, Kenneth Joseph Schafer, and Johan Mauritsson
Journal of Physics B: Atomic, Molecular and Optical Physics **49**(9) 095002 (2016)
A theoretical study of an extension to the phase measurement technique by Wittmann et al. (2009) for ultrashort pulses to two-colour, long driving fields. I wrote the code that was used to perform the calculations involved, I supervised Leon Petersson in performing them, helped interpreting the results, and writing the manuscript.

III 'Sub-cycle ionization dynamics revealed by trajectory resolved, elliptically-driven high-order harmonic generation'
Esben Witting Larsen, Stefanos Carlström, Eleonora Lorek, Christoph Michael Heyl, David Paleček, Kenneth Joseph Schafer, Anne L'Huillier, Donatas Zigmantas, and Johan Mauritsson
Scientific Reports **6** 39006 (2016)
A detailed experimental and theoretical characterization of the ellipticity response of high-order harmonic generation, in a trajectory-resolved fashion. I helped build the setup and perform the experiments. I helped in the analysis of the experimental data and performed the semi-classical modelling of the threshold ellipticity. I wrote major parts of the manuscript.

IV 'Spatially and spectrally resolved quantum path interference with chirped driving pulses'
Stefanos Carlström, Jana Preclíková, Eleonora Lorek, Esben Witting Larsen, Christoph Michael Heyl, David Paleček, Donatas Zigmantas, Kenneth Joseph Schafer, Mette B Gaarde, and Johan Mauritsson
Accepted for publication in: *New Journal of Physics*
The effects of quantum path interference on high-order harmonic generation are the topic of this paper, the dipole phase parameters which quantify the single-atom response are extracted from the observed interferograms. I helped build the setup and perform the experiments. I helped in the analysis of the experimental data and performed the quantum mechanical calculations for the quantum path analysis of the short–long trajectory interference, as well as developing the model for the long–long trajectory interference. I wrote major parts of the manuscript.

V 'Dispersion control of attosecond pulse trains'
Chen Guo, Anne Harth, Stefanos Carlström, Yu-Chen Cheng, Sara Mikaelsson, Erik Mårsell, Arthur Losquin, Miguel Miranda, Kenneth Joseph Schafer, Anders Mikkelsen, Johan Mauritsson, Cord Louis Arnold, and Anne L'Huillier
Manuscript in preparation
Through a dispersion, a host of phenomena in high-order harmonic generation are revealed and studied in detail. I performed time-dependent Schrödinger equation calculations of high-order harmonic generation, to compare with the experimental results, as well as partaking in the discussion of the observed phenomena.

VI 'Quantum coherence in photo-ionization with tailored XUV pulses'
Stefanos Carlström, Johan Mauritsson, Kenneth Joseph Schafer, Anne L'Huillier, and Mathieu Gisselbrecht
Manuscript in preparation
A theoretical concept for inducing and controlling the coherence between residual nionic substates in photoionization, using interaction fields of arbitrarily long durations is presented. Mathieu Gisselbrecht presented me with the exciting idea of studying hole coherence in the residual ion in photoionization, after which I researched the methodological framework necessary, the tools, performed the calculations, partook in the interpretation, and wrote major parts of the manuscript.

I

Noncollinear optical gating

Christoph Michael Heyl, Samuel Nils Bengtsson, Stefanos Carlström, Johan Mauritsson, Cord Louis Arnold, and Anne L'Huillier

New Journal of Physics
16(5) 052001 (2014)

New Journal of Physics
The open access journal at the forefront of physics
Deutsche Physikalische Gesellschaft DPG | IOP Institute of Physics

Fast Track Communication

Noncollinear optical gating

C M Heyl, S N Bengtsson, S Carlström, J Mauritsson, C L Arnold and A L'Huillier

Department of Physics, Lund University, PO Box 118, SE-22100 Lund, Sweden
E-mail: christoph.heyl@fysik.lth.se

Received 25 April 2014
Accepted for publication 7 May 2014
Published 23 May 2014
New Journal of Physics **16** (2014) 052001
doi:10.1088/1367-2630/16/5/052001

Abstract

We present a novel scheme for high-order harmonic generation, enabling the production of spatially separated isolated attosecond pulses. This can be achieved by driving the generation process with two identical, but temporally delayed laser pulses, which are noncollinearly overlapping in the generation medium. Our approach provides intense attosecond pulses directly separated from the fundamental field, which is left undistorted. The method is therefore ideally suited for pump-probe studies in the extreme ultraviolet regime and promises new advances for intra-cavity attosecond pulse generation. We present a theoretical description of noncollinear optical gating, with an analytical derivation and simulations using the strong field approximation.

Keywords: isolated attosecond pulses, high harmonic generation, attosecond physics, extreme nonlinear optics

1. Introduction

The generation of single attosecond pulses (SAPs) via high-order harmonic generation (HHG) has enabled a multitude of experiments providing insight into attosecond dynamics in atoms [1], molecules [2] and solids [3]. While the generation of trains of attosecond pulses, i.e. high-order harmonics, does not present any technical difficulty with present ultrafast laser

technology, the generation of SAPs remains challenging, requiring carrier-envelope-phase (CEP)-stable few-cycle driving laser pulses and/or advanced gating methods to confine the extreme ultraviolet (XUV) emission to a single half-cycle of the driving field. Commonly-used techniques are based on manipulating the polarization state of the driving field [4, 5], utilizing a high laser intensity to rapidly deplete the nonlinear medium [6] or altering the shape of the driving field via multi-color field synthesis [7]. Vincenti and co-workers recently introduced a conceptually different technique [8], named attosecond lighthouse, utilizing spatio-temporal couplings to angularly streak the generated attosecond pulses. The technique was experimentally implemented both in gases [9] and using plasma mirrors [10].

Most gating techniques imply extensive manipulation of the fundamental field and require spectral filtering of the harmonic radiation, limiting the efficiency and restricting any further use of the laser pulse. Using the fundamental field after generation is of interest for pump-probe experiments and essential for intra-cavity HHG [11, 12], a promising scheme that enables the generation of attosecond pulses at unprecedented power levels and repetition rates, with applications in ultrahigh precision frequency metrology. While the generation of high-order harmonics inside a cavity has been experimentally demonstrated [11, 12], that of isolated attosecond pulses remains an unsolved challenge, requiring broadband enhancement cavities [13] and suitable gating methods [14].

Here, we introduce an efficient gating technique, noncollinear optical gating (NOG), based on driving the HHG process in a noncollinear geometry. Noncollinear HHG has recently been employed for several applications [18, 19], including *in situ* diagnostics of the generation process [20], and proposed as out-coupling method for intra-cavity HHG [21, 22]. Here, we present a new implementation of noncollinear HHG, which is used to generate angularly streaked attosecond pulse trains, thus providing an efficient gate for SAP generation. Two identical but time-delayed, noncollinearly overlapping laser pulses form a driving field with rotating wave fronts. Consecutive attosecond pulses are emitted in different directions, as illustrated in figure 1. The two driving laser pulses are left unperturbed[1] after generation and are spatially separated from the XUV radiation emitted at the bisector of the two driving field propagation angles. Thus, our method opens new possibilities for attosecond pump-probe experiments [15–17] as well as for frequency-comb spectroscopy studies in the XUV regime.

The article is organized as follows: the method is described in sections 2 and 3. Numerical simulations are presented in section 4. In section 5, we discuss the influence of macroscopic propagation effects. Finally, in section 6, we compare our gating scheme with the attosecond lighthouse technique.

2. Principle of the gating method

We consider two identical laser pulses, which are overlapped in time and superimposed noncollinearly with an angle 2γ at the focus, thus forming a spatial intensity grating in the focal plane [19]. The far-field angular distribution of the harmonics generated in such a geometry is determined by the interference of multiple sources. In general, the harmonics are emitted in different directions [23], and consequently the corresponding attosecond pulses are angularly distorted. The angular emission characteristics simplify considerably at small noncollinear

[1] Perturbations intrinsic to the HHG process, e.g. due to plasma formation as well as possible perturbations induced when splitting an initial laser pulse into two pulses might of course occur.

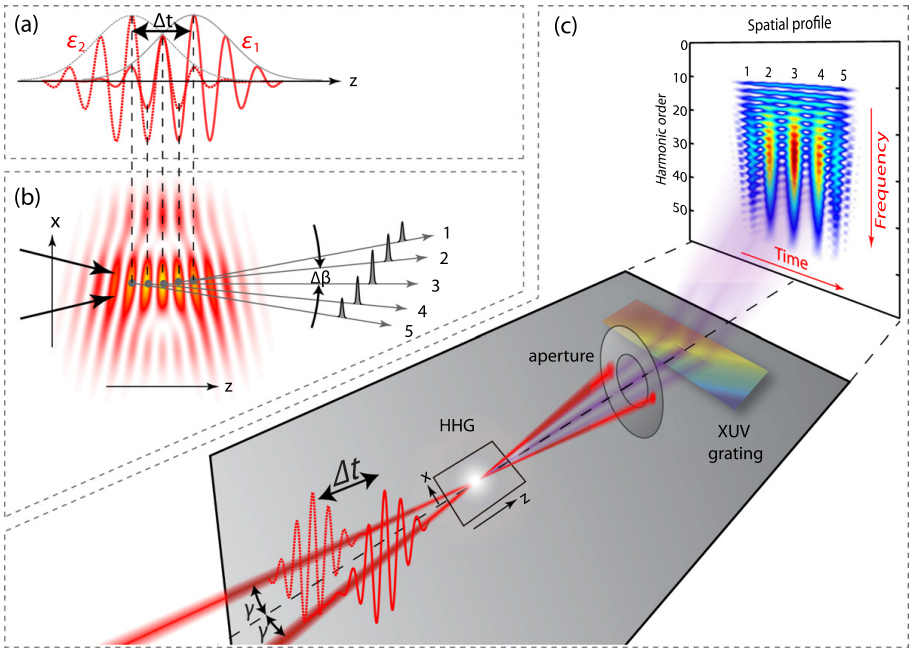

Figure 1. Principle of noncollinear optical gating. (a) A temporal delay between two few-cycle pulses leads to a rapidly changing amplitude ratio between subsequent half-cycles. (b) Overlapping these pulses noncollinearly causes a temporal rotation of the wavefronts (the figure displays $\Re(E)^2$ of the total field E). Attosecond pulses generated from subsequent half-cycles are therefore emitted in different directions. (c) Illustration of the experimental scheme: two noncollinearly overlapping driving pulses generate spatially separated isolated attosecond pulses in the angle sector between the fundamental propagation directions. The displayed spectrogram was calculated using a quasi-classical approach, considering a pulse duration and temporal delay of $2\,T$, where T is the field-cycle period. The observed continua, labelled 1–5, are characteristic of spatially separated attosecond pulses.

angle, when the intensity grating in the generation medium becomes a single maximum with weak satellites, as discussed in more detail below. In these conditions, the XUV emission follows the instantaneous direction of propagation of the total driving field (the z-axis in figure 1(c)), defined by the bisector of the two driving field propagation angles.

The wave front orientation in the focus of two noncollinearly overlapping laser fields with field envelope $\mathcal{E}_1$ and $\mathcal{E}_2$, propagating along the wavevectors $\mathbf{k}_1$ and $\mathbf{k}_2$ respectively, can be defined through the composite wavevector at the point of intersection:

$$\mathbf{k}_{\text{tot}} = \frac{(\mathcal{E}_1\mathbf{k}_1 + \mathcal{E}_2\mathbf{k}_2)}{\sqrt{\mathcal{E}_1^2 + \mathcal{E}_2^2}}. \tag{1}$$

By taking the scalar product $\hat{\mathbf{x}} \cdot \mathbf{k}_{\text{tot}} / \left|\mathbf{k}_{\text{tot}}\right| = -\sin(\beta)$, in which $\hat{\mathbf{x}}$ is the unit vector in lateral direction (see figure 1(b), (c)) and β is the angle between $\mathbf{k}_{\text{tot}}$ and the z-axis, we obtain for small γ:

$$\beta = \gamma \frac{1-\xi}{1+\xi}. \tag{2}$$

A variation of the amplitude ratio of the laser fields, $\xi = \mathcal{E}_2/\mathcal{E}_1$, results in a macroscopic tilt of the wave fronts and a change in the emission direction β. The introduction of a temporal delay Δt between two driving laser pulses leads to an amplitude ratio that changes rapidly from one half-cycle to the next (figure 1(a)), defining a unique orientation angle of the corresponding wave fronts as a function of time. The consequence is an ultrafast wave front rotation (WFR) in the focus (figure 1(b)), with attosecond pulses emitted in different directions [8]. The emission of XUV light is thus angularly streaked, mapping time into spatial position in the far-field [9]. A conventional imaging-XUV spectrometer displaying the spatially resolved spectral profile will therefore provide a spectrogram of the generated attosecond pulse train, i.e. frequency versus time, as illustrated in figure 1(c). The time-to-space mapping is defined through equation (2) where ξ varies with time depending on the envelope and separation of the driving fields. Considering two Gaussian laser pulses with $\mathcal{E}_{1,2} = \exp\left[-2\ln(2)\left(t \pm \Delta t/2\right)^2/\tau^2\right]$ and pulse duration τ (FWHM), we can deduce the emission angle as a function of time. The time-to-space mapping is approximately linear around $t = 0$, i.e. at the temporal center of the total driving field, where maximum WFR speed is achieved, with

$$\beta(t) = 2\ln(2)\gamma\frac{\Delta t}{\tau^2}\, t. \tag{3}$$

In the temporal wings of the pulses, the WFR speed is reduced. The direction of the time axis itself is determined by the sign of the temporal delay, i.e. the order of the driving pulses. The WFR velocity increases linearly with Δt. Choosing $\Delta t \approx \tau$ ensures that the total field intensity does not exhibit a local minimum at $t = 0$.

3. Angular separation of the attosecond pulses

In order to isolate attosecond pulses emitted from subsequent half-cycles, the angle difference $\Delta\beta \approx \beta(T/2)$ has to be larger than the divergence angle of a SAP. We define this angle as $\Theta_q = W_q(z)/z$, with $W_q(z)$ denoting the beam radius in the far field at a distance z from the focus for a beam with central frequency $q\omega$. To estimate Θ_q, we consider the intensity grating of the fundamental field in the focal plane with a Gaussian envelope at the beam waist and radius W_0. All spatial beam widths are defined at $1/e^2$ of the intensity profile. For small γ, the intensity distribution in the focal plane can be written as:

$$I(x, z=0) \propto \cos^2\left[kx\sin(\gamma)\right]\exp\left(-\frac{2x^2}{W_0^2}\right). \tag{4}$$

In order to avoid interference effects due to multiple harmonic sources formed by the interference grating in the focus, we consider a degenerated grating with only one central maximum at $x = 0$ and weak satellites. Limiting the intensity of the first satellites to $1/e^2$ of the

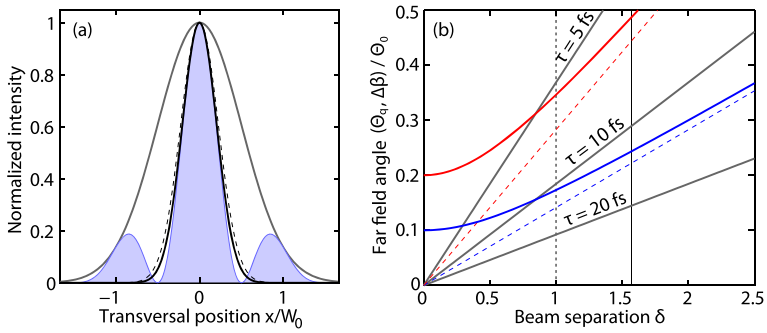

Figure 2. Intensity grating and gating condition. (a) Fundamental intensity distribution at $z = 0$ for $\gamma = \gamma_{opt}$ together with its Gaussian approximations considering (black solid line) and neglecting (black dashed line) the influence of the spatial envelope (gray solid line). (b) Θ_q, for $\eta = 5$ (solid red line) and $\eta = 10$ (solid blue line) together with their asymptotic approximations (dashed red and blue lines), plotted as a function of δ; the solid gray lines indicate $\Delta\beta$ for different pulse lengths, considering a central wavelength of 800 nm. Both Θ_q and $\Delta\beta$ are normalized to the divergence Θ_0. We also indicate the minimum δ which allows a direct separation of fundamental and SAP (dashed vertical line) and the maximum δ ($=\pi/2$) for which the statellite peaks can be neglected and for which gating can be achieved (solid vertical line).

central maximum implies that γ must be smaller than $\gamma_{opt} = \lambda/2W_0$ with λ denoting the carrier wavelength. Using Gaussian optics, we have $W_0 = f\lambda/(\pi W_f)$, where f is the focal length and W_f the beam radius before focusing. Defining $2x_0$ as the center-to-center separation of the two generation beams before focusing and $\delta = x_0/W_f$, the required intensity grating is obtained when $\delta \leqslant \pi/2$.

For small γ, the cosine^2-intensity distribution caused by the beam interference can be approximated with a Gaussian function, $I(x, z = 0) \propto \exp(-2x^2/W_\gamma^2)$, with $W_\gamma^2 = 1/[k^2\gamma^2/2 + 1/W_0^2]$, as illustrated in figure 2(a). With the scaling relation $\Theta_q \propto 1/W_\gamma$, this leads to an expression for the divergence angle $\Theta_q = \Theta_q(\gamma)$ in units of $\Theta_q(0)$:

$$\frac{\Theta_q(\gamma)}{\Theta_q(0)} = \frac{W_0}{W_\gamma} = W_0\sqrt{\frac{k^2\gamma^2}{2} + \frac{1}{W_0^2}}\,. \tag{5}$$

In order to determine whether the condition for SAP emission $\Delta\beta > \Theta_q$ is satisfied, we look at the scaling of $\Delta\beta$ and Θ_q with increasing noncollinear angle, or equivalently beam separation δ (figure 2(b)). $\Delta\beta$ is plotted as a function of γ for three different pulse lengths while Θ_q is shown for two different values of the ratio between the fundamental and the attosecond pulse divergence $\eta = \Theta_0/\Theta_q(0)$. While $\Delta\beta$ increases linearly with γ, Θ_q follows a nonlinear scaling relation. The conditions for SAP generation improve with increasing γ until Θ_q approaches an asymptotic linear dependence. Figure 2(b) shows that efficient gating requires short driving pulses and collimated harmonic beams. For $\eta = 10$ and $\lambda = 800$ nm, gating is achieved for

$\tau \leqslant 10$ fs and $\delta \geqslant 1$, while if $\eta = 5$, gating needs pulses of the order of 5 fs or less and similarly $\delta \geqslant 1$. The gating conditions improve until $\delta \simeq \pi/2$, which corresponds to the maximum allowed noncollinear angle $\gamma = \gamma_{\mathrm{opt}}$. As an example, for $f = 0.5$ m and $W_f = 2$ mm we obtain $\gamma_{\mathrm{opt}} = 6.3$ mrad.

In summary, optimal conditions for SAP generation, which ensure minimized temporal satellite pulses as well as suppression of interference effects due to multiple sources in the focus, are obtained when the beam separation before focusing is approximately $\pi/2$ times the $1/e^2$-diameter of the intensity profile. This condition is valid for loose and tight focal geometries, since the NOG scheme does not depend on focusing as long as η remains the same (see figure 2). With decreasing focal length, W_0 decreases and the SAP divergence increases. However, $\Delta\beta$ increases accordingly, and identical temporal SAP characteristics are obtained.

For $\gamma \simeq \gamma_{\mathrm{opt}}$, the influence of the Gaussian envelope on the radial dimension of the harmonic source can be neglected, and the divergence can be approximated by its asympotic value

$$\Theta_q \approx \Theta_q(0) W_0 \frac{k\gamma}{\sqrt{2}} = \frac{\lambda k}{\pi\sqrt{2}\eta}\gamma = \frac{\sqrt{2}\gamma}{\eta}. \tag{6}$$

Using equation (3) this leads to a simple condition for the maximum pulse duration allowing an angular separation of the generated attosecond pulses:

$$\tau \leqslant \frac{\ln(2)}{\sqrt{2}}\frac{\eta\lambda}{c}, \tag{7}$$

c denoting the speed of light. If the above condition is fulfilled, the emission direction between consecutive SAPs changes by at least the divergence angle of the same pulses. This is equivalent to limiting the on-axis intensity of pre- and post pulses to $1/e^2$ of the main pulse. For $\lambda = 800$ nm, and $\eta = 10$, we obtain $\tau \leqslant 13$ fs.

The factor $1/\eta$ can also be interpreted as a lower limit for the angular divergence of the harmonic emission at frequency $\eta\omega$, defined in units of the fundamental beam divergence. Thus, equation (7) leads to an approximate limit for the low-energy cutoff $E_{\mathrm{low}} = \hbar\omega\eta$ of the generated spectral continua:

$$E_{\mathrm{low}} \approx \frac{\hbar\omega^2\tau}{\pi\sqrt{2}\ln(2)}, \tag{8}$$

the high-energy limit being determined by the fundamental intensity. Using the above parameters and considering $\tau = 5$ fs at $\lambda = 800$ nm and a peak intensity of 2×10^{14} W cm^{-2}, we have $E_{\mathrm{low}} = 5.9$ eV, leading to SAPs with up to 48 eV bandwidth if Ar is used for generation.

4. Simulations

We performed numerical calculations in order to simulate HHG in a noncollinear geometry. The single atom response was obtained by solving the time dependent Schrödinger equation within the strong field approximation [24], selecting the short trajectory contribution. The harmonic dipole response was calculated numerically on a finite temporal grid for all points

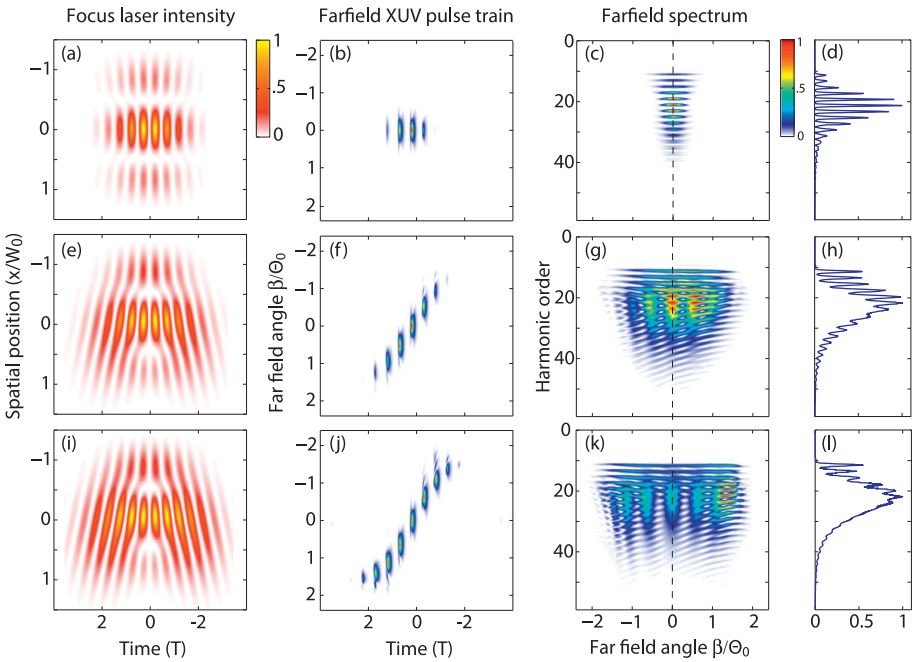

Figure 3. Simulations of noncollinear optical gating. Normalized spatio-temporal distribution $\Re(E)^2$ of the fundamental field interference pattern in the focus (first column), far-field intensity distribution of the attosecond pulse trains (second column), spatially-resolved spectrum (third column) and spectrum at $\beta = 0$ (fourth column) for three different cases: $\Delta t = 0$ (first row), $\Delta t = 2\,T = \tau$ (second row), and $\Delta t = 2.5\,T$ (third row).

along a one dimensional grid in the focal plane. The far-field emission was computed using Fraunhofer diffraction integrals. Propagation effects (see section 5) were not taken into account.

Figure 3 presents simulations of HHG in neon for two-cycle driving pulses ($\tau = 2\,T$), considering $\delta = \pi/2$. The first row (a) shows the focused laser field $\Re(E)^2$, the attosecond pulse train in the far field (b), the far field spectrum (c) and a spectral line-out at $\beta = 0$ (d) when the two pulses are superposed with no time delay at the focus. The far-field intensity distribution is shown as a function of the propagation angle β, normalized to the divergence of the focused fundamental laser pulses. The generated attosecond pulse train includes approximately four pulses, which interfere in the far field, leading to a discrete HHG spectrum. The second and third rows present the same quantities for temporally-delayed driving pulses, with $\Delta t = 2\,T = \tau$ and $\Delta t = 2.5\,T$ respectively. The WFR ((e) and (i)) induced by the temporal separation streaks the attosecond pulses angularly as shown in (f) and (j). With increasing temporal delay, the discrete spectrum becomes a characteristic XUV spectrogram with discrete harmonic peaks at low energies and spectral continua towards the high-energy cut-off. The spatially overlapping contributions from consecutive attosecond pulses interfere, leading to a fringe pattern between

the spectral continua. The slope of the interference fringes, which increases with energy, reflects the harmonic dipole phase variation with driving field intensity [25].

A variation of the CEP ϕ_{CE} of the driving fields moves the wavefronts in time and leads to a spatial shift of the corresponding XUV spectrogram [9, 10], providing direct access to the CEP of the driving laser field. For the simulations presented in figure 3, ϕ_{CE} was chosen in order to emit a SAP at $\beta = 0$. Changing ϕ_{CE} by $\pi/2$ leads to the emission of two pulses at $\beta \approx \pm\Delta\beta/2$, thus providing two synchronized but spatially separated SAPs, of interest for attosecond-pump-attosecond-probe studies.

A variation of the relative phase between the two driving fields moves the fundamental intensity grating across the focal plane. A zero relative phase at the point of intersection ensures a central intensity maxima at $x = 0$, as shown in figure 3 (first column) while a phase shift of π leads to two intensity maxima in the focal plane and a phase singularity at $x = z = 0$ [26]. In the latter case, interference effects between the two harmonic sources in the focus lead to angularly distorted attosecond pulses, thus preventing efficient gating.

5. Propagation effects

Propagation effects in the nonlinear medium can be described in a similar way as for a collinear geometry. The noncollinear geometry adds a geometrical component to the total wavevector missmatch between fundamental beam and generated XUV field with central frequency $q\omega$ [19]. In the focus, the geometrical wave vector mismatch can be taken into account by replacing the component arising from the Gouy phase shift for one beam $\Delta k_c^q \approx -q/z_0$ (z_0 denotes the Rayleigh length) by:

$$\Delta k_{nc}^{q} = \Delta k_c^{q}\left(1 + \frac{\pi^2}{4} - \frac{\lambda\pi}{8z_0}\right). \tag{9}$$

The second term in equation (9) can be attributed to the noncollinear geometry considering plane waves (equivalent to the Gouy phase shift of a Gaussian beam with an initial beam radius of $W_f\pi/2$), the last term is caused by the of off-axis components of the Gouy phase shift.

Δk_{nc}^{q} is equivalent to the wave vector mismatch for a collinear geometry with tighter focusing, which does not imply a lower conversion efficiency if the generation parameter are selected adequately [27]. As for collinear HHG, phase matching can be achieved by minimizing the total wave vector mismatch, i.e. adjusting gas pressure, medium length and laser intensity [28]. Our numerical simulations confirm the robustness of the NOG scheme even for a long medium, which is consistent with the findings presented in the supplementary information of [9] for the case of the lighthouse technique (see section 6).

6. Comparison with the attosecond lighthouse

Finally, we compare NOG with the attosecond lighthouse technique [8]. Both methods are based on WFR of the fundamental field, introducing an angular streaking effect. In the lighthouse configuration, WFR is achieved by focusing an angularly chirped laser pulse while an ultrafast amplitude modulation induces a rotating wave front in the NOG scheme. The lighthouse can also be seen as the continuous analog of NOG. The two techniques are compared

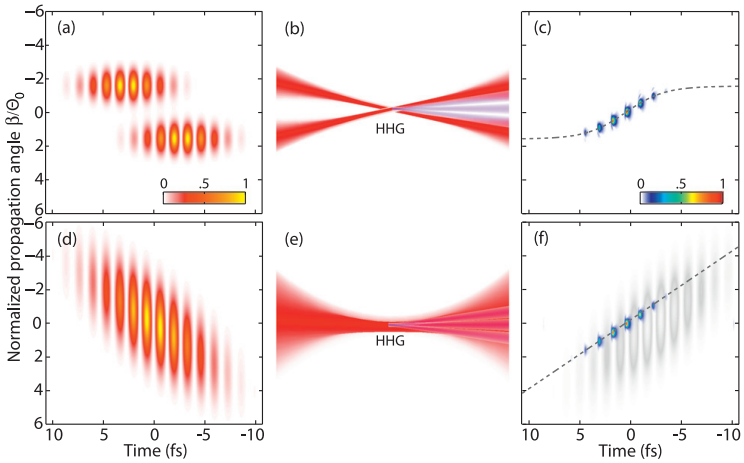

Figure 4. Comparison between NOG (a)–(c) and lighthouse (d)–(f). Normalized spatio-temporal field distribution $\Re(E)^2$ of the generation field before focusing (a), (d), focusing scheme (b), (e) and generated XUV intensity distribution (c), (f) at a focal length distance behind the focus. In order to achieve comparable spatio-temporal XUV pulse characteristics we consider $\Delta t = \tau$ for NOG, a beam radius before focusing that is factor of 3.7 larger for the lighthouse scheme than for NOG and laser pulses that have the same spectral bandwidth, corresponding to $\tau = 2\,T$. The dashed lines in (c), (f) indicate the time-to-space mapping.

in figure 4 for a two-cycle fundamental pulse and maximum WFR speed for the lighthouse scheme. Figures 4(a) and (d) show the spatio-temporal representation of the driving field distribution before focusing, while (c) and (f) present the angularly streaked attosecond pulse train in the far field together with the driving field after generation (in gray). Considering $\Delta t = \tau$ for the NOG scheme, both methods lead to angularly streaked attosecond pulse trains with very similar spatio-temporal characteristics and identical streaking efficiency at $t = 0$. Interestingly, the NOG scheme allows even faster WFR for $\Delta t > \tau$ (figure 2, third row) and thus a better spatial separation of the generated attosecond pulses while the WFR speed is limited in the lighthouse scheme [8]. Another important difference emerges for the fundamental field characteristics after generation. In the lighthouse scheme the fundamental field is chirped and distributed over the angle sector in which attosecond pulses are emitted. In the NOG scheme, two, nearly transform limited fundamental pulses (see footnote 1), leave the interaction process after generation and isolated attosecond pulses are emitted in the angle sector between the two driving fields.

7. Conclusion and outlook

In conclusion, we have introduced a new method for streaking attosecond pulse trains, which gives access to multiple, perfectly synchronized SAPs. NOG constitutes the first gating scheme that allows a direct spatial separation of fundamental driving field and generated attosecond pulses. It is therefore ideally suited for attosecond-pump-attosecond-probe studies, which

require high pulse energies. Finally, NOG can be applied to intracavity HHG, leading to the generation of isolated attosecond pulses at unprecedented average power levels and MHz repetition rates, promising advances in XUV-frequency-comb spectroscopy.

Acknowledgments

This research was supported by the Marie Curie program ATTOFEL (ITN), the European Research Council (ALMA, PALP), the Swedish Research Council, the Swedish Foundation for Strategic Research and the Knut and Alice Wallenberg Foundation.

References

[1] Goulielmakis E *et al* 2010 Real-time observation of valence electron motion *Nature* **466** 739
[2] Sansone G *et al* 2010 Electron localization following attosecond molecular photoionization *Nature* **465** 763
[3] Cavalieri A *et al* 2007 Attosecond spectroscopy in condensed matter *Nature* **449** 1029
[4] Sola I *et al* 2006 Controlling attosecond electron dynamics by phase-stabilized polarization gating *Nat. Phys.* **2** 319
[5] Sansone G *et al* 2006 Isolated single-cycle attosecond pulses *Science* **314** 443
[6] Ferrari F *et al* 2010 High-energy isolated attosecond pulses generated by above-saturation few-cycle fields *Nat. Photonics* **4** 875
[7] Wirth A *et al* 2011 Synthesized light transients *Science* **334** 195
[8] Vincenti H and Quéré F 2012 Attosecond lighthouses: how to use spatiotemporally coupled light fields to generate isolated attosecond pulses *Phys. Rev. Lett.* **108**
[9] Kim K *et al* 2013 Photonic streaking of attosecond pulse trains *Nat. Photonics* **7** 651
[10] Wheeler J *et al* 2012 Attosecond lighthouses from plasma mirrors *Nat. Photonics* **6** 829
[11] Cingöz A *et al* 2012 Direct frequency comb spectroscopy in the extreme ultraviolet *Nature* **482** 68
[12] Gohle C *et al* 2005 A frequency comb in the extreme ultraviolet *Nature* **436** 234
[13] Pupeza I *et al* 2013 Compact high-repetition-rate source of coherent 100 eV radiation *Nat. Photonics* **7** 608
[14] Pupeza I *et al* 2014 Cavity-enhanced high-harmonic generation with spatially tailored driving fields *Phys. Rev. Lett.* **112** 103902
[15] Tzallas P *et al* 2011 Extreme-ultraviolet pump-probe studies of one-femtosecond-scale electron dynamics *Nat. Phys.* **7** 781
[16] See reviews on attosecond photonics in *Nature Photonics*, March 2014
[17] Nabekawa Y *et al* 2009 Interferometry of attosecond pulse trains in the extreme ultraviolet wavelength region *Phys. Rev. Lett.* **102** 213904
[18] Daboussi S *et al* 2013 Double pulse quasi-collinear high harmonic generation scheme as a tool for x-ray laser plasma gain probing *Appl. Phys.* B **111** 7
[19] Heyl C M *et al* 2014 Macroscopic effects in noncollinear high-order harmonic generation *Phys. Rev. Lett.* **112** 143902
[20] Kim K *et al* 2013 Manipulation of quantum paths for space-time characterization of attosecond pulses *Nat. Phys.* **9** 159
[21] Wu J and Zeng H 2007 Cavity-enhanced noncollinear high-harmonic generation for extreme ultraviolet frequency combs *Opt. Lett.* **32** 3315
[22] Ozawa A *et al* 2008 Non-collinear high harmonic generation: a promising outcoupling method for cavity-assisted XUV generation *Opt. Express* **16** 6233

[23] Bertrand J *et al* 2011 Ultrahigh-orderwave mixing in noncollinear high harmonic generation *Phys. Rev. Lett.* **106** 023001
[24] Lewenstein M *et al* 1994 Theory of high-harmonic generation by low-frequency laser fields *Phys. Rev.* A **49** 2117
[25] Varjú K *et al* 2005 Frequency chirp of harmonic and attosecond pulses *J. Mod. Opt.* **52** 379
[26] Nye J and Berry M V 1974 Dislocations in wave trains *Proc. R. Soc. London* **336** 165
[27] Heyl C M, Güdde J, L'Huillier A and Höfer U 2012 High-order harmonic generation with μJ laser pulses at high repetition rates *J. Phys. B: At. Mol. Opt. Phys.* **45** 074020
[28] Gaarde M, Tate J and Schafer K 2008 Macroscopic aspects of attosecond pulse generation *J. Phys. B: At. Mol. Opt. Phys.* **41** 132001

New Journal of Physics
The open access journal at the forefront of physics
Deutsche Physikalische Gesellschaft DPG | IOP Institute of Physics

Corrigendum: Noncollinear optical gating (2014 *New J. Phys.* 16 052001)

C M Heyl, S N Bengtsson, S Carlström, J Mauritsson, C L Arnold and A L'Huillier

Department of Physics, Lund University, P. O. Box 118, SE-22100 Lund, Sweden
E-mail: christoph.heyl@fysik.lth.se

Received 20 August 2014
Accepted for publication 20 August 2014
Published 28 October 2014
New Journal of Physics **16** (2014) 109501
doi:10.1088/1367-2630/16/10/109501

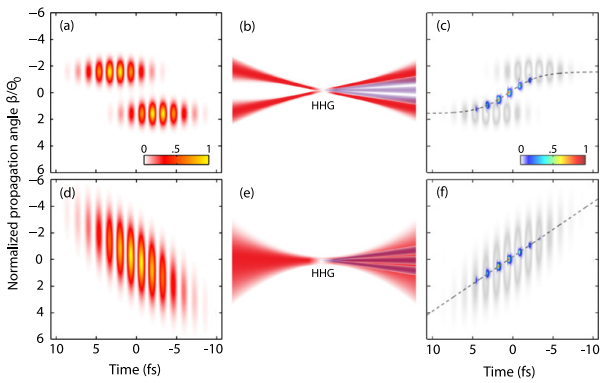

Figure 1. Comparison between NOG (a)–(c) and lighthouse (d)–(f). Normalized spatio-temporal field distribution $\Re(E)^2$ of the generation field before focusing (a), (d), focusing scheme (b), (e) and generated XUV intensity distribution together with the fundamental field (grayscale) at a focal length distance behind the focus (c), (f). In order to achieve comparable spatio-temporal XUV pulse characteristics we consider $\Delta t = \tau$ for NOG, a beam radius before focusing that is a factor of 3.7 larger for the lighthouse scheme than for NOG and laser pulses that have the same spectral bandwidth, corresponding to $\tau = 2\,T$. The dashed lines in (c), (f) indicate the time-to-space mapping.

The original article was published on 23 May 2014 with a production error in figure 4. One layer of this figure was shifted (figure 4(f)) and another was missing completely (figure 4(c)), leading to incorrect timing information between the fundamental field and the generated XUV field. The corrected figure is shown as figure 1 in this corrigendum.

II

Phase metrology with multi-cycle two-colour pulses

Carl Leon Michael Petersson, Stefanos Carlström, Kenneth Joseph Schafer, and Johan Mauritsson

Journal of Physics B: Atomic, Molecular and Optical Physics
49(9) 095002 (2016)

J. Phys. B: At. Mol. Opt. Phys. **49** (2016) 095002 (7pp) doi:10.1088/0953-4075/49/9/095002

Phase metrology with multi-cycle two-colour pulses

C L M Petersson[1,2], S Carlström[1], K J Schafer[3] and J Mauritsson[1]

[1] Department of Physics, Lund University, PO Box 118, SE-22100 Lund, Sweden
[2] Departamento de Química, Modulo 13, Universidad Autónoma de Madrid, E-28049, Madrid, Spain
[3] Department of Physics and Astronomy, Louisiana State University, Baton Rouge, LA 70803, USA

E-mail: leon.petersson@uam.es

Received 15 November 2015, revised 10 March 2016
Accepted for publication 15 March 2016
Published 13 April 2016

Abstract

Strong-field phenomena driven by an intense infrared (IR) laser depend on during what part of the field cycle they are initiated. By changing the sub-cycle character of the laser electric field it is possible to control such phenomena. For long pulses, sub-cycle shaping of the field can be done by adding a relatively weak, second harmonic of the driving field to the pulse. Through constructive and destructive interference, the combination of strong and weak fields can be used to change the probability of a strong-field process being initiated at any given part of the cycle. In order to control sub-cycle phenomena with optimal accuracy, it is necessary to know the phase difference of the strong and the weak fields precisely. If the weaker field is an even harmonic of the driving field, electrons ionized by the field will be asymmetrically distributed between the positive and negative directions of the combined fields. Information about the asymmetry can yield information about the phase difference. A technique to measure asymmetry for few-cycle pulses, called stereo-ATI (above threshold ionization), has been developed by Paulus *et al* (2003 *Phys. Rev. Lett.* **91** 253004). This paper outlines an extension of this method to measure the phase difference between a strong IR and its second harmonic.

Keywords: attosecond physics, above-threshold ionization, phase metrology

(Some figures may appear in colour only in the online journal)

1. Introduction

Strong field processes such as high-order harmonic generation (HHG) and above threshold ionization (ATI) depend on the sub-cycle structure of the strong infrared (IR) field driving the process. By tailoring the sub-cycle structure of the field, one can control the processes. This can be done either by using very short laser pulses [1–3] or by mixing pulses with different colours [4–6]. HHG with few-cycle laser pulses has enabled the generation of isolated attosecond pulses [7] and in this case the process is controlled by changing the so-called carrier-envelope phase (CEP) [8–12]:

$$\boldsymbol{E}(t) = \boldsymbol{E}_0 f(t) \sin(\omega t + \phi_{\mathrm{CEP}}), \tag{1}$$

where $f(t)$ describes the envelope of the pulse with respect to which ϕ_{CEP} is measured.

The CEP relates the phase of the driving frequency to the envelope of the pulse and changing it may lead to the generation of one or two attosecond pulses if the duration is sufficiently short [13]. The rapid change of amplitude of a short pulse broadens the pulse frequency distribution and breaks the symmetrical distribution of electron paths between the positive and negative directions of the field [14, 15]. How this depends on the CEP is illustrated in figure 1.

For two-coloured, multi-cycle fields with commensurate frequencies, the total electric is given by

$$\boldsymbol{E}(t) = \boldsymbol{E}_1 \sin(\omega t) + \boldsymbol{E}_2 \sin(n\omega t + \phi), \tag{2}$$

where $\boldsymbol{E}_1$, $\boldsymbol{E}_2$ are the amplitudes of the fundamental frequency and its nth harmonic (in this letter, $n = 2$), respectively, and ϕ is the relative phase between the two fields. The CEP is neglected in (2), since it has a negligible effect on the symmetry for multi-cycle pulses. Changing the relative phase of the two-coloured field may for instance result in one or two pulses per cycle [16] (see figure 2). One would assume that maximizing the asymmetry would also maximize the

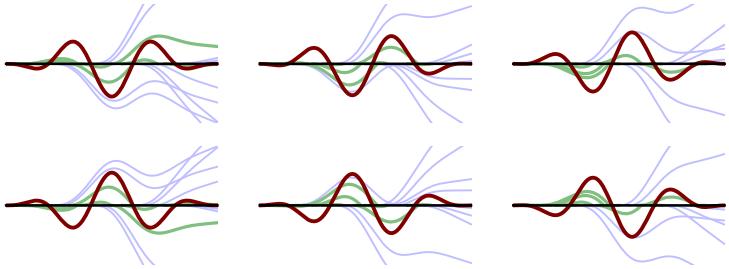

Figure 1. An illustration of the classical paths of electrons ionized by a few-cycle pulse, for six different CEPs. The green paths lead the electrons back to the atom, opening for the possibility of rescattering, whereas the blue paths guarantee direct ionization. The CEP of the driving field, shown in red, is changed by increments of $\frac{1}{3}\pi$ between each figure, giving phase difference of π between the two pictures in each column. Note the asymmetry between the rows.

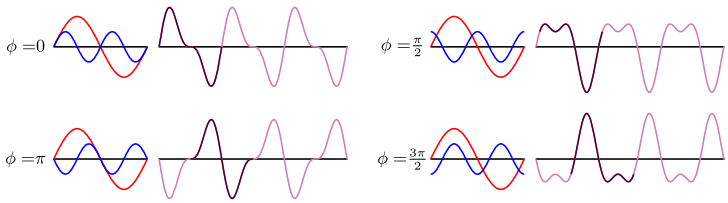

Figure 2. A constant-amplitude field is shown together with its weaker, second harmonic for four different values of ϕ. For each value of ϕ the driving field and its second harmonic are shown, in red and blue respectively, to the left, and their sum in purple to the right. To the right an interval corresponding to that in the left figure is shown in a darker colour.

harmonic yield, since the harmonic yield scales with the field maximum, which is maximized at biggest asymmetry—when the maxima of the two harmonics coincide. However, strong field approximation calculations showed [16] that there is a phase offset between maximum asymmetry and maximum harmonic yield. To truly understand and measure the impact of the sub-cycle structure, and enable the comparison between theory and experiment, the relative phase has to be measured independently from the process being studied and it has to be measured 'on target', where the harmonics are being generated.

For few-cycle pulses the phase is measured using a method known as stereo-ATI [17, 18]. In stereo-ATI the direction of the ionized electrons is measured and related to the CEP. In this letter we show that the stereo-ATI technique can be used to measure the relative phase of a two-coloured field with commensurate frequencies and also the relative strength of the two fields, since varying ϕ has an impact on the field structure very similar to that of the CEP on short pulses [4].

1.1. Multi-cycle pulses

For multi-cycle pulses, the asymmetry due to variations in amplitude is very small from half-cycle to half-cycle. By approximating the amplitude as constant, the path of a directly ionized electron, leaving the atom at time t_0, can be seen as depending on the instant of ionization. This also decides its final energy, which is the same as the energy of an electron leaving the atom one half-cycle later, but in the opposite direction so that they do not overlap. The classical paths of electrons ionized by a strong one-coloured field are shown in figure 3(a). In this figure, the blue lines correspond to directly ionized electrons, which may reach a maximum energy of $2U_\mathrm{p}$, where U_p is the ponderomotive energy given by

$$U_\mathrm{p} = \frac{q^2\,|\boldsymbol{E}|^2}{4\,m\omega^2}, \tag{3}$$

where q is the elementary charge, $|\boldsymbol{E}|$ the field amplitude, m the electron mass and ω the field frequency. The green lines, instead, correspond to electrons that return to the ion core, where they may rescatter. The maximum energy attainable for the rescattered electrons is reached by elastic scattering when the velocity is completely reversed [19]. In this way, the electron may reach final electron energies up to $10U_\mathrm{p}$. Figure 3(b) shows the energy of directly ionized electrons and the maximum classical energy of rescattered electrons as a function of ionization time.

The acceleration of the free electrons is proportional to the field strength, and when the second harmonic is much weaker than the driving field, the electron paths through the field are approximately the same as for the monochromatic

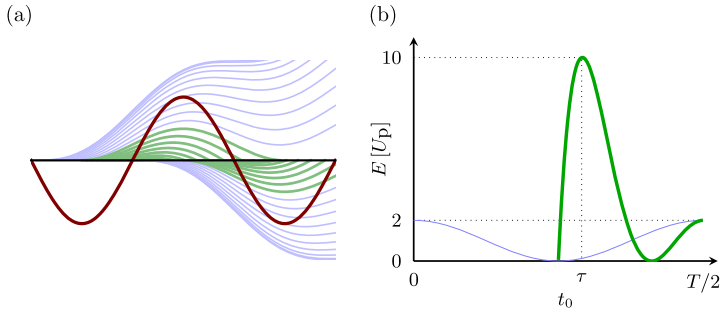

Figure 3. In (a), the classical paths of electrons ionized during one cycle of a laser field, shown in red, is displayed. Analogously to figure 1, the green paths lead back to the core, giving a possibility of rescattering, whereas the blue ensure direct ionization. In (b), the energy E of the directly ionized electrons is shown in blue, and the maximum classical energy of the rescattered electrons is shown in green, both as a function of the ionization time, t_0, over one half cycle of the field. Classically, electrons can only gain energies of $10U_\mathrm{p}$ if they are ionized at time τ.

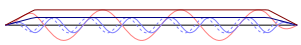

Figure 4. An illustration of how the pulses are simulated. The trapezoidal envelopes for the high- and low-frequency pulses are shown in dark blue and red, respectively. The relative intensity is exaggerated for illustrative purposes. In light red, the low-frequency pulse is shown; in light blue, the high-frequency pulse is shown as a continuous line for $\phi = 0$ and as a dashed line for $\phi = \frac{\pi}{4}$.

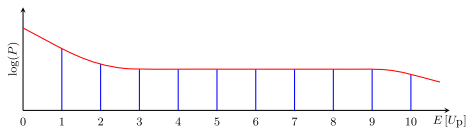

Figure 5. A simplified version of the general characteristics of an ATI spectrum is shown in red, and a division of $[0, 10U_\mathrm{p}]$ into ten sections, is shown in blue.

case [20, 21]. The nonlinear ionization probability, however, is significantly influenced by the second harmonic [6]. As the electron energy depends on the ionization time, the same principle that was used for short pulses can be utilized for the two-colour case [5, 22]. This paper outlines a method for measuring the phase difference between the first and second harmonic of a multi-cycle, two-coloured field, by studying the asymmetry of the ATI spectrum.

2. Numerical computations

The calculations were done using a newly developed version of the code described in [23], designed to run on graphical processing units. It solves the time-dependent Schrödinger equation in the single active electron approximation and a combined basis consisting of a radial grid and spherical harmonics.

Unless otherwise stated, the pulses were modeled using trapezoidal pulse envelopes. This is advantageous as the asymmetry due to the frequency mixing is present during a majority of the simulated pulse. To study the asymmetry for different ϕ, the CEP of the high-frequency wave was varied between pulses. Due to the relatively low intensity of the high-frequency pulse, changes to the asymmetry due to boundary effects caused by changing CEP are relatively small. The simulated pulse is illustrated in figure 4.

3. Theory

3.1. Asymmetry as a basis for phase metrology

The force, $\boldsymbol{F}$, on an electron in a two-colour laser field can for non-relativistic velocities be approximated as

$$\boldsymbol{F} = -q\boldsymbol{E}_\omega[\sin(\omega t) + \sqrt{I_\mathrm{rel}}\sin(2\omega t + \phi)], \tag{4}$$

where $\boldsymbol{E}_\omega$ is the envelope of the driving field, I_rel the relative intensity of the second harmonic, q the elementary charge, ω the driving field frequency. The carrier waves are shown for four different values of ϕ in figure 2.

In figure 5 a schematic ATI spectrum is shown in red. In the monochromatic case, there would be an approximate symmetry between the directions of the field. The addition of the second harmonic, however, breaks that symmetry.

The energy of the electrons depend on when during the half-cycle of the field they are ionized, as shown in the right of figure 3. This means that the energy distribution of electrons in the positive direction of the field, $P_+(E)$, will be different from that in the negative direction of the field, $P_-(E)$.

If $\sin(\omega t)$ and $\sin(2\omega t + \phi)$ constructively interfere at $t = t'$ they interfere destructively at $t = t' + \pi$. This is shown in figure 2. As a result, the parts of the sub-half cycle when the driving field is positive, for which there is constructive interference, are the same parts of the sub-half cycle when the driving field is negative, for which the interference is

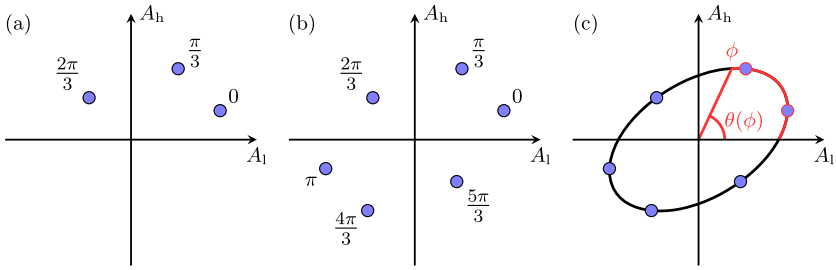

Figure 6. An illustration of the A_l–A_h plane. In (a), the representation of a two-colour pulse has been given for $\phi \in \left\{0, \frac{\pi}{2}, \frac{2\pi}{3}\right\}$. In (b), an extrapolation of the values in (a) based on symmetry can be seen. In (c), the ϕ-dependent angle θ is shown.

destructive, and vice versa. This will in turn mean that an overrepresentation, due to constructive interference, of electrons with energy E in one direction of the field will coincide with an underrepresentation, due to destructive interference, in the other.

In order to gain information about ϕ, the asymmetry between $P_+(E)$ and $P_-(E)$ can be studied. Analogously with [17, 18], the asymmetry of two energy ranges, ε_l and ε_h, of the ATI spectrum will be studied in this paper. The subscripts l and h will below be used to differentiate between the low and the high energy range.

To provide metrics for the respective asymmetries of ε_l and ε_h, $A_l = A(\varepsilon_l)$ and $A_h = A(\varepsilon_h)$ were used, where

$$A(\varepsilon) = \frac{\int_\varepsilon \mathrm{d}E\,[P_+(E) - P_-(E)]}{\int_\varepsilon \mathrm{d}E\,[P_+(E) + P_-(E)]} \tag{5}$$

is the asymmetry over an energy interval ε of the ATI spectrum.

For different values of ϕ, a two-colour pulse can be represented in the A_l–A_h plane. Figure 6(a) illustrates this for a hypothetical wave and $\phi \in \left\{0, \frac{\pi}{3}, \frac{2\pi}{3}\right\}$. As can be seen in figure 2, changing the value of ϕ by π completely inverts the asymmetry coming from the second harmonic. Because of this, figure 6(a) can be extrapolated to give the values in figure 6(b).

Denote the angular coordinate in the A_l–A_h plane θ. As is shown in figure 6(c), there exists for certain A_l–A_h representations a bijective mapping between ϕ and θ. By choosing ε_l and ε_h that result in such a mapping, it is possible to gain a measure of ϕ.

It interesting to note that neither $\phi \to A_l$ or $\phi \to A_h$ are injective, which can easily be seen in figure 6(c). As injectivity is a requirement for inversion, it would not be possible to determine a non-ambiguous measure of ϕ by observing the asymmetry of a single range of the ATI spectrum, which justifies the previous selection of two energy ranges.

3.2. Measurement of the absolute phase difference

The second harmonic gives rise to constructive and destructive interference during predetermined parts of each cycle. During experiments it is important to be certain of which data point in the A_l–A_h plane corresponds to which ϕ. However, even if the values of θ in the mapping

$$\theta(\phi) \in \left\{\theta(\phi_0), \theta\left(\phi_0 + \frac{2\pi}{N}\right), \cdots, \theta\left(\phi_0 - (N-1)\frac{2\pi}{N}\right)\right\} \tag{6}$$

have been ascertained for given ε_l and ε_h by changing ϕ in increments of $\frac{2\pi}{N}$, it can be risky to speculate on the value of ϕ_0.

One solution to this problem is found in the right-hand side of figure 3, which shows that there is only one ionization time per half-cycle, here called τ, for which electrons can classically obtain energies as high as $10U_p$. Due to quantum mechanical effects, it is possible for electrons with other ionization times to obtain equally high energies, but the probability of doing so is small for ionization times which notably differ from τ. Because of this, the highest asymmetry near $10U_p$ is observed when the peak of the second harmonic occur at τ. In other words, for some small δ, $A([10U_p - \delta, 10U_p + \delta])$ will be maximized when the peak of the second harmonic in the positive field direction occurs at τ. The peak of the second harmonic occurring at $\tau + \pi$, on the other hand, maximizes $-A([10U_p - \delta, 10U_p + \delta])$.

3.3. Selection of ε_l and ε_h

Because the asymmetries of ε_l and ε_h are measured to determine ϕ, it is important how the ATI spectrum is divided — the effect of the second harmonic on $P_+(E)$ and $P_-(E)$ is not equal for all E. To make the selection of ε_l and ε_h, $[0, 10U_p]$ was sectioned into 10 equally spaced sections, as illustrated in figure 5. The energy was cut at $10U_p$, because it is the highest energy the electrons can classically obtain [19], as illustrated in figure 3(b).

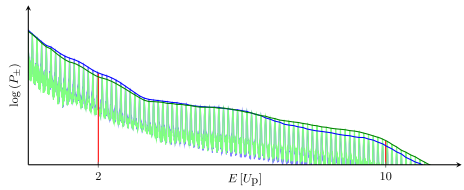

Figure 7. The ATI spectra in the positive and negative directions of a two-colour field, P_+ and P_-, shown In blue and green respectively. The peaks of the spectra are outlined in darker colours. The relative intensity of the pulse used to generate the spectrum was $I_{\mathrm{rel}} = 0.15$ and the phase difference was $\phi = \frac{\pi}{4}$.

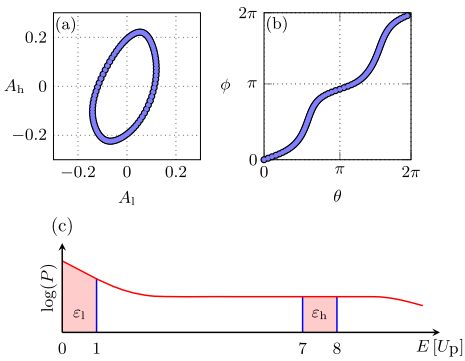

Figure 8. The A_{l}–A_{h} representation of a two-colour pulse is shown in (a). In (b), the corresponding θ–ϕ mapping is shown. The relative intensity was $I_{\mathrm{rel}} = 0.01$, and the energy ranges, $\varepsilon_{\mathrm{l}} = [0U_{\mathrm{p}}, U_{\mathrm{p}}]$ and $\varepsilon_{\mathrm{h}} = [7U_{\mathrm{p}}, 8U_{\mathrm{p}}]$, are shown in (c).

In the case of few-cycle pulses, directly ionized electrons are not asymmetrically distributed [17, 24]. The reason for this is that the asymmetry of a two-colour field can be much larger than that of a few-cycle pulse.

For every pulse, both ε_{l} and ε_{h} were generated from one or multiple neighbouring sections. The sections were chosen so that

$$\forall E_{\mathrm{l}} \in \varepsilon_{\mathrm{l}}, E_{\mathrm{h}} \in \varepsilon_{\mathrm{h}} : E_{\mathrm{l}} \leqslant E_{\mathrm{h}}. \tag{7}$$

A total of 495 A_{l}–A_{h} representations of the energy spectrum were generated, out of which the most useful ones were manually selected. For more information on how the energy spectrum was divided, see [25].

4. Results

In figure 7 P_+ and P_- for a two-colour pulse are shown. There is an asymmetry between the directions of the field, which can be seen by observing the peaks of the spectra. For high energies, P_+ is dominant, whereas P_- dominates for low energies. When ϕ is varied, the asymmetry of electrons with an energy of $10U_{\mathrm{p}}$ is largest when the peak of the second harmonic occurs slightly after τ.

Figure 8(a) shows the A_{l}–A_{h} representation of a two-colour pulse. In figure 8(b), the θ–ϕ mapping can be seen, where θ is defined as in figure 6(c). For the pulse and energy ranges selected in figure 8,

$$\left.\frac{\mathrm{d}\phi}{\mathrm{d}\theta}\right|_{\theta\in\{0,\pi\}} \ll \left.\frac{\mathrm{d}\phi}{\mathrm{d}\theta}\right|_{\theta\in\left\{\frac{\pi}{2},\frac{3\pi}{2}\right\}}, \tag{8}$$

giving a lower error e_ϕ of ϕ for a given error e_θ in θ when ϕ is close to 0 and π. If ϕ is close to $\frac{\pi}{2}$ or $\frac{3\pi}{2}$, another selection of energy ranges might be preferable.

A problem which might arise due to careless selection of the energy ranges is that $\theta(\phi)$ stops being bijective. This can be seen in figure 9(c), where neither $\phi(0)$ nor $\phi(\pi)$ are unique. This can always be circumvented by proper selection of energy ranges.

As illustrated in figure 9, where I_{rel} is increased exponentially between figures (a)–(c), the asymmetry increases with I_{rel}. This is to be expected, as the addition of the second harmonic is the cause of the asymmetry, and the radius of the A_{l}–A_{h} representation can be used to give information about the relative intensity. Note that the A_{l}–A_{h} representation can change shape as the relative intensity increases. In figure 9(c), the $\theta(\phi)$ has lost the bijectivity it had for the cases shown in figures 9(a) and (b).

The asymmetry caused by the second harmonic in the two-colour case can be compared to that caused by rapid change of amplitude during few-cycle pulses—changing the CEP affects the asymmetry of the short pulse just as changing ϕ affects the asymmetry of the two-colour field. The similarities of two-colour fields to short pulses can be seen in figure 10, where the A_{l}–A_{h} representation of two short pulses is shown. The pulse shown in figure 10(a) is of half the duration of the one in figure 10(b). It also has significantly higher asymmetry. For short pulses the rapid amplitude change is the cause of the asymmetry. As the amplitude gradient is greater for short pulses, the asymmetry is as well.

5. Conclusions

By adding the second harmonic to a strong field, it is possible to control the effects it has on matter. To control the effects to an as accurate degree as possible, it is important to know the phase difference, ϕ, between the two harmonics with good precision. We have shown that it is possible to measure ϕ by using stereo-ATI. The process consists of selecting two ranges of the ATI spectrum and mapping their respective asymmetry to different relative phases. As the asymmetry is caused by the second harmonic, it is also possible to determine the relative intensity of the pulses by measuring the magnitude of the asymmetry.

The second harmonic of a two-colour field can be compared to the rapid change of amplitude of a short pulse. In both cases, the asymmetry of each cycle results in an

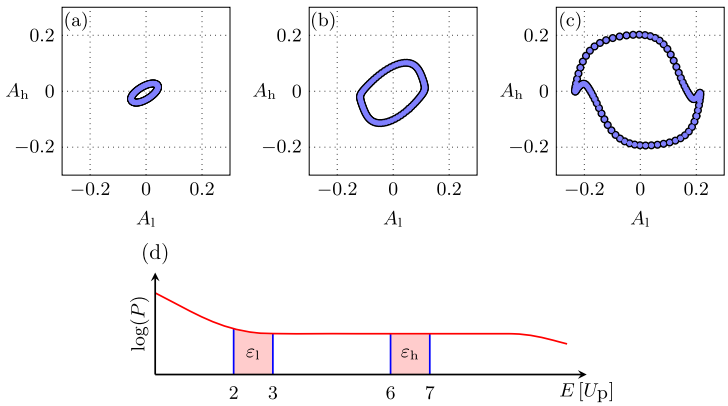

Figure 9. The A_l–A_h representations of three two-colour pulses. Between each figure, $I_{rel} \in \{0.001, 0.0125, 0.15\}$ is increased by a factor $\approx$12.5. In all three figures the energy ranges were $\varepsilon_l = [2U_p, 3U_p]$ and $\varepsilon_h = [6U_p, 7U_p]$, as illustrated below figures (a)–(c).

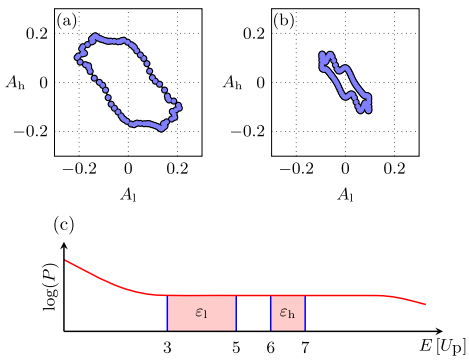

Figure 10. The A_l–A_h representations of two short, Gaussian pulses, created by changing the CEP by increments. The pulse used to generate (a) has a Full Width at Half Maximum (FWHM) of two field cycles, whereas the one used to generate (b) has a FWHM of four field cycles. The different data points displayed in figures (a) and (b) were generated by changing the CEP incrementally. The bottom picture shows the studied energy ranges, $\varepsilon_l = [3U_p, 5U_p]$ and $\varepsilon_l = [6U_p, 7U_p]$.

asymmetrical distribution of ionized electrons. The effect is strengthened by increasing the intensity of the second harmonic and decreasing the pulse width respectively. The asymmetry of the electron distribution can be used to measure ϕ and the CEP respectively.

Acknowledgments

The calculations were performed on resources provided by the Swedish National Infrastructure for Computing (SNIC) at Lunarc, Lund University, in project no. SNIC 2014/1-276.

His work was supported in part by funding from the Swedish Foundation for Strategic Research, the Swedish Research Council and the NSF under grant PHY-1307083.

Note added in proof. After this paper was accepted, a closely related experimental work was published by Prince K C *et al* [26].

References

[1] Perry M D and Crane J K 1993 *Phys. Rev.* A **48** R4051–4
[2] Eichmann H, Egbert A, Nolte S, Momma C, Wellegehausen B, Becker W, Long S and McIver J K 1995 *Phys. Rev.* A **51** R3414–7
[3] Dudovich N, Smirnova O, Levesque J, Mairesse Y, Ivanov M Y, Villeneuve D M and Corkum P B 2006 *Nat. Phys.* **2** 781–6
[4] Mauritsson J, Dahlström J M, Mansten E and Fordell T 2009 *J. Phys. B: At. Mol. Opt. Phys.* **42** 134003
[5] Nguyen H S, Bandrauk A D and Ullrich C A 2004 *Phys. Rev.* A **69** 1094–622
[6] Brizuela F, Heyl C M, Rudawski P, Kroon D, Rading L, Dahlström J M, Mauritsson J, Johnsson P, Arnold C L and L'Huillier A 2013 *Sci. Rep.* **3** 2045–322
[7] Hentschel M, Kienberger R, Spielmann C, Reider G A, Milosevic N, Brabec T, Corkum P, Heinzmann U, Drescher M and Krausz F 2001 *Nature* **414** 509–13
[8] Reichert J, Holzwarth R, Udem T and Hänsch T 1999 *Opt. Commun.* **172** 59–68
[9] Udem T, Holzwarth R and Hänsch T W 2002 *Nature* **416** 233–7
[10] Goulielmakis E 2004 *Science* **305** 1267–9
[11] Brabec T and Krausz F 2000 *Rev. Mod. Phys.* **72** 545–91
[12] Jones D J 2000 *Science* **288** 635–9
[13] Baltuška A *et al* 2003 *Nature* **421** 611–5
[14] Paulus G G, Grasbon F, Walther H, Villoresi P, Nisoli M, Stagira S, Priori E and De Silvestri S 2001 *Nature* **414** 182–4
[15] Paulus G G, Lindner F, Walther H, Baltuška A, Goulielmakis E, Lezius M and Krausz F 2003 *Phys. Rev. Lett.* **91**

[16] Mauritsson J, Johnsson P, Gustafsson E, L'Huillier A, Schafer K J and Gaarde M B 2006 *Phys. Rev. Lett.* **97** 013001
[17] Wittmann T, Horvath B, Helml W, Schätzel M G, Gu X, Cavalieri A L, Paulus G G and Kienberger R 2009 *Nat. Phys.* **5** 357–62
[18] Rathje T, Johnson N G, Möller M, Süßmann F, Adolph D, Kübel M, Kienberger R, Kling M F, Paulus G G and Sayler A M 2012 *J. Phys. B: At. Mol. Opt. Phys.* **45** 074003
[19] Paulus G, Becker W and Walther H 1995 *Phys. Rev.* A **52** 4043–53
[20] Dahlström J M, Fordell T, Mansten E, Ruchon T, Swoboda M, Klünder K, Gisselbrecht M, L'Huillier A and Mauritsson J 2009 *Phys. Rev.* A **80** 033836
[21] Dahlström J M, L'Huillier A and Mauritsson J 2011 *J. Phys. B: At. Mol. Opt. Phys.* **44** 095602
[22] Yin Y Y, Chen C, Elliott D S and Smith A V 1992 *Phys. Rev. Lett.* **69** 2353–6
[23] Schafer K J 2009 *Numerical Methods in Strong Field Physics vol Strong Field Laser Physics* (Berlin: Springer) pp 111–45
[24] Paulus G G, Lindner F, Milosevic D B and Becker W 2004 *Phys. Scr.* **110** 120
[25] Petersson C L M 2014 Above-threshold ionisation with two-colour laser fields *Master's Thesis* Lund University(URL http://lup.lub.lu.se/student-papers/record/4856377/file/4856382.pdf)
[26] Prince K C *et al* 2016 *Nature Photonics* **10** 179–9

III

Sub-cycle ionization dynamics revealed by trajectory resolved, elliptically-driven high-order harmonic generation

Esben Witting Larsen, Stefanos Carlström, Eleonora Lorek, Christoph Michael Heyl, David Paleček, Kenneth Joseph Schafer, Anne L'Huillier, Donatas Zigmantas, and Johan Mauritsson

Scientific Reports
6 39006 (2016)

SCIENTIFIC REPORTS

Sub-cycle ionization dynamics revealed by trajectory resolved, elliptically-driven high-order harmonic generation

E. W. Larsen[1], S. Carlström[1], E. Lorek[1], C. M. Heyl[1], D. Paleček[2,3], K. J. Schafer[4], A. L'Huillier[1], D. Zigmantas[2] & J. Mauritsson[1]

The sub-cycle dynamics of electrons driven by strong laser fields is central to the emerging field of attosecond science. We demonstrate how the dynamics can be probed through high-order harmonic generation, where different trajectories leading to the same harmonic order are initiated at different times, thereby probing different field strengths. We find large differences between the trajectories with respect to both their sensitivity to driving field ellipticity and resonant enhancement. To accurately describe the ellipticity dependence of the long trajectory harmonics we must include a sub-cycle change of the initial velocity distribution of the electron and its excursion time. The resonant enhancement is observed only for the long trajectory contribution of a particular harmonic when a window resonance in argon, which is off-resonant in the field-free case, is shifted into resonance due to a large dynamic Stark shift.

The process of high-order harmonic generation (HHG)[1,2] driven by a strong infrared (IR) laser field interacting with a rapidly ionizing medium is the main light source for the field of attosecond science[3–6]. The HHG process can be used to produce attosecond pulses because there is a natural, sub-cycle electron dynamics built into the physics of HHG[7,8], which leads to a very broad plateau of emitted harmonics. This means that studying the HHG process itself in detail can, in principle, provide a deeper understanding of strong field electron dynamics at the attosecond time scale. Over the last decade experiments[9,10] have indeed shown that the sub-cycle dynamics of HHG are encoded in the harmonic spectrum, though extracting them is complicated because of the highly non-linear nature of the process.

Much of the promise in using HHG to better understand strong field physics at the sub-cycle level can be attributed to the effectiveness of the simple, semi-classical three-step model commonly used to describe the generation process[11,12]. In this model, an electron is first tunnel ionized and then accelerated by a strong laser field. If the electron is driven back to the vicinity of the ion by the oscillating strong field, the accumulated energy may be emitted as a photon[11–13] when the electron and ion recollide. The sequence of ionization and return times leading to a specific harmonic frequency is loosely referred to as a trajectory because much of the physics can be understood by considering classical electron trajectories in a strong laser field, ignoring atomic effects after the ionization step and before the return. Depending on when during the laser cycle the ionization occurs, the electron will have different excursion and return times to the ion leading to different photon emission frequencies, resulting in a comb of odd harmonics of the laser field if the process is repeated over many laser cycles. Even in this simple model, however, there is not a one-to-one correspondence between the harmonic emission strengths and specific trajectories, because there are different trajectories leading to the same final energy. Trajectories that lead to the same photon energy interfere at the single atom level. The effect of this can either be studied[14–16] or circumvented, for example, through phase matching or spatial separation in the far field of the harmonics as is done in the present work.

[1]Department of Physics, Lund University, P.O. Box 118, SE-221 00 Lund, Sweden. [2]Department of Chemical Physics, Lund University, P.O. Box 124, SE-22100 Lund, Sweden. [3]Department of Chemical Physics, Charles University in Prague, Ke Karlovu 3, 121 16 Prague, Czech Republic. [4]Department of Physics and Astronomy, Louisiana State University, Baton Rouge, Louisiana, 70803, United States of America. Correspondence and requests for materials should be addressed to E.W.L. (email: elarsen@imperial.ac.uk) or J.M. (email: johan.mauritsson@fysik.lth.se)

Studying trajectory resolved contributions to the HHG spectrum is an attractive proposition because different trajectories probe very different ionization conditions and have different excursion times. The most prominent contributions to the harmonic emission strengths come from the so-called short and long trajectories, which have excursion times of less than one laser cycle. Within a laser cycle the long trajectories are ionized close to the peak field strength and have an excursion time exceeding 0.65 laser cycles. The short trajectories are ionized at low field strengths and have shorter excursion times. Fortunately, the emission from these two trajectory classes can be separated experimentally in the far field enabling, for each harmonic frequency, comparison between ionization at two different sub-cycle field strengths, followed by two different excursion times. This requires, ideally, that high accuracy measurements of both long and short trajectory contributions to each harmonic are made in the same experimental setup[17].

Until recently most experimental efforts that make use of high harmonics have been concentrated on optimizing HHG from short trajectories, since their emission is well collimated and spectrally narrow. In addition, trains of attosecond pulses have been successfully created and measured by selecting the short trajectories' contributions[3,18]. The emission from the long trajectories is more challenging to use because it is spectrally broader and more divergent, hence it is usually removed by spatial filtering and/or the selection of specific phase matching conditions in experiments as they otherwise can affect the temporal structure of the attosecond pulses[19]. In this paper we report on measurements made with very well-controlled, high repetition-rate laser pulses, which allow us to make trajectory resolved HHG measurements in argon gas while varying the ellipticity and the peak field strength of the driving laser pulses. The results allow us to elucidate new features in the sub-cycle ionization step that lead to long trajectories, that is, ionization at high field strengths followed by long excursion times.

In this article, we present two methods of probing sub-cycle strong-field dynamics by comparing the trajectory resolved emission of high harmonics and then studying the long trajectories in depth. In the first part of the article, a detailed experimental comparison of the ellipticity dependence as a function of harmonic order is presented, for both the short and the long trajectories. While harmonic generation using elliptically polarized driving fields has been extensively studied for the short trajectories both experimentally and theoretically[20–26], the polarization dependence of the long trajectories have so far only been investigated theoretically[24,25,27]. It follows from the simple three-step model that harmonic generation will be very sensitive to the ellipticity of the driving laser since the field acting on the electron while it is far from the ion can cause it to miss the recollision. Since the long and the short trajectories have different excursion times, the impact of changing the ellipticity will be different for the two classes of trajectories.

To explain the ellipticity dependence of the short trajectories it is sufficient to include wave packet spreading due to quantum diffusion, which we can model by including a distribution of momenta transverse to the instantaneous field vector at the moment of ionization. This distribution does not need to depend in detail on the moment of ionization, since the ionization field strength is low for short trajectories. In order to explain the ellipticity dependence of the long trajectories, however, this simple quantum diffusion model is not enough. Due to a larger variation in ionization field strength for the different long trajectories, a field-strength dependent momentum distribution has to be taken into account. We expect that at higher field strengths a broader transverse momentum distribution results from the lowering of the ionization barrier. We include this effect in our theoretical analysis of the long trajectory data via a simple extension of the three step model and find that it fits the our experimental data very well over the HHG plateau.

In the second part of our study, the sub-cycle sensitivity of trajectory resolved HHG measurements is used to study a region of the spectrum in which atomic resonances can alter the HHG signal. In particular, a window resonance in argon that is far from any harmonic of the laser frequency in the field-free case is shown to have a large effect on the long trajectory harmonic closest to it, but little or no effect on the short trajectory. We attribute this to the fact that the long trajectory component is dynamically Stark shifted into resonance by the laser field, which leads to a drastic enhancement of the emission from the long trajectory, but not the short where the field strength is much weaker and is not sufficient to shift the state into resonance. We measure this effect for a set of resonant harmonics over a range of driving field intensities.

Experimental setup

The experimental setup used for the experiment presented in this article is described in a recent publication[28] and is briefly outlined here. An Yb:KGW based laser system ("Pharos", Light Conversion Ltd.) was used to deliver 170 fs, pulses with a central wavelength of 1030 nm. The laser system has a variable repetition rate between 1 and 600 kHz, but all the presented data were recorded at a repetition rate of 20 kHz. The pulses were focused tightly into a continuous argon gas jet, with a 90 m orifice, using a 100 mm focal length achromatic lens. Directly after the interaction region, a differential pumping hole with an inner diameter of 0.5 mm was placed to minimize the background gas in the detection chamber. The differential pump hole allowed for a pressure difference of the background gas between the generation and detection chambers of 4–5 orders of magnitude. The HHG spectrum was measured using a home-built imaging spectrometer based on a variable-line-spacing grating and a microchannel-plate with an attached phosphor screen and a camera with a resolution of 2456×2058 pixels and a dynamic range of 14 bits. The grating diffracts and refocuses the XUV in the horizontal direction while the vertical direction is left unaffected. Therefore the vertical direction provides the divergence of the XUV light while the horizontal direction shows the spectrum.

Ellipticity measurement

Figure 1 shows a typical harmonic spectrum when a linearly polarized driving laser is used and the gas jet is placed in the focal plane of the generating beam. The experimental parameters (pulse energy, gas density, spot size, etc.) were optimized to generate harmonics from both the short and the long trajectories.

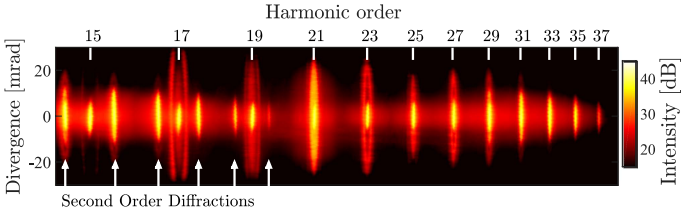

Figure 1. Typical harmonic spectra optimized to generate harmonics from both the short and the long trajectories.

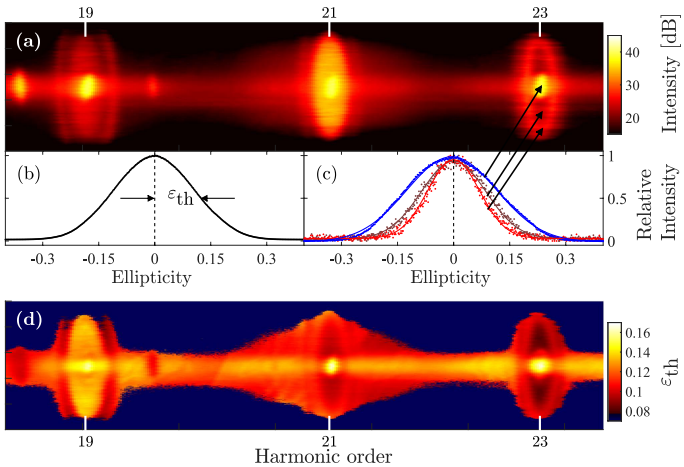

Figure 2. (**a**) Enlarged view of the harmonic spectrum at linear polarization for H19–H23 of Fig. 1. (**b**) Spatially and spectrally integrated signal of H23 as a function of ellipticity. (**c**) Measurement of the ellipticity dependence of three different spatial–spectral parts of H23 as indicated by the three arrows. The solid lines represent Gaussian fits to the experimental data. (**d**) Pixel-by-pixel threshold ellipticity of the spatial–spectral region of part (**a**).

The Gaussian transverse and temporal intensity profile of the driving laser, in combination with the fact that the dipole phase of the long trajectories has a stronger intensity dependence than the short trajectories, result in a larger wavefront curvature and more divergent light generated by the long trajectories[29–31], this also explains the spatial–spectral rings observed in the far field. We therefore attribute the inner part of the harmonic spectrum to be dominated by the short trajectories, while the spatial–spectral rings are attributed to interference between long trajectories of different emitters. As the trajectory dependent dipole phase is strongest for the low orders, the interference rings are mainly seen for the low end of the plateau region. This spatial separation was exploited to study the contributions from the long trajectories only.

A quarter-wave plate was used to introduce ellipticity, defined as the ratio between the minor and major axis components of the driving laser field. Figure 2(a) shows an enlarged view of the spatial–spectral profile of harmonics 19–23 of Fig. 1. Figure 2(b) shows a measurement of the spatially and spectrally integrated strength of harmonic 23 (H23) as a function of ellipticity of the driving laser relative to the strength at linear polarization. The integrated signal clearly follows a Gaussian distribution with respect to ellipticity as previously observed[20].

We define the threshold ellipticity, ε_{th}, as the amount of ellipticity required for the harmonic signal to drop by a factor of two compared with linear polarization. Our very high signal-to-noise ratio allows us to analyze the ellipticity dependence of each pixel rather than the spatially and spectrally integrated signal. Figure 2(c) presents the strength of three different pixels within H23 as a function of ellipticity. The strength of each pixel is fitted with a Gaussian profile to extract the corresponding threshold ellipticity of each pixel, which are used to create a two-dimensional map of the threshold ellipticity as a function of energy and divergence angle. The full threshold ellipticity maps for the conditions of Fig. 1 can be found in the Methods section. Focusing on H23 in Fig. 2(d), we observe three different regions of threshold ellipticity; an inner region with a threshold ellipticity around 0.16, and two outer regions with threshold ellipticities of around 0.09 and 0.1 respectively.

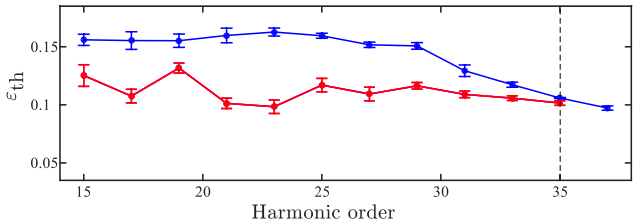

Figure 3. The red (blue) line show the measured threshold ellipticity as a function of harmonic order for the long (short) trajectories when the laser is focused in the middle of the gas jet. The error bars indicate the standard deviations of the corresponding threshold ellipticity.

Figure 3 presents the average threshold ellipticity for both the long and the short trajectories as a function of harmonic order for the conditions of Fig. 1. For the short trajectories, we observe a behavior similar to previous measurements[20,22,26], *i.e.*, the threshold ellipticity decreases slowly with increasing harmonic order. A similar trend is also observed for the long trajectories, in contrast to what would be expected if only the excursion time of these trajectories is considered.

Ellipticity theory

In a semi-classical model where the propagation step is calculated classically and the electron only has a velocity parallel to the electric field, only linearly polarized light would produce high-order harmonics since any ellipticity will prevent the electron from returning to its original position. The fact that high-order harmonics are observed even for elliptically polarized light is usually attributed to quantum diffusion; the electron wave packet spreads out as it is accelerated in the laser field. The wave packet spread allows for an overlap between the electron and the parent ion, even when the electron is transversely displaced due to the elliptically polarized laser field.

Quantum diffusion can be seen as resulting from an initial distribution of velocities of the electron – the more confined the electron is in one direction, the more it will spread. In particular, a spatial confinement in the direction perpendicular to the laser field, will lead to a transverse velocity distribution which is necessary for HHG. A rough estimate of the confinement is given by the size of the groundstate. Using this estimate, a trajectory spending longer time in the continuum will diffuse more which results in a lower HHG yield.

For the short trajectories, the above estimate of the quantum diffusion, which is independent of the ionization time, is sufficient to explain the increase in sensitivity, as a function of harmonic order. For this set of trajectories the highest energy photons are produced by electrons with the longest excursion time. As the transverse displacement of the electron at the point of recombination increases with the excursion time, the trajectories leading to the higher harmonics are displaced more than those leading to the low orders. Therefore the overlap between the ion and the electron at the recombination time decreases with harmonic order.

For the long trajectories, this effect leads to the opposite result, as the kinetic energy of the returning electrons decreases with increasing excursion time. To understand the experimentally observed ellipticity dependence of this set of trajectories, we apply a model that also takes the sub-cycle variation of the initial electron velocity distributions into account, as well as the change in excursion time for the different trajectories as the ellipticity is varied. This effect plays a major role in the initial velocity distribution as the long trajectory electrons are ionized closer to the peak of laser field, where the atomic potential is more distorted in the direction of the laser field, and thus the electron wave packet is more perpendicularly confined at the time of ionization[32]. The perpendicular confinement of the electron at the ionization time leads to a large uncertainty in the perpendicular velocity distribution.

Our method is similar to references 24–26, but the definition of threshold ellipticity is not the same in the different studies. The procedure is as follows: First, we calculate the return energy of the electrons for the two first sets of trajectories as a function of both ionization time and ellipticity. The position of an electron released at time t_i in an elliptical field $F(t) = F/\sqrt{1+\varepsilon^2}\,[\sin(\omega t);\, \varepsilon\cos(\omega t)]$ is found by integrating the Newtonian equations of motion twice:

$$\mathbf{r}(t) = \frac{F}{\omega^2\sqrt{1+\varepsilon^2}}\left[\begin{array}{c}\sin(\omega t) - \sin(\omega t_i) - \omega(t-t_i)\cos(\omega t_i) \\ \varepsilon\left[\cos(\omega t) - \cos(\omega t_i) + \omega(t-t_i)\sin(\omega t_i)\right]\end{array}\right] + (t-t_i)\mathbf{v}_i + \mathbf{r}_i, \quad (1)$$

where $\mathbf{v}_i$ and $\mathbf{r}_i$ are the initial velocity and position, respectively; F is the field amplitude, ω the frequency of the fundamental field, $\varepsilon \in [-1, +1]$ is the ellipticity, with 0 meaning linear polarization along the x axis. Atomic units are used. We assume that $\mathbf{r}_i = \mathbf{r}(t_r) = 0$, where t_r is the moment of return. Finding this time requires solving the transcendental equation numerically. For elliptical polarization, the drift acquired by the electron can be countered by an initial velocity $\mathbf{v}_i$ that is transverse to the driving field at the time of ionization (this is analogous to quantum diffusion of the electron wavepacket as it is accelerated in the laser field). Thus, we solve (1) for t_r and $\mathbf{v}_i$ for each $t_i \in [0.25T, 0.5T]$, T being the period, and each $\varepsilon \in [0, 1]$. We assume that $\mathbf{v}_i = \mathbf{v}_{\parallel} + \mathbf{v}_{\perp}$, where the two

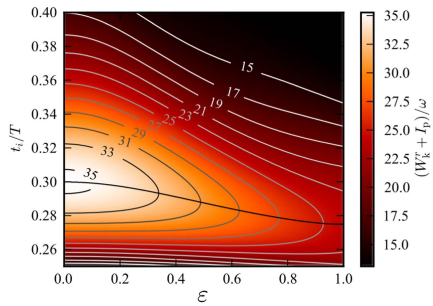

Figure 4. Map of return energies, as a function of ellipticity ε and ionization time t_i. I_p is the ionization potential of the ground state. Plotted are also isoenergetic curves corresponding to the harmonics of the fundamental field, and the cut-off energy (shown by the solid black line), which decreases for increasing ellipticity. Trajectories, which are ionized earlier than the cut-off energy, correspond to the long trajectories. It is easy to see that a specific time of ionization does not correspond to a certain recombination energy.

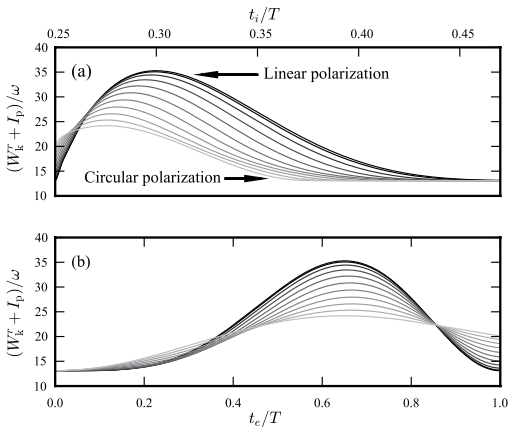

Figure 5. (**a**) Lineouts of Fig. 4 for 11 equidistant ellipticities from linear to circular polarization. From this plot it is obvious that the cut-off decreases with increasing ellipticity and that it occurs for earlier ionization times. It is also clear that the initial timing necessary to produce a specific harmonic changes with the ellipticity. (**b**) The same as (**a**), but plotted as a function of excursion time $t_e = t_r - t_i$ instead.

components are parallel and perpendicular to the driving field at the time of ionization. Furthermore, we assume that $v_{||} = 0$, such that all uncertainty is in the initial transverse momentum, $p_\perp = m_e v_\perp$, ($m_e = 1$ in atomic units).

The kinetic energy at the time of return is given by $W_k^r = p^2(t_r)/2$; this gives the map of energies seen in Fig. 4.

As can be seen in Fig. 4, the cut-off position is shifted when the ellipticity is increased (*i.e.* the highest energy photons can only be produced from linearly polarized light) and the initial timing leading to a specific harmonic order is also changed. This trend is even more clear when lineouts at different ellipticities are presented as in Fig. 5.

The next step to estimate the harmonic yield is to calculate the combined probability of ionizing at time t_i and having the required initial velocity for the electron to return. This is possible since the correspondence between a certain harmonic and its ionization time for different ellipticities is already calculated. Since the required transverse momenta for the long trajectories to return are quite large for high ellipticities, we use the full expression for the transverse momentum distribution found in reference 33,

$$w(p_\perp) \propto \exp\left[-\frac{2(2I_p + p_\perp^2)^{3/2}}{3F(t_i)}\right]. \quad (2)$$

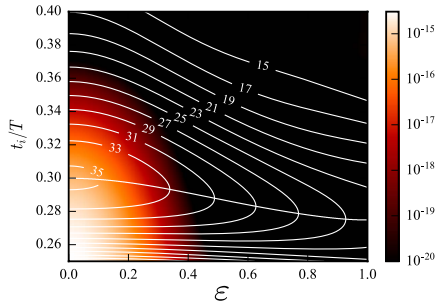

Figure 6. Map representing the combined probability of ionizing at time t_i and having the initial transverse velocity required for return as a function of ellipticity and ionization time. The isocurves are the same as in Fig. 4, representing constant return energy. Following an isocurve gives the probability of generating a certain harmonic, as a function of ellipticity.

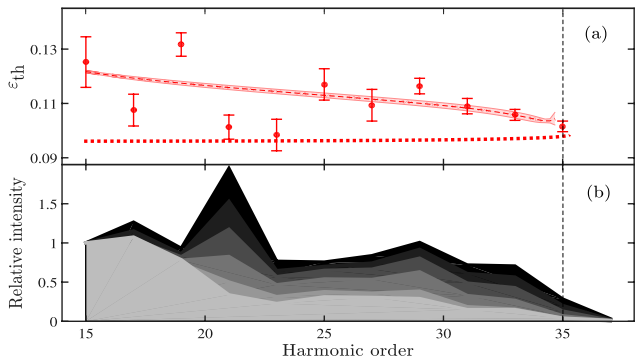

Figure 7. (**a**) The dashed lines show the numerically calculated threshold ellipticities for the long trajectories in the plateau region according to our model. Correspondingly, the dotted lines show the threshold ellipticity given by ref. 25. For comparison, the experimental data for the long trajectories are shown. The simulations were done for a laser intensity of $8.5 \cdot 10^{13}$ W/cm^2 and a wavelength of 1030 nm. (**b**) Integrated harmonic spectra for in-focus generation with various ellipticities. The color scale corresponds to different ellipticities from black ($\varepsilon = 0$) to light gray ($\varepsilon = 0.25$) in steps of 0.05. The fillings between the different harmonics allow us to better visualize the differences. The various spectra have been normalized to the level of H15. The error bars used in (**a**) show the standard deviations of the threshold ellipticities of the corresponding harmonic.

I_p is the ionization potential of the ground state. The tunneling rate is taken from ADK theory[34]. This combined probability, which is the product of the separate probabilities described above, is displayed using a colour scale in Fig. 6, as a function of ellipticity and ionization time.

The isoenergetic curves from Fig. 4 are also included in the figure. To calculate the yield of a given harmonic order as a function of ellipticity, one extracts the probability along the corresponding isoenergetic curve.

Finally, in the last step of our model, the calculated yield as a function of ellipticity is fitted with Gaussian functions for each harmonic to obtain the threshold ellipticities in a similar manner to the experimental data. The result of the model for the long trajectories is presented in Fig. 7(a) together with the experimental data.

Our extended model compares very well with the experiment presented in this work; in particular the decrease in threshold ellipticity with increasing harmonic order is explained. This is opposite to what would be expected from sub-cycle field-independent quantum diffusion. It is also opposite to the analytical expression presented in reference 39 which is included for comparison in Fig. 7(a) as a dotted line.

From Fig. 7(a) it is clear that some of the long trajectory harmonics (17, 21 and 23) have a lower threshold ellipticity than what is predicted by the model. We attribute this to the presence of atomic resonances in the vicinity of the corresponding energies, which clearly cannot be captured by the model we are using. In what follows, we demonstrate that these resonances can be dynamically Stark shifted by the sub-cycle field strength and will therefore influence the harmonic generation differently for the short and the long trajectories. The spatial separation of the short and long trajectories leading to the same energy, enable us to directly compare the influence of

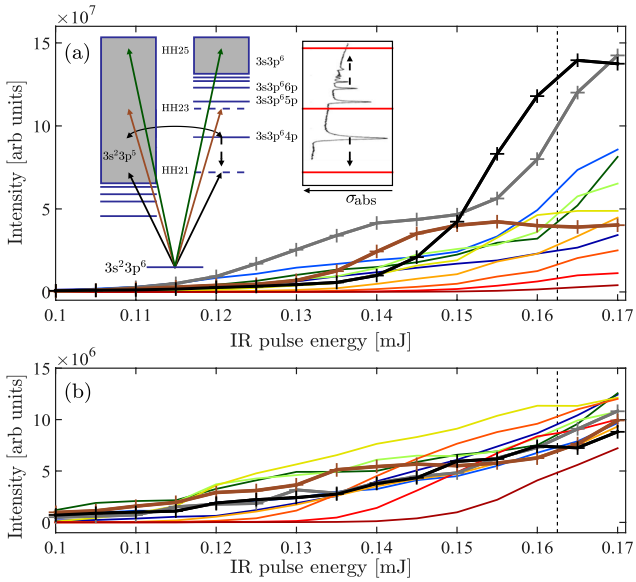

Figure 8. Experimentally measured long (**a**) and short (**b**) trajectory intensities of H15–H37 as a function of pulse energy of the fundamental field. H17 is shown in gray, H21 in black, and H23 in brown, while the remaining harmonics are shown in a rainbow color scale from dark blue (H15) to dark red (H37) with increasing order. The dashed line indicates roughly the conditions of Fig. 1. The inset of (**a**) schematically shows how the Rydberg series for the 3s electrons in combination with the continuum for the 3p electrons creates a series of window resonances. Absorption of an XUV photon can create a coherent superposition of the two valence electrons which interfere and affects the absorption cross-section σ_{abs}[42]. In argon this amounts to a reduction of the absorption cross-section[43]. The vertical arrows within the inset indicate the expected direction of the light induced energy-shift of the respective $3s^1 3p^6 np^1$ states.

the sub-cycle field strength. For a given harmonic order, the short trajectory is initiated at a field strength which is insufficient to shift the state into resonance, thereby precluding the enhancement observed for the long trajectory initiated at a higher sub-cycle field strength.

Resonant HHG

Resonant HHG in argon at a photon energy corresponding to H17 in our experiment has previously been observed[35]. In our study, we also see an effect for H21 and H23 [Fig. 7(b)]. We will focus the discussion on H21, where the effect is most pronounced. At linear polarization a strong enhancement of H21 is clearly observed, while this enhancement is gone for an ellipticity of 0.2 as can be seen in Fig. 7(b). The change in ellipticity leads to a variation in the intensity, since the pulse energy is kept constant. This means that the observed effect can be due to either the intensity or the ellipticity. In order to disentangle the two, an intensity scan was performed for linearly polarized light. Figure 8 shows the experimentally measured intensities of the long (a) and short (b) trajectories for H15–H37 as a function of IR pulse energy. As clearly observed, the yield of H21 rises more rapidly for the long trajectories once the IR pulse energy exceeds 0.14 mJ [Fig. 8(a)], while the emission from the short trajectories are left unaffected [Fig. 8(b)]. Enhancement of the long trajectories can also be clearly seen for H17 and H23, albeit, at slightly lower pulse energies. Harmonic 17 qualitatively follows the trend predicted for the single atom response given in reference 35, thus H17 is not further discussed in the present work. Harmonic 23 reaches a maximal strength at 0.15 mJ whereafter a slow decrease with respect to increased pulse energy is observed.

We interpret the behavior of H21 (but also H17 & H23) to be the result of HHG in the presence of an atomic resonance. Resonant HHG may increase the harmonic yield through a number of different mechanisms[35–41]. For H21 with photon energy of 25.2 eV, the closest resonance is the $3s^2 3p^6 \rightarrow 3s^1 3p^6 4p^1$ transition (26.6 eV), which is a window resonance[42,43]. Our interpretation requires that the $3s^1 3p^6 4p^1$ state, which is lowest state in the $3s \rightarrow np$ closed channels, is red-shifted by approximately 1.4 eV [see inset in Fig. 8(a)]. This is feasible as the dynamical Stark shift of the $3s^1 3p^6 4p^1$ state should be dominated by the interaction with the $3s \rightarrow np$ closed channel, rather than through coupling with the $3p \rightarrow \Sigma(s, d)$ open channels[44,45], and the Stark shifts on the order of the ponderomotive energy are well known[46,47]. In addition to the Stark effect, the IR intensity also causes a blueshift of the IR energy, and thereby the XUV photon energies. However, it was confirmed from the intensity scan that this effect is too small to explain the results, as the central frequencies of the harmonics did not change. Since we only observe

the enhancement for the long trajectory, we interpret this as an effect of the comparably higher field strength for this trajectory, at the time of ionization.

Reshaping of the argon HHG spectrum by this particular window resonance has previously been observed[48], however, the interpretation is fundamentally different in the work presented here. In reference 48, a few-cycle pulse was used to generate broadband harmonics by HHG in a gas jet. The backing pressure for the continuous gas jet was then increased significantly so that all other wavelengths than exactly the resonant wavelength were suppressed by re-absorption in the generating gas. This led to a narrowing of H17 (of 800 nm) from a width of roughly 1.5 eV to a width comparable to the field-free width of the window resonance[43]. This leads us to believe that the effect observed in reference 48 happens over a large volume, where the IR intensity is weak. The results presented in this article, however, is clearly an effect that take place at high laser intensity, where the dynamical Stark effect is strong.

The behavior of H23 with respect pulse energy of the driving laser can be understood as an effect of over-shifting of the atomic resonances causing the enhancement. As indicated in the inset of Fig. 8(a) the field-free detuning of H23 is less than the detuning of H21 with respect to both the transition energies into the $3s^13p^64p^1$ and the $3s^13p^65p^1$ states, so the minimal required pulse energy for enhancement of this harmonic is lower. Nevertheless, the maximal enhancement factor is largest for H21, due to the strong dipole coupling with the red-shifted $3s^13p^64p^1$ state.

As the pulse energy is increased beyond the optimum energy for resonant generation of H23 the enhancement of this harmonic starts to vanish. The slow decrease likely originates from the long pulse duration of the driving laser, which means that a number of cycles will have the optimum energy shift. A similar effect is expected to occur for H21 at higher pulse energies, however, due to limitations of the laser system this was not seen in the present work.

Apart from the major effects on H17, H21 and H23 observed both in the ellipticity and the intensity measurements a minor amount of enhancement of H19, H25 and H27 can be observed for the long trajectories once the IR pulse energy exceeds 0.15 mJ [Fig. 8(a)]. The field-free detuning from the 3s3p6np manifold of resonances are larger for these harmonics, so any enhancement effect on these harmonics is both expected to be less, and to occur at higher pulse energies in full agreement with the observation.

In conclusion, we have experimentally investigated the ellipticity and intensity dependencies of HHG from the long and the short trajectories. This type of measurements enables us to probe the influence of the sub-cycle field strength on HHG process. We have shown that the well-established semi-classical model has to be extended by taking the instantaneous field strength into account, to also describe the general behavior of the long trajectories. We have demonstrated how off-resonant states embedded in the continuum can enhance long trajectory harmonics by being shifted into resonance by the strong driving laser, different amounts for different trajectories due to the sub-cycle nature of the generation process. When the driving laser field is strong enough to cause an enhancement at linear polarization, these harmonics show a stronger ellipticity dependence as the dynamical Stark shift depends on the polarization.

This study highlights the importance of systematical studies of the generation process under various conditions. Furthermore, the extension of the knowledge of the harmonic generation process to the long trajectories will be beneficial for high-order harmonic spectroscopy studies.

Methods

Evaluation of experimental data. In this section we present the details of the analysis method used for the experimental data.

It is well-known from the strong field approximation that for harmonics in the plateau region, there are several electronic trajectories, which may contribute to the generation process. Emission from these different trajectories interferes and shapes the far field spatial spectral profile. The phase of these trajectories can be approximated with a phase proportional to the intensity $I(x, y, z, t)$ such that

$$\phi_q^{\text{traj}} = \alpha_q^{\text{traj}} I(x, y, z, t), \tag{3}$$

where ϕ_q^{traj} is the trajectory dependent dipole phase and α_q^{traj} is the proportionality constant. The first two sets of electron trajectories are usually referred to as the short and long trajectories. It well-established that in the plateau region the proportionality constants are much larger for the long trajectories than for the short trajectories[31,49].

The short trajectories can be isolated in the generation process by placing the gas jet behind the focal plane and adjusting gas pressure and pulse energy accordingly[50,51]. A spectrum optimized for this is shown in Fig. 9(a). Figure 9(b) shows the corresponding threshold ellipticity map, which is extracted in a similar manner as in the main article. When the gas jet instead is placed at the focus of the laser both sets of trajectories can efficiently be phase-matched by adjusting the other experimental parameters accordingly. Figure 9(c) shows a spectrum optimized to generate with both sets of trajectories, while Fig. 9(d) is the corresponding threshold ellipticity map. As a consequence of the larger dipole phase of the long trajectories, the light produced by the these trajectories are more divergent. This effect was used to spatially separate the contributions from only the long trajectories in Fig. 9(c,d).

Figure 10 shows enlarged views of H19 for out-of-focus generation [(a)] and in-focus generation [(b)]. In the out-of-focus case the harmonic exhibits a homogeneous spatial-spectral dependence with respect to ellipticity, this is not observed for the in-focus case, where several regions of ellipticity dependence are clearly observed.

The homogeneity of the ellipticity dependence for out-of-focus generation [Fig. 10(a)] reveal that in order to study ellipticity dependence of the short trajectories out-of-focus an imaging spectrometer is not needed and a spatial-spectral integration with respect to harmonic order would be sufficient. This is clearly not the case of in-focus generation [Fig. 10(b)].

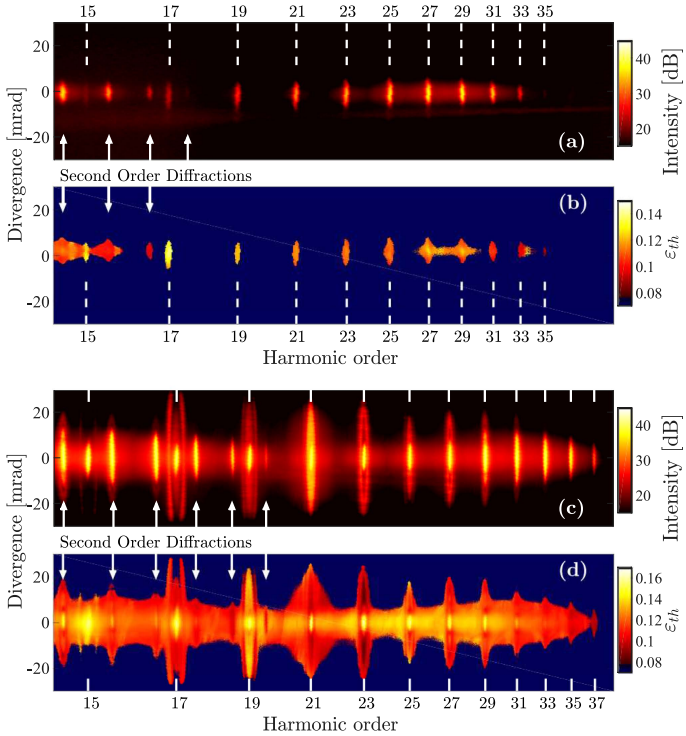

Figure 9. (**a**) Harmonic spectrum at linear polarization when the gas jet is placed behind the focal plane of the laser. (**b**) Threshold ellipticity map as a function of energy and divergence angle for out-of-focus generation. (**c**) Harmonic spectrum at linear polarization when the gas jet is placed in the focal plane of the laser. (**d**) Threshold ellipticity map as a function of energy and divergence angle for in-focus generation.

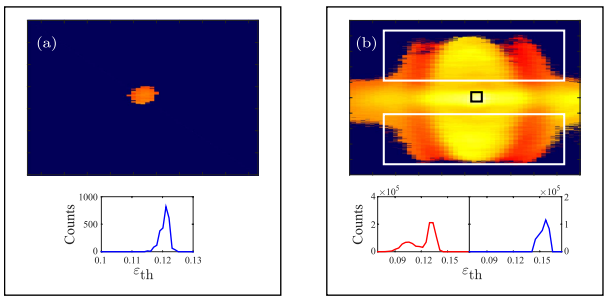

Figure 10. (**a**) An enlarged view of the ellipticity map of H19 for out-of-focus generation [Fig. 9(b)]. The lower panel shows a histogram of the threshold ellipticities. Each pixel is weighted with the corresponding pixel strength at linear polarization. (**b**) An enlarged view of the ellipticity map of H19 for in-focus generation [Fig. 9(d)]. The lower panels show histograms of the threshold ellipticities within the white boxes (left panel) and the black box (right panel). The histograms are weighted with the corresponding pixel strength at linear polarization.

Figure 11 shows the threshold ellipticity as function of harmonic order for the conditions of Fig. 9. Figure 11 shows normalized threshold ellipticity histograms as function of harmonic order. In the in-focus generation case both the on-axis emission and off-axis emission are shown, in (b) and (c) respectively, while for out-of-focus

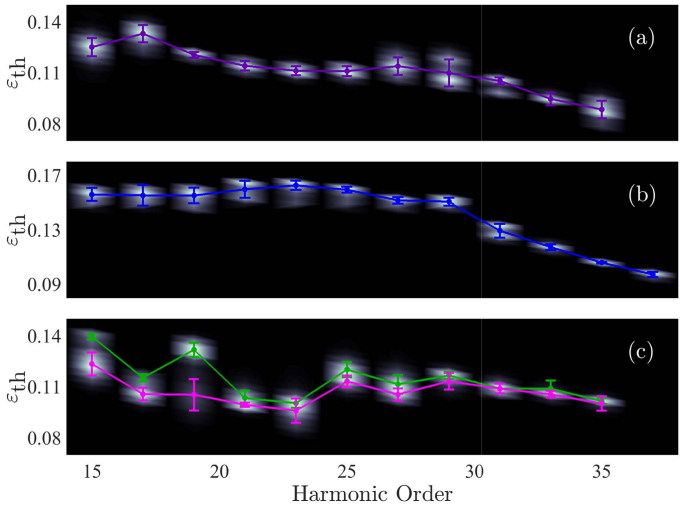

Figure 11. Normalized threshold ellipticity histograms as a function of harmonic order together with the extracted expectation values and standard deviations for: (**a**). The center of H15–H33 for out-of-focus generation. (**b**) The center of H15–H37 for the in-focus generation. (**c**) The outer regions of harmonic H15–H35 for in-focus generation.

case only the on-axis emission is shown in (a). We note that for harmonics close to the cut-off indications of the long trajectory appears also for the out-of-focus case. In order to extract expectation values and standard deviations for the various threshold ellipticities as a function of harmonic order and trajectories the experimental data is smoothened using the Kernel density estimation method[52,53]. After smoothing, the data was fitted with two Gaussian distributions for the long trajectories, while the short trajectories where fitted with a single Gaussian distribution. The expectation value of the fitted Gaussian distributions are plotted as solid lines in Fig. 11, while the uncertainty bars show the corresponding standard deviations of the fits.

Detection efficiency. We measured the ratio in detection efficiency between horizontal and vertical polarization to be 1.38. 3 Three dimensional time-dependent Schrödinger equation calculations[25] show that the plateau harmonics exhibit a smaller ellipticity than the driving infrared laser. We therefore estimate that the upper limit of the non-fixed major axis impact on the measurement to be given by the following expression:

$$I_{\text{det}} \propto E_a^2 D_a + E_b^2 D_b, \tag{4}$$

where E_a and E_b are the major and minor axis component of the infrared electrical fields, and D_a and D_b are the respective detection efficiencies. Using this expression together with the standard Jones matrix calculus for polarization of the infrared light we estimated the upper limit on the determination of the threshold ellipticity to be less than the presented standard deviations. The presented data was performed around the linear polarization direction with the highest detection efficiency. Therefore the threshold ellipticity might be systematically underestimated slightly.

References

1. McPherson, A. *et al.* Studies of multiphoton production of vacuum-ultraviolet radiation in the rare gases. *Journal of the Optical Society of America B* **4,** 595 (1987).
2. Ferray, M., L'Huillier, A., Li, X. F., Mainfray, G. & Manus, C. Multiple-harmonic conversion of 1064 nm radiation in rare gases. *J. Phys. B: At., Mol. Opt. Phys.* **21,** L31 (1988).
3. Paul, P. M. *et al.* Observation of a train of attosecond pulses from high harmonic generation. *Science* **292,** 1689 (2001).
4. Hentschel, M. *et al.* Attosecond metrology. *Nature* **414,** 509–513 (2001).
5. Agostini, P. & DiMauro, L. F. The physics of attosecond light pulses. *Rep. Prog. Phys.* **67,** 813–855 (2004).
6. Krausz, F. & Ivanov, M. Attosecond physics. *Reviews of Modern Physics* **81,** 163–234 (2009).
7. Hänsch, T. A proposed sub-femtosecond pulse synthesizer using separate phase-locked laser oscillators. *Optics Communications* **80,** 71–75 (1990).
8. Farkas, G. & Tóth, C. Proposal for attosecond light pulse generation using laser induced multiple-harmonic conversion processes in rare gases. *Physics Letters A* **168,** 447–450 (1992).
9. Baker, S. *et al.* Probing proton dynamics in molecules on an attosecond time scale. *Science* **312,** 424–427 (2006).
10. Smirnova, O. *et al.* High harmonic interferometry of multi-electron dynamics in molecules. *Nature* **460,** 972–977 (2009).
11. Schafer, K. J., Yang, B., DiMauro, L. F. & Kulander, K. C. Above threshold ionization beyond the high harmonic cutoff. *Phys. Rev. Lett.* **70,** 1599 (1993).
12. Corkum, P. B. Plasma perspective on strong-field multiphoton ionization. *Phys. Rev. Lett.* **71,** 1994 (1993).

13. Lewenstein, M., Balcou, P., Ivanov, M., L'Huillier, A. & Corkum, P. B. Theory of high-order harmonic generation by low-frequency laser fields. *Phys. Rev. A* **49,** 2117 (1994).
14. Zaïr, A. *et al.* Quantum path interferences in high-order harmonic generation. *Phys. Rev. Lett.* **100,** 143902 (2008).
15. Kolliopoulos, G. *et al.* Revealing quantum path details in high-field physics. *Phys. Rev. A* **90,** 013822 (2014).
16. Preclíková, J. *et al.* Spatially and spectrally resolved quantum path interference with chirped driving pulses. *arXiv* **1606**, 08697v1 (2016).
17. Corsi, C., Pirri, A., Sali, E., Tortora, A. & Bellini, M. Direct interferometric measurement of the atomic dipole phase in high-order harmonic generation. *Phys. Rev. Lett.* **97,** 023901 (2006).
18. López-Martens, R. *et al.* Amplitude and phase control of attosecond light pulses. *Phys. Rev. Lett.* **94,** 033001 (2005).
19. Kruse, J. E. *et al.* Inconsistencies between two attosecond pulse metrology methods: A comparative study. *Phys. Rev. A* **82,** 021402 (2010).
20. Budil, K. S., Salières, P., L'Huillier, A., Ditmire, T. & Perry, M. D. Influence of ellipticity on harmonic generation. *Phys. Rev. A* **48,** R3437 (1993).
21. Burnett, N. H., Kan, C. & Corkum, P. B. Ellipticity and polarization effects in harmonic generation in ionizing neon. *Phys. Rev. A* **51,** R3418 (1995).
22. Sola, I. J. *et al.* Controlling attosecond electron dynamics by phase-stabilized polarization gating. *Nature Phys.* **2,** 319 (2006).
23. Chang, Z. Single attosecond pulse and xuv supercontinuum in the high-order harmonic plateau. *Phys. Rev. A* **70,** 043802 (2004).
24. Strelkov, V. V. Theory of high-order harmonic generation and attosecond pulse emission by a low-frequency elliptically polarized laser field. *Phys. Rev. A* **74,** 013405 (2006).
25. Strelkov, V. V., Khokhlova, M. A., Gonoskov, A. A., Gonoskov, I. A. & Ryabikin, M. Y. High-order harmonic generation by atoms in an elliptically polarized laser field: Harmonic polarization properties and laser threshold ellipticity. *Phys. Rev. A* **86,** 013404-1-10 (2012).
26. Möller, M. *et al.* Dependence of high-order-harmonic-generation yield on driving-laser ellipticity. *Phys. Rev. A* **86,** 011401 (2012).
27. Shvetsov-Shilovski, N. I., Goreslavski, S. P., Popruzhenko, S. V. & Becker, W. Ellipticity effects and the contributions of long orbits in nonsequential double ionization of atoms. *Phys. Rev. A* **77,** 063405 (2008).
28. Lorek, E. *et al.* High-order harmonic generation using a high-repetition-rate turnkey laser. *Rev. Sci. Instrum.* **85,** 123106-1-5 (2014).
29. Bellini, M. *et al.* Temporal coherence of ultrashort high-order harmonic pulses. *Phys. Rev. Lett.* **81,** 297 (1998).
30. Lyngå, C. *et al.* Temporal coherence of high-order harmonics. *Physical Review A* **60,** 4823–4830 (1999).
31. Gaarde, M. B. *et al.* Spatiotemporal separation of high harmonic radiation into two quantum path components. *Phys. Rev. A* **59,** 1367–1373 (1999).
32. Torlina, L. & Smirnova, O. Time-dependent analytical *r*-matrix approach for strong-field dynamics. i. one-electron systems. *Phys. Rev. A* **86,** 043408 (2012).
33. Delone, N. B. & Kraïnov, V. P. Energy and angular electron spectra for the tunnel ionization of atoms by strong low-frequency radiation. *J. Opt. Soc. Am. B* **8,** 1207–1211 (1991).
34. Ammosov, M. V., Delone, N. B. & Kraïnov, V. P. Tunnel ionization of complex atoms and of atomic ions in alternating electromagnetic field. *Sov. Phys. JETP* **64,** 1191–1194 (1986).
35. Toma, E. S., Antoine, P., de Bohan, A. & Muller, H. G. Resonance-enhanced high-harmonic generation. *J. Phys. B: At., Mol. Opt. Phys.* **32,** 5843 (1999).
36. Taïeb, R., Véniard, V., Wassaf, J. & Maquet, A. Roles of resonances and recollisions in strong-field atomic phenomena. ii. high-order harmonic generation. *Phys. Rev. A* **68,** 033403 (2003).
37. Ganeev, R. A., Suzuki, M., Baba, M., Kuroda, H. & Ozaki, T. Strong resonance enhancement of a single harmonic generated in the extreme ultraviolet range. *Opt. Lett.* **31,** 1699–1701 (2006).
38. Milošević, D. B. High-energy stimulated emission from plasma ablation pumped by resonant high-order harmonic generation. *J. Phys. B: At., Mol. Opt. Phys.* **40,** 3367 (2007).
39. Strelkov, V. V. Role of autoionizing state in resonant high-order harmonic generation and attosecond pulse production. *Phys. Rev. Lett.* **104,** 123901 (2010).
40. Ackermann, P., Münch, H. & Halfmann, T. Resonantly-enhanced harmonic generation in argon. *Opt. Express* **20,** 13824–13832 (2012).
41. Ganeev, R. A. High-order harmonic generation in laser surface ablation: current trends. *Physics-Uspekhi* **56,** 772 (2013).
42. Fano, U. Effects of configuration interaction on intensities and phase shifts. *Phys. Rev.* **124,** 1866–1878 (1961).
43. Sörensen, S. L. *et al.* Argon 3s autoionization resonances. *Phys. Rev. A* **50,** 1218–1230 (1994).
44. Wang, H. *et al.* Attosecond time-resolved autoionization of argon. *Phys. Rev. Lett.* **105,** 143002 (2010).
45. Ott, C. *et al.* Reconstruction and control of a time-dependent two-electron wave packet. *Nature* **516,** 374–378 (2014).
46. de Boer, M. P. & Muller, H. G. A systematic study of ac stark shifts in xenon at super-high laser intensities. *J. Phys. B: At., Mol. Opt. Phys.* **27,** 721 (1994).
47. Mevel, E. *et al.* Contrasted behaviour of stark-induced resonances in multiphoton ionization of krypton. *J. Phys. B: At., Mol. Opt. Phys.* **25,** L401 (1992).
48. Rothhardt, J. *et al.* Enhancing the macroscopic yield of narrow-band high-order harmonic generation by fano resonances. *Phys. Rev. Lett.* **112,** 233002 (2014).
49. Varjú, K. *et al.* Frequency chirp of harmonic and attosecond pulses. *J. Mod. Opt.* **52,** 379 (2005).
50. L'Huillier, A. & Balcou, P. High-order harmonic generation in rare gases with a 1-ps 1053-nm laser. *Phys. Rev. Lett.* **70,** 774–777 (1993).
51. Salières, P. *et al.* Feynman's Path-Integral Approach for Intense-Laser-Atom Interactions. *Science* **292,** 902 (2001).
52. Rosenblatt, M. Remarks on some nonparametric estimates of a density function. *Ann. Math. Statist.* **27,** 832–837 (1956).
53. Parzen, E. On estimation of a probability density function and mode. *Ann. Math. Statist.* **33,** 1065–1076 (1962).

Acknowledgements

The authors acknowledge fruitful discussions with P. Johnsson, V. V. Strelkov, and M. B. Gaarde and thank S. L. Sörensen for the cross-section data for argon. This research was supported by the Swedish Foundation for Strategic Research, the Marie Curie program ATTOFEL (ITN), the European Research Council (PALP), National Science Foundation Grant number: PHY-1307083, the Swedish Research Council and the Knut and Alice Wallenberg Foundation.

Author Contributions

J.M. designed the experiment, E.L., C.M.H., E.W.L., A.L.H. and J.M. designed and built the experimental apparatus. D.Z. and D.P. provided the laser system. E.W.L., E.L. and S.C. conducted the experiments. E.W.L. performed the experimental data analysis and interpretation. S.C., E.W.L., K.J.S. and J.M. developed the semi-classical modeling. E.W.L., S.C., K.J.S. and J.M. wrote major parts of the manuscript. All authors contributed to the discussion of the results and commented on the manuscript.

Additional Information

Competing financial interests: The authors declare no competing financial interests.

How to cite this article: Larsen, E. W. *et al.* Sub-cycle ionization dynamics revealed by trajectory resolved, elliptically-driven high-order harmonic generation. *Sci. Rep.* **6**, 39006; doi: 10.1038/srep39006 (2016).

Publisher's note: Springer Nature remains neutral with regard to jurisdictional claims in published maps and institutional affiliations.

IV

Spatially and spectrally resolved quantum path interference with chirped driving pulses

Stefanos Carlström, Jana Preclíková, Eleonora Lorek, Esben Witting Larsen, Christoph Michael Heyl, David Paleček, Donatas Zigmantas, Kenneth Joseph Schafer, Mette B Gaarde, and Johan Mauritsson

Accepted for publication in: *New Journal of Physics*

Spatially and spectrally resolved quantum path interference with chirped driving pulses

Stefanos Carlström[1,6,*], Jana Preclíková[1,2,6], Eleonora Lorek[1], Esben Witting Larsen[1], Christoph M Heyl[1], David Paleček[3,4], Donatas Zigmantas[3], Kenneth J Schafer[5], Mette B Gaarde[5], and Johan Mauritsson[1,†]

[1]Department of Physics, Lund University, Box 118, 222 10 Lund, Sweden
[2]Department of Physics and Technology, University of Bergen, 5007 Bergen, Norway
[3]Department of Chemical Physics, Lund University, Box 124, 222 10 Lund, Sweden
[4]Department of Chemical Physics, Charles University in Prague, Ke Karlovu 3, 121 16 Praha 2, Czech Republic.
[5]Louisiana State University, Baton Rouge, 70803-4001, Louisiana, United States of America.
[6]These authors contributed equally to this work.

E-mail: *stefanos.carlstrom@fysik.lth.se, †johan.mauritsson@fysik.lth.se

Abstract. We measure spectrally and spatially resolved high-order harmonics generated in argon using chirped multi-cycle laser pulses. Using a stable, high-repetition rate laser we observe detailed interference structures in the far-field. The structures are of two kinds; off-axis interference from the long trajectory only and on-axis interference including the short and long trajectories. The former is readily visible in the far-field spectrum, modulating both the spectral and spatial profile. To access the latter, we vary the chirp of the fundamental, imparting different phases on the different trajectories, thereby changing their relative phase. Using this method together with an analytical model, we are able to explain the on-axis behaviour and access the dipole phase parameters for the short (α_s) and long (α_l) trajectories. The extracted results compare very well with phase parameters calculated by solving the time-dependent Schrödinger equation. Going beyond the analytical model, we are also able to successfully reproduce the off-axis interference structure.

PACS numbers: 42.65.Ky, 42.65.Re

Keywords: Quantum path interference, high-order harmonic generation, dipole phase parameters

Submitted to: *New J. Phys.*

1. Introduction

High-order harmonic generation (HHG) is a nonlinear optical process, in which a comb consisting of multiples of the driving laser frequency ω_0 is emitted coherently after interaction with a target [1, 2]. HHG and the understanding of the process itself has led to the field of attosecond physics [3], which enables the time-resolved observation of electron dynamics [4, 5, 6, 7].

The HHG process can be understood using a semi-classical three step model in which an electron is first ionized by tunnelling, is subsequently accelerated in the laser field, and finally returns to the ion core and upon recombination releases its excess kinetic energy leading to the emission of high energy photons [8, 9]. The generated harmonics are of odd orders since the process is repeated every half cycle of the laser field. This semi-classical understanding has been verified extensively through comparison with experiments and with more sophisticated calculations based on the integration of the time-dependent Schrödinger equation (TDSE) within the single-active-electron (SAE) approximation, either in its full numerical form [10] or within the strong field approximation (SFA) [11]. From this three-step model for HHG, it follows that for each harmonic energy there are multiple quantum paths (QPs) the electron can follow in the continuum. They correspond to different pairs of ionization and return times (t_i, t_r), that give rise to the same kinetic energy upon return. The two first QPs, termed the short and long QPs, both return within one cycle after ionization, with the short QP being released later and returning earlier than the long QP. The emission generated from each of these two QP contributions has different macroscopic coherence properties [12, 13, 14] because of the different microscopic phase that is imparted via the semi-classical action accumulated along each path. As we will describe in more detail below, this phase is approximately proportional to the cycle-averaged laser intensity with a phase coefficient α that increases with the time spent in the continuum. This means that the intensity dependence of the short-path contribution to the harmonic emission is much smaller than that of the long-path contribution. Therefore, the short QP emission has a smaller spectral and spatial divergence imparted by the temporal and radial variation of the laser intensity in the generation region.

The dipole properties of the HHG process may lead to various interference effects, since the same final energy is generated from several different trajectories. Interferences appearing as spectral and/or spatial structures in the harmonic far-field emission have been reported and identified as interferences between the short and the long quantum path contribution, known as quantum path interferences (QPI) [15, 16, 17, 18, 19]. Other works identify complicated spatial and spectral features of harmonics produced by individual quantum paths at high driving intensities, due to strong spatio-temporal phase and amplitude modulations in the generation medium [20, 21] or due to the spectral interference of adjacent harmonics [22].The emission from the short QP contribution has been characterized in much more detail [23, 24, 25] than that from the long QP contribution [22] as the latter is more difficult to accurately phase match and control experimentally [15, 19].

In this paper we present a detailed experimental characterization of the phase properties of the short and long QP contributions to HHG, via QPI in both the spectral and spatial

domain which we control through the chirp of the generating laser pulse, also changing the pulse duration and the intensity. We identify and distinguish quantum path interferences from macroscopic interference effects arising within the emission of the long trajectory. We use a commercial turn-key laser system that produces long multi-cycle pulses (with durations ≥ 170 fs, corresponding to ≥ 50 cycles at the driving wavelength $\lambda = 1030$ nm), which yield spatially and spectrally well-resolved harmonics with high signal-to-noise ratio. The stable operation of the laser in combination with the long and controllable pulses allow us to observe and characterize the QPI for a range of harmonics in argon spanning from harmonic 11, which is below the ionization threshold, to harmonic 37. In a single spectrum, clear spatial and spectral modulation of the harmonic order is visible, predominantly for the contribution of larger spatial and spectral divergence, i.e. the long QP contribution. The interference between the short and the long QPs, however, is not visible from one spectrum alone, but it is sensitive to intensity variation of the driving field. Therefore, controlling the shape of the driving pulse by adding a frequency chirp, the HHG process is affected through the increase in pulse duration and a decrease of the peak intensity. This reveals the interference between the short and long QPs, since their respective phases depend differently on the peak intensity. Additionally, the sign of the driving pulse chirp changes the spectral phase of the harmonic emission and in particular influences the QPs differently.

We implement a model based on the semi-classical description of HHG [14] as driven by a laser pulse, which is Gaussian in the temporal and spatial domain. This simple model captures the observed on-axis short–long QPI features very well and can be used to extract the phase coefficients α_s and α_l from the experimental results. We also compare the experimental results to numerical calculations performed both within the SAE-TDSE and the SFA. We measure experimental values for α_l in good agreement with those obtained in [15, 26]. For α_s we measure values that are small and negative for a range of low-order harmonics, indicating that the interaction between the returning electron and the ionic potential plays a substantial role in the generation of these harmonics. Negative values for α_s have been predicted in some calculations [24, 25] but have not to our knowledge been observed experimentally to this date.

We further investigate the off-axis interference structures by employing a more complete, but numerical model. The spectral–spatial modulation due to the long QP is very well reproduced by this model and explains the significance of the contributions that go beyond the analytical model, namely phase curvature effects of higher order than parabolic and the intensity dependence of the dipole phase parameters $\alpha_{s/l}$.

The paper is organized as follows: in section 2, the experimental method used to obtain the data is briefly outlined, and in section 3, these data are presented. In section 4, the mathematical model is described and in section 5 the quantum mechanical calculations used to verify our modelling are presented. Whereas sections 4–5 are mainly concerned with the short–long QPI, section 6 describes the interference structures visible off-axis, where no short QP is present. Finally, in section 7 we discuss our results and what we can extract from them.

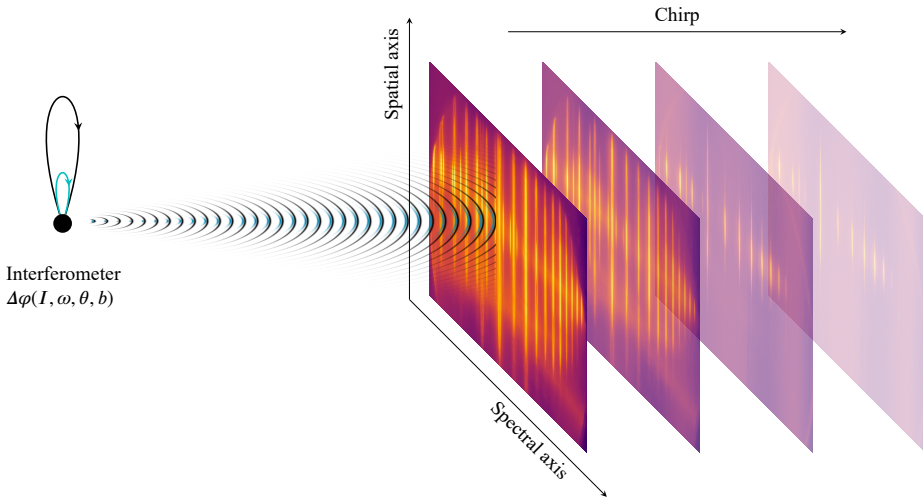

Figure 1. Experimental scheme; in our experiment the HH emission consists of contributions related to the two shortest QPs: short (blue) and long (black). We gradually vary the chirp of the driving pulses and observe spatially and spectrally resolved HH. The experiment can be understood as an interferometer, where the phase difference $\Delta\varphi$ between the long and short trajectories varies with the driving intensity I, the emitted frequency ω and the angle of emission θ and the chirp parameter b.

2. Experimental method

The high-order harmonics (HHs) were generated in argon by a commercially available compact Yb:KGW PHAROS laser (Light Conversion). The pulse energy was 150 µJ, the central wavelength $\lambda = 1030$ nm and the repetition rate was set to 20 kHz. The pulse-to-pulse stability of this laser is < 0.5 % rms over 24 hours. The duration and chirp of the pulses were varied by adjusting the grating compressor. The adjustment of the grating enabled a gradual change of the pulse duration from negatively chirped pulses of 500 fs to Fourier-transform (FT) limited pulses of $\tau_{\mathrm{FT}} = 170$ fs to positively chirped pulses of 500 fs (corresponding to 50–145 cycles) in 106 steps. The acquisition time for one image was around 80 ms, averaging around 1600 shots.

The calibration of the pulse duration as a function of the grating position was based on the peak intensity of the pulse. The observed cut-offs of HHs 25–37 were mapped to a specific driving intensity using the cut-off law

$$q\hbar\omega_0 = 3.17\frac{e^2 I_0(\tau)}{2c\epsilon_0 m\omega_0^2} + I_{\mathrm{p}} = 3.17U_{\mathrm{p}} + I_{\mathrm{p}}, \tag{1}$$

where q is the harmonic order, $\hbar$ is the reduced Planck constant, ω_0 is the angular central frequency of the driving laser, I_{p} is the ionization potential of argon, e and m are the charge and the mass of electron, ϵ_0 is the permittivity of vacuum and $I_0(\tau)$ is the peak laser intensity for the pulse of duration τ, at the centre of the driving field. The laser peak intensity is taken

to vary as

$$I_0(\tau) = I_0(\tau_{\mathrm{FT}})\frac{\tau_{\mathrm{FT}}}{\tau}, \tag{2}$$

where the peak intensity at FT-limited duration $I_0(\tau_{\mathrm{FT}})$ is on the order of $10^{14}\,\mathrm{W\,cm^{-2}}$. The laser beam with a diameter of 3.5 mm was focused by an achromatic lens with a focal length 100 mm, resulting in a beam waist of 18 µm (estimated using Gaussian optics). As generating medium argon gas was used, supplied through an open-ended, movable gas nozzle with 90 µm inner diameter. The relative position of the nozzle and the laser focus was such that phase matching allowed the observation of both short and long trajectory harmonics [27, 28].

The generated harmonic emission was analysed by a flat-field grazing-incidence XUV spectrometer (based on Hitachi Grating 001-0639, with the nominal line-spacing of 600 lines/mm). The grating diffracted and focused the harmonics in the dispersive plane and reflected them in the perpendicular direction onto a 78 mm diameter microchannel plate (MCP, Photonis), which was imaged by a CCD camera (Allied Vision Technologies, Pike F-505B with a pixel size of 3.45 µm × 3.45 µm; the resolution was set to 2000 pixels × 2000 pixels and the dynamic range to 14 bits). This arrangement allowed to study the spectral content of the emission as well as the divergence of the individual harmonics. The HH spectra were recorded for 106 positions of the pulse compressor grating, see figure 1. A more detailed description of the setup can be found in [29].

3. Experimental results

A typical image of HHs on an MCP is displayed in figure 2(a) for the case of a FT-limited driving pulse. The HHs are both spatially and spectrally divergent, with clear ring structures appearing around a strong, narrow central structure. The off-axis structures are attributed to the long QP only, whereas the on-axis structures contain both QPs. However, the on-axis structures do not show to any visible modulation in a single spectrum. To reveal the on-axis interference, the acquired HH spatial–spectral profiles for 106 different values of the chirp parameter were analysed by plotting different lineouts of the images as a function of the driving pulse duration. The spatial–spectral profile of $q = 17$ is shown magnified in figure 2(b). The horizontal axis (and lineouts) correspond to the spectral variation, whereas the vertical axis (and lineouts) to the spatial variation. The lines represent regions of interest, from which subfigures (c)–(f) are extracted. (d) and (e) are the spectral and spatial lineouts of the central area of the generated harmonics with contribution from both the long and short trajectories, while the off-axis lineouts (c) and (f) show mainly behaviour of the long trajectory contribution, therefore lacking interference between the two trajectories (however, long–long interference remains). In the following analysis we focus on the on-axis areas, where short–long QPI patterns are apparent, as in (d) and (e). The spatial and spectral lineouts for other orders are presented in sections 4.1 and 4.2. We return to the off-axis interference structures in section 6.

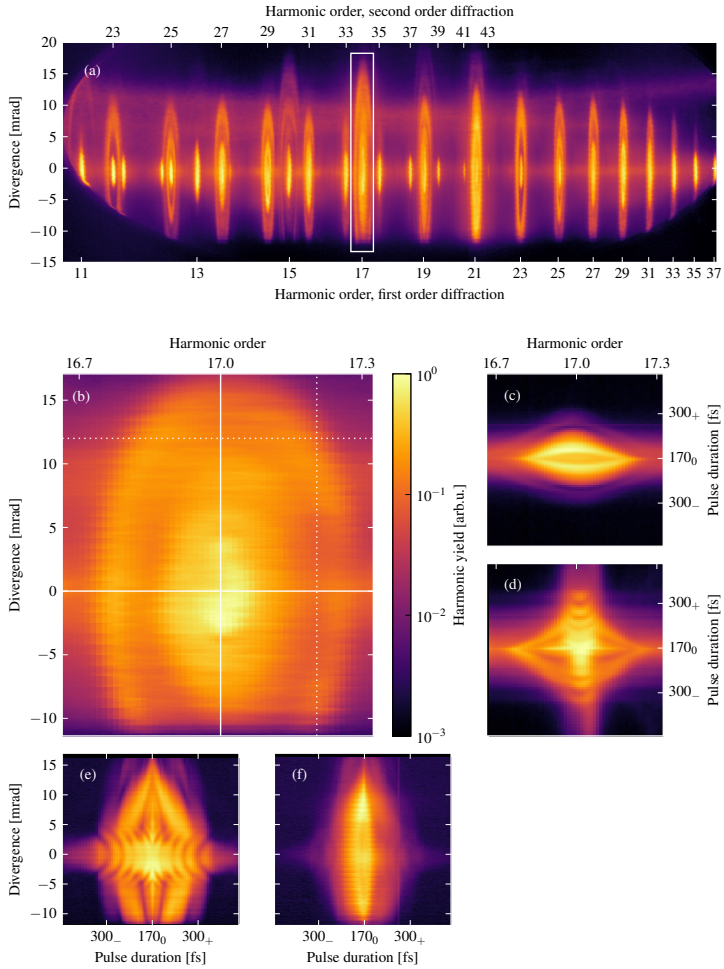

Figure 2. (a) Observed HHs as recorded by MCP under driving with transform-limited pulses, numbers indicate the spectral position of the first and second order diffraction of HHs for $q = 11 - 43$, the rectangle shows the area, for which an example of the analysis is given. (b) Magnified image of the area around HH17. The solid lines indicate where the lineouts on-axis and on the central harmonic energy, respectively, were made. Similarly, the dotted lines indicate where the lineouts off-axis and off the central harmonic energy were made. (c) shows the off-axis spectral lineouts corresponding mainly to the long trajectory contribution, while (d) shows the on-axis spectral lineout with a clear QPI pattern. Similarly, (e) shows the on-centre spatial lineout with a clear QPI pattern and (f) is a spatial lineout covering mainly the long trajectory contribution. $300_{+/-}$ fs means 300 fs pulse duration with positive/negative chirp; 170_0 fs means FT-limited duration. The colour scale is logarithmic and is the same in all figures throughout the article, unless stated otherwise.

4. Mathematical model

To explain and analyse the observed QPI, we have developed a mathematical model based on the interplay of the HH contributions from different QPs; similar to the simple model of [14]. We concentrate on the two first trajectories, the so called short (s) and long (l). The main difference is that, since the long trajectory spends more time in the continuum, it acquires more phase which leads to larger divergence, both spatially and spectrally. This phase is labelled $\Phi_{s/l}$. Using the SFA, the dipole phase can be calculated by integrating the semi-classical action [11, 25] (in atomic units):

$$\Phi_{s/l}(t_i, t_r, \mathbf{p}) = q\omega_0 t_r - \int_{t_i}^{t_r} \mathrm{d}t \left\{ \frac{[\mathbf{p} + \mathbf{A}(t)]^2}{2} + I_\mathrm{p} \right\}, \tag{3}$$

where the trajectory of the electron is defined by its ionization time, t_i, return time, t_r, and momentum $\mathbf{p}$. $\mathbf{A}(t)$ is the vector potential of the driving field. In figure 3, (3) is plotted for a few different harmonic orders, using the experimental conditions of the present work. The ionization time t_i and the return time t_r are found by solving Newton's equations of an electron in an electric field. The general behaviour of the phases as a function of intensity leads us to the following approximate expression:

$$\Phi_{s/l}(r, z, t) = \Phi^0_{s/l} + \alpha_{s/l} I(r, z, t), \tag{4}$$

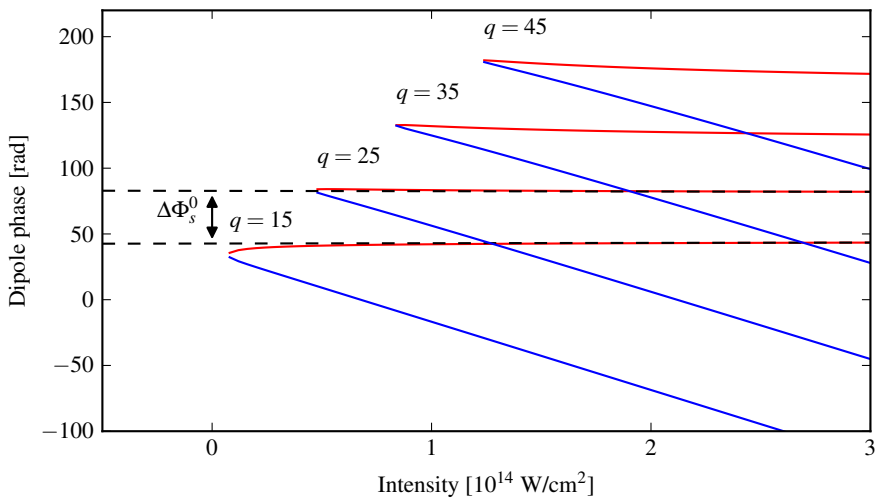

Figure 3. Dipole phase as a function of intensity, for different high-order harmonics of $\lambda = 1030\,\mathrm{nm}$, calculated using (3). The red (blue) lines correspond to the short (long) trajectories. For the intensities used in the experiment ($4 \times 10^{13}\,\mathrm{W\,cm^{-2}}$ to $1 \times 10^{14}\,\mathrm{W\,cm^{-2}}$), the curves are well approximated by (4). The two dashed lines are fits to the asymptotes of the red lines, i.e. they are not perfectly horizontal. The slopes of these fits are $-\alpha_s$.

where $\Phi^0_{s/l}$ is a phase offset and $\alpha_{s/l}$ are slopes of the phases as function of the intensity [14]. This adiabatic model is valid for the experimental conditions of the present work [30].

In our simple model, we assume a tight-focus geometry with a small interaction volume and we only consider HH generated in the focal plane $z = 0$.

4.1. Divergence

To model the behaviour of the harmonics along the divergence axis as the pulse duration varies, the emission from the two trajectories is approximated as a sum of Gaussian beams. Such beams can be propagated to the far field analytically (in the paraxial approximation), and the geometrical properties necessary are determined from the experimental conditions. In Appendix A.1, the full derivation of the divergence model can be found. The main result is that the total far field can be written in cylindrical coordinates as

$$E_{\text{detector}}(r, z) = E_s(r, z) + E_l(r, z), \tag{5}$$

where

$$E_{s/l}(r, z) = C_{s/l} I_0^{\frac{n}{2}}(\tau) W(z) \exp\left[-\mathrm{i}G(r, z; r_0, z^R) + \mathrm{i}\Phi_{s/l}(r, z)\right]. \tag{6}$$

$C_{s/l}$ are weights for the trajectories, n is a nonlinearity parameter, $W(z)$ and $G(r, z; r_0, z^R)$ are functions depending on the geometry as well as the ionization process, whereas $\Phi_{s/l}$ is the phase in (4), which only depends on the atomic properties. r_0 is the beam waist (18 µm) and z^R the effective Rayleigh range (∼1 mm).

The spatial profiles of the generated HH beams are calculated for $q = 11 - 37$, using the variation of the pulse duration τ as in the experiment. The experimental input values are λ, r_0, z and $I_0(\tau)$ [determined using (1)], whereas unknown parameters are Φ^0_s,Φ^0_l,α_s, α_l, n and the ratio $C_l^2 : C_s^2$. In our procedure we neglect the influence of phase offset difference $|\Phi^0_s - \Phi^0_l|$ – it influences only the phase of the fringe pattern (with 2π periodicity), but not the shape. The procedure for retrieving the values of $\alpha_{s/l}$ for the different harmonics is the following: 1) The experimental spatial lineouts are normalized separately for each harmonic, 2) positions of interference maxima and minima are determined [shown as the white and black lines overlaid in figure 4] in order to highlight the shape of the interference pattern, 3) the parameters of the model are then fitted such that the frequency of the fringes and their curvature in the model match that of the experiment (see figure 4 for $q = 17$). The phase difference $(\alpha_l - \alpha_s)I$ between the two trajectories can by itself explain the observed frequency of the fringes, on-axis. However, we have more information available in that the fringe pattern has a curvature, which allows us to retrieve not only the difference between $\alpha_{l/s}$, but also their absolute values. This is because the curvature of the fringes depends on mean value $(\alpha_l + \alpha_s)/2$ as well as on the difference $\alpha_l - \alpha_s$, which is why an iterative fit has to be made. The contrast and the overall intensity of the divergence pattern, are mainly affected by nonlinearity parameter n and by the ratio of long and short trajectory contribution $C_l^2 : C_s^2$.

For $q = 15 - 21$, automated fitting of the model to the experimental data could be done, while for the higher harmonics, a visual fit was the only option, since the interference signal was too weak for these harmonics. The retrieved values of the parameters are listed in table 1.

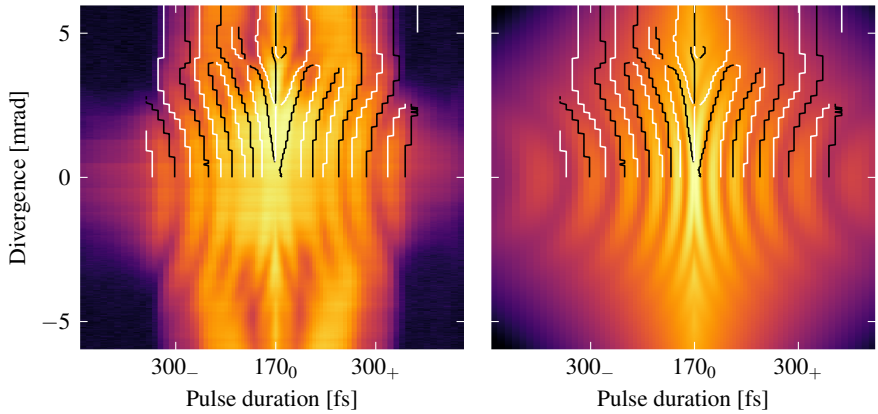

Figure 4. Illustration of the fitting procedure for retrieval of the values of $\alpha_{s/l}$ for the different harmonics. In the left panel the experimental data are shown with the maxima (white lines) and minima (black lines) extracted. In the right panel, the coloured map is the result of the mathematical model described in section 4.1, while the lines are the same as in the left panel. $300_{+/-}$ fs means 300 fs pulse duration with positive/negative chirp; 170_0 fs means FT-limited duration.

In figure 5(b), the far-field divergence profiles as simulated by the spatial model are shown for the values of $\alpha_{s/l}$ as extracted by the fitting procedure described above (these values are presented in table 1). To be noted is that the model manages to reproduce the hyperbolic fringes visible for divergences smaller than ~ 5 mrad; however, the prominent ring structure visible for larger divergences are not reproduced by this model. As will be discussed in more detail in section 6, the rings arise when including higher-order terms than parabolic in the phase curvature. The ring structure in a given harmonic depend on higher-order corrections to the harmonic phase beyond the simple linear dependence on the intensity with phase coefficient α. In particular, the far-field radiation pattern for the long-trajectory harmonics consists of interfering contributions from parts of the near-field where these harmonics belong to the plateau and parts of the near-field where these harmonics belong to the cut-off. Such contributions to the same harmonic will have different values of α.

Table 1. Values of parameters used in the divergence model [see figure 5(b)] for the simulation of the spatial profiles of generated HH.

q	11	13	15	17	19	21	23	25	27	29	31	33	35	37
$\alpha_s/(10^{-14}\,\mathrm{cm^2\,W^{-1}})$	−10	−11	−10	−10	−10	−9	−7	−5	5	15	15	18	20	24
$\alpha_l/(10^{-14}\,\mathrm{cm^2\,W^{-1}})$	50	50	51	50	43	43	40	38	35	35	33	31	28	24
n	6	8	7	7	6	6	6	6	7	10	10	11	14	17
$C_l^2 : C_s^2$	2	2	100	100	100	100	100	100	100	100	100	30	50	5

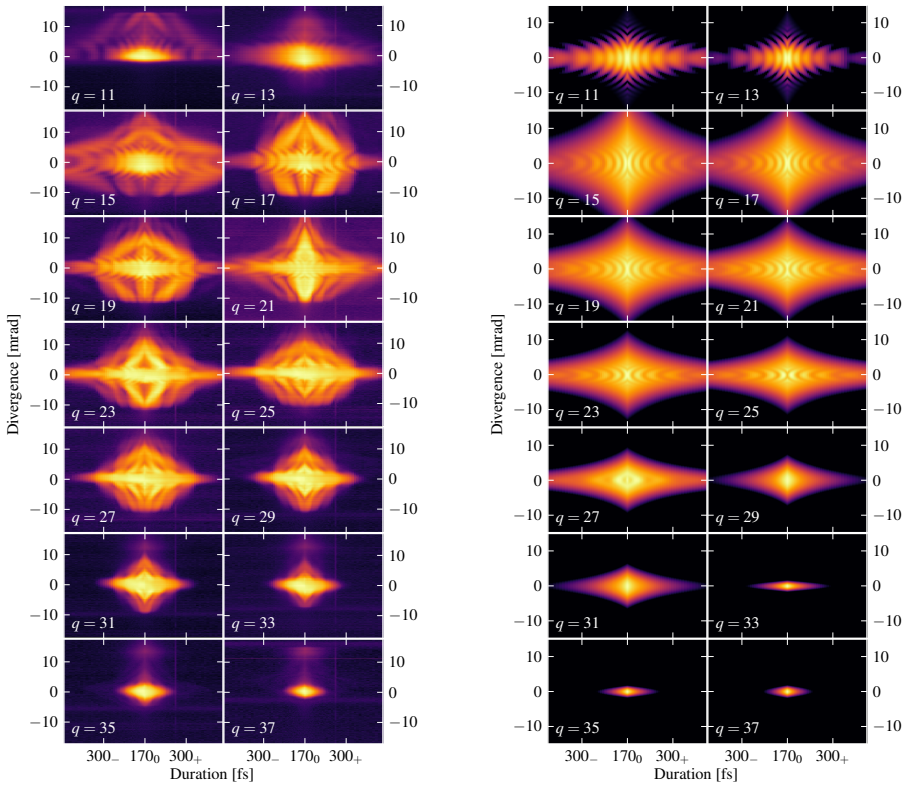

(a) Experiment. (b) Model.

Figure 5. Comparison of experimental and modelled data for variation of divergence profiles with gradually varied duration of the driving pulses for $q = 11 - 37$. In the left part of the images the driving pulses are negatively chirped, whereas in the right part are positively chirped. The signal for the low harmonic orders, especially apparent for $q = 11$, is limited to positive divergence by the shape of the MCP.

4.2. Spectrum

To understand the variation of the spectral profile as a function of the driving field chirp, it is important to model the temporal behaviour of the harmonic generation, and particularly its response to change in instantaneous frequency. The detailed derivation can be found in Appendix A.2. The main result this time is that the field contribution for a given harmonic from the short/long trajectory can be written

$$E_{s/l}(t) = C_{s/l} I^{\frac{n}{2}}(t) \exp\left[\mathrm{i}q\omega_0 + \mathrm{i}\frac{qb(\tau)}{2}t^2 + \mathrm{i}\alpha_{s/l} I(t) + \mathrm{i}\Phi^0_{s/l}\right]. \tag{7}$$

The far-field spectra of the generated HHs are computed as the Fourier transform of the

sum of the fields generated by the short and long trajectory contributions

$$S(\omega) = \mathcal{F}[E_s(t) + E_l(t)], \tag{8}$$

and the intensity in the far field is given by

$$I(\omega) \propto |S(\omega)|^2. \tag{9}$$

The simulated spectra are shown in figure 6(b). The experimental input parameters are the same as for the spatial profile simulation and the retrieved values of the parameters are listed in table 2. Again, $\Phi^0_{s/l}$ is assumed to be zero, since it only influences the phase of the interference fringes, but not their shape. When determining the values of $\alpha_{s/l}$, the main attention is given to the width of the measured spectra and to the curvature of the QPI fringes. The values were found by a pure visual fit of the model to the experimental data, no automated fitting was employed. The n was kept same as in the simulation of the divergence lineouts, while the ratio $C_l^2 : C_s^2$ had to be decreased, due to the fact that only the middle part of the divergence cone is evaluated [see figure 2(d)]. In this cone, the relative contribution of the short trajectory is much stronger than when a broad divergence region is considered, leading to a lower ratio $C_l^2 : C_s^2$.

The asymmetric behaviour of the central part of the spectra with respect to the chirp parameter (clearly apparent in figure 6(a) for $q = 13, 15, 17$), enables us to determine negative values of α_s in the region below threshold and in the plateau. It is possible to make this identification, since the central part of the spectrum is dominated by the short trajectory contribution. The instantaneous frequency of the generated HH field is described by (A.15) – the time derivative of the argument of (7). For negatively chirped pulses, the chirp of the driving pulse [the second term in (A.15)] has the same sign as the chirp introduced by the dipole phase [third term in (A.15)] and a broad spectrum of frequencies is generated. In contrast, when the pulse is positively chirped, the second and third terms have opposite signs and partly compensate each other, with a narrower spectrum as the result. The negative sign of α_s for the low orders leads to this compensation occurring for negatively chirped pulses (the left side of the spectra in figure 6), while for higher orders, the compensation occurs for positively chirped pulses (the right side of the spectra in figure 6). The sign change occurs around harmonic 23, where the narrowest spectrum of short trajectory is found for FT-limited pulses. For the long trajectory, all α_l are positive, such that the compensation always occurs for positively chirped pulses.

Table 2. Values of parameters used in the spectral model [see figure 6(b)] for the simulation of the spectral profiles of generated HH.

q	11	13	15	17	19	21	23	25	27	29	31	33	35	37
$\alpha_s/(10^{-14}\,\mathrm{cm^2\,W^{-1}})$	−10	−11	−9	−10	−8	−4	−2	4	10	14	16	20	20	20
$\alpha_l/(10^{-14}\,\mathrm{cm^2\,W^{-1}})$	35	40	48	55	56	50	45	50	40	35	30	27	27	27
n	6	8	7	7	6	6	6	6	7	10	10	11	14	17
$2C_l^2 : C_s^2$	1	1	1	1	1	1	1	1	1	1	1	1	1	1

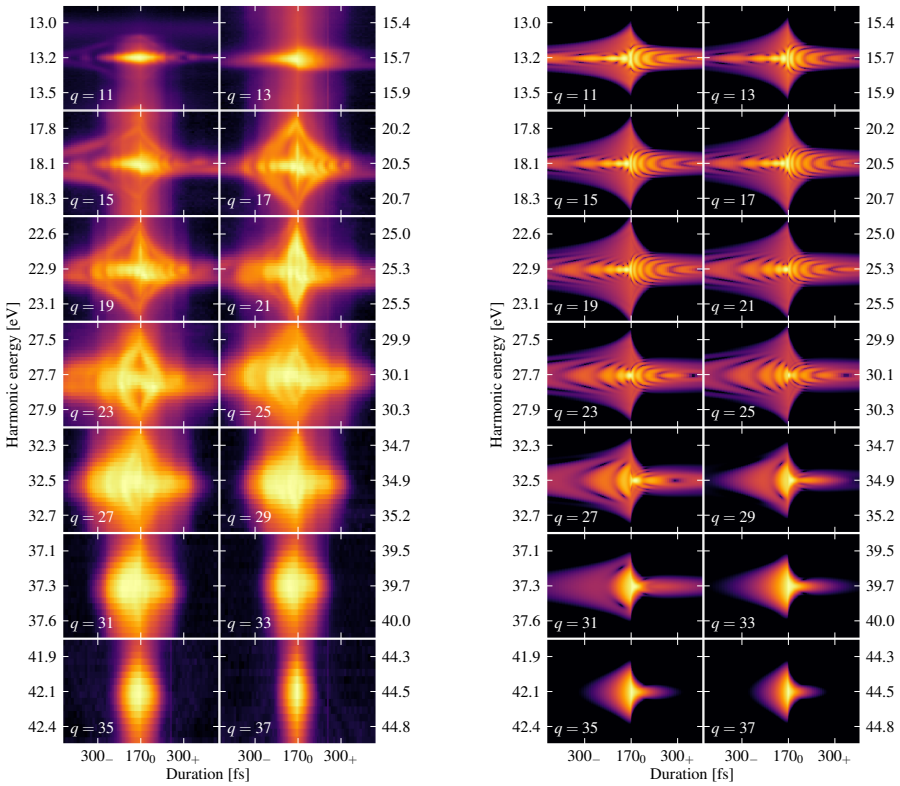

(a) Experiment. (b) Model.

Figure 6. Comparison of experimental and modelled data for variation of HH spectra with gradually varied duration of the driving pulses for $q = 11 - 37$. In the left part of the images the driving pulses are negatively chirped, whereas in the right part they are positively chirped. As is explained section 4.2, the fit of the spectral model to the data was purely visual, matching the the amount of fringes and their positions.

4.3. Dipole phase parameters

In figure 7, the retrieved values of $\alpha_{s/l}$ from both the divergence model and the spectral model, are shown. The values of $\alpha_{s/l}$ predicted by different theoretical calculations and retrieved for various experimental conditions (driving wavelengths λ and intensities I) can be compared, by expressing them in dimensionless values $\alpha^*_{s/l}$ related to the optical cycle of the driving pulse:

$$\alpha^*_{s/l} = \frac{2c\epsilon_0 m\omega_0^3\hbar}{e^2}\alpha_{s/l}. \tag{10}$$

The theory predicts the values of $\alpha^*_l \approx 2\pi$ and $\alpha^*_s \approx 0$ in the plateau region, with both values converging to π towards the cut-off [31, 25]. The errors in the parameters $\alpha_{s/l}$ are difficult

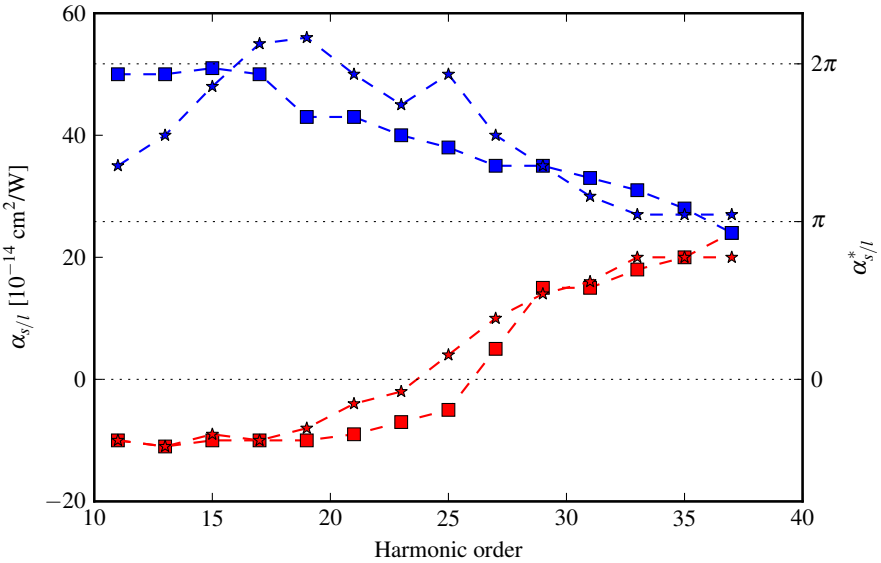

Figure 7. Overview of the retrieved dipole phase parameters α_s and α_l from the divergence model (squares) and from the spectral model (stars), for long (blue) and short (red) trajectory, along with their estimated uncertainties. The right-hand scale is calculated according to equation (10).

to quantify. It is possible to make an estimate by comparing the values extracted using the divergence model and spectral model. They should in principle yield the same values, since they are both based on the assumption that the phase can be written as stated in (4). However, since the spectral data are extracted from a smaller part of the divergence cone than the spatial data, the former are more sensitive to errors which could explain the larger variation in the data. An estimate of the error is given by the mean discrepancy between the two models, which is $\sim 2.5 \times 10^{-14}$ cm^2 W^{-1} for the short trajectory and $\sim 6 \times 10^{-14}$ cm^2 W^{-1} for the long trajectory.

5. Quantum mechanical calculations

For comparison, calculations of the HH yield are performed by integrating the TDSE for a range of intensities using a newly developed graphics processing unit (GPU) implementation of the algorithm outlined in [32]. For a large range of intensities, the time-dependent dipole acceleration $a(t, I)$ of the atom is computed, and the quantum path distributions (QPDs) are extracted in the same manner as described in great detail in [33]; first a Fourier transform is performed to get the spectrum $a(\omega, I)$ and subsequently, for each harmonic order q, a Gabor transform is performed along the intensity axis to obtain the QPDs $a(q; I, \alpha)$. In figure 8, the

QPDs leading to emission of the different harmonics are plotted in an intensity range around the experimental intensity, along with the experimentally retrieved values of $\alpha_{s/l}$ as presented in tables 1, 2. For comparison, the same procedure is performed for the SFA; the main difference is that the long trajectory is much more pronounced in the SFA, whilst the TDSE also shows longer trajectories. In general, though, they both agree well with the experimental results.

One important difference compared to the models presented above, is that these calculations are performed at slightly lower intensity, $7 \times 10^{13}\,\mathrm{W\,cm^{-2}}$ as compared to $1 \times 10^{14}\,\mathrm{W\,cm^{-2}}$. These calculations are performed using a trapezoidal pulse shape, with exactly this intensity, while in the experiment and the models, the pulse shape is Gaussian, which naturally spans a distribution of intensities, up to the nominal intensity, $I_0(\tau_{\mathrm{FT}})$.

6. Analysis of off-axis ring-like structures

In figure 9, a theoretical far-field spectrum calculated for the parameters of the experiment is shown. The time-dependent dipole acceleration $a(t)$ is calculated by the TDSE for a set of atoms in the focal plane. The collective emission is propagated to the far-field, as is described below in section 6.2. Qualitatively, the agreement with the experimental spectrum in figure 2(a) is very good; the appearance of further spatial modulation can be attributed to the lack of intensity averaging as is present in the experiment. Notably, the ring-like structures off-axis (i.e. for divergences ≥ 5 mrad) are present, whereas they are missing in the results of the Gaussian model in its parabolic phase approximation as presented in figure 5(b). This can be understood as follows: The harmonic emission can be written as

$$E(r,t) = A(r,t)\exp[\mathrm{i}\Phi(r,t)], \tag{11}$$

where $A(r,t)$ is the amplitude and $\Phi(r,t)$ the phase, both dependent on the location and time of emission. If we assume we can divide the emission into different contributions from different harmonic orders q and different trajectories j, we get

$$E(r,t) = \sum_{qj} A_q(r,t)\exp[\mathrm{i}\Phi_{qj}(r,t)], \tag{12}$$

with

$$\Phi_{qj} = \Phi^0_{qj} + \underbrace{\frac{\partial \Phi_{qj}}{\partial I}}_{\alpha_{qj}} I(r,t) + O\left(\frac{\partial^2 \Phi_{qj}}{\partial I^2}\right),$$

and

$$\Phi^0_{qj} = q\Phi_0(t) + \Phi_{qj}(I_0)$$

contains the phase of the fundamental $\Phi_0(t)$ and the atomic dipole response at the peak of the field. In the Gaussian model, the amplitude $A_q(r,t)$ is of the form $I^{\frac{n}{2}}(r,t)$, where the

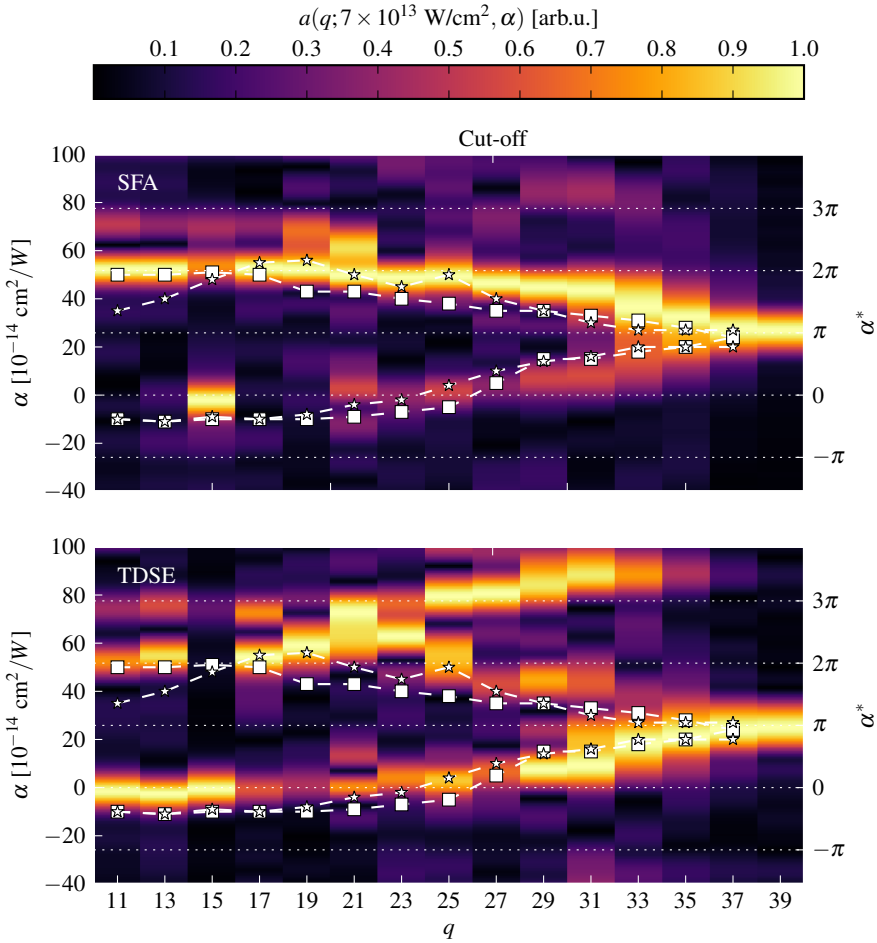

Figure 8. Quantum path distributions (QPDs), normalized, for the harmonics q =11–39, calculated at the driving field intensity 7×10^{13} W cm^{-2}. Bright regions correspond to more likely values of α for a certain harmonic order. The white lines correspond to the experimentally retrieved values of α, with the lower values belonging the short trajectories and the higher values to the long trajectory. The right-hand α^* (the variable conjugate to I) scale is given in radians in accordance with (10).

In the SFA, the long trajectory is significantly more prevalent compared to the short trajectory, and this has been observed before [33]. In contrast, the TDSE yields short and long trajectories of comparable weight, and even longer trajectories are visible; also this is a previously known result [34]. The third trajectory has not been observed in the experiments, which might be due to the unfavourable phase matching conditions.

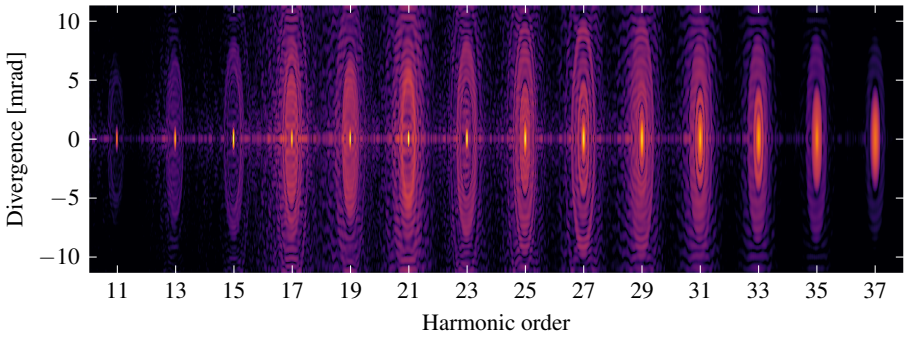

Figure 9. Theoretical far-field spectrum [cf. figure 2(a)], for the case for FT-limited driving pulse (170 fs). The single-atom response of a set of atoms is calculated using the TDSE and propagated via a Hankel transform to the far-field.

fundamental field intensity is given by

$$\begin{aligned} I(r,t) &= I_0(\tau)\exp\left(-\frac{t^2}{2\tau^2}\right)\exp\left(-\frac{r^2}{2r_0^2}\right) \\ &= I_0(\tau)\exp\left(-\frac{t^2}{2\tau^2}\right)\left[1-\frac{r^2}{2r_0^2}+\frac{r^4}{8r_0^4}+O(r^6)\right]. \end{aligned} \tag{13}$$

The normal approximation is to neglect terms of $O\left(\frac{\partial^2\Phi_{qj}}{\partial I^2}\right)$ and higher. Furthermore, it is only possible to analytically propagate the emission to the far-field if the radial profile of the intensity in the phase is approximated up to second order in r. By including higher-order terms of the spatial profile through a numerical far-field transform, ring structures appear in the far-field amplitude (see figure 10). It is not enough, however, to fully explain the off-axis behaviour of the interference rings – the long trajectory also probes a wider range of intensities, also those for which a certain harmonic would be considered to be in the cut-off regime. This means we cannot ignore the influence of $\frac{\partial^2\Phi_{qj}}{\partial I^2}$ and higher-order terms in the expansion of the phase with respect to the intensity. The effects of these considerations will be briefly surveyed below.

6.1. Adiabatic model

The Gaussian model in its simplest form does not explain the correct behaviour of the off-axis emission. To find the missing link, we employ an adiabatic model, where instead of assuming the form (12), we opt for something in-between (11) and (12):

$$A(r) = \sum_q a[q; I(r)], \tag{14}$$

that is, we still decompose the emission into different harmonic orders, but it is not trajectory-resolved anymore. $a[q; I(r)]$) can be the dipole acceleration moment for harmonic order q as calculated using the TDSE, in the manner described in section 5, or the dipole spectrum from the SFA. The model is adiabatic inasmuch it does not consider the temporal intensity variation of the driving pulse, but only the spatial intensity variation $I(r)$ at the peak of the pulse. Furthermore, only emission from the focal plane is considered.

6.2. Exact far-field propagation

The far-field amplitude of the emission is found by propagation. In cylindrical coordinates and cylindrical symmetry, this is given by [35]:

$$U_0(\rho) = -\mathrm{i}\frac{k}{2\pi z}\exp(\mathrm{i}kz)\exp\left(\mathrm{i}\frac{k}{2z}\rho^2\right)\mathcal{H}_0\{A(r)\}(k\rho/2\pi z), \tag{15}$$

where $\mathcal{H}_0\{A(r)\}$ is the zeroth-order Hankel transform of the near-field radial amplitude $A(r)$, r is the near-field radial coordinate, ρ is the far-field radial coordinate, k is the wavevector $q2\pi/\lambda$ (q is the harmonic order and λ is the fundamental wavelength) and z is the propagation distance. The Hankel transform is computed numerically using the algorithm presented in [36].

6.3. Off-axis interference structures

Propagating a Gaussian profile with a non-flat phase variation gives modulation of the far-field amplitude, as seen in figure 10. Depending on the form of the near-field phase variation with the spatial profile, different structures appear.

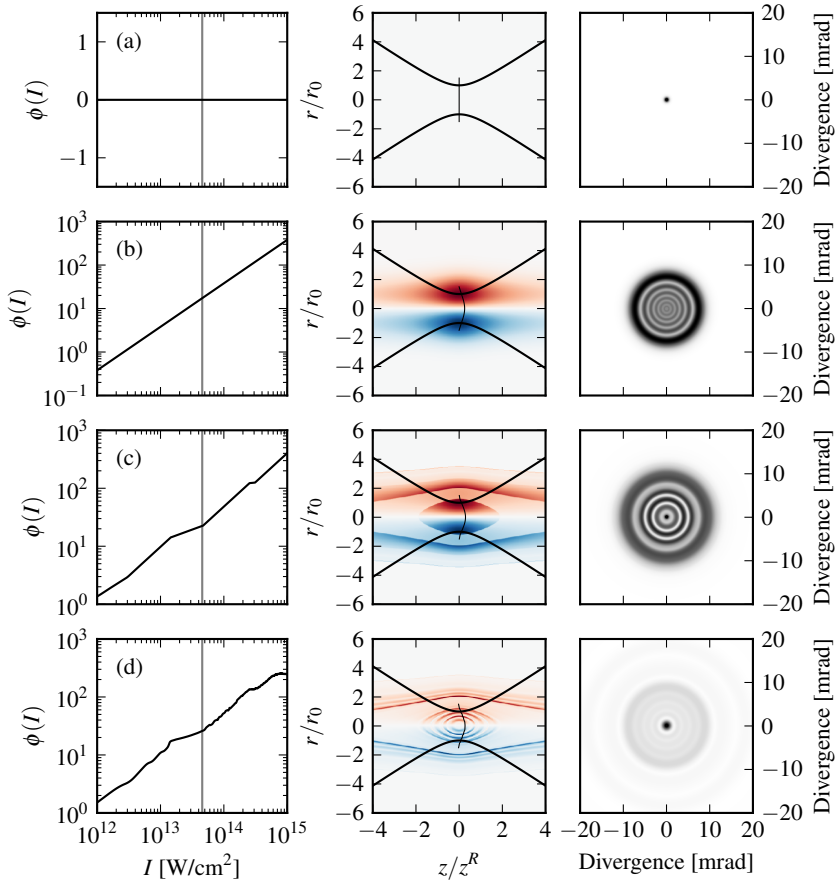

Figure 10. Explanation of how the off-axis rings come about. The left-most column shows the phase variation of HH25 in the focal plane, as a function of the fundamental intensity, for the case of no variation (a), a phase proportional to the intensity (b), a crude fit to the phase as calculated by the SFA (c) and the full SFA phase (d). The second case corresponds to (4). The grey, vertical line indicates the cut-off intensity for HH25; for lower intensities, HH25 is a cut-off harmonic, while for higher intensities, it is in the plateau regime. The middle column indicates with solid black lines, the beam waist of the driving field as a function of z, and the wavefront in the focal plane. The colour map behind shows $\frac{\partial \phi}{\partial r}$, which is related to the k vector; emission from areas of the same colour will have the same direction. The right-most column shows the far-field amplitude. With a flat phase in the focal plane, the Gaussian shape will be preserved. With a simple Gaussian phase (as the intensity profile of the fundamental is Gaussian) in the near-field, ring structures will appear in the far-field amplitude. With more complicated phase behaviour in the near-field, the far-field amplitude will also be more complicated.

In figure 11, the interference pattern for $q = 25$ is displayed, from the experiment as well as calculated using the adiabatic model, for a few different phase variations with the spatial profile. Whereas both the TDSE and the SFA qualitatively agree quite well with the experiment, the Gaussian beam model does not. It is thus necessary, but not sufficient, to include higher-order terms in the expansion of the intensity profile. Indeed, one must also include higher-order terms in the variation of the phase with the intensity. For the short–long interference, this mainly takes place where two trajectories actually *exist*, namely in the plateau regime. The values of $\alpha_{s/l}$ as presented in tables 1, 2, reflect this by successfully reproducing the short–long interference, but not the long–long, as is evident when comparing with the TDSE/SFA.

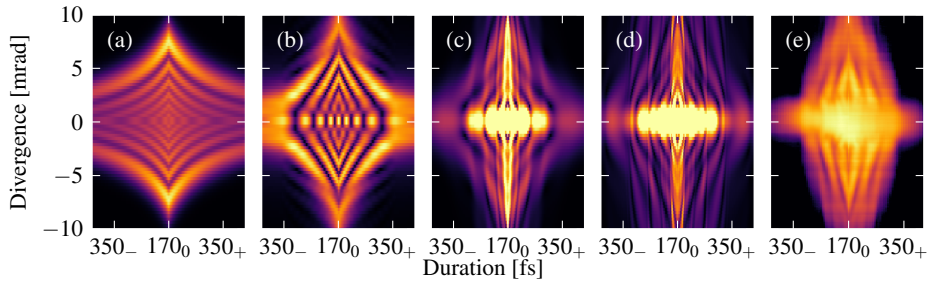

Figure 11. Far-field propagation of HH25 for a few different cases: (a) Gaussian model, long trajectory only [figure 10 (b)], (b) SFA log-fit phase [figure 10 (c)], (c) SFA [figure 10 (d)], (d) TDSE, (e) experiment. The short–long trajectory contributions has been saturated to focus on the off-axis interference; the colour scale of the theory (a–d) is linear while that of the experiment (e) is logarithmic as above, due to the much higher dynamic range of the theory.

It cannot be said that the model presented in figure 10 (c), figure 11 (b) only probes the long–long interference, since it is a fit to the phase as given by the SFA; however, as seen in figure 8, the SFA underestimates the short trajectory contribution compared the long trajectory. A crude fit to the SFA phase would thus smooth out any contribution of low amplitude such as the short trajectory one. We can thus say that the model essentially shows the long trajectory behaviour as is apparent from the emphasis on off-axis ring behaviour and suppression of the short–long interference at 0 mrad, which *is* visible in the SFA calculation shown in figure 11 (c).

7. Discussion

We find that our mathematical models agree well with the experimental data in the central regions of the spatial and spectral lineouts (figures 5 and 6). They show the robustness of the simple model introduced in [14], even when it is extended to chirped driving fields. It is a clear sign of QPI, similar to the one described in [37], where QPI was studied using excitation by a weak perturbation consisting of a laser pulse with controlled delay. In analogy with that

study, we can think of varying the chirp of the driving pulse as the addition of a controlled perturbation to the driving field.

As noted above, the pulse intensity is only dependent on the magnitude of the chirp parameter b. This behaviour is clearly reflected in the spatial lineouts, for which the peak intensity is the parameter with largest influence; the lineouts are vertically and horizontally symmetric. The data presented in figure 5(a) are analogue to the intensity scans presented in earlier work [17, 38, 39, 40, 41, 19]. However, the sign of the chirp parameter is important in the spectral lineouts, which substantially differ for negatively and positively chirped driving laser pulses.

The values found by comparison of our mathematical model with the experimental data are in good agreement with the theoretical prediction for α_l in the whole region of q and for α_s close to the cut-off region (see figure 7). Our measured and calculated values of α_l are also in good agreement with earlier experimental work [15, 19] and theoretical predictions [24, 25, 42, 39]. In this study we have consistently extracted, in both the spectral and spatial measurements, negative values for α_s for a range of harmonics below and near the ionization threshold. While negative values of α_s have been theoretically predicted [24, 25], this is to our knowledge the first experimental measurement of negative α_s. Also our theoretical data as calculated by the TDSE yield negative values of α_s for the low orders, although not in perfect agreement with the experimental data. It is worth noting that negative values of α_s are a clear sign of interactions between the returning electron wave packet and the ionic core, i.e. that the atomic potential cannot be neglected in the description of the low-order short-trajectory harmonics. If this effect can be reproduced with even higher precision, it could lead to either a possible improvement of the accuracy of the short-range part of the pseudo-potential used or point towards the need for inclusion of multi-electron effects in the description of the atom used in the calculations.

We have shown in this paper that it is possible to measure $\alpha_{s/l}$ for the different harmonics. To fully characterize the temporal structure of the generated radiation, however, it is not enough to determine the values of $\alpha_{s/l}$ for the different frequency components. One would also need to measure the value of $\Phi^0_{s/l}$ in (4). Using our method, we would also be able to determine $|\Phi^0_s - \Phi^0_l|$ to within 2π, but not their absolute values, therefore prohibiting the full temporal reconstruction. If one would have interference between, e.g., the long trajectories of two neighbouring harmonics as was the case in [22], one would be able to determine $\Phi^0_l(q) - \Phi^0_l(q+1)$, thereby enabling the full reconstruction.

Under our experimental conditions, the harmonics $q = 11$ and $q = 13$ correspond to energies below the ionization potential threshold I_p and are so called below-threshold harmonics. In both cases, we observed the QPI mainly in the divergence lineouts. The experimental observation and theoretical explanation of the QPI for below-threshold harmonics were first made by D. C. Yost et al. in 2009 [43] and α^*_l was expected to be $\alpha^*_l \approx 2.5\pi - 3\pi$ and $\alpha^*_s \approx 0$. However, in our model we found values $\alpha^*_l \approx 2\pi$ and $\alpha^*_s \approx -0.4\pi$; these values are in a good agreement with later theoretical calculations [42, 26].

The prominent ring structures, clearly observed for regions of large spatial and spectral divergence, thus mainly due to the long trajectory, are covered by our extended model. The

rings appear when higher orders than parabolic in the phase curvature are included in the propagation of the Gaussian beams. To reproduce the detailed structures of the rings, one has to also include higher orders in the intensity dependence of the phase. This is of particular importance for harmonics that have comparable contributions from the plateau and cut-off regimes. In [20], similar structures were observed, interpreted as temporal Maker fringes, e.g. an effect of phase matching between subsequent planes of generation. The presence of this kind of phase matching in the present work cannot be ruled out, but the qualitative agreement of our theoretical results [figure 11(c–d)] with the experimental results [figure 11(e)] suggests that the explanation presented here is viable.

8. Summary

In this paper, we have presented experimental data with interference structures, observed in HHG from argon. The structures are of two kinds; firstly due to QPI between the first two trajectories and secondly due to long trajectory emission from atoms experiencing different local field strengths. The former interference has been systematically investigated by varying the chirp of the driving laser pulses and the observed patterns are well explained by a simple mathematical model based on a semi-classical description of HHG. By careful comparison of the experimental observations with the model, we are able to determine the dipole phase parameters α_s and α_l for $q = 11-37$, which are in a good agreement with theoretical predictions ([25]), except for the short trajectory contribution in the below-threshold harmonics and plateau regions, where we found α_s^* to be negative with a value $\alpha_s^* \approx -0.4\pi$.

Furthermore, the long trajectory interference was successfully modelled by taking into account phase curvature effects beyond the parabolic term. It was shown that the variation of the dipole phase parameters with respect to intensity has to be considered, to obtain the right behaviour of the resultant interference patterns.

Acknowledgments

This research was supported by the Swedish Foundation for Strategic Research, the Swedish Research Council and the Knut and Alice Wallenberg Foundation and by funding from the NSF under grant PHY-1307083 and PHY-1403236. The quantum mechanical calculations were performed at the Lunarc computing facility at Lund University, within the supercomputing network of Sweden, SNIC, under the project SNIC 2015/1-386.

Note added in proof. After acceptance of this article, we became aware of recent related work: [44].

Appendix A. Derivation of Gaussian model

Appendix A.1. Divergence model

Modelling the spatial profiles, we suppose that the main contribution to the generated HHs arises around the temporal maximum of the laser peak $I_0(\tau)$, that the driving laser field has

a Gaussian profile in the focal plane ($z = 0$) characterized by the beam waist r_0, and that the generated HH fields of the long and short trajectory (E_s^q, E_l^q) can be expressed [using (4)] as

$$\begin{aligned} E_{s/l}^q &= C_{s/l}\left[\sqrt{I_0(\tau)}\exp\left(-\frac{r^2}{r_0^2}\right)\right]^n \mathrm{e}^{\mathrm{i}\Phi_{s/l}} \\ &= C_{s/l}\left[\sqrt{I_0(\tau)}\exp\left(-\frac{r^2}{r_0^2}\right)\right]^n \mathrm{e}^{\mathrm{i}\Phi_{s/l}^0}\exp\left[\mathrm{i}\alpha_{s/l}I_0(\tau)\exp\left(-\frac{2r^2}{r_0^2}\right)\right], \end{aligned} \tag{A.1}$$

where $C_{s/l}$ is a proportionality constant and n is the nonlinearity order of the HH conversion. By Taylor expansion to second order in r, the phase term $\mathrm{i}\alpha_{s/l}I_0(\tau)\exp\left(-\frac{2r^2}{r_0^2}\right)$ can be simplified to $\mathrm{i}\alpha_{s/l}I_0(\tau) - \mathrm{i}2\alpha_{s/l}I_0(\tau)\frac{r^2}{r_0^2}$. In this approximation the generated field has a Gaussian intensity profile, a parabolic wavefront, and a phase offset. It is straightforward to identify these with a wavefront and an intensity profile of a *shifted* Gaussian beam (GB), which has its waist position located at $-z_{s/l}^f$:

$$E_{s/l}(r, z=0) = E_{0s/l}\frac{w_{0s/l}}{w(z_{s/l}^f)}\exp\left[-\frac{r^2}{w^2(z_{s/l}^f)} - \mathrm{i}k_q z_{s/l}^f - \mathrm{i}k_q\frac{r^2}{2R_{s/l}(z_{s/l}^f)} + \mathrm{i}\zeta(z_{s/l}^f) + \mathrm{i}\eta_{s/l}\right]. \tag{A.2}$$

Subsequently the propagation of the generated HH can be treated as a propagation of two GBs. These sought-after GBs can be fully characterized by the amplitudes $E_{0s/l}$, the distances of their waists from the HH interaction region (plane) $z_{s/l}^f$, the Rayleigh distances $z_{s/l}^R$, the wavevector of the generated HH k_q (corresponding to the wavelength λ_q), and the phases $\eta_{s/l}$. $\zeta(z) = \arctan(z/z^R)$ is the Gouy phase. For a thorough treatment of GBs, we refer the reader to [45]. k_q is given and all other variables can be found by comparing (A.1) in the parabolic approximation and (A.2). From comparison of the spatial parts of the equations, we get

$$E_{0s/l} = C_{s/l}\frac{w(z_{s/l}^f)}{w_{0s/l}}I_0^{\frac{n}{2}}(\tau), \qquad w(z_{s/l}^f) = \frac{r_0}{\sqrt{n}}, \tag{A.3}$$

and from the phase parts we find

$$R_{s/l}^f = R(z_{s/l}^f) = \frac{kr_0^2}{4\alpha_{s/l}I_0(\tau)}, \qquad \eta_{s/l} = \Phi_{s/l}^0 + \alpha_{s/l}I_0(\tau) + k_q z_{s/l}^f - \zeta(z_{s/l}^f). \tag{A.4}$$

If we express the (A.3) and (A.4) using GBs

$$w_{s/l}(z) = w_{0s/l}\left[1 + z^2/(z_{s/l}^R)^2\right]^{1/2}, \qquad R_{s/l}(z) = z\left[1 + (z_{s/l}^R)^2/z^2\right],$$

we get a set of two equations for two unknown variables $z_{s/l}^f$ and $z_{s/l}^R$ with solutions

$$z_{s/l}^R = \frac{\pi\lambda_q(R_{s/l}^f)^2 r_0^2/n}{\lambda_q^2(R_{s/l}^f)^2 + \pi r_0^4/n^2}, \qquad z_{s/l}^f = \frac{\pi^2 R_{s/l}^f r_0^4/n^2}{\lambda_q^2(R_{s/l}^f)^2 + \pi r_0^4/n^2}. \tag{A.5}$$

Finally, the generated HH field at the detector at distance z can be modelled as a sum of GBs representing short and long QP contribution, $E_{\text{detector}}(r,z) = E_s(r,z) + E_l(r,z)$, where

$$E_{s/l}(r,z) = E_{0s/l}\frac{w_{0s/l}}{w_{s/l}(\tilde{z}_{s/l})}\exp\left[-\frac{r^2}{w^2_{s/l}(\tilde{z}_{s/l})} - \mathrm{i}k_q\tilde{z}_{s/l} - \mathrm{i}k_q\frac{r^2}{2R_{s/l}(\tilde{z}_{s/l})} + \mathrm{i}\zeta(\tilde{z}_{s/l}) + \mathrm{i}\eta_{s/l}\right], \tag{A.6}$$

and $\tilde{z}_{s/l} \equiv z + z^f_{s/l}$. The quantity that is measured is proportional to

$$|E_{\text{detector}}(r,z)|^2 = |E_s(r,z)|^2 + |E_l(r,z)|^2 + 2|E_s(r,z)||E_l(r,z)|\cos[\chi(r,z)], \tag{A.7}$$

where

$$\begin{aligned}\chi(r,z) = &-\frac{k_q r^2}{2}\left[\frac{1}{R_s(\tilde{z}_s)} - \frac{1}{R_l(\tilde{z}_l)}\right] + [\zeta(\tilde{z}_s) - \zeta(\tilde{z}_l)] - [\zeta(z^f_s) - \zeta(z^f_l)] \\ &+ (\Phi^0_s - \Phi^0_l) + (\alpha_s - \alpha_l)I_0(\tau).\end{aligned} \tag{A.8}$$

Appendix A.2. Spectral model

Turning to the spectral behaviour of the harmonics, we can assume that the main contribution is generated in the middle of the focus and that we can neglect the spatial variation of $\Phi_{s/l}$. We describe the short and long trajectory contributions as

$$E_{s/l}(t) = E_{0s/l}(t)\exp\left[\mathrm{i}q\omega(t)t + \mathrm{i}\Phi_{s/l}(t)\right], \tag{A.9}$$

where $E_{0s/l}(t)$ is the amplitude of the generated field approximated by

$$E_{0s/l}(t) = C_{s/l}I^{\frac{n}{2}}(t). \tag{A.10}$$

$I(t)$ is the time-varying intensity in the middle of generation plane and $\omega(t)$ is the frequency of the driving laser. The instantaneous frequency of the generated HH $\omega_{s/l}(t)$ is determined as the time derivative of the phase of (A.9):

$$\omega_{s/l}(t) = q\omega(t) + \alpha_{s/l}\frac{\partial I(t)}{\partial t}. \tag{A.11}$$

We suppose that the driving pulse is linearly chirped

$$\omega(t) = \omega_0 + b(\tau)t, \tag{A.12}$$

where ω_0 is the central frequency of the driving laser field and $b(\tau)$ is the chirp rate. The driving field intensity varies as

$$I(t) = I_0(\tau)\exp\left(-\frac{4\ln 2}{\tau^2}t^2\right), \tag{A.13}$$

where $I_0(\tau)$ can be determined from (2). The chirp rate b is then related to the duration of the laser pulse τ and to the duration of the Fourier transform limited pulse τ_{FT} as

$$b(\tau) = \pm\frac{4\ln 2}{\tau^2}\sqrt{\frac{\tau^2}{\tau^2_{\text{FT}}} - 1}. \tag{A.14}$$

In the presented lineouts, the negatively chirped pulses are on the left side (negative sign in the above equation), whereas the positively chirped pulses (positive sign) on the right side.

Together with (A.12) and the time derivative of (A.13), we find the instantaneous frequency of the generated HH:

$$\omega_{s/l}(t) = q\omega_0 + qb(\tau)t - \alpha_{s/l}\frac{8\ln 2}{\tau^2}I(t). \tag{A.15}$$

For our simulation, the generated HH field is described as

$$E_{s/l}(t) = C_{s/l}I^{\frac{n}{2}}(t)\exp\left[\mathrm{i}q\omega_0 t + \mathrm{i}\frac{qb(\tau)}{2}t^2 + \mathrm{i}\alpha_{s/l}I(t) + \mathrm{i}\Phi^0_{s/l}\right]. \tag{A.16}$$

The far-field spectra of the generated HHs are computed as the Fourier transform of the sum of the fields generated by the short and long trajectory contributions

$$S(\omega) = \mathcal{F}[E_s(t) + E_l(t)], \tag{A.17}$$

and the intensity in the far field is given by

$$I(\omega) \propto |S(\omega)|^2. \tag{A.18}$$

References

[1] McPherson A, Gibson G, Jara H, Johann U, Luk T S, McIntyre I A, Boyer K and Rhodes C K 1987 *J. Opt. Soc. Am. B* **4** 595 ISSN 1520-8540 URL http://dx.doi.org/10.1364/JOSAB.4.000595

[2] Ferray M, L'Huillier A, Li X F, Lompre L A, Mainfray G and Manus C 1988 *Journal of Physics B: Atomic, Molecular and Optical Physics* **21** L31–L35 ISSN 1361-6455 URL http://dx.doi.org/10.1088/0953-4075/21/3/001

[3] Corkum P B and Krausz F 2007 *Nature Physics* **3** 381–387 URL http://dx.doi.org/10.1038/nphys620

[4] Drescher M, Hentschel M, Kienberger R, Uiberacker M, Yakovlev V, Scrinzi A, Westerwalbesloh T, Kleineberg U, Heinzmann U and Krausz F 2002 *Nature* **419** 803–807 URL http://dx.doi.org/10.1038/nature01143

[5] Mauritsson J, Remetter T, Swoboda M, Klünder K, L'Huillier A, Schafer K J, Ghafur O, Kelkensberg F, Siu W, Johnsson P, Vrakking M J J, Znakovskaya I, Uphues T, Zherebtsov S, Kling M F, Lépine F, Benedetti E, Ferrari F, Sansone G and Nisoli M 2010 *Physical Review Letters* **105**(5) 053001

[6] Schultze M, Fieß M, Karpowicz N, Gagnon J, Korbman M, Hofstetter M, Neppl S, Cavalieri A, Komninos Y, Mercouris T *et al.* 2010 *Science* **328** 1658–1662 URL http://www.sciencemag.org/content/328/5986/1658.short

[7] Klünder K, Dahlström J M, Gisselbrecht M, Fordell T, Swoboda M, Guénot D, Johnsson P, Caillat J, Mauritsson J, Maquet A and et al 2011 *Physical Review Letters* **106** ISSN 1079-7114 URL http://dx.doi.org/10.1103/PhysRevLett.106.143002

[8] Schafer K J, Yang B, DiMauro L F and Kulander K C 1993 *Physical Review Letters* **70** 1599–1602 ISSN 0031-9007 URL http://dx.doi.org/10.1103/PhysRevLett.70.1599

[9] Corkum P B 1993 *Physical Review Letters* **71** 1994–1997 ISSN 0031-9007 URL http://dx.doi.org/10.1103/PhysRevLett.71.1994

[10] Krause J L, Schafer K J and Kulander K C 1992 *Phys. Rev. Lett.* **68** 3535–3538 URL http://dx.doi.org/10.1103/PhysRevLett.68.3535

[11] Lewenstein M, Balcou P, Ivanov M Y, L'Huillier A and Corkum P B 1994 *Physical Review A* **49** 2117–2132 ISSN 1094-1622 URL http://dx.doi.org/10.1103/PhysRevA.49.2117

[12] Bellini M, Lyngå C, Tozzi A, Gaarde M B, Hänsch T W, L'Huillier A and Wahlström C G 1998 *Physical Review Letters* **81** 297–300 URL http://dx.doi.org/10.1103/PhysRevLett.81.297

[13] Lyngå C, Gaarde M B, Delfin C, Bellini M, Hänsch T W, L'Huillier A and Wahlström C G 1999 *Physical Review A* **60** 4823–4830 ISSN 1094-1622 URL http://dx.doi.org/10.1103/PhysRevA.60.4823

[14] Gaarde M B, Salin F, Constant E, Balcou P, Schafer K J, Kulander K C and L'Huillier A 1999 *Physical Review A* **59** 1367–1373 ISSN 1094-1622 URL http://dx.doi.org/10.1103/PhysRevA.59.1367

[15] Benedetti E, Caumes J P, Sansone G, Stagira S, Vozzi C and Nisoli M 2006 *Optics Express* **14** 2242 ISSN 1094-4087 URL http://dx.doi.org/10.1364/OE.14.002242

[16] Corsi C, Pirri A, Sali E, Tortora A and Bellini M 2006 *Physical Review Letters* **97** ISSN 1079-7114 URL http://dx.doi.org/10.1103/PhysRevLett.97.023901

[17] Zaïr A, Holler M, Guandalini A, Schapper F, Biegert J, Gallmann L, Keller U, Wyatt A S, Monmayrant A, Walmsley I A and et al 2008 *Physical Review Letters* **100** ISSN 1079-7114 URL http://dx.doi.org/10.1103/PhysRevLett.100.143902

[18] Ganeev R A, Hutchison C, Siegel T, Zaïr A and Marangos J P 2011 *Physical Review A* **83** ISSN 1094-1622 URL http://dx.doi.org/10.1103/PhysRevA.83.063837

[19] He L, Lan P, Zhang Q, Zhai C, Wang F, Shi W and Lu P 2015 *Physical Review A* **92** ISSN 1094-1622 URL http://dx.doi.org/10.1103/PhysRevA.92.043403

[20] Heyl C M, Güdde J, Höfer U and L'Huillier A 2011 *Physical Review Letters* **107** ISSN 1079-7114 URL http://dx.doi.org/10.1103/PhysRevLett.107.033903

[21] Dubrouil A, Hort O, Catoire F, Descamps D, Petit S, Mével E, Strelkov V V and Constant E 2014 *Nature Communications* **5** URL http://dx.doi.org/10.1038/ncomms5637

[22] Sansone G, Benedetti E, Caumes J P, Stagira S, Vozzi C, Pascolini M, Poletto L, Villoresi P, Silvestri S D and Nisoli M 2005 *Phys. Rev. Lett.* **94** URL http://dx.doi.org/10.1103/PhysRevLett.94.193903

[23] Paul P M 2001 *Science* **292** 1689–1692 URL http://dx.doi.org/10.1126/science.1059413

[24] Mauritsson J, Johnsson P, López-Martens R, Varjú K, Kornelis W, Biegert J, Keller U, Gaarde M B, Schafer K J and L'Huillier A 2004 *Physical Review A* **70** ISSN 1094-1622 URL http://dx.doi.org/10.1103/PhysRevA.70.021801

[25] Varjú K, Mairesse Y, Carré B, Gaarde M, Johnsson P, Kazamias S, López-Martens R, Mauritsson J, Schafer K, Balcou P *et al.* 2005 *Journal of Modern Optics* **52** 379–394

[26] He L, Lan P, Zhai C, Li Y, Wang Z, Zhang Q and Lu P 2015 *Physical Review A* **91** ISSN 1094-1622 URL http://dx.doi.org/10.1103/PhysRevA.91.023428

[27] Salières P, L'Huillier A and Lewenstein M 1995 *Physical Review Letters* **74** 3776–3779 ISSN 1079-7114 URL http://dx.doi.org/10.1103/PhysRevLett.74.3776

[28] Salières P 2001 *Science* **292** 902–905 ISSN 1095-9203

[29] Lorek E, Larsen E W, Heyl C M, Carlström S, Paleček D, Zigmantas D and Mauritsson J 2014 *Review of Scientific Instruments* **85** 123106 ISSN 1089-7623 URL http://dx.doi.org/10.1063/1.4902819

[30] Murakami M, Mauritsson J and Gaarde M B 2005 *Physical Review A* **72** ISSN 1094-1622 URL http://dx.doi.org/10.1103/PhysRevA.72.023413

[31] Lewenstein M, Salières P and L'Huillier A 1995 *Physical Review A* **52** 4747–4754 ISSN 1094-1622 URL http://dx.doi.org/10.1103/PhysRevA.52.4747

[32] Schafer K J 2009 *Numerical Methods in Strong Field Physics* vol Strong Field Laser Physics (Springer) pp 111–145

[33] Balcou P, Dederichs A S, Gaarde M B and L'Huillier A 1999 *Journal of Physics B: Atomic, Molecular and Optical Physics* **32** 2973–2989 ISSN 1361-6455 URL http://dx.doi.org/10.1088/0953-4075/32/12/315

[34] Murakami M, Mauritsson J, L'Huillier A, Schafer K J and Gaarde M B 2005 *Physical Review A* **71** ISSN 1094-1622 URL http://dx.doi.org/10.1103/PhysRevA.71.013410

[35] Goodman J 1996 *Introduction to Fourier optics* (New York: McGraw-Hill) ISBN 0071142576

[36] Guizar-Sicairos M and Gutiérrez-Vega J C 2004 *Journal of the Optical Society of America A* **21** 53 ISSN 1520-8532 URL http://dx.doi.org/10.1364/JOSAA.21.000053

[37] Kim K T, Zhang C, Shiner A D, Kirkwood S E, Frumker E, Gariepy G, Naumov A, Villeneuve D M and Corkum P B 2013 *Nature Physics* **9** 159–163 ISSN 1745-2481 URL http://dx.doi.org/10.1038/nphys2525

[38] Schapper F, Holler M, Auguste T, Zaïr A, Weger M, Salières P, Gallmann L and Keller U 2010 *Optics Express* **18** 2987 ISSN 1094-4087 URL http://dx.doi.org/10.1364/OE.18.002987

[39] Auguste T, Salières P, Wyatt A S, Monmayrant A, Walmsley I A, Cormier E, Zaïr A, Holler M, Guandalini A, Schapper F and et al 2009 *Physical Review A* **80** ISSN 1094-1622 URL http://dx.doi.org/10.1103/PhysRevA.80.033817

[40] Xu H, Xiong H, Zeng Z, Fu Y, Yao J, Li R, Cheng Y and Xu Z 2008 *Physical Review A* **78** ISSN 1094-1622 URL http://dx.doi.org/10.1103/PhysRevA.78.033841

[41] Jiang J, Wei P, Zeng Z, Miao J, Zheng Y, Ge X, Li C, Li R and Xu Z 2014 *Optics Express* **22** 15975 ISSN 1094-4087 URL http://dx.doi.org/10.1364/OE.22.015975

[42] Hostetter J A, Tate J L, Schafer K J and Gaarde M B 2010 *Physical Review A* **82** ISSN 1094-1622 URL http://dx.doi.org/10.1103/PhysRevA.82.023401

[43] Yost D C, Schibli T R, Ye J, Tate J L, Hostetter J, Gaarde M B and Schafer K J 2009 *Nature Physics* **5** 815–820 ISSN 1745-2481 URL http://dx.doi.org/10.1038/nphys1398

[44] Catoire F, Ferré A, Hort O, Dubrouil A, Quintard L, Descamps D, Petit S, Burgy F, Mével E, Mairesse Y and Constant E 2016 *Physical Review A* **94** URL http://dx.doi.org/10.1103/PhysRevA.94.063401

[45] Saleh B 2007 *Fundamentals of photonics* (Hoboken, N.J: Wiley-Interscience) ISBN 978-0-471-35832-9

V

Dispersion control of attosecond pulse trains

Chen Guo, Anne Harth, Stefanos Carlström, Yu-Chen Cheng, Sara Mikaelsson, Erik Mårsell, Arthur Losquin, Miguel Miranda, Kenneth Joseph Schafer, Anders Mikkelsen, Johan Mauritsson, Cord Louis Arnold, and Anne L'Huillier

Manuscript in preparation

Dispersion Control of Attosecond Pulse Trains

Chen Guo[1], Anne Harth[1], Stefanos Carlström[1], Yu-Chen Cheng[1], Sara Mikaelsson[1], Erik Mårsell[1,*], Arthur Losquin[1], Miguel Miranda[1], Kenneth J Schafer[2], Anders Mikkelsen[1], Johan Mauritsson[1], Cord Arnold[1], and Anne L'Huillier[1,**]

[1]*Department of Physics, Lund University, P. O. Box 118, SE-22100 Lund, Sweden*
[2]*Louisiana State University Department of Physics and Astronomy, 222-B Nicholson Hall, Tower Dr., Baton Rouge, LA 70803-4001*
[*]*Present address: University of British Columbia - Vancouver, BC*
[**]*Corresponding author: Anne.LHuillier@fysik.lth.se*

December 19, 2016

Abstract

We study high-order harmonic generation in argon driven by a carrier–envelope phase stabilized few-cycle 200 kHz optical parametric chirped pulse amplifier system, as a function of CEP and dispersion. The spectra exhibit a complex pattern of interference fringes when the dispersion is changed. These structures are well reproduced by simulations based on the solution of the time-dependent Schrödinger equation as well as by a simple multiple-pulse interference model. This allows us to deduce the temporal structure of the attosecond pulse train, including the relative phase between consecutive attosecond pulses. This relative phase can be controlled by varying the CEP of the driving field.

1 Introduction

The use of few-cycle optical pulses for time-resolved measurements requires detailed characterization and control of the amplitude and phase of the pulses, including the carrier-envelope phase (CEP), i.e. the offset between the electric field oscillation and the maximum of the envelope. While the frontier in pulse duration has moved to the attosecond range fifteen years ago using high-order harmonic generation (HHG) in gases [1, 2], the level of characterization and control of these attosecond pulses with a central frequency in the extreme ultraviolet (XUV) spectrum and a duration reaching down to a few cycles [3, 4], is far from reaching that of optical or infrared few-cycle pulses. Three main techniques exist today for attosecond pulse characterization: Streaking (or FROG-CRAB; frequency resolved optical gating for complete reconstruction of attosecond bursts [5]) has been developed for the characterization of single attosecond pulses, while RABBITT (reconstruction of attosecond harmonic beating by interference of two-photon transitions [6]) determines the characteristics of an average attosecond pulse in a train. Autocorrelation of XUV attosecond pulses is a challenging method which requires high XUV flux. None of these techniques give information on the CEP of the attosecond pulses, and how it varies from one pulse to the next in a train.

High-order harmonic generation strongly depends on the phase modulation (chirp) of the driving laser [7, 8], as well as, for a few-cycle pulse, on its CEP [9]. The spectral width of the generated harmonics becomes narrower when the fundamental pulses are negatively chirped, due to compensation of the phase modulation due to the generation process (so-called dipole phase), which leads to a positive chirp [10]. Control of the CEP is important when HHG is driven by few-cycle pulses, since the process is sensitive to the electric field oscillations. Changing the CEP may lead to spectral shifts between odd and even orders, or for very short driving pulses, between harmonic peaks and quasi-continuum [9]; it may also lead to the appearance of substructures between harmonic peaks [11]. The generation of single attosecond pulses requires asymmetric electric fields [12] and therefore precise control of the laser CEP.

The recent progress of optical parametric amplifier systems based upon chirped pulse amplification (OPCPA) now allows the study of HHG and attosecond pulse trains using few-cycle pulses, at high repetition rate ($\geq$ 100 kHz), with excellent stability regarding intensity, phase and CEP [13, 14]. In this work, we study HHG in argon as a function of dispersion of the driving pulse (and consequently also of its CEP) using a 200 kHz, CEP stabilized, 6 fs, 800 nm OPCPA system. The dispersion scans, obtained when recording harmonic spectra as a function of glass thickness transmission, present complex interference patterns over a large (40 eV) bandwidth. To understand these structures, we perform simulations based upon the time-dependent

Schrödinger equation (TDSE) and we develop an analytical multiple pulse interference model, based upon the semi-classical description of HHG. Our model is validated by comparison with the TDSE results and applied to the experimental pulses characterized in our experiment [15]. The calculations reproduce most characteristics observed in the experimental data. Furthermore, we are able to deduce the spectral phase and CEP of the individual attosecond pulses in the train. The dispersion of the fundamental pulses allows us to precisely control the phase difference between consecutive attosecond pulses.

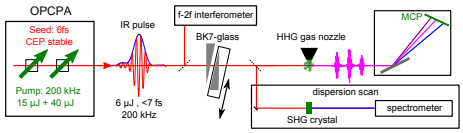

Figure 1: Experimental Setup. The dispersion of a few-cycle IR pulse from a CEP stabilized 200 kHz OPCPA system is controlled with a BK7 glass wedge pair. The IR pulses drive dispersion controlled HHG. With a flip mirror the pulse can be characterized via a dispersion scan method.

2 EXPERIMENT

The laser used in our experiment is a few-cycle, 200 kHz repetition rate, CEP stabilized OPCPA laser system [16]. The system provides 6 µJ pulses with a duration of <7 fs. The CEP is measured in an f-$2f$ interferometer to be 400 mrad (integrated over two pulses), which corresponds to a timing jitter of the carrier of 160 as. The pulse duration is measured by a dispersion scan characterization method which uses second harmonic generation in a thin crystal (see Fig. 1 and [15]). The laser pulses are focused tightly, using an achromat with a focal length of 5 cm, into a high pressure gas jet filled with argon, where HHG takes place (see Fig. 1). The dimension of the medium is estimated to be slightly larger that 50 µm and the gas pressure to be approximately 1 bar. The high-pressure gas jet was designed to optimize phase matching of the short trajectory harmonics in these tight focusing geometrical conditions [17]. After passing through a 200 nm thick Al filter in order to block the infrared (IR) radiation, the harmonics are detected by a flat-field XUV-spectrometer, consisting of an XUV-grating and a MCP detector. The dispersion, including obviously the CEP, of the few-cycle IR driving pulses is varied using the same motorized BK7-glass wedge pair that is used for the d-scan IR pulse characterization. The induced group delay dispersion (GDD) by transmission trough BK7 is equal to 44 fs^2/mm at 800 nm. The laser compressor, consisting of chirped mirrors and a wedge pair, is set up in order to precompensate transmission through air, glass (entrance window, and achromat) such that the shortest pulse in the HHG interaction region is obtained at the position called "zero glass insertion". In order to obtain good signal-to-noise ratio, each harmonic spectrum is acquired by integrating over about 200 000 shots.

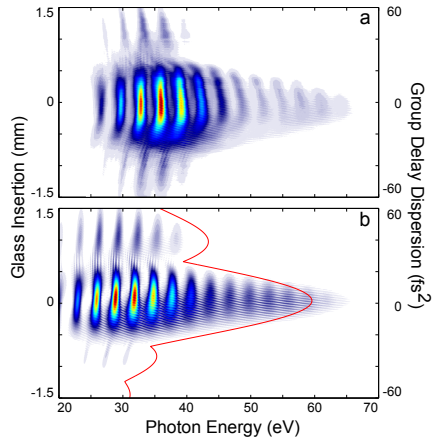

Figure 2: XUV-spectra as a function of dispersion. (a) Experimental result; (b) Calculation using the interference model with the retrieved pulse from the experiment. The red line in (b) represents the position of the classical cut-off.

The experimental key result of this work is presented in Fig. 2a which shows the harmonic spectrum (harmonic 17th to 41th) obtained in argon gas as a function of glass insertion from the BK7 wedge pair. The corresponding GDD is indicated on the right axis. The strongest HHG signal and highest cut-off is observed close to a Fourier-transform limited IR pulse at zero glass insertion. The harmonic signal also decreases significantly for orders larger than 31th, due to the proximity of the Cooper minimum in the photoionization cross-section of argon, which affects the recombination step in the single atom response [18]. The signal decreases for large GDDs (glass insertion of $\pm$ 0.7 mm) due to the decrease in IR-pulse intensity. Harmonic generation can, however, be observed at large glass insertion, an effect that we attribute to the compression of some spectral parts of the complex IR pulse at these large dispersion values, as retrieved from our d-scan measurements. The harmonics, are spectrally broader for

negative GDD than for positive GDD, in agreement with previous results [7, 8, 19].

Furthermore, two different interference pattern can be observed. The most striking pattern is visible over the whole spectral range and consists of almost horizontal fringes, separated by $\approx 28\,\mu m$ BK7-glass which corresponds to a π shift of the CEP of the driving pulse. The slope of these fringes varies from slightly positive at negative GDD to negative at insertion values larger than 0.3 mm. At larger insertions, around $\pm 0.75\,mm$, vertical interference fringes can be observed.

For a temporal interpretation of these IR-chirp and CEP dependent observations, we first perform a spectral analysis. We introduce a simple interference model and verify it by comparing with the results from the experiment and the TDSE calculations.

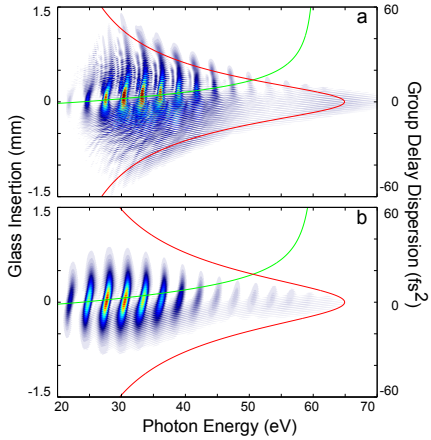

Figure 3: Calculated XUV-spectra as a function of dispersion. (a) TDSE result; (b) Analytical calculation using the interference model. The red lines represent the position of the cut-off; the green curves in both (a) and (b) are the calculated position where the harmonics are spectrally compressed, by solving $s(\Omega, l) = 0$ according to (7).

3 SPECTRAL ANALYSIS

In order to calculate the high-order harmonic spectra as a function of dispersion, we solve the TDSE in the single-active-electron approximation [20] with an argon model atom [21]. We assume a fundamental Gaussian pulse with 6.2 fs pulse duration (FWHM of the temporal intensity profile) at zero glass insertion. The fundamental wavelength is 850 nm, which corresponds to the center of mass of the experimental spectrum, and the peak intensity at Fourier-transform limited pulse duration is $2.3\times10^{14}\,W/cm^2$. HHG spectra are obtained by Fourier transforming the time-dependent acceleration of the dipole moment. We do not include propagation in the nonlinear medium. Only the effect of the short trajectory contribution is included, at least for the shortest pulse duration; to isolate the response from the short trajectory, a soft mask is placed in close vicinity of the nucleus, such that long electron trajectories are absorbed and do not contribute to the emission.

The results are presented in Fig. 3. Many of the features observed in the experiment are qualitatively reproduced. CEP-fringes are observed throughout the spectra, with a dispersion-dependent slope, the Cooper minimum of argon is found at about 50 eV, and the harmonic peaks are narrower, as well as slightly blue-shifted for positive dispersion.

The spectra in Fig. 2a and 3a are quite different at large positive or negative dispersion, which we attribute to the difference between the theoretical fundamental pulse (purely Gaussian) and the experimental fundamental pulse (complex temporal structure) as well as to the influence of the long trajectory in the theoretical results. The latter effect is most likely responsible for the splitting of the harmonics which occurs in the theory at a glass insertion of about 0.5 mm.

To understand more quantitatively the complex spectra observed in the experiment as well as in the TDSE calculations, we develop a simple model based upon interferences between attosecond pulses [11, 14]. The characteristics of the attosecond pulses are calculated using a semi-classical approach, [18, 22], which includes three steps: tunnel ionization, propagation of a free electron in the laser field and recombination leading to the emission of an XUV photon. The three steps are repeated every half cycle of the laser field. For a few-cycle field, these three steps are slightly different from one half-cycle to the next one.

The complex spectral amplitude of the total XUV field is given by

$$\tilde{E}(\Omega) = \sum_m |A_m(\Omega)| e^{i[\Omega t_m + m\pi + \Phi_m(\Omega)]}, \qquad (1)$$

where Ω is the angular frequency, m the pulse index, $|A_m|$ the modulus of the spectral amplitude of the mth attosecond pulse, t_m the timing of the attosecond pulse and $\Phi_m(\Omega)$ the spectral phase of the mth attosecond pulse. Ωt_m represents the group delay of the attosecond pulse, while $\Phi_m(\Omega)$ also includes higher-order effects (GDD, etc). The sign flip between consecutive attosecond pulses is described by the $m\pi$ term.

We evaluate (1) with the following approximations. The m-th pulse timing, t_m, is taken as the zero crossing

of the fundamental electric field, which corresponds to the time of return corresponding to the lowest 'plateau' harmonic in the three step model. Both CEP and dispersion of the fundamental pulse is transferred to the attosecond pulses via the variation of the timing t_m. The XUV spectrum $A_m(\Omega)$ is assumed to have a super-Gaussian shape for every attosecond pulse m spanning from the ionization potential of the generation gas up to the classical cut-off, which depends on the intensity of the fundamental field at t_m [$I_m = I(t_m)$]. The position of the cutoff is indicated by a red line in Fig. 2b. The integrated power spectrum $\int_0^\infty |A_m(\Omega)|^2 d\Omega$ of the attosecond pulses varies with the laser intensity as the ionization rate, which can be determined from the Ammosov–Delone–Kraĭnov approximation [23]. The spectral intensity $|A_m(\Omega)|^2$ is weighted by the probability for recombination, extracted from [24]. We calculate $\Phi_m(\Omega)$ as the classical action of the electron trajectory in the continuum (divided by $\hbar$). The spectral phase and amplitude of the driving IR-pulse is obtained by assuming a Gaussian pulse as in the TDSE or by using a d-scan measurement of the laser pulse (see Fig. 1), in order to mimic the experimental conditions as close as possible. As shown in Fig. 2b and Fig. 3b, almost all experimental and TDSE features are very well reproduced by our interference model. This confirms that the multi-pulse interference model can indeed be used to understand the spectral observations qualitatively.

Furthermore, this excellent agreement motivated us to look for an analytical expression for the phase of the HHG radiation field, to determine, for example, the position of the interference fringes. We consider a fundamental Gaussian pulse with central frequency ω, peak amplitude $E_0 = \sqrt{I}$, duration τ, chirp coefficient b, CEP φ_{CEP},

$$E(t) = E_0 \exp\left(-\frac{t^2}{2\tau^2}\right) \sin\left(\omega t - \varphi_{\text{CEP}} - \frac{b}{2}t^2\right). \quad (2)$$

The zeros of the electric field, which define the timing t_m, are such that

$$t_m = \frac{\omega}{b} \pm \sqrt{\frac{\omega^2}{b^2} - \frac{2\varphi_{\text{CEP}}}{b} - \frac{2m\pi}{b}}. \quad (3)$$

Only one of the solutions is physically correct and for small dispersion, t_m can be approximated by

$$t_m \approx \frac{m\pi}{\omega} + \frac{\varphi_{\text{CEP}}}{\omega} + \frac{b}{2\omega^3}(\varphi_{\text{CEP}}^2 + 2m\pi\varphi_{\text{CEP}} + m^2\pi^2). \quad (4)$$

A similar expansion can be derived for the phase Φ_m. We first approximate its frequency dependence using a polynomial expansion, which reads as,

$$\Phi_m(\Omega) = \alpha I_m + \beta(\Omega - \Omega_i) + \frac{\gamma}{I_m}(\Omega - \Omega_i)^2, \quad (5)$$

where α, β and γ are the polynomial coefficients, while Ω_i represents the lowest-order harmonic above threshold (see Supplementary Information). With $I_m \approx I(1 - t_m^2/\tau^2)$, Φ_m becomes

$$\Phi_m(\Omega) = \alpha I + \beta(\Omega - \Omega_i) + \frac{\gamma}{I}(\Omega - \Omega_i)^2 + \left(-\frac{\varphi_{\text{CEP}}^2}{\tau^2\omega^2} + \frac{2m\pi\varphi_{\text{CEP}}}{\omega^2\tau^2} + \frac{m^2\pi^2}{\omega^2\tau^2}\right)\left[-\alpha I + \frac{\gamma}{I}(\Omega - \Omega_i)^2\right] \quad (6)$$

The next step in this derivation is to relate b, τ and φ_{CEP} to the glass insertion ℓ (see Supplementary Information for details). (1) can therefore be written as

$$\tilde{E}(\Omega, \ell) = e^{iz(\Omega,\ell)} \sum_m |A_m(\Omega)| e^{imf(\Omega,\ell) + im^2 s(\Omega,\ell)}, \quad (7)$$

where z, f and s describe the phase contributions which are independent of m, proportional to m and to m^2 respectively. Their expression is indicated in the Supplementary Information. Let us first neglect the influence of the m^2 term. In this case, (7) describes a spectrum of harmonics. Constructive interferences are obtained for $f(\Omega, \ell) = 2q\pi$, where q is an integer, which determines the position of the harmonics for a given dispersion (or CEP). The m^2-term contributes to broaden and ultimately deteriorate the harmonic spectra. The zero of $s(\Omega, \ell)$ gives the position where harmonics are sharpest. It is indicated by the green line in Fig. 2b and 3b in perfect agreement with the numerical calculation. Finally the position of the interference fringes can be estimated from the m-term by requiring that the phase difference between consecutive attosecond pulse is equal to a multiple of 2π.

4 TEMPORAL ANALYSIS

Finally, we examine the temporal structure of the harmonic spectrum by Fourier transforming the calculated electric field, both in the case of the TDSE and with our numerical model. Figure 4a,b presents the attosecond pulse train at zero glass insertion for the case corresponding to Fig. 3a,b. The two calculations are based on the same fundamental electric field (blue curves) and the results are quite similar (red curves). Five attosecond pulses with different chirp and timing can be identified. Their duration in the intensity profile vary from 223 as at the center of the fundamental pulse to 779 as at the edges according to the TDSE simulation. The three central XUV bursts exhibit a minimum in the middle, with lower frequency of the emission for times earlier than the minimum and higher frequencies after. The minimum results from the Cooper minimum at 50 eV in the photoionization cross-section. This spectral minimum is transferred to the temporal profile of the XUV bursts through the time–energy link inherently present

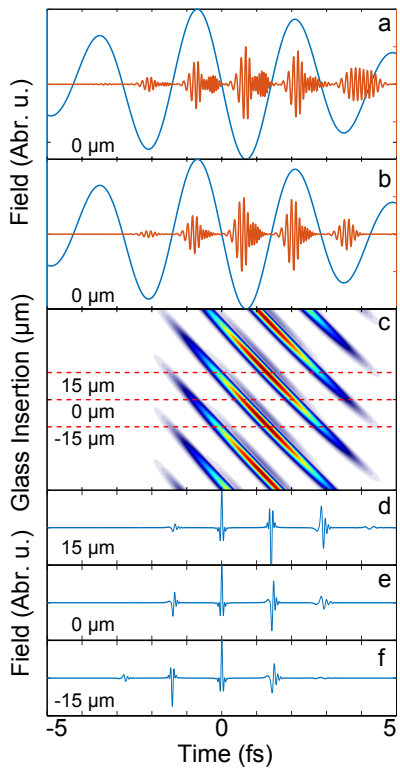

Figure 4: The temporal structure analysis of HHG simulated by TDSE, solving the interference model numerically and analytically. Subfigures a and b show the generated XUV field (red) by a *sine* fundamental field (blue) by solving TDSE and the interference model numerically respectively. The 2D plot in c is the numerical solution of the interference model and shows the modulus square of the complex field a function of the glass insertion around $\pm 50\,\mu m$. Three lineouts are marked at 15, 0 and -15 µm of the glass insertion. Plot d,e and f are the pulse trains calculated from the analytic model corresponding to these three glass insertions.

in the HHG process; for the short trajectory contribution, earlier times correspond to lower energy of the emission and vice versa [25]. The XUV bursts emitted before and after the three central ones, do not exhibit this minimum since the instantaneous intensity is too low the generate harmonics with high enough energy.

Figure 4c presents the evolution in time of the attosecond pulse train as as function of the glass insertion around $\pm 50\,\mu m$. The color plot shows the modulus of the attosecond pulses. The position of these pulses moves as the CEP changes. We indicate three lineouts which correspond to a π phase change of the fundamental CEP. To evaluate the variation of the relative CEP *variation* between consecutive attosecond pulses a constant phase $z(\Omega, \ell)$ in (7) is removed from all the pulses and the resulting attosecond fields are indicated in Fig. 4d,e,f. Firstly, it can be observed that the pulses at 0 fs are Fourier-transform limited, since we have chosen this pulse as $m = 0$, and have removed $z(\Omega, \ell)$. Secondly, the CEP of the pulse at 1.3 fs ($m = 1$) varies from π, to 0.65π and 0.56π as the fundamental CEP varies by π. The pulse becomes also weaker at negative dispersion and slightly broader, due to the lower intensity leading to a lower ionization rate as well as a narrower bandwidth. In contrast, the pulse at -1.3 fs presents a similar but reversed variation. Hence, it is shown that relative phase, including the atto-CEP and chirp, between attosecond pulse can be controlled by applying dispersion on the fundamental pulse.

5 CONCLUSION

We presented a dispersion dependent HHG spectrum obtained in argon with highly resolved CEP fringe patterns over the whole dispersion and spectral range. We could show that the relative phase of consecutive pulses in an attosecond-pulse train generated from a few cycle CEP-stablized can be controlled by the dispersion of the driving IR pulse.

REFERENCES

[1] P M Paul, ES Toma, P Breger, Genevive Mullot, F Augé, Ph Balcou, HG Muller, and P Agostini. 'Observation of a train of attosecond pulses from high harmonic generation'. *Science* **292**.5522 (2001), pp. 1689–1692. DOI: 10.1126/science.1059413.

[2] M Hentschel, R Kienberger, Ch Spielmann, Georg A Reider, N Milosevic, Thomas Brabec, Paul Corkum, Ulrich Heinzmann, Markus Drescher, and Ferenc Krausz. 'Attosecond metrology'. *Nature* **414**.6863 (2001), pp. 509–513. DOI: 10.1038/35107000.

[3] Rodrigo Lopez-Martens, Katalin Varjú, Per Johnsson, Johan Mauritsson, Yann Mairesse, Pascal Salieres, Mette B Gaarde, Kenneth J Schafer, Anders Persson, Sune Svanberg, et al. 'Amplitude and phase control of attosecond light pulses'. *Physical review letters* **94**.3 (2005), p. 033001. DOI: 10.1103/physrevlett.94.033001.

[4] Giuseppe Sansone, E Benedetti, Francesca Calegari, Caterina Vozzi, Lorenzo Avaldi, Roberto Flammini, Luca Poletto, P Villoresi, C Altucci, R Velotta, et al. 'Isolated single-cycle attosecond pulses'. *Science* **314**.5798 (2006), pp. 443–446. DOI: 10.1126/science.1132838.

[5] Y Mairesse and F Quéré. 'Frequency-resolved optical gating for complete reconstruction of attosecond bursts'. *Physical Review A* **71**.1 (2005), p. 011401. DOI: 10.1103/physreva.71.011401.

[6] H G Muller. 'Reconstruction of attosecond harmonic beating by interference of two-photon transitions'. *Applied Physics B* **74**.1 (2002), s17–s21. DOI: 10.1007/s00340-002-0894-8.

[7] Hyung Taek Kim, I Jong Kim, Kyung-Han Hong, Dong Gun Lee, Jung-Hoon Kim, and Chang Hee Nam. 'Chirp analysis of high-order harmonics from atoms driven by intense femtosecond laser pulses'. *Journal of Physics B: Atomic, Molecular and Optical Physics* **37**.5 (2004), p. 1141. DOI: 10.1364/hfsw.2001.tue12.

[8] Z Chang, A Rundquist, H Wang, I Christov, HC Kapteyn, and MM Murnane. 'Temporal phase control of soft-x-ray harmonic emission'. *Physical Review A* **58**.1 (1998), R30. DOI: 10.1103/physreva.58.r30.

[9] IJ Sola, E Mével, L Elouga, E Constant, V Strelkov, L Poletto, P Villoresi, E Benedetti, J-P Caumes, S Stagira, et al. 'Controlling attosecond electron dynamics by phase-stabilized polarization gating'. *Nature Physics* **2**.5 (2006), pp. 319–322. DOI: 10.1038/nphys281.

[10] Katalin Varjú, Y Mairesse, B Carré, MB Gaarde, Per Johnsson, S Kazamias, R López-Martens, Johan Mauritsson, KJ Schafer, Ph Balcou, et al. 'Frequency chirp of harmonic and attosecond pulses'. *Journal of Modern Optics* **52**.2-3 (2005), pp. 379–394. DOI: 10.1080/09500340412331301542.

[11] Erik Mansten, JM Dahlström, Johan Mauritsson, Thierry Ruchon, Anne L'Huillier, J Tate, MB Gaarde, P Eckle, A Guandalini, M Holler, et al. 'Spectral signature of short attosecond pulse trains'. *Physical review letters* **102**.8 (2009), p. 083002. DOI: 10.1103/physrevlett.102.083002.

[12] Andrius Baltuska, Matthias Uiberacker, Eleftherios Goulielmakis, Reinhard Kienberger, Vladislav S Yakovlev, Thomas Udem, Theodor W Hänsch, and Ferenc Krausz. 'Phase-controlled amplification of few-cycle laser pulses'. *IEEE Journal of Selected Topics in Quantum Electronics* **9**.4 (2003), pp. 972–989. DOI: 10.1109/eqec.2003.1314288.

[13] Manuel Krebs, Steffen Hädrich, Stefan Demmler, Jan Rothhardt, Amelle Zaïr, Luke Chipperfield, Jens Limpert, and Andreas Tünnermann. 'Towards isolated attosecond pulses at megahertz repetition rates'. *Nature Photonics* **7**.7 (2013), pp. 555–559. DOI: 10.1038/nphoton.2013.131.

[14] Piotr Rudawski, Anne Harth, Chen Guo, Eleonora Lorek, Miguel Miranda, Christoph M Heyl, Esben W Larsen, Jan Ahrens, Oliver Prochnow, Thomas Binhammer, et al. 'Carrier-envelope phase dependent high-order harmonic generation with a high-repetition rate OPCPA-system'. *The European Physical Journal D* **69**.3 (2015), pp. 1–6. DOI: 10.1140/epjd/e2015-50568-y.

[15] Miguel Miranda, Cord L Arnold, Thomas Fordell, Francisco Silva, Benjamín Alonso, Rosa Weigand, Anne L'Huillier, and Helder Crespo. 'Characterization of broadband few-cycle laser pulses with the d-scan technique'. *Optics express* **20**.17 (2012), pp. 18732–18743. DOI: 10.1364/oe.20.018732.

[16] Anne Harth, Chen Guo, Yu-Chen Cheng, Miguel Miranda, Sara Mikaelsson, Christoph Heyl, Oliver Prochnow, Jan Ahrens, Uwe Morgner, Anne L'Huillier, and Cord Arnold. *Compact 200 kHz HHG source driven by a few-cycle OPCPA*.

[17] CM Heyl, H Coudert-Alteirac, M Miranda, M Louisy, K Kovacs, V Tosa, E Balogh, K Varjú, A L'Huillier, A Couairon, et al. 'Scale-invariant nonlinear optics in gases'. *Optica* **3**.1 (2016), pp. 75–81. DOI: 10.1364/OPTICA.3.000075.

[18] Paul B Corkum. 'Plasma perspective on strong field multiphoton ionization'. *Physical Review Letters* **71**.13 (1993), p. 1994. DOI: 10.1103/physrevlett.71.1994.

[19] Warein Holgado, C Hernández-García, B Alonso, Miguel Miranda, F Silva, L Plaja, H Crespo, and IJ Sola. 'Continuous spectra in high-harmonic generation driven by multicycle laser pulses'. *Physical Review A* **93**.1 (2016), p. 013816. DOI: 10.1103/physreva.93.013816.

[20] Kenneth Joseph Schafer. 'Numerical Methods in Strong Field Physics'. In: ed. by Thomas Brabec. Vol. Strong Field Laser Physics. Springer, 2009, pp. 111–145. ISBN: 978-0-387-40077-8. DOI: 10.1007/978-0-387-34755-4_6.

[21] KC Kulander and TN Rescigno. 'Effective potentials for time-dependent calculations of multiphoton processes in atoms'. *Computer Physics Communications* **63**.1-3 (1991), pp. 523–528. DOI: 10.1016/0010-4655(91)90273-n.

[22] M Lewenstein, Ph Balcou, M Yu Ivanov, Anne L'huillier, and Paul B Corkum. 'Theory of high-harmonic generation by low-frequency laser fields'. *Physical Review A* **49**.3 (1994), p. 2117. DOI: 10.1103/physreva.49.2117.

[23] MV Ammosov, NB Delone, and VP Kraĭnov. 'Tunnelling ionization of complex atoms and of atomic ions in an alternating electromagnetic field'. *Sov. Phys. JETP* **64**.6 (1986), pp. 1191–1194.

[24] JAR Samson and Wayne C Stolte. 'Precision measurements of the total photoionization cross-sections of He, Ne, Ar, Kr, and Xe'. *Journal of electron spectroscopy and related phenomena* **123**.2 (2002), pp. 265–276. DOI: 10.1016/s0368-2048(02)00026-9.

[25] SB Schoun, R Chirla, J Wheeler, C Roedig, P Agostini, LF DiMauro, KJ Schafer, and MB Gaarde. 'Attosecond pulse shaping around a Cooper minimum'. *Physical review letters* **112**.15 (2014), p. 153001. DOI: 10.1103/PhysRevLett.112.153001.

Dispersion Control of Attosecond Pulse Trains
Supplementary Information

Chen Guo[1], Anne Harth[1], Stefanos Carlström[1], Yu-Chen Cheng[1], Sara Mikaelsson[1], Erik Mårsell[1,*], Arthur Losquin[1], Miguel Miranda[1], Kenneth J Schafer[2], Anders Mikkelsen[1], Johan Mauritsson[1], Cord Arnold[1], and Anne L'Huillier[1,**]

[1]*Department of Physics, Lund University, P. O. Box 118, SE-22100 Lund, Sweden*
[2]*Louisiana State University Department of Physics and Astronomy, 222-B Nicholson Hall, Tower Dr., Baton Rouge, LA 70803-4001*
[*]*Present address: University of British Columbia - Vancouver, BC*
[**]*Corresponding author: Anne.LHuillier@fysik.lth.se*

December 19, 2016

Abstract

Supplementary material for 'Dispersion Control of Attosecond Pulse Trains'

1 multiple pulse interference model

The total XUV field as defined in the main article, is given by

$$\tilde{E}(\Omega) = \sum_m A_m(\Omega) e^{i[\Omega t_m + m\pi + \Phi_m(\Omega)]} \quad (1)$$

where Ω is the angular frequency, m labels a pulse in the pulse train, A_m the spectral amplitude of the m^{th} attosecond pulse, t_m the timing of the attosecond pulse, and $\Phi_m(\Omega)$ the spectral phase of the m^{th} attosecond pulse. Ωt_m represents the group delay of the attosecond pulse, while $\Phi_m(\Omega)$ includes higher-order effects (GDD, etc). The sign flip between consecutive attosecond pulses is accounted for by the $m\pi$ term.

A key step to solve this model, either numerically or analytically, is to define and determine the spectral envelope $A_m(\Omega)$, the generation time t_m and the phase term $\Phi_m(\Omega)$. In the following sections, we present and discuss how we choose these components.

1.1 The spectral envelope

The XUV spectrum for each burst, $A_m(\Omega)$, is assumed to be super-Gaussian, spanning from the ionization potential of the generation gas to the classical cut-off. For each cycle, the spectrum is multiplied by the cycle-averaged tunnel-ionization rate and modulated by the recombination cross-section (including the Cooper minimum). The ionization rate is calculated from the Ammosov–Delone–Kraĭnov approximation. The cycle-averaging leads to a lower yield in the cut-off regime.

1.2 The generation time

The generation times t_m are set to be the zero-crossings of the driving fundamental field. This is only valid for the generation time of the lowest high-order harmonic (shown in fig 1), however, using this scheme the generation time t_m can be numerically determined for an almost arbitrary driving field. An analytic solution only works in simple cases.

Here, we consider a chirped Gaussian pulse, given by

$$\tilde{E}(t) = E \exp\left[-\frac{t^2}{2\tau^2} + i\left(\frac{b}{2}t^2 - \omega_0 t + \varphi_{\text{CEP}}\right)\right] \quad (2)$$

where E is the amplitude, τ is the pulse duration at the given dispersion, b is the chirp coefficient, ω_0 is the central frequency, and φ_{CEP} is the CEP of the fundamental. b and τ can also be calculated from the Fourier-transform limited pulse duration τ_0 and the group delay dispersion (GDD) ϕ. Considering that the pulse is a sine wave, the field crosses zero when the total phase is $m\pi$, $m \in \mathbb{Z}$. Hence, the time t_m can be determined by solving the quadratic equation

$$\frac{b}{2}t^2 - \omega_0 t + \varphi_{\text{CEP}} = -m\pi, \quad (3)$$

where the solutions are

$$t_m = \frac{\omega_0 \pm \sqrt{\omega_0^2 - 2b(\varphi_{\text{CEP}} + m\pi)}}{b}. \quad (4)$$

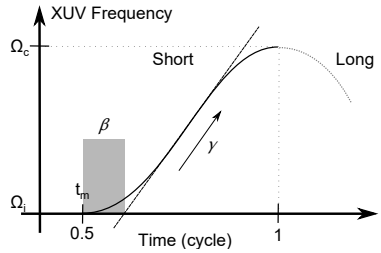

Figure 1: A schematic of the generation timing for short trajectory in three step model.

By Taylor-expanding the term within the square root, t_m is reduced to

$$t_m \approx \frac{m\pi}{\omega_0} + \frac{\varphi_{\text{CEP}}}{\omega_0} + \frac{b}{2\omega_0^3}(\varphi_{\text{CEP}}^2 + 2m\pi\varphi_{\text{CEP}} + m^2\pi^2). \quad (5)$$

1.3 The phase $\Phi_m(\Omega)$

The reduced dipole phase coefficient $\alpha^*(\Omega)$ can be expressed in a polynomial form

$$\alpha_m^*(\Omega) = \alpha_0^* + \beta^* \frac{\Omega - \Omega_i}{\Omega_c^{(m)} - \Omega_i} + \gamma^* \frac{(\Omega - \Omega_i)^2}{(\Omega_c^{(m)} - \Omega_i)^2} \ldots \quad (6)$$

with

$$\alpha_m^*(\Omega) = \frac{2c\epsilon_0 m\omega_0^3\hbar}{e^2}\alpha_m(\Omega), \quad (7)$$

where Ω_i is the frequency corresponding to the ionizion potential of the gas media $\Omega_i = I_p/\hbar$, $\Omega_c^{(m)}$ is the frequency at classical cut-off and, α_0^*, β^*, and γ^* are the first three polynomial coefficients which are dimensionless. The benefit of using the dimensionless constants is that they are invariant with respect to the unit system. $\Omega_c^{(m)} - \Omega_i$ can be substituted through the cut-off law

$$\Omega_c^{(m)} - \Omega_i = \frac{3.17U_{\text{P}}^{(m)}}{\hbar} \quad (8)$$

where $U_{\text{P}}^{(m)}$ is the ponderomotive energy which is proportional to the intensity I_m. Hence, if we put in the ponderomotive energy as well as

$$\beta' \equiv \frac{\beta^*}{\frac{3.17e^2}{2\hbar c\epsilon_0 m\omega_0^2}}, \quad (9a)$$

$$\gamma' \equiv \frac{\gamma^*}{\left(\frac{3.17e^2}{2\hbar c\epsilon_0 m\omega_0^2}\right)^2}, \quad (9b)$$

the total phase can be expressed as

$$\Phi_m(\Omega) = \frac{e^2}{2c\epsilon_0 m\omega_0^3\hbar} \times \left[\alpha_0^* I_m + \beta'(\Omega - \Omega_i) + \frac{\gamma'}{I_m}(\Omega - \Omega_i)^2\right] + \ldots \quad (10a)$$

$$\equiv \alpha_0 I_m + \beta(\Omega - \Omega_i) + \frac{\gamma}{I_m}(\Omega - \Omega_i)^2 + \ldots \quad (10b)$$

In atomic units, this expression is reduced to

$$\Phi_m(\Omega) = \frac{\alpha_0^* E_m^2}{4\omega_0^3} + \frac{\beta^*}{3.17\omega_0}(\Omega - \Omega_i) + \frac{4\gamma^*\omega_0}{3.17^2 E_m^2}(\Omega - \Omega_i)^2 + \ldots, \quad (11)$$

where E_m is the electric field strength of the fundamental field.

The group delay (GD) of the XUV pulse can be given by the derivative of the phase $\Phi(\Omega)$

$$\text{GD}(\Omega) = \frac{\partial\Phi_m(\Omega)}{\partial\Omega} = \beta + \gamma\frac{3.17e^2}{\hbar c\epsilon_0 m\omega_0^2}\frac{\Omega - \Omega_i}{\Omega_c^{(m)} - \Omega_i} \ldots \quad (12)$$

This equation reflects the fact that the frequency components between the lowest 'plateau' harmonic and the cut-off are generated in a similar temporal distribution for different cut-offs (or generation intensities). When only considering the first three coefficients (α_0, β, and γ), the contribution to the GD can be seen in Fig. 1: β gives a constant time shift which is marked as a gray box and γ indicates the chirp of the XUV pulse.

To express (10b) as a function of index m, the analytic expression of the intensity I_m is required. I_m can be found by putting t_m into the Gaussian pulse

$$I_m = I\exp\left(-\frac{t_m^2}{\tau^2}\right) \approx I\left(1 - \frac{t_m^2}{\tau^2}\right) \quad (13)$$

where I is the peak intensity for the given dispersion ϕ.

By inserting the expression for t_m from (5), we get

$$I_m \approx -\frac{Ib^2}{4\tau^2\omega_0^2}\frac{m^4\pi^4}{\omega_0^4} \tag{14a}$$

$$-\frac{Ib}{\tau^2\omega_0}\frac{m^3\pi^3}{\omega_0^3}\left(1+\frac{b\varphi_{\text{CEP}}}{\omega_0^2}\right) \tag{14b}$$

$$-\frac{I}{\tau^2}\frac{m^2\pi^2}{\omega_0^2}\left(1+\frac{3b\varphi_{\text{CEP}}}{\omega_0^2}+\frac{3b^2\varphi_{\text{CEP}}^2}{2\omega_0^4}\right) \tag{14c}$$

$$-\frac{2I\varphi_{\text{CEP}}}{\tau^2\omega_0}\frac{m\pi}{\omega_0}\left(1+\frac{3b\varphi_{\text{CEP}}}{2\omega_0^2}+\frac{b^2\varphi_{\text{CEP}}^2}{2\omega_0^4}\right) \tag{14d}$$

$$+I\left[1-\frac{\varphi_{cep}^2}{\tau^2\omega_0^2}\left(1+\frac{b\varphi_{\text{CEP}}}{\omega_0^2}+\frac{b^2\varphi_{\text{CEP}}^2}{4\omega_0^4}\right)\right]. \tag{14e}$$

Due to the small prefactors, the m^4 and m^3 terms are neglected. For the maximum value we consider ($\tau_0 = 6$ fs, $\lambda_0 = 850$ nm) the term $b\varphi_{\text{CEP}}/\omega_0^2$ is also much less than unity. Thus I_m can be further simplified as

$$I_m \approx -\frac{I}{\tau^2}\frac{m^2\pi^2}{\omega_0^2}-\frac{2I\varphi_{\text{CEP}}}{\tau^2\omega_0}\frac{m\pi}{\omega_0}+I\left(1-\frac{\varphi_{cep}^2}{\tau^2\omega_0^2}\right) \tag{15}$$

Similarly, the inverted intensity can be calculated to

$$\begin{aligned}\frac{1}{I_m} &= \frac{1}{I}\exp\left(\frac{t_m^2}{\tau^2}\right)\\ &\approx \frac{1}{I}\left(1+\frac{t_m^2}{\tau^2}\right).\end{aligned} \tag{16}$$

Again inserting (5), we get

$$\frac{1}{I_m} \approx \frac{1}{I\tau^2}\frac{m^2\pi^2}{\omega_0^2}+\frac{2\varphi_{\text{CEP}}}{I\tau^2\omega_0}\frac{m\pi}{\omega_0}+\frac{1}{I}\left(1+\frac{\varphi_{cep}^2}{\tau^2\omega_0^2}\right). \tag{17}$$

Hence, the phase $\Phi(\Omega)$ can be expressed as

$$\begin{aligned}\Phi_m(\Omega) &= \alpha I+\beta(\Omega-\Omega_i)+\frac{\gamma}{I}(\Omega-\Omega_i)^2\\ &+\left(-\frac{\varphi_{\text{CEP}}^2}{\tau^2\omega^2}+\frac{2m\pi\varphi_{\text{CEP}}}{\omega^2\tau^2}+\frac{m^2\pi^2}{\omega^2\tau^2}\right)\left[-\alpha I+\frac{\gamma}{I}(\Omega-\Omega_i)^2\right].\end{aligned} \tag{18}$$

2 ANALYTIC SOLUTION

By inserting thhe timings (5), the dipole phase (10b), and the intensities (15) into the interference model (1), we get

$$\begin{aligned}\tilde{E}(\Omega) &= \sum_m A_m(\Omega)e^{i[\Omega t_m+m\pi+\Phi_m(\Omega)]}\\ &= e^{iz(\Omega)}\sum_m A_m(\Omega)e^{[i(mf(\Omega)+m^2s(\Omega))]},\end{aligned} \tag{19}$$

where

$$\begin{aligned}z(\Omega) =& \frac{\Omega\varphi_{\text{CEP}}}{\omega_0}\left(1+\frac{b\varphi_{\text{CEP}}}{2\omega_0^2}\right)+\alpha I+\beta(\Omega-\Omega_i)\\ &+\frac{\gamma}{I}(\Omega-\Omega_i)^2+\frac{\varphi_{\text{CEP}}^2}{\tau^2\omega_0^2}\left[-\alpha_0 I+\frac{\gamma}{I}(\Omega-\Omega_i)^2\right],\end{aligned} \tag{20a}$$

$$\begin{aligned}f(\Omega) =& (1+\frac{b\varphi_{\text{CEP}}}{\omega_0^2})\frac{\pi\Omega}{\omega_0}+\pi\\ &+\frac{2\pi\varphi_{\text{CEP}}}{\omega_0^2\tau^2}\left[-\alpha_0 I+\frac{\gamma}{I}(\Omega-\Omega_i)^2\right],\end{aligned} \tag{20b}$$

and

$$s(\Omega) = \frac{\pi^2 b\Omega}{2\omega_0^3}+\frac{\pi^2}{\omega_0^2\tau^2}\left[-\alpha_0 I+\frac{\gamma}{I}(\Omega-\Omega_i)^2\right]. \tag{20c}$$

VI

Quantum coherence in photo-ionization with tailored XUV pulses

Stefanos Carlström, Johan Mauritsson, Kenneth Joseph Schafer, Anne L'Huillier, and Mathieu Gisselbrecht

Manuscript in preparation

Quantum Coherence in Photo-Ionization with Tailored XUV Pulses

Stefanos Carlström[1,*], Johan Mauritsson[1], Kenneth J. Schafer[2], Anne L'Huillier[1], and Mathieu Gisselbrecht[1]

[1]*Department of Physics, Lund University, Box 118, 221 10 Lund, Sweden*
[2]*Department of Physics and Astronomy, Louisiana State University, Baton Rouge, LA 70803*
[*]*Email: stefanos.carlstrom@fysik.lth.se*

December 19, 2016

Abstract

Ionization with ultrashort pulses in the extreme ultraviolet (XUV) regime can be used to prepare an ion in a superposition of spin–orbit substates. In this work, we study the coherence properties of such a superposition, created by ionizing xenon atoms using two phase-locked XUV pulses at different frequencies. In general, if the duration of the driving pulse exceeds the quantum beat period, dephasing will occur. If however, the frequency difference of the two pulses matches the spin–orbit splitting, the coherence can be efficiently increased and dephasing does not occur.

1 Introduction

The wave nature of matter is central to the quantum mechanical description of microcosmos; therefore coherence is an important property of any quantum system. An example of a coherent system is the superposition of two pure states, $|\psi\rangle = a|1\rangle + b|2\rangle$; such superpositions form the basis for the field of quantum information, where they are used to represent qubits. The manipulation of qubits for quantum computing necessarily requires that the coherence of the system is retained; if not, the information contained within the qubit is lost. In quantum optics, superpositions between two states may be created via a transition between the two states with an appropriately tailored pulse (e.g. a $\pi/2$-pulse) [figure 1 (a)].

Superpositions of states can also be achieved by direct excitation using short light pulses [figure 1 (b)], provided the bandwidth of the pulse is larger than the energy difference ($\hbar\omega_{21}$) between the two states.

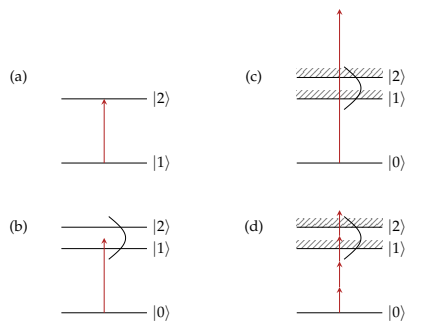

Figure 1: Different ways of preparing coherent superpositions using light; (a) excitation of a two-level system, such as those used for qubits in quantum information; (b) coherent excitation from the ground state to two excited bound states; (c) single-photon ionization, with the ion left in a superposition of substates; (d) strong-field ionization, also leaving the ion in a superposition of substates.

This requires a pulse duration short enough, $\tau \leq 2\pi/\omega_{21}$. If the superposition is successfully created, it may be observed through quantum beats (Teets, Eckstein, and Hänsch 1977; Salour and

Cohen-Tannoudji 1977; Mauritsson et al. 2010; Tzallas et al. 2011) which usually last substantially longer than the pulse duration. The characteristic decay time is termed the *coherence time*. In the cases depicted in 1 (a) and (b), the light couples the bound states and enables coherent population transfer in both directions.

Another way to produce a superposition of states is via short-pulse ionization, when the ion is left in different final states, e.g. due to spin–orbit interaction. This can be done using either high-frequency [figure 1 (c)] or high-intensity short-pulse [figure 1 (d)] radiation. As previously, the bandwidth of the ionizing pulse has to exceed the energy splitting between the ion states. Kurka et al. (2009) investigated case 1 (c) by photo-ionizing neon using short XUV pulses from a free-electron laser. A coherent superposition of the ionic fine-structure substates was prepared and probed by subsequent ionization. Using a strong laser field [figure 1 (d)], Goulielmakis et al. (2010) photo-ionized krypton, leaving the residual Kr^+ ion in a coherent superposition of the ionic substates. The quantum beat was observed by probing with a delayed attosecond (as) XUV pulse. This experimental activity stimulated an important theoretical effort to investigate the coherence of superpositions of states produced either directly by photo-excitation [figure 1 (b); Tzallas et al. 2011; Klünder et al. 2013], single-photon ionization [figure 1 (c); Nikolopoulos 2013], or strong-field ionization [figure 1 (d); Pabst et al. 2011; Pabst, Lein, and Wörner 2016].

In this article, we present a theoretical study of single-photon ionization of a rare gas using tailored XUV pulses. We use two phase-locked pulses of different frequencies (e.g. two high-order harmonics), to ionize xenon atoms, leaving the ion in a superposition of the ionic substates $5p^5\ ^2P^o_{3/2,1/2}$ (figure 2). When the frequency difference between the two pulses equals the spin–orbit splitting, the coherence can be retained, in principle, indefinitely. This resonance condition corresponds to a situation where the two quantum paths to the same final photo-electron energy cannot be distinguished. We investigate the tolerance of this resonance condition, i.e. given a ionizing pulse duration, how strict is the requirement on the driving pulse being in resonance to while still maintaining a certain level of coherence? Our method is based on an exact solution of the time-dependent Schrödinger equation using a fully correlated atomic model and assuming weak-field (perturbative) ionization. The coherence of the quantum system is analyzed using the density matrix formalism.

This paper is organized as follows; in the following section, the model is presented, along with the tools that are used to calculate the evolution of the superposition of states in the presence of the pump pulse. We then present the results and conclude with a discussion. Atomic units are used throughout, unless otherwise stated.

2 THEORETICAL FRAMEWORK

We are interested in studying the coherence of different ionic states produced by photo-ionization with tailored XUV pulses. To this end, we use as a model system noble gases, which have a spin–orbit splitting of the ground state ($np^5\ ^2P^o_{j_i}$, $j_i = 3/2, 1/2$), in particular xenon ($n = 5$).

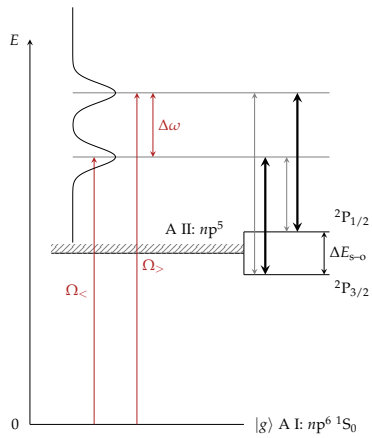

FIGURE 2: Resonant ionization; we photo-ionize with two frequencies $\Omega_<$, $\Omega_>$, which have a spacing of $\Delta\omega$.

Figure 2 shows a simplified diagram of photo-ionization of a np electron. The ionic ground state

has a spin–orbit splitting, which in xenon is 1.3 eV. We ionize with a weak XUV pulse with two frequency components, whose difference is $\Delta\omega$. The two frequency components, $\Omega_>$ and $\Omega_<$, can leave the ion in either $\mathrm{P}^{\mathrm{o}}_{3/2}$ or $\mathrm{P}^{\mathrm{o}}_{1/2}$, resulting in four different pathways. If the frequency difference is equal to the spin–orbit spacing, there will be two indistinguishable pathways (indicated by bold arrows) to the same final photo-electron energy; we call this the *resonant case*. We introduce the *detuning ratio* $d \equiv \Delta\omega/\Delta E_{\text{s–o}}$, and study photoionization in the vicinity of this resonance ($d = 1$).

The calculations are performed by solving the time-dependent Schrödinger equation (TDSE) in a limited subspace,

$$\mathrm{i}\frac{\partial}{\partial t}|\Psi(t)\rangle = \mathcal{H}(t)|\Psi(t)\rangle, \tag{1}$$

where the Hamiltonian in the dipole approximation is

$$\mathcal{H}(t) = \mathcal{H}_0 + \mathcal{E}(t)z. \tag{2}$$

$\mathcal{H}_0$ is the atomic Hamiltonian, $\mathcal{E}(t)$ the electric field, and z is the dipole operator. The solution is found by propagating the initial state (the neutral ground state) to time t

$$|\Psi(t)\rangle = \mathcal{U}(t,0)|\Psi_0\rangle, \tag{3}$$

where the short-time propagator is approximated by a Magnus (1954) propagator of fourth order (Saad 1992; Alvermann, Fehske, and Littlewood 2012).

The basis functions and the dipole matrix elements are determined using ATSP2K (Froese Fischer et al. 2007) and BSR (Zatsarinny 2006; Zatsarinny and Froese Fischer 2009). The time-dependent wavefunction is expanded as

$$|\Psi(t)\rangle = c_0(t)|\Psi_0\rangle + \sum_i \sum_e \int \mathrm{d}\varepsilon\, c_i^e(t;\varepsilon)|i\varepsilon e\rangle, \tag{4}$$

where $|\Psi_0\rangle$ is the ground state $n\mathrm{s}^2n\mathrm{p}^6\ {}^1\mathrm{S}_0$, $c_0(t)$ its complex, time-dependent amplitude, i denotes the different residual ions, and εe the photo-electron of angular momentum e and energy ε (related to the momentum k by $\varepsilon = k^2/2$). The ionization channels formed by different possible combinations of i and e, are listed in table 1 (in the case of jK coupling).

TABLE 1: Ionization channels accessible via one-photon ionization from the valence shell of a noble gas (final $J = 1$), in the case of jK coupling (Cowan 1981).

№	Channel configuration
1	$n\mathrm{p}^5(^2\mathrm{P}^{\mathrm{o}}_{3/2})k\mathrm{d}\ ^2[1/2]_1$
2	$n\mathrm{p}^5(^2\mathrm{P}^{\mathrm{o}}_{3/2})k\mathrm{s}\ ^2[3/2]_1$
3	$n\mathrm{p}^5(^2\mathrm{P}^{\mathrm{o}}_{3/2})k\mathrm{d}\ ^2[3/2]_1$
4	$n\mathrm{p}^5(^2\mathrm{P}^{\mathrm{o}}_{1/2})k\mathrm{s}\ ^2[1/2]_1$
5	$n\mathrm{p}^5(^2\mathrm{P}^{\mathrm{o}}_{1/2})k\mathrm{d}\ ^2[3/2]_1$
6	$ns n\mathrm{p}^6(^2\mathrm{S}_{1/2})k\mathrm{p}\ ^2[1/2]_1$
7	$ns n\mathrm{p}^6(^2\mathrm{S}_{1/2})k\mathrm{p}\ ^2[3/2]_1$

In the field-free basis, $\mathcal{H}_0$ is simply a diagonal matrix, with the energies of the photo-electron with respect to the lowest ionization threshold as matrix elements. In the weak-field limit, the partial-wave expansion is restricted to total angular momentum $J \leq 1$, i.e. no multi-photon processes are considered. Furthermore, ionization is only allowed from the outer np shell (photo-electron energies in the range 0 eV to 11 eV in the case of xenon), to avoid autoionization of embedded Rydberg states in the vicinity of the $ns n\mathrm{p}^6\ {}^2\mathrm{S}_{1/2}$ threshold. We also neglect mixing of singlet and triplet terms. Thus, the only non-zero matrix elements of the dipole operator z are $\langle i\varepsilon e|z|\Psi_0\rangle$ (and the complex conjugate), which are spin-averaged by BSR.

The analysis of the coherence is made using the density matrix formalism [Landau and Lifshitz 1977, §14], where the full *density matrix* operator is defined (time dependence t suppressed)

$$\rho_T = |\Psi\rangle\langle\Psi|, \tag{5}$$

with matrix elements of the continuum block

$$\rho^{e_1e_2}_{i_1i_2}(\varepsilon_1,\varepsilon_2) \equiv c^{e_1}_{i_1}(\varepsilon_1)c^{e_2*}_{i_2}(\varepsilon_2). \tag{6}$$

We reduce this density matrix to a ion–channel density matrix by first taking the trace over the photo-electron energies:

$$\begin{aligned}\rho_{ie} &\equiv \int \mathrm{d}\varepsilon\ \langle\varepsilon|\Psi\rangle\langle\Psi|\varepsilon\rangle \\ &= \int \mathrm{d}\varepsilon \sum_{i_1i_2}\sum_{e_1e_2}\int \mathrm{d}\varepsilon_1\,\mathrm{d}\varepsilon_2\ \langle\varepsilon|i_1\varepsilon_1e_1\rangle c^{e_1}_{i_1}(\varepsilon_1) \\ &\qquad\qquad \times c^{e_2*}_{i_2}(\varepsilon_2)\langle i_2\varepsilon_2e_2|\varepsilon\rangle \\ &= \sum_{i_1i_2}\sum_{e_1e_2}\int \mathrm{d}\varepsilon\ |i_1e_1\rangle\rho^{e_1e_2}_{i_1i_2}(\varepsilon,\varepsilon)\langle i_2e_2|.\end{aligned} \tag{7}$$

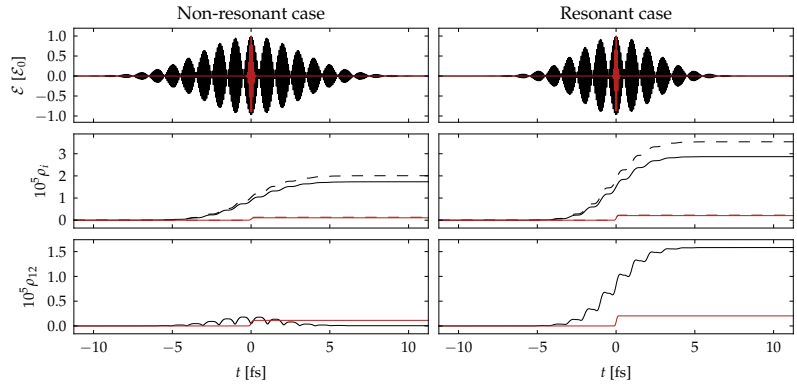

FIGURE 3: Real time coherence build-up, for the case of ionization with two harmonics, 13 and 14 of a fundamental frequency $d\Delta E_{s-o}$, in the non-resonant case ($d = 1.3$) left and the resonant case ($d = 1$) right. The upper panels show the driving fields used; the red curve correspond to a pulse duration (FWHM of the temporal intensity profile) of 500 as while the black curve correspond to a pulse duration of 15 fs. The middle panels show the populations in the residual ionic substates (solid: contribution from channel 3 to $^2P^o_{3/2}$; dashed: contribution from channel 5 to $^2P^o_{1/2}$), which increases with time. The lower panels show the induced coherence between the ionic substates, which is built up over time. For the short-pulse case, there is always coherence left at the end of the pulse, while for the longer pulse duration, the resonance criterion has to be fulfilled $d \approx 1$. The lower population in the non-resonant case is explained by the decrease in photoionization cross-section with increasing photon energy.

Finally, we construct the ion density matrix by tracing over the photo-electron angular momenta:

$$\begin{aligned}\rho_i &\equiv \sum_e \sum_{i_1 i_2} \sum_{e_1 e_2} \langle e|i_1 e_1\rangle \rho_{i_1 i_2}^{e_1 e_2} \langle i_2 e_2|e\rangle \\ &= \sum_e \sum_{i_1 i_2} |i_1\rangle \rho_{i_1 i_2}^{ee} \langle i_2|.\end{aligned} \tag{8}$$

Only channels for which all quantum numbers are the same (except for the angular momentum of the ion) are considered in (8); here only channels 3 and 5 in table 1 contribute. The diagonal elements (ρ_{mm}) of this matrix measure the population in each of the ionic states ($np^5\ ^2P^o_{3/2,1/2}$ and $nsnp^6\ ^2S$), while the off-diagonal elements (ρ_{mn}) contain the coherences between the ionic states. Decoherence due to the spin–orbit interaction is neglected.

3 RESULTS

We investigate the real time build-up of coherence with a XUV pulse of short or long duration in the general case (see figure 3; left-hand side: non-resonant case, right-hand side: resonant case). The electromagnetic fields are presented in the upper panels. In both cases, they consist of harmonics 13 & 14 of a fundamental driving field. The short-pulse duration is 500 as, while the long-pulse duration is 15 fs resulting in the formation of a periodic beating of the XUV pulse. Regardless of the pulse duration, the population in the ionic substates (middle shown in solid and dashed lines) increases as pulse ionizes the atom. The population is proportional to the integral of the pulse intensity, hence the appearance of steps in the population.

We first consider the non-resonant case (left panels of figure 3), where the fundamental driving frequency is $d = 1.3\Delta E_{s-o}$. For a short pulse duration, the coherence increases during the interaction and stays constant after the pulse has passed. In contrast for long pulse duration, the coherence is transiently built up and vanishes completely at the end of the pulse. The decoherence time, i.e. the time from the onset of the pulse to the decrease of the coherence (see lower panel of figure 3), is

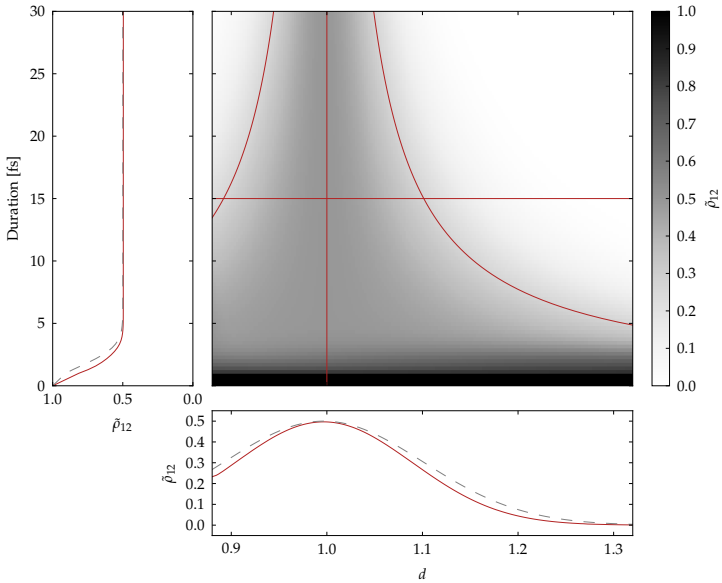

FIGURE 4: Degree of coherence as a function of pulse duration (FWHM of temporal intensity profile) and detuning ratio d. The hyperbolas in the main panel indicate the 'detuning bandwidth' within which $\tilde{\rho}_{12} > (2\sqrt{e})^{-1}$. The red horizontal/vertical lines mark lineouts at constant duration/detuning ratio, which are shown in the lower/left panels. The grey, dashed line in the lower panel is a Gaussian function whose width is the energy uncertainty for which 15 fs is the quantum beat period. Correspondingly, the grey, dashed line in the left panel is the combined overlap of four Gaussian functions (representing the electron spectral peaks), two centred at the same energy, and two offset by $\pm\Delta E_{s\text{–}o}$. At vanishing pulse duration, the spectral uncertainties of the Gaussian functions are infinite. As the pulse duration exceeds the quantum beat period, the peaks become spectrally resolvable, and the total overlap at the central frequency becomes half of that at vanishing pulse duration.

related to the quantum beat period of the ionic substates; for xenon with a spin–orbit splitting of 1.3 eV, it is 3.2 fs.

In the resonant case (right panels of figure 3), the situation is completely different. The coherence is built up during all the interaction time, and remains after the end of the pulse. The existence of this resonant condition can be understood by considering the population of the ionic substates (labelled $|1\rangle$ and $|2\rangle$, for simplicity) resulting from a periodic sequence of ionization events occuring at times t_k ($k \in \mathbb{N}$). The wavefunction is then

$$|\Psi(t_1)\rangle = c_1(t_1)e^{i\phi_{XUV}(t_1)}|1\rangle + c_2(t_1)e^{i\phi_{XUV}(t_1)}|2\rangle, \tag{9}$$

where ϕ_{XUV} is the phase of the ionizing XUV field at time t_1. At the kth event, the wavefunction becomes

$$\begin{aligned}|\Psi(t_k)\rangle =& c_1(t_2)e^{i\phi_{XUV}(t_k)}|1\rangle + c_2(t_2)e^{i\phi_{XUV}(t_k)}|2\rangle \\ &+ \mathcal{U}(t_k, t_{k-1})|\Psi(t_{k-1})\rangle,\end{aligned} \tag{10}$$

where $\mathcal{U}(t_k, t_{k-1})$ propagates the wavefunction from an earlier time step. The propagator can be written

$$\mathcal{U}(t_k, t_{k-1}) = \exp(-iH\Delta t), \tag{11}$$

where the Hamiltonian matrix (assuming no spin–orbit coupling) is

$$H = \begin{pmatrix} E_1 & 0 \\ 0 & E_2 \end{pmatrix}, \tag{12}$$

and $\Delta t \equiv t_k - t_{k-1}$ is the separation between the ionization events. Finally, the wavefunction reads

as

$$|\Psi(t_k)\rangle = \sum_{a=0}^{k} c_1(t_a) e^{i[\phi_{XUV}(t_a) - E_1(k-a)\Delta t]} \times \left[|1\rangle + \tilde{c} e^{-i\Delta E \Delta t(k-a)}|2\rangle\right], \quad (13)$$

where $\tilde{c} \equiv c_2(t_a)/c_1(t_a)$ (this ratio is assumed to be constant with t_a; i.e. it only depends on the relative photoionization cross-section) and $\Delta E \equiv E_2 - E_1$. The last factor expresses the fact that the periodic ionization does not introduce dephasing between the two substates, as long as

$$\Delta t = \frac{2\pi q}{\Delta E}, \quad (14)$$

is fulfilled, where q is a rational number. This is a generalization of the quantum beat period for an energy separation ΔE, which does not depend on the duration of the XUV pulse. In the spectral domain, this corresponds to requiring the final electron kinetic energy to be the same (for $q = 1$).

In order to assess to which degree the ionic states are coherent, we use the *degree of coherence*:

$$\tilde{\rho}_{mn} \equiv \frac{|\rho_{mn}|}{\sqrt{\rho_{mm}\rho_{nn}}}, \quad (15)$$

which normalizes the coherence between two ions to their respective populations. We study the degree of coherence, as a function of XUV pulse duration and detuning ratio (figure 4). For short pulse durations, this quantity is larger than ½ (left panel of figure 4). In this regime, the interaction with the XUV pulse occurs within one quantum beat period (3.2 fs), and the four pathways indicated in figure 2 into the continuum have a partial spectral overlap. For larger pulse durations, two of the pathways become distinguishable, and do not contribute to the coherence between the ionic substates. The two remaining pathways, namely via $\Omega_<$ leaving the ion in $P^o_{3/2}$, and $\Omega_>$ leaving the ion in $P^o_{1/2}$, are indistinguishable, provided the resonance condition $d = 1$ is met. The maximum degree coherence is ½. If $d \neq 1$, complete decoherence occurs in the long-pulse limit.

4 CONCLUSION

In summary, we have shown that it is possible to induce coherence using pulses of duration longer than the coherence time, provided a resonance condition is fulfilled, namely that the driving field has at least two frequency components spaced by the energy difference of the levels of interest. This result shows that when the electron wave packets arising from different pathways have the same kinetic energy, we cannot know which way the ionization occurred. This situation is reminiscent of a Young's double slit experiment.

5 ACKNOWLEDGMENTS

SCM acknowledges the help of Oleg Zatsarinny, and would like to thank Tomas Brage, Kevin Dunseath, and Andreas Wacker for helpful discussions. This work was supported by the Swedish Foundation for Strategic Research, the Swedish Research Council, the Knut and Alice Wallenberg Foundation, the European Research Council (PALP), and by funding from the NSF under grant PHY-1307083.

REFERENCES

Alvermann, A, H Fehske, and P B Littlewood (2012). 'Numerical time propagation of quantum systems in radiation fields'. *New Journal of Physics* **14**.10, p. 105008. DOI: 10.1088/1367-2630/14/10/105008.

Cowan, Robert (1981). *The theory of atomic structure and spectra*. Berkeley: University of California Press. ISBN: 0520038215.

Froese Fischer, Charlotte, Georgio Tachiev, Gediminas Gaigalas, and Michel R. Godefroid (2007). 'An MCHF atomic-structure package for large-scale calculations'. *Computer Physics Communications* **176**.8, pp. 559–579. DOI: 10.1016/j.cpc.2007.01.006.

Goulielmakis, Eleftherios, Zhi-Heng Loh, Adrian Wirth, Robin Santra, Nina Rohringer, Vladislav S. Yakovlev, Sergey Zherebtsov, Thomas Pfeifer, Abdallah M. Azzeer, Matthias F. Kling, Stephen R. Leone, and Ferenc Krausz (2010). 'Real-time observation of valence electron motion'. *Nature* **466**.7307, pp. 739–743. DOI: 10.1038/nature09212.

Klünder, K, Per Johnsson, Marko Swoboda, Anne L'Huillier, Giuseppe Sansone, M Nisoli, Mark JJ Vrakking, Kenneth Joseph Schafer, and Johan Mauritsson (2013). 'Reconstruction of attosecond electron wave packets using quantum state holography'. *Physical Review A* **88**.3, p. 033404. DOI: 10.1103/PhysRevA.88.033404.

Kurka, M, A Rudenko, L Foucar, KU Kühnel, YH Jiang, Th Ergler, Th Havermeier, M Smolarski, S Schössler, K Cole, et al. (2009). 'Two-photon double ionization of Ne by free-electron laser radiation: a kinematically complete experiment'. *Journal of Physics B: Atomic, Molecular and Optical Physics* **42**.14, p. 141002.

Landau, Lev Davidovich and Evgeny Mikhailovich Lifshitz (1977). *Quantum mechanics : non-relativistic theory*. 3rd. Vol. 3. Course of Theoretical Physics. Oxford New York: Pergamon Press. ISBN: 978-0-08-020940-1.

Magnus, Wilhelm (1954). 'On the exponential solution of differential equations for a linear operator'. *Communications on Pure and Applied Mathematics* **7**.4, pp. 649–673. DOI: 10.1002/cpa.3160070404.

Mauritsson, Johan, Thomas Remetter, Marko Swoboda, Kathrin Klünder, Anne L'Huillier, Kenneth Joseph Schafer, O. Ghafur, F. Kelkensberg, W. Siu, Per Johnsson, Marc J J Vrakking, I. Znakovskaya, T. Uphues, S. Zherebtsov, M. F. Kling, F. Lépine, E. Benedetti, F. Ferrari, Giuseppe Sansone, and M. Nisoli (2010). 'Attosecond and Electron Spectroscopy Using a Novel Interferometric Pump-Probe Technique'. *Physical Review Letters* **105** (5), p. 053001. DOI: 10.1103/PhysRevLett.105.053001.

Nikolopoulos, L. A. A. (2013). 'Time-Dependent Theory of Angular Correlations in Sequential Double Ionization'. *Physical Review Letters* **111**.9. DOI: 10.1103/physrevlett.111.093001.

Pabst, Stefan, Loren Greenman, Phay J. Ho, David A. Mazziotti, and Robin Santra (2011). 'Decoherence in Attosecond Photoionization'. *Physical Review Letters* **106**.5. DOI: 10.1103/physrevlett.106.053003.

Pabst, Stefan, Manfred Lein, and Hans Jakob Wörner (2016). 'Preparing attosecond coherences by strong-field ionization'. *Physical Review A* **93**.2. DOI: 10.1103/physreva.93.023412.

Saad, Yousef (1992). 'Analysis of some Krylov subspace approximations'. *SIAM Journal on Numerical Analysis*.

Salour, MM and C Cohen-Tannoudji (1977). 'Observation of Ramsey's interference fringes in the profile of Doppler-free two-photon resonances'. *Physical Review Letters* **38**.14, p. 757. DOI: 10.1103/PhysRevLett.38.757.

Teets, R, J Eckstein, and TW Hänsch (1977). 'Coherent two-photon excitation by multiple light pulses'. *Physical Review Letters* **38**.14, p. 760.

Tzallas, P., E. Skantzakis, L. A. A. Nikolopoulos, G. D. Tsakiris, and D. Charalambidis (2011). 'Extreme-ultraviolet pump–probe studies of one-femtosecond-scale electron dynamics'. *Nature Physics* **7**.10, pp. 781–784. DOI: 10.1038/nphys2033.

Zatsarinny, Oleg (2006). 'BSR: B-spline atomic R-matrix codes'. *Computer Physics Communications* **174**.4, pp. 273–356. DOI: 10.1016/j.cpc.2005.10.006.

Zatsarinny, Oleg and Charlotte Froese Fischer (2009). 'Atomic structure calculations using MCHF and BSR'. *Computer Physics Communications* **180**.11, pp. 2041–2065. DOI: 10.1016/j.cpc.2009.06.007.

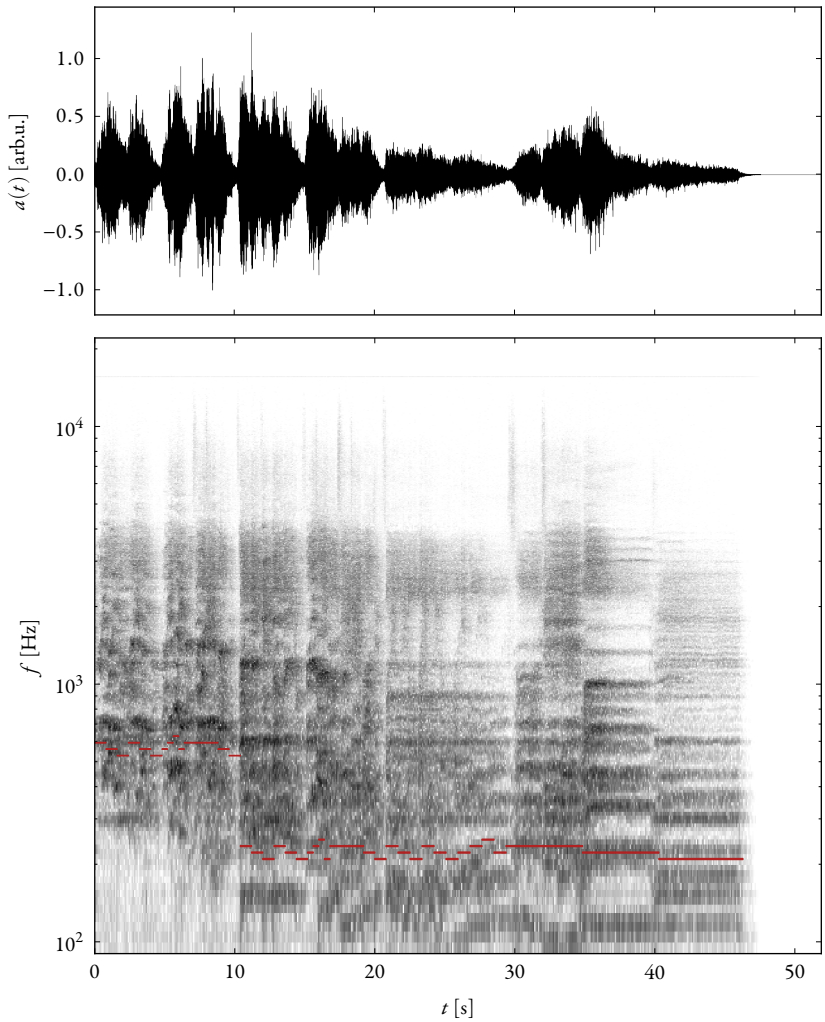

FIGURE Ω.1: The time–frequency representation of the score on p iii, as rendered in 1965 by the USSR Russian Academic Chorus under the conduction of Alexander Sveshnikov (Александр Васильевич Свешников; 1890–1980). Upper panel: the sound wave as a function of time. Lower panel: the same signal represented simultaneously in the time–frequency domain, visualizing the time-dependent frequency content variation of the signal. Indicated in red is the nominal pitch of the lead voice; the pattern is reproduced at higher frequencies, the harmonics of the fundamental.